UNIVERSITY OF Southampton

University of Southampton Research Repository
ePrints Soton

Copyright © and Moral Rights for this thesis are retained by the author and/or other copyright owners. A copy can be downloaded for personal non-commercial research or study, without prior permission or charge. This thesis cannot be reproduced or quoted extensively from without first obtaining permission in writing from the copyright holder/s. The content must not be changed in any way or sold commercially in any format or medium without the formal permission of the copyright holders.

When referring to this work, full bibliographic details including the author, title, awarding institution and date of the thesis must be given e.g.

AUTHOR (year of submission) "Full thesis title", University of Southampton, name of the University School or Department, PhD Thesis, pagination

http://eprints.soton.ac.uk

University of Southampton

Faculty of Engineering, Science and Mathematics

SCHOOL OF CIVIL ENGINEERING AND THE ENVIRONMENT

New approach to tidal stream energy analysis at sites in the English Channel

L. S. Blunden

Thesis submitted for the degree of Doctor of Philosophy

February 2009

UNIVERSITY OF SOUTHAMPTON

ABSTRACT

FACULTY OF ENGINEERING, SCIENCE AND MATHEMATICS
SCHOOL OF CIVIL ENGINEERING AND THE ENVIRONMENT

Doctor of Philosophy

EVALUATION OF TIDAL STREAM ENERGY RESOURCES AT SITES IN THE ENGLISH CHANNEL

by Luke Stephen Blunden

Tidal stream power generation offers the prospect of predictable, low-CO_2 power at a number of locations around the UK and the world. Previous assessments of tidal energy resources have taken the form of desk studies based on simplified navigational data. Where numerical model data has been used it has been at too low a resolution to capture high velocity tidal flows constrained by coastal topography. Analytical solutions for maximum energy extraction in simple tidal channels have been produced, but they have not been extended to more complex open-boundary cases such as flow around headlands and islands. There is therefore a role for site-specific numerical modelling, which when validated, offers the twin advantages of a high-resolution picture of the resource and allowing simulation of momentum extraction within the model to take place.

In order to parameterize the sub-grid-scale momentum extraction in such models, a new analytical model of the velocity reduction in a large array of tidal turbines has been derived. The model extends previous models of large wind turbine arrays and uses analogies with flow through submerged vegetation. It provides an equivalent added drag coefficient suitable for use in a 2-D coastal numerical model.

A numerical model of the flows in the region of the Portland Bill headland has been produced, forced by tidal elevations at the free boundary. A site selection exercise was carried out for the Portland Bill location and an area of around 12 km^2 was identified as having a high potential for development using mean cubed speed found through tidal analysis of model results without energy extraction.

A large tidal stream generator array has also been simulated within the Portland Bill model—linked to the new model for momentum extraction—and was found to have a significant effect on the tidal parameters in the locality. This was the first time that a large tidal array has been simulated in a realistic coastal domain of large extent, with a parameterization that takes into account the interaction of the turbines with the rough-wall flow in the natural state. Results predict that there is a region downstream of the array extending approximately 5–10 km around the simulated tidal stream turbine array in which the tidal stream ellipse major axis is reduced by at least 5%. In the area of momentum extraction the principal semi-diurnal tidal stream ellipse major axis length was reduced by 10–15%.

Contents

List of Figures

List of Tables

DECLARATION OF AUTHORSHIP

I, Luke Stephen Blunden

Declare that the thesis entitled:

Evaluation of tidal stream energy resources at sites in the English Channel

And the work presented in the thesis are both my own, and have been generated by me as the result of my own original research. I confirm that:

- this work was done wholly or mainly while in candidature for a research degree at this University;
- where any part of this thesis has previously been submitted for a degree or any other qualification at this University or any other institution, this has been clearly stated;
- where I have consulted the published work of others, this is always clearly attributed;
- where I have quoted from the work of others, the source is always given. With the exception of such quotations, this thesis is entirely my own work;
- I have acknowledged all main sources of help;
- where the thesis is based on work done by myself jointly with others, I have made clear exactly what was done by others and what I have contributed myself;
- parts of this work have been published in the references listed in Appendix A

Signed: ....

Date: ....

Acknowledgments

Bathymetric data from Portland was provided by Dr. Alex Bastos, formerly of the National Oceanography Centre, Southampton.

Tide gauge and current meter records from UK locations were obtained from the British Oceanographic Data Centre (BODC).

Tide gauge records from locations in France were obtained from Système d'Observation du Niveau des Eaux Littorales (SONEL).

TASK tidal analysis code © Proudman Oceanographic Laboratory. 1999.

T_TIDE tidal analysis toolbox for MATLAB by Pawlowicz et al. (2002).

The TÉLÉMAC system, TÉLÉMAC-2D, MATISSE and RUBENS © Électricité de France—Direction des Études et Recherches (EDF-DRD), Département Laboratoire National d'Hydraulique (LNH). Distributed in the UK by HR Wallingford.

MATLAB © The Mathworks, Inc. 1994–2008.

Ordnance Survey maps and data obtained from Digimap (`http://edina.ac.uk/digimap/`). Crown Copyright.

I would like to thank my supervisor Prof. AbuBakr Bahaj and my colleagues William Batten, Luke Myers and Ivan Haigh for helpful comments and advice during the project.

This document was produced in LaTeX

To Dad, Mum, Nathan and Christelle

Sonnet LXX:
On being cautioned against walking on an headland overlooking the sea, because it was frequented by a lunatic.

Is there a solitary wretch who hies
    To the tall cliff, with starting pace or slow,
And, measuring, views with wild and hollow eyes
    Its distance from the waves that chide below;
Who, as the sea-born gale with frequent sighs
    Chills his cold bed upon the mountain turf,
With hoarse, half-utter'd lamentation, lies
    Murmuring responses to the dashing surf?
In moody sadness, on the giddy brink,
    I see him more with envy than with fear;
He has no nice felicities that shrink
    From giant horrors; wildly wandering here,
He seems (uncursed with reason) not to know
The depth or the duration of his woe.

Charlotte Smith (1749-1806)

Nomenclature

a	Amplitude of tidal elevation difference	m
A	Area	m^2
A_c	Area of channel cross-section	m^2
A_r	Area of generator rotor disk	m^2
c_f	Sea-bed drag coefficient $= \tau/\frac{1}{2}\rho u_h^2$	
c_P	Power coefficient	
c_d	Isolated turbine drag coefficient $= T/\frac{1}{2}\rho u_h^2 A$	
d	Distance from the centre of mass of the earth to an astronomical body	m
l	Distance from a point on the earth's surface to an astronomical body	m
$\dot{E}$	Energy flux per unit width	J/m/s
ΔE_G	Change of specific potential energy	J/kg
f	Nodal amplitude correction factor	
Fr	Froude Number of channel $= \frac{U\sqrt{W}}{\sqrt{gA_c}} = \frac{U}{\sqrt{gH}}$ for a rectangular channel	
g	Acceleration due to gravity	9.81 m/s^2
G	Gravitational constant	$6.67 \times 10^{-}11$ m^3/kg/s^2
H	Geometric roughness height, turbine hub height	m
H	Amplitude of sea surface elevation harmonic constituent	m
h	Depth of water	m
κ	Von Kármán constant $= 0.4$	
K	Channel calibration constant	m^5/s^2
M	Mass of an astronomical body	kg
m	Mass	kg
M_E	Mass of the earth	kg
N	Number of turbines in array	
P	Power developed by generator	W

Q	Flow rate in channel	m^3/s
t	Time GMT	hour
T	Drag on isolated turbine	N
u	Nodal phase correction	°
u	Spatially-averaged mean velocity	m/s
U	Complex velocity of tidal stream ellipse	m/s
U	Flow speed	m/s
$\overline{U^3}$	mean cube flow speed over 18.6 year period	$(\mathrm{m/s})^3$
$\left\langle\overline{U^3}\right\rangle$	spatial average of time mean cube speed	$(\mathrm{m/s})^3$
u_*	Friction velocity	m/s
u, v	Velocity components	m/s
V	Equilibrium phase of harmonic constituent	°
W	Width of free surface	m
x	Longitudinal coordinate	m
X	General variable	
y	Latitudinal coordinate	m
z	Vertical coordinate	m
Z	Free surface elevation	m
z_0	Roughness length of sea-bed	m
α, β	Complex amplitudes of tidal stream ellipse	m/s
δ	Boundary layer thickness	m
ϵ_r	Relative error	
ϕ	phase of harmonic constituent	°
λ	Ratio of frontal area of obstacles or turbines to array area parallel to flow	
ν	Kinematic molecular viscosity	m^2/s
ν_t	Turbulence viscosity	m^2/s
ω	Angular speed of harmonic constituent	°/hour
ρ	Density of fluid	$\mathrm{kg/m}^3$
τ	Frictional stress on sea bed	$\mathrm{N/m}^2$
θ	Orientation of tidal stream ellipse major axis	°
ψ_h	Roughness sub-layer influence function	

Ω	Angular speed of rotation of the earth	7.29×10^{-5} rad/s
ζ	difference in surface elevation between channel ends	m

Subscripts

$+$	Far downstream of the leading edge of obstacle or turbine array
$-$	Upstream of the leading edge of obstacle or turbine array
0	Undisturbed
a	array
r	rotor disk
i	node number in finite element mesh
k	harmonic constituent
$\max$	Maximum
r	rated (thrust or power of turbine)
R	Radius of the earth
x	along x axis

Chapter 1

Introduction

1.1 Overview

1.1.1 The need to reduce carbon dioxide emissions

Working Group I (WG–1) of the Inter-governmental Panel on Climate Change found, in its fourth assessment report on the Physical science basis, that it was 'very likely'* that anthropogenic greenhouse gas increases contributed to sea-level rise and caused most of the observed increase in global average temperatures since 1950 (Solomon et al. 2007). It was further predicted that these trends in sea-level and temperature will continue and may accelerate over the next one hundred years. The second working group, on Impacts and adaptation, gathered a large amount of evidence that the net impacts of anthropogenic climate change will be negative to human life, both in the short and long term, through phenomena such as increased coastal flooding, ocean acidification and species extinction (WG–2). The third working group found but that cuts in emissions are likely to reduce these impacts and also have knock-on benefits (WG–3). Carbon dioxide emissions (CO_2) contribute 70% to the total potential effect of greenhouse gases and therefore are the most important to target for reductions. In response to such concerns, the UK Government's Climate Change Bill (UK Government 2007) aims to achieve at least a 60% reduction in carbon dioxide emissions by 2050, and a 26%

---

[*] greater than 90% probability

reduction by 2020, with respect to emissions in 1990.

1.1.2 Carbon dioxide emissions from electricity generation

Carbon dioxide from electrical power generation was estimated to make up 32% of all CO_2 emissions in the UK in 2006 (UK Department of Trade and Industry 2006, ch. 5) and therefore reducing such emissions must play an important part in an overall UK greenhouse gas reduction strategy. In 2007, UK electricity generating capacity from non-fossil fuel as a proportion of total capacity consisted of 13% nuclear, 1.7% hydroelectric and 2.6% of other renewables. The actual proportion of energy supplied by these sources reflect the high capacity factor of nuclear in comparison to other forms of generation; 19% nuclear, 1.2% hydroelectric and 3.6% of other renewables, as a proportion of total electrical energy supply.

It is important to note that over its life cycle, non-fossil-fuelled electrical power generating plant will nevertheless result in some CO_2 emissions due to for example the extraction, processing and transportation of raw materials; fabrication and construction; maintenance and decommissioning of the plant. These emissions are normalized with respect to the total actual or predicted electrical energy generated over the lifetime of the plant. Typical figures quoted for nuclear are around 10–100 gCO_2/kWh (Sovacool 2008) compared with 10 gCO_2/kWh for hydroelectric and wind or 100 gCO_2/kWh for photovoltaics (Pehnt 2006). As a reference, coal-fired power stations emit around 1000 gCO_2/kWh over a lifetime (Weisser 2007). A recent study of a prototype tidal stream turbine, indicated similar values to those given for wind power (Douglas et al. 2008). It is important to note that the field of life-cycle assessment is a controversial one, involving a large number of assumptions that may be incorrect, or be used by vested interests to promote their preferred technologies.

The UK will lose two-thirds of its existing (2007) nuclear capacity by 2020 and none of the stations due for closure are likely to be replaced by that date; a recent government report has suggested that developing new nuclear power stations would take around fourteen years (UK Department of Trade and

Industry 2007a).

One way to maintain the UK's electrical capacity while not increasing (and ideally decreasing) CO_2 emissions would be to import electricity generated from non-fossil fuel sources abroad. A HVDC interconnector with France has existed since 1986 and is capable of transmitting 2 GW. The UK is a net importer, drawing on base-load nuclear generation in France. However, imports are limited by the capacity of the interconnector and the price of French electricity. A similar 500 MW link exists to Northern Ireland and an additional 1 GW link to the Netherlands is planned for 2010 (National Grid 2008). For a number of years an interconnector with Iceland has been discussed to make use of that country's abundance of easily extractable renewable energy resources. This would require over 1000 km of sub-sea cable-laying just to make landfall in Scotland, and would entail significant power losses along the route. Once again, the maximum power transmitted would be limited, to around 600 MW (Landsvirkjun 2008). In summary, imports of renewable electricity will not be sufficient to replace or increase the UK's non-fossil fuel generating capacity.

1.1.3 The role of renewable generation in reducing emissions

If the UK is to meet its CO_2 reduction targets and maintain sufficient generating capacity to meet demand, it is clear that a rapid increase in renewable electricity generation capacity would be desirable.

In addition to the need to reduce CO_2 emissions, security of supply is a concern for the UK as indigenous North Sea oil and gas production has peaked and since 2005, the UK has been a net importer of those commodities. Coal imports are greater than indigenous production by a factor of around five to one and all uranium for nuclear power must be imported (UK Department of Trade and Industry 2007b).

In contrast to imported fossil fuels, the cost of indigenous renewable energy generation is not sensitive to volatility in fuel price due to market speculation, external political factors or the underlying trend of increasing costs of fossil fuel extraction as proven reserves are exhausted. Neither is renewable power associated with the real or perceived risks of transportation, containment and disposal of radioactive materials used in nuclear reactors.

The projected cost of energy required for a new renewable generating plant is, in most instances, greater than that of fossil fuel generation, particularly when it is the marginal cost of increasing the output of existing fossil-fuelled plant that is being compared. As a consequence, market forces alone are not sufficient to bring about the rapid growth of renewable generation, independently of unpredictable increases in the cost of fuel. A report commissioned by the UK government in 2005 found that even mature technologies such as onshore wind and sewage gas combustion would be unlikely to be commercially viable within a decade, without government support (Oxera 2005).

1.1.4 Measures to support the growth of renewables

The principal existing mechanism to support the growth of renewable energy in the UK is the Renewables Obligation, introduced by the UK Government in 2002 (UK Department of Trade and Industry 2006), which forces power suppliers (retailers) to either source a minimum proportion of their energy from renewable means—set at 9.1% in 2008—or 'buy-out' Renewables Obligation Certificates (ROCs), equivalent to 1 MWh, to make up the difference. These may be bought from a central authority at a set price per unit of energy, linked to inflation and currently around £35/MWh. However, this represents a cost to the retailer as there is no return on the certificates purchased through this source. The money raised by the central sale of ROCs is then redistributed to the retailers according to the number of ROCs that they have sourced from renewable power generators, as a proportion of the total. ROCs are bought and sold in regular auctions independently of the central authority and currently raise around £51/MWh for renewable generators (e-ROC 2008). Revenue from the sale of ROCs is independent of any revenues raised through the sale of electricity. The cost of the subsidy is ultimately passed on to energy consumers, through increased bills. By 2010, the cost of the subsidy will represent 5.7% of the average cost of electrical energy (National Audit Office 2005). This mechanism has claimed a degree of success as renewable energy supplied in the UK has increased as a proportion of total electrical power generation from 1.8% in 2002 to 4.8% in 2006, largely through the rapid expansion of onshore and offshore wind power (UK Department for Business, Enterprise and Regulatory Reform 2007). The Renewables Obligation is expected to continue at least until 2027, by which time it is hoped that at least some renewable generating technologies will have achieved commercial viability. In 2008, the UK Government indicated that banding of the Renewables Obligation will be introduced from 2009 in order to support currently emerging renewable technologies, by awarding them up to two Renewables Obligation Certificates per MWh generated (UK Department of Trade and Industry 2008). Significantly, tidal stream turbines will be among the technologies entitled to 2 ROCs/MWh, while offshore wind will be in the band below, at 1.5 ROCs/MWh and mature technologies such as onshore wind turbines, energy from waste and hydro-electricity will only be entitled to 1 ROC/MWh or fewer.

1.1.5 Tidal stream power and its competitors

After the support measures for new renewable energy described above are taken into account, new tidal stream power generation must compete for investment with other generating technologies, on the basis of cost of energy. It might be expected that the cost of energy generated by tidal stream power could not be less than that of offshore wind turbines—even assuming a similar level of technological maturity—for while the technologies are similar, the nature of sub-sea work in deep, fast tidal currents is more onerous. Proponents of tidal stream power point to a major potential advantage of tidal over offshore wind, namely the predictability of tidal phenomena (Fraenkel 2007). Under the New Electricity Trading Arrangements (NETA) in the UK, contracts for generation may be struck on time-scales varying from hours to years (Office of Gas and Electricity Markets (OFGEM) 2002). In theory, this would make a unit of tidal-generated energy more valuable than the same amount of wind-generated energy—if traded under these arrangements—as the probability of under-generating would be much less in the case of tidal.

Up until the present decade, tidal stream power has been considered too expensive to be competitive with other generating plant in all but a few niche applications. However, the more favorable regulatory framework and political climate, combined with technology transfer from on- and offshore wind generation, have led in recent years to private and public funds being invested in prototype tidal stream turbines. At the time of writing there are more than ten companies who have got to the stage of developing a scale physical model and/or a prototype tidal stream turbine and are still actively pursuing the development of their device:

Demonstration Marine current turbines, Hammerfest Strøm, Verdant Power

Prototype Atlantis, Ponte di Archimede International, Open Hydro, Tocardo, Hydrohelix, Pulse tidal, Underwater Electric Kite, Clean Current

Scale model Lunar Energy, Swanturbines, Eolpower/PSTML, Ocean Flow Energy, Tidal Generation

The breadth of competition and—crucially—the involvement of major energy generating utilities, are evidence that there are many who believe that tidal stream devices will ultimately provide a reasonable return on investment. Whether this will be the case when subsidies end remains to be seen.

1.1.6 Key uncertainties for tidal stream power

1.1.6.1 Sparse field data for tidal streams

While in theory, tidal streams may be predictable for years ahead, in practice, assessment of the available energy resource relies on possessing a suitable data-set for that location, with adequate coverage in space and time. As will be discussed in §7 and §9, in many locations such data are sparsely distributed and are rarely in primary form. Simple interpolation is an option in such cases, used in resource assessments reviewed in §2.6, but may be inaccurate where there are significant changes in topography and flow velocity in space.

Before an expensive hydrographic survey is commissioned—which is limited to a small area of sea and carries the risk of no data return—it would be desirable to obtain a first estimate of the resource over an area wide enough to include all possible generator locations within a general site area, but with resolution detailed enough to include details of the flow at spatial and temporal scales relevant to an array of turbines.

Scale physical models of tidal seas have been constructed in the past (LEGI 2008), but are expensive and difficult to develop due to complex geometry and the need to rotate the entire model to simulate the rotation of the earth. By contrast, comparatively cheap numerical models have proven successful in the field of operational oceanography at reproducing tidal elevations at coastlines. These models have been forced at their external boundaries, with validation or tuning provided with respect to interior (within the modelling domain) data (Flather 2000). Accurate reproduction of tidal streams is more difficult to achieve, partly because velocity components are usually unknown on the open sea boundary and also due to the nature of the governing equations of motion where velocities are more sensitive to topography than are elevations.

It is possible to create numerical models that assimilate interior velocity and elevation data as a constraint to the solution of the governing equations, making more direct use of available survey data and reducing the requirement for accurate boundary conditions (Egbert and Erofeeva 2002). This method can be used to estimate unknown parameters such as sea-bed roughness and open-boundary velocities. Where relatively well-spaced interior data are available e.g. from satellite altimeter or ground based radar back-scatter returns, this method has produced reasonable results. However, the sparsity of such data in coastal regions and the relative complexity of this approach have meant that it has not yet gained wide acceptance (Lee and Davies 2001). To summarize, boundary-forced numerical models remain the most effective way to intelligently interpolate the available data, for the purpose of resource assessment.

1.1.6.2 Effects of arrays of turbines on tidal flows

A separate but related uncertainty are the possible effects that a large number of tidal turbines would have on the local tidal regime. Being able to predict these effects is important, for two main reasons. Firstly, from the perspective of environmental impact assessment, 'downstream' changes in flow velocity will need to be estimated and any possible knock-on effects considered, for example on sediment transport. Second, if tidal stream power grows to the stage where developers are competing for sites within areas where there are existing tidal stream arrays, prospective developers will need to estimate what, if any, reduction in energy output may be expected from the existing arrays. Field data on these effects are lacking, as arrays of turbines are yet to be constructed, although lessons may be learnt from wind turbine arrays (§6). Physical models of arrays using simulators such as mesh fences or disks can provide valuable insights but are restricted to unidirectional flow in a flume. A way of generalizing the approach to any location would be some form of parameterization of arrays within the type of numerical models discussed above in §1.1.6.1. A recent desk study, the UK Tidal Stream Energy Resource Assessment (Black and Veatch Ltd 2005) highlighted the need for modelling of potential sites to ascertain what are the local effects energy extraction upon the tidal flow.

1.1.6.3 Spacing of generators in large arrays

In conjunction with assessment of the effects of large arrays on the flow, the optimum spacing of generators needs to be established. There are two competing objectives in determining the longitudinal spacing of units in an array of turbine generators, whether wind or tidal:

1. To make the array as compact as possible in order to both maximize the flow capture area of the array and to minimize the extent of cable-laying and other works required.
2. To make the inter-unit spacing large enough to minimize the downstream velocity deficit at each successive row, caused by upstream turbines.

The result is a compromise, where the wake does not fully recover to free-stream conditions before encountering the next turbine in the row of an array. The per-unit power loss of an array of wind turbines when compared to the first row facing the wind is thought to be of the order 10-20%, so there is scope for optimization of the longitudinal spacing of turbines within the available area (Barthelmie et al. 2007). The area might be limited in size either by natural constraints of topography or flow speed; or artificial constraints such as sea-bed licensed to the developer. In a given case this optimization would take into account the aggregated energy yield (income) of the project in present value, offset against the capital and operational expenditure (related to the number of devices). Before this can be carried out, it is necessary to be able to predict the power output of the array as a function of relative spacing between generating units.

For the first commercial arrays of tidal turbines, the uncertainty involved in wake interactions may be avoided by configuration in a single row normal to the predominant flow direction. Tidal turbines have an advantage in this case with respect to wind turbines as tidal flows are mainly rectilinear, so the units in a single-row tidal turbine array may have much closer lateral spacing than a wind turbine array. Despite this advantage, individual units are limited in size by the depth of water and if tidal stream arrays are to make a significant contribution to sustainable power generation on a national scale, then multiple row arrays will need to be built. Therefore, the interaction of wakes and the overall performance of large tidal arrays needs to be considered.

1.1.7 Summary

Reductions in carbon dioxide emissions from the UK are required to demonstrate the nation's commitment to international cuts which, if implemented on a global scale, may in turn mitigate the negative impacts of climate change on human life. Emissions from electrical power generation represent an important source of CO_2 in the UK and will grow by 2020 unless there is a rapid expansion in renewable energy. Tidal stream power is among the renewable technologies competing for new investment, supported by incentives, but currently yet to be commercialized. In order for tidal stream power to be competitive, the potential advantage of the predictability of tidal streams needs to be realized by a methodology for resource assessment that can take account of local site characteristics, the dynamics of the sea and the performance of the tidal stream generators themselves.

1.2 Aim and Objectives

The principal aim of this work is to investigate the simulation of tidal stream generator arrays using coastal hydrodynamic numerical models. This aim will be fulfilled through the following objectives.

Objective 1

Evaluate sources of data for use in tidal stream energy resource assessment.

These sources of data fall broadly into the categories of bathymetric data, coastal tide gauge data and tidal stream data; the availability of data will partially determine the site or sites to model.

Objective 2 *Develop a coastal numerical model of a site or sites with high potential for tidal stream power.*

The results of the model will be used for two main purposes. Firstly for selecting specific sub-sites within a larger site area with potential for development based on tidal parameters. Secondly in order to provide a baseline case to compare with the cases where momentum and energy extraction are simulated. The model will be constructed using the data processed under Objective 1 above.

Objective 3 *Develop methods for parameterizing the effects of tidal stream generator farms within the numerical models.*

The parameterization of turbine drag may then be used to investigate the effects of a possible tidal stream generator array upon the mesoscale (order 10 km) tidal flow patterns. This methodology may be used to estimate the potential knock-on effects on the coastal environment and on other existing or planned tidal stream developments in the region. Where possible, these models should be validated against experimental data.

1.3 Scope

The geographic scope of this research project is limited to sites in the English Channel, including sites around the Channel Islands and Portland Bill. The justification for this decision is that the Channel poses a well constrained problem as there are tide gauge data available at a number of locations along both land boundaries; other sites (particularly in Scotland) are the subject of research by other groups.

Moreover, a large proportion of the UK's conventional generation is based in sparsely populated areas of the UK, far from load centres and requiring a considerable North-South flow of power (around 10 GW), with associated transmission losses. This situation is mirrored on a smaller scale by renewable generation, for example in the South East region. The National Grid Company has estimated the effectiveness of new generation in the Central South Coast and South West Zones as 110% compared to less than 95% for zones 7 and northwards [†]. 'Effectiveness' was defined in this context as the power supplied, minus transmission losses, expressed as a percentage of the power supplied (National Grid Company plc 2005, Chapter 7, page 20).

The data used in the project to construct and validate numerical models will be limited to that supplied by third-parties, as there are not the funds or time available to commission hydrographic surveys for the purpose of this work.

1.4 Document structure

This thesis is divided into the following chapters:

Chapter 2 Literature review covering previous research into the field of tidal stream power generation.

Chapter 3 Theoretical background to tides and analysis of tidal signals.

Chapter 4 Derivation of the hydrodynamic equations used to model tidal flows in a coastal setting

---

[†] The southern boundary of Zone 7 stretches from St. Bee's Head to Robin Hood's Bay

Chapter 5 Details of the methodology applied in setting up the TÉLÉMAC numerical model, applied later in Chapters 8, 9 and 10

Chapter 6 Application of boundary layer, wind turbine and hydraulic theory to tidal turbine arrays, in order to develop new models of energy extraction by large arrays of tidal turbines.

Chapter 7 Analysis and comparison of available tidal stream data from navigational and primary sources at sites of interest in the English Channel.

Chapter 8 Development of a numerical model of the English Channel for the purpose of providing exterior boundary conditions for more localized models.

Chapter 9 Development of a localized numerical model of the Portland Bill headland for the purpose of site selection.

Chapter 10 Enhancement of the Portland Bill model to include the effects of energy extraction.

Chapter 11 Overall discussion of results, conclusions and recommendations for future work.

Chapter 2

Review of tidal power generation

2.1 Tidal barrages

Tidemills have existed for centuries on tidal rivers; a local example is at Eling (Southampton, UK), mentioned in the Domesday Book in 1086 and grinding flour commercially until the 1930s. Around the same time that the Eling tidemill was falling into disrepair, tidal barrages were being considered for the purpose of electrical power generation; a medium-sized scheme proposed in 1933 for the River Severn would have generated 240 MW on average and supplied 8% of UK electricity demand at the time, had it gone ahead (Ministry of Fuel and Power 1945). In the subsequent seventy-five years, tidal mega-projects in the Severn, the Bay of Fundy and Îles Chausey have not materialized and nuclear power has grown to provide the majority of non-fossil-fuelled generation in those countries. More modest schemes such as La Rance with an installed capacity of 240 MW; Annapolis-Royal (Canada, 18 MW); Jiangxia (China, 3.2 MW) and Kislogubskaya (Russia, 400 kW) have succeeded, albeit on a much reduced scale (Charlier 1997). Tidal barrage schemes form a subset of well-established hydroelectric installations, at the lower end of the range of static head-difference. Consequently, high flow-rates are needed to generate significant amounts of power, which requires the use of large, propeller-type, bulb or Straflo turbines (Bosc and Megnint 1984). The technologies involved in tidal barrage schemes—such as turbine installations, caisson construction, embankments, ship locks and sluice gates—are all mature and have been described in detail by Baker (1991).

The potential resource for a barrage scheme is simply related to the basin area A, the tidal range R and the frequency f of the principal tidal constituent (although all schemes proposed so far have been in semi-diurnal tidal regions).

$$\overline{P} = k\rho g A f R^2 \tag{2.1}$$

where k is a coefficient depending on the efficiency of the turbines, the effect of head losses and the proportion of the tidal period over which the barrage is generating. The cost of the scheme is further constrained by the length of embankment required necessary to enclose the basin and the number of sluice gates, ruling out multiple basin schemes (Hammons 1993). Experience with the La Rance scheme has indicated that the most economical mode of operation of a tidal barrage is single-effect i.e. generating on the ebb tide only (Watson and Shaw 2007). Equation 2.1 has been used as a reference for comparison with a tidal stream scheme at the mouth of an enclosed bay by Garrett and Cummins (2004), reviewed in more detail in §2.2.

2.2 Tidal fences

To make progress in understanding the performance of tidal stream generators in real conditions, in the context of resource assessment, simplified analytical models have been developed to try and establish relationships between the power extracted and the changes in flow conditions. An analogy can be made between power transfer in hydraulic channels and flow in alternating-current electrical circuits (Miles 1971; Snyder 1980), but the analogy is not exact as hydraulic friction is quadratic in flow speed, whereas electrical resistance varies linearly with current.

In Garrett and Cummins (2004), the authors initially considered a turbine in the free-stream and then the case of turbines partly blocking a closed conduit. There was assumed to be no decrease in pressure (below that of far-upstream) immediately behind the rotor disk, contrary to the classic analysis. This lacked realism as it did not allow for expansion of the wake and resulted in a much reduced maximum c_p in the free-stream case of 0.38. As an aside, wake blockage corrections—originally derived for wind turbine rotors in wind tunnels—were applied to a horizontal axis tidal turbine in a closed water tunnel Bahaj et al. (2007a). These corrections are important for translating results from model to full-scale and have not been explicitly reported elsewhere in the existing literature on scale testing of tidal turbines (see §2.3).

The second part of Garrett and Cummins' paper considered power generation at the mouth of an enclosed bay subject to sinusoidal elevation variation. The theoretical maximum average power achievable by a barrage scheme in unidirectional operation (the most likely scheme from an economic point of view) was compared to a scheme with tidal stream generators located at the bay entrance, modelled as a resistance proportional to the square of current speed. The force applied by the turbines was assumed to be uniform across the mouth of the bay. It was found that the tidal stream scheme could generate 76% of the maximum possible average power from the tidal barrage scheme, while maintaining the tidal range inside the bay at 74% of that outside. Increasing the tidal range inside the bay to 90% of that outside did not result in a large loss in average power (down to 67%), from which the authors argued that a tidal stream power generation scheme at the entrance of an enclosed bay could give a power output comparable to a barrage scheme, but with far less impact on the flow regime inside the bay. This is a result of interest, for example, for those reconsidering the Severn tidal barrage scheme in the UK. However as the authors admit, the analysis did not include energy losses (other than introduced by turbines) at the mouth of the bay, which are likely to be significant.

The analysis was extended to a channel of gradually-variable cross section between two large bodies of water in Garrett and Cummins (2005), subject to sinusoidal surface elevation difference between its ends. The equation of motion was solved in integral form (integrated between the ends of the channel), including terms representing bed friction; drag due to tidal stream generators; advection of momentum from the channel due to a jet formed at the exit, where the flow separates from the channel sides.

For the case of a lossless channel, the maximum average power P_{max} that could be generated by turbines modelled as a linear resistance in flow speed was $\frac{1}{4}\rho g a Q_{max}$, where Q_{max} was the maximum flow-rate in the channel over a tidal period in the absence of turbines and a was the amplitude of the difference in surface elevation between the ends of the channel.

The maximum flow-rate in the channel was reduced to 71% of that in the absence of turbines and friction. Now linear resistance is not physical, but the authors showed by numerical solution that the maximum power for the case of turbine resistance proportional to the square of flow speed (again in a lossless channel) was only 3% less than the linear case. The change in maximum flow-rate was more significant; it was reduced to 53% of that in the absence of turbines and friction.

The ratio of P_{max} to the mean kinetic energy flux was found and it was shown to depend on the flow speed, not simply on the physical characteristics of the channel. From this the authors argued that the mean kinetic energy flux was not a useful guide to the power that could be extracted from the channel, as there was no simple relationship between the two. This argument only applies to the case where energy losses in the channel are small in the natural state and the momentum equation is a balance between pressure difference and flow inertia. Real tidal channels are likely to be subject to significant energy losses, the balance being mainly between pressure difference and friction with the current and elevation difference nearly in phase (Pugh 1987). This situation was also considered in Garrett and Cummins (2005) and the maximum average power extractable found to be $0.21\rho g a Q_{max}$. The flow rate in this case was reduced to 58% of that in the natural state.

The relationship $Q^2 = K\zeta$ applies to such channels, where K is a calibration constant for a particular channel and ζ is the water surface elevation difference between the two ends of the channel. As the pressure is assumed hydrostatic, ζ is proportional to the pressure difference, so this problem is analogous to unsteady emptying of a container. The constant K can be evaluated using only a limited set of current meter observations; tidal stream velocities can then be calculated using tidal elevation data, which are easier and cheaper to obtain (Wilcox 1958). It can then be shown that the ratio of P_{max} to the mean kinetic energy flux is $1.01A_c^2\, g/K$, where A_c is the cross-sectional area of the channel.

This ratio only depends on the channel, not on the tidal forcing (neglecting second order effects), but is not necessarily less than unity.

The sensitivity of the solutions of the equation of motion to the amount of energy dissipation within the channel was further investigated by Garrett and Cummins (2005) and it was found that for all values of combined friction and separation losses, the maximum average power that could be generated was $(0.22 \pm 0.03)\rho g a Q_{max}$ where again Q_{max} was the maximum flow-rate in the channel in the absence of turbines. This is an important and general result, that can be used for estimating the maximum power that could be generated from a tidal stream in a channel, assuming that the resistance to the flow is uniform across the channel. In order to evaluate the expression, elevation data are required from locations at both ends of the channel, which may be combined vectorially to give the amplitude of the elevation difference a. Q_{max} may be obtained from a using the calibration mentioned above and knowledge of the cross-sectional area at the calibration section.

Garrett and Cummins (2005) also concluded that the effect of several harmonic constituents could be included simply in the analysis, providing it was known how important friction was in the channel.

A similar channel was also considered by Bryden et al. (2006), but in this case the flow was steady and the elevation difference between the two ends of the channel was fixed. The equations of motion were solved numerically in their differential form with particular regard to the changes in flow speed for a given level of energy extraction. It was found that there was a close to linear relationship between the fractional decrease in flow speed and a dimensionless number, the ratio of energy extraction to other energy losses in the channel. The model was extended to time-varying currents in Bryden and Melville (2004), where the scenario was the quasi-steady filling and discharging of a basin through a channel (similar to that in Garrett and Cummins (2004) mentioned above). The reduction in flow speed was found to be less severe than the steady flow case, with small changes even with energy extraction at 30% of the kinetic energy flux in the absence of turbines. This qualitatively agrees with Garrett and Cummins (2004) that, in this situation, a large proportion of the energy can be extracted without large changes in tidal regime in the basin.

In most of the foregoing work, turbines have been considered as ‘fences’ applying to the flow a uniform retarding force across a channel. There are many reasons why this is not realistic, including the need to avoid cavitation and high wave loads on turbine blades; the shape of the rotor disk; the effect of vertical velocity profile; the number of turbines required to ‘block’ the channel. Adding realism by extending models to two and three dimensions tends to require numerical modelling and raises questions about turbulence parameters in the flow and their role in mixing of the turbine wake. A 3-D numerical modelling study of an array of permeable disks, simulating the effect of turbines as pressure drops, found positive wake interference effects with staggered arrays (Batten and Bahaj 2006). The largest thrusts were experienced by the second row of disks in this case. Experimental data on the effects of wake interaction in arrays of tidal stream generators are required for validation of this and other models.

Another restriction of the models considered in this section was that the tidal flow was constrained to a channel, either with open sea at both ends, or one end connecting an enclosed bay or inlet. Further analysis needs to be undertaken for situations with less well bounded geometry such as accelerated flow around headlands.

2.3 Tidal stream generators

Modern interest in generating power from tidal streams, or other marine currents such as the Florida current—without the need for a barrage or the impounding of water in a basin—has existed since at least the early 1970s (Heronomus et al. 1974; Lissaman and Radkey 1979). In order to compare reports of performance given in the literature and characterize the hydrodynamics of tidal stream turbines in the context of resource assessment, some dimensionless groups are introduced below.

2.3.1 Dimensionless groups relevant to tidal turbines

Power coefficient

The power coefficient,

$$c_p = \frac{P}{\frac{1}{2}\rho U_0^3 A} \tag{2.2}$$

is the output power non-dimensionalized by the undisturbed flow speed and the flow capture area. In the case of a turbine without any duct or diffuser, the flow capture area is defined as the vertical area swept by the hydrofoils. In the case of ducted turbines, the flow capture area is less well defined, but should perhaps be taken as the largest cross-sectional area of the duct. This is because an equivalent sized non-ducted device could have been constructed in the same space. The factor of 1/2 is to make the denominator look like kinetic power and ties in with actuator disk theory, but is occasionally omitted from the definition by authors. The power value cited is variously before or after mechanical and/or electrical losses. Unless otherwise stated, c_p will denote a performance coefficient based on input shaft power to the power take-off subsystem, prior to any losses. The power coefficient represents the effectiveness of the device in generating power, regardless of flow speed or area of device. It is a function of the tip speed ratio (below) with a maximum at a particular value and may peak sharply or with a flatter profile. A sketch of a typical plot of power coefficient against tip speed ratio is given in Figure 2.1(a). The sketch is for the case where the characteristic blade or hydrofoil angle is held constant.

Thrust coefficient

The thrust coefficient,

$$C_T = \frac{T}{\frac{1}{2}\rho U_0^2 A} \tag{2.3}$$

is the thrust on the hydrodynamic subsystem non-dimensionalized by the undisturbed flow speed and the flow capture area. It represents the loading of the subsystem, independent of scale. The thrust coefficient is also a function of the speed ratio (Equation 2.3.1). A sketch of a typical plot of thrust coefficient against tip speed ratio is given in Figure 2.1(b). To the left of the curve is a

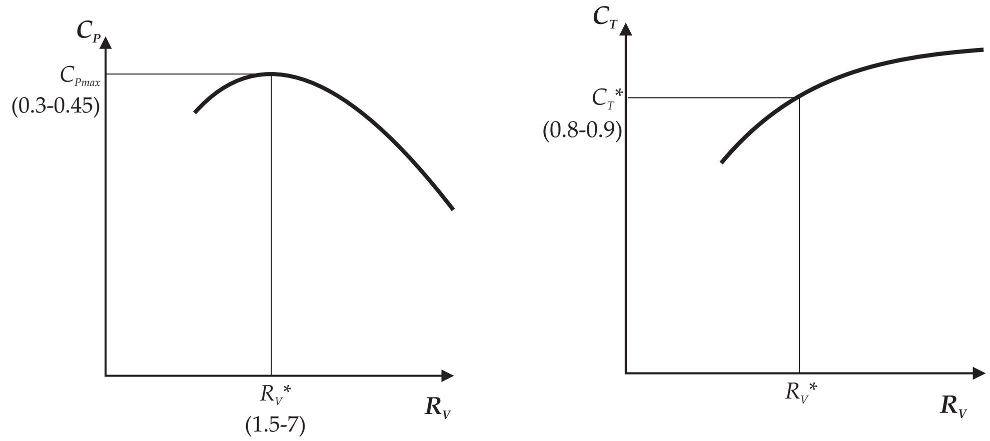

(a) Power coefficient

(b) Thrust coefficient

Figure 2.1: Sketch of typical variation of power and thrust coefficients with speed ratio

stalled region with bulk flow separation; towards the right hand side, frictional drag is high and the rotor tends towards an impermeable disk.

Speed Ratio

The speed ratio,

$$R_V = \frac{V_H}{U_0} \tag{2.4}$$

for axial or orthogonal flow device, V_H is the speed of the blade tip with respect to a stationary point; for oscillating devices, is the tangential speed of the hydrofoil. The speed ratio is also known as Tip Speed Ratio (TSR) for axial flow devices. Lift-type devices tend to be characterized by a speed ratio greater than 1, whereas inefficient drag-type devices must necessarily have a speed ratio lower than 1. For oscillating hydrofoil devices, the speed ratio varies significantly throughout a cycle.

Froude number

The Froude Number of the channel,

$$Fr = \frac{U_0}{\sqrt{gH}} \tag{2.5}$$

represents the ratio of the flow speed to the shallow water free-surface wave speed. Even in comparatively shallow coastal conditions (e.g. 15 m depth) and very fast currents (4 m/s), the Froude number of the channel will remain well inside the subcritical region (typically $Fr < 0.5$) which implies that free-surface gradients will be small.

Solidity

The solidity is the proportion of the flow capture area occupied by the blades or hydrofoils, projected normal to the flow:

$$S = \frac{A_N}{A_H} \tag{2.6}$$

where A_N is the total area of the hydrofoils projected onto a plane normal to flow direction and A_H is the swept area. When designed for optimum energy capture across a range of flow speeds, turbines will generally have a low solidity.

Area blockage ratio

The area blockage ratio is defined as:

$$R_A = \frac{A_H}{A_C} \tag{2.7}$$

where A_H is the area swept by hydrofoils projected onto a plane normal to flow direction and A_C is the cross-sectional area of the channel. When converting the results of tests in a channel or a tunnel to full-scale, corrections should be applied for the constraining effect of the walls on the continuity of fluid, under the principle of dynamic similitude at the location of the hydrofoils (Bahaj et al. 2005). The blockage corrections may be based on simple continuity and momentum requirements, or may be derived from measurements of flow speed in the wake of the device. Where the wake is effectively unconstrained in the lateral direction, a vertical blockage ratio could be defined as L_H/h.

Immersion ratio

The immersion ratio is defined here as:

$$R_I = \frac{h_I}{H} \tag{2.8}$$

where h_I is the minimum immersion depth e.g. the depth to the blade tips in the case of a horizontal axis device. Reduced power has been observed when turbine rotors have been moved from a higher immersion ratio (deeper tip depth in comparison to height of hydrofoils) to a lower value (Bahaj et al. 2007a). It was thought to be the result of both the action of the free surface as a reflection plane and the generation of waves on the surface. It should be noted that this observation was made in a towing tank where the rotor is advancing into still water, rather than the full-scale case where the inflow turbulence intensity would be considerably higher.

2.3.2 Theoretical performance of tidal stream turbines

The theory of power extraction using horizontal-axis wind turbines is well established; the classic analysis of power extraction from the wind by an actuator disk (see Betz (1966))[*] stated that the maximum power that can be extracted by a single turbine in an unconstrained flow is the fraction $\frac{16}{27}$ (0.59) of the kinetic energy flux through the rotor disk area in the case of no extraction, $\frac{1}{2}\rho U_0^3 A_r$. In general, the fraction is known as the power coefficient c_P, defined as $P/\frac{1}{2}\rho U_0^3 A_r$. For all wind turbines yet designed, $c_P < 0.59$; more sophisticated design methods allowing for the effects of finite numbers of blades predict for typical designs, maximum values of C_P in the range 0.4–0.5 (Burton et al. 2001). The classic analysis applies to the case of a similar turbine in a tidal stream providing the tideway is wide and deep compared to the rotor disk diameter and that there is only a small change in free surface elevation across the turbine location. Corrections will be required if the flow around the wake is constrained by the free surface or solid boundaries, causing significant acceleration due to the continuity requirement. The presence of a free surface also means that in general that the far upstream and far downstream static pressures are not equal (an assumption of actuator disk theory is that the stream-tube enclosing the rotor is surrounded by fluid at constant pressure); however, this is likely to be a small effect as the Froude number will be low ($Fr < 0.3$).

---

[*] Froude and Lanchester derived similar results independently

2.3.3 Published performance data

A summary of the available data on the performance of tidal stream generation devices published in journal articles, conference papers and technical reports, is included in Table 2.1 in order of approximate date of operation or deployment. It should be noted that there are several significant prototypes that have been tested, for which there are no published data on performance; an indication of commercial sensitivity or embarrassment. The numbered columns of Table 2.1 represent the following:

1. Type of device. The symbols ◫, ⊙ and ⊲ represent orthogonal flow, axial flow and oscillating hydrofoil designs.
2. Type of device developer. A, B and C represent academic experimental model, commercial/academic model and commercial device, respectively.
3. D: Equivalent diameter (m): the diameter of a circle with the same area as the flow capture area of the device.
4. $c_{P\,\max}$: maximum attained value of power coefficient
5. R_V: Speed ratio at $c_{P\,\max}$
6. U_0: Design or test flow speed (m/s)
7. ! Indicates that the results were not corrected for blockage (in cases where there was a significant blockage ratio)
8. Testing environment/facility: circulating water channel (CWC); towing tank (TT); cavitation tunnel (CT); sea; river; head-race of an hydraulic impoundment structure.
9. Device is fixed to a structure; attached to a set of moorings or towed by a vessel.
10. Extra phenomena investigated: cavitation inception (cav); imposed wave loading (wav); effect of rotor yaw angle (yaw) and effect of immersion ratio (imm) on performance.

Table 2.1: Published data on hydrodynamic performance of tidal stream generators, including model and full-scale. In column 2, The symbols ◫, ⊙ and ◁ represent orthogonal flow, axial flow and oscillating hydrofoil designs. In column 3, A=Academic B=academic/commercial; C=commercial. Further explanation in the text

Ref			D	C_P	R_V	U					Comments
	(1)	(2)	(3)	(4)	(5)	(6)	(7)	(8)	(9)	(10)	
Kiho et al. (1996)	◫	A	1.81	0.56	2.1	1.50		Sea	Fixed		Three bladed Darrieus turbine tested in a tidal stream for extended period. No record of flow measurement technique.
Tuckey et al. (1997)	⊙	A	2.00	0.30	3.0	1.50		Sea	Fixed		Four bladed axial flow turbine tested beneath a static platform in a tidal stream. Unexplained errors in flow speed measurements.
Shiono et al. (2000)	◫	A	0.28	0.24	1.8	1.40	!	CWC	Fixed		Darrieus turbine. Eight different sets of blades tested in three and four blade configurations in a circulating water channel. Blockage ratio around 10
Coiro et al. (2005)	◫	B	6.20	0.25	2.0	2.00		Sea	Moored		Three-bladed cyclic pitch orthogonal flow turbine tested beneath moored platform. Uncertainty of 25% in inflow velocity.
Abu Sharkh et al. (2002)	⊙	B	0.25	0.35	1.5	1.90		TT	Fixed		Ducted tip driven integrated thruster, run as a generator. Tested in a towing tank.
The Engineering Business Ltd (2005)	◁	C	15.80	0.15		2.00		Sea	Fixed		Single oscillating hydrofoil design. C_P calculated from values cited in The Engineering Business Ltd (2005, page 107)
Thake (2005)	⊙	C	11.00	0.45	3.6	2.20		Sea	Fixed		Two bladed axial flow turbine. Operated with flow upstream of supporting structure (i.e. in one direction). Flow speed measured by ADCP 50m upstream of turbine. Large variance in measured flow speed and power, filtered to give smoothed signal.
Bahaj et al. (2007a)	⊙	A	0.80	0.45	6.0	1.70		CT, TT	Fixed	cav., yaw, imm.	Three bladed axial flow turbine, tested in a cavitation tunnel and a towing tank. Blockage corrections made. Power measured before any mechanical or electrical losses.
Wang et al. (2007); Barltrop et al. (2007)	⊙	A	0.40	0.37	3.6	2.00		CT, TT	Fixed	cav., wav.	Three bladed axial flow turbine tested in a cavitation tunnel and towing tank. Investigations carried out on cavitation and oscillating loads due to waves. Low blockage ratio.
Clarke et al. (2007a)	⊙	A	0.82	0.39	7.0	0.80	!	TT	Fixed		Contra-rotating axial flow turbine tested in a towing tank. Three blades on first rotor, four on second. Blockage ratio 5
Orme and Masters (2005)	⊙	B	1.00	0.46	4.0	2.75		River	Vessel		Four bladed axial flow turbine, towed behind vessel. C_P quoted includes mechanical losses. Global C_{PE} is 0.24 after electrical losses.
Damen et al. (2006)	⊙	B	2.80	0.40	3.0	3.20	!	Head-race	Fixed		Two bladed axial flow turbine, tested in dam spillway. Turbine occupied significant fraction of channel, but blockage corrections not cited. Uncertainty over undisturbed flow speed measurement. Significant scatter in results.
Coiro et al. (2006)	⊙	B	0.80	0.45	3.5	2.50		TT	Fixed	cav.	Tested in a towing tank at a low blockage ratio. Effects of immersion investigated. No cavitation observed.
Clarke et al. (2007b)	⊙	A	2.50	0.38		1.50		Sea	Vessel		Contra-rotating axial flow turbine towed in a tidal channel. Three blades on first rotor, four on second. Limited by towing vessel to 1.5 m/s, designed for 3.5 m/s

2.3.3.1 Conventional propeller-type turbines

It is apparent from Table 2.1 that reported performance, expressed in terms of the power coefficient, fell in the relatively narrow range of 0.3–0.46 regardless of the scale of the model tested, from 0.25 m to 11 m diameter. For example, the results of the Seaflow project (Thake 2005) indicated that a power coefficient of 0.4 was achieved. By comparison, peak c_p values of 0.45 were reported by Bahaj et al. (2007a) in a series of scale model tests. The results in this case agreed well with blade element momentum theory (Batten et al. 2005). This gives confidence in the process of scale testing for tidal stream energy devices. Overall this suggests that the downwardly-revised maximum power coefficient of 0.30 for an horizontal axis turbine derived in Gorban et al. (2001) from a theoretical curvilinear flow field, was unduly pessimistic. In the cases where a device was tested statically in non-controlled conditions (not in a towing tank or circulating tunnel or channel) practical difficulties were encountered in measuring the free-stream flow speed. These arose from instrument uncertainty, vertical velocity profile, turbulence and topography (Coiro et al. 2005).

A higher power coefficient than predicted by numerical modelling was reported for the Seaflow device, but lower power output, due to lower incident flow speeds than expected. This highlights the fact that prediction of the economic performance of a full-scale device depends on accurate assessment of the full-scale flow conditions in conjunction with the technical characteristics of the device.

As tidal stream technology has not yet reached maturity, it is possible that alternative configurations of generator to the familiar horizontal axis turbine may have economic advantages in tidal streams, not previously found in wind generation.

2.3.3.2 Flow augmentation

Diffuser augmentation for wind turbines has not proved successful, as constructing a larger diameter rotor has always been more cost-effective than enclosing a small rotor in a large diffuser (of equivalent exit area to the large rotor). In addition, theoretical performance gains due to additional back-suction from the diffuser have not been achieved in practice (van Bussel 2007). However, in the case of tidal turbines the potential advantages of placing the rotor in a duct are somewhat different than in the case of a wind turbine in a diffuser. The low comparative velocities of tidal streams to wind result in very high thrust loadings on the tidal turbine rotor disk; flow acceleration through a duct may help to reduce these loads and gearbox requirements, although the degree to which this can be effected will be limited by flow separation or cavitation, caused by the associated pressure decreases. Parasitic drag will reduce performance below idealized flow solutions. As tidal turbines are naturally limited in size, it is practical to integrate the bearings into the rim of the rotor, resulting in a stiffer rotor assembly than an open device.

The major disadvantages of diffuser augmentation for wind, namely the large size and weight of the diffuser and the necessity for a yaw mechanism, are less applicable in the tidal case due to buoyancy and the natural limitation on the size of rotor by the water depth. As discussed in Chapter 7, tidal streams tend to flow back and forth parallel to an axis and there is little to lose in terms of incident resource in fixing the orientation of a horizontal axis device. Consequently, no mechanism for yawing a large duct would be required. However, in this case the duct would need to be symmetrical, which would be less effective than a diffuser configuration with the exit area larger than that of the inlet, unless a switching brim arrangement was employed (Setoguchi et al. 2004). Unfortunately, no experimental data from ducted tidal stream turbines has yet been published.

2.3.3.3 Orthogonal flow turbines

Orthogonal flow turbines (a subset of which are vertical axis turbines) may also have advantages in tidal streams due to insensitivity to flow direction in reversing or non-rectilinear currents. The analysis of such turbines is complicated due to the asymmetry between upwind and downwind blades and blade-blade (and possibly structure-blade) interactions. Furthermore, higher drag losses than propeller-type turbines are inevitable as some rotating structure is required to support the blades. In Table 2.1 it can be seen that while axial-flow turbines had reported maximum c_p in the range 0.3–0.46, performance in orthogonal flow turbines tended to be lower, around 0.25. An obvious anomaly was the Nihon University 1.8 m Darrieus turbine, which performed abnormally well (maximum c_p of 0.56), particularly as the power value used was net of mechanical and electrical losses (Kiho et al. 1996). No numerical predictions were given for comparison along with the power coefficient values in this case; nor were the details of the flow speed measurements provided. Consequently, little confidence can be placed in this particular set of results.

2.3.3.4 Oscillating hydrofoils

In Table 2.1, it can be seen that the Stingray device had a predicted power coefficient of around 0.15 (The Engineering Business Ltd (2002, page 15)) and therefore performed similar to expectations, while at the same time poorly when compared to other devices. This low power coefficient contributed to a very high predicted cost of energy (22 p/kWh in 2005; The Engineering Business Ltd (2005, page 108)) for a 5 MW farm of when compared to a similar sized farm of SeaFlow-type devices (approximately 8p/kWh in 2005; Thake (2005, pages 46–48)). Both costs were produced assuming a second-generation device. After being abandoned by its originators, the oscillating hydrofoil concept has been resurrected by another company, Pulse Tidal, who claim that their new tandem dual coupled hydrofoil design will overcome the weaknesses of Stingray, namely the low effective tip speed ratio and the need to input work to the device during parts of the operating cycle.

2.4 Wakes of individual turbines

Experimental characterization of the wakes of tidal turbines has only recently begun, for example by using porous disk simulators as described in Bahaj et al. (2007b). Attempts have been made to simulate the interactions of wakes in tidal turbine arrays using Computational Fluid Dynamics (CFD) models representing the turbines as porous disks (MacLeod et al. 2002; Batten and Bahaj 2006), but these have not been validated by experimental data. By contrast, the interaction of the wakes of wind turbines has been the subject of theoretical and experimental study for over thirty years (for a comprehensive review, see Vermeer et al. (2003)) and continues to be so today (Barthelmie et al. 2006). Much can be learned from wind turbine research in predicting the performance of tidal generator arrays, but there are specific differences in terms of boundary conditions, namely the constrained nature of the flow and the presence of a free surface.

In general, wakes of turbines are characterized by a near-wake region, extending up to five rotor diameters (5D) downstream; followed by a transition region, and a far-wake region beyond this. In the near-wake region, the wake is dominated by the properties of the rotor. The vortices shed by the rotor merge and form a annular shear layer, which thickens downstream—mainly due to mechanical turbulence production but also influenced by ambient turbulence levels—until the layer reaches the axis of rotation. Downstream of this location, the swirl introduced in the flow has dissipated and the velocity in the wake can be considered as a jet, with a core velocity lower than free-stream (Lissaman 1979). The far-wake region is the region of interest when considering wake interactions.

The downstream velocity deficit in the wake of wind turbines is known to be strongly affected by the ambient turbulence of the flow (Baker et al. 1985). Part of the challenge involved in predicting tidal turbine wake interactions is the paucity of available data on the turbulence structure of continental shelf tidal flows. Velocity profiles from tidal locations have only recently become available due to the availability of acoustic-Doppler current profilers (ADCPs). Turbulence profiles are rarer still, as they are difficult to measure remotely. The use of commercial-off-the shelf ADCPs for estimating turbulence quantities has been investigated by Wiles et al. (2006). This method may in the future provide a cost-effective means for producing turbulence profiles in the sea, although there are presently unresolved issues surrounding the influence of waves in the upper part of the water column.

2.5 Tidal stream energy resource assessment

In an academic context, the discussion of resource assessment is restricted to issues around maximizing energy extraction. It is recognized that in the real world there are other factors that may constrain the choice of sites, including survival of equipment; access for maintenance; integration with the power distribution network; environmental and ecological impacts (Thake 2005). Aside from these issues, it is suggested that the following tasks are involved in resource assessment as part of an iterative design process:

Task 1 Selection of sites suitable for placing arrays of tidal stream generators. This is primarily constrained by a minimum value of mean cube flow speed (for a fixed generation efficiency, this value will be proportional to the average power output for a single turbine; see §2.3.2) and a suitable range of depths for a particular type of generator.

Task 2 Initial sizing and rating of the generating device to maximize energy extracted over the life of the device taking into account factors such as the long term variations in flow speed; deviation of the flow from rectilinear movement; vertical profile of flow velocity.

Task 3 Given the device parameters above, investigation of different arrangements (lateral spacing, longitudinal spacing and orientation) of generators within the selected area to maximize combined power output. Revision of generator parameters if necessary.

Task 4 Investigation of the extent of significant effect of the proposed tidal stream generator array on tidal parameters (extracting tidal energy in one location may lead to a reduction in available energy elsewhere). If necessary, corrections made to power output estimates due to resulting changes in boundary conditions.

For most resource assessments to date, Task 1 has been based on navigational data, although some work has been done using numerical modelling (see §2.6). Full-scale deployment would require high quality survey data once the site was initially selected. Task 2 requires understanding of the individual generating devices; clear parallels exist between the extraction of wind energy and the extraction of energy from marine currents (see §2.3.2). Little work has been done on Task 3, which requires consideration of three-dimensional and turbulent features of the flow. In most assessments, an approximate value of the ratio of rotor area to surface area of site has been used. Task 4 has been carried out for simple analytical models with well constrained geometry, for example a tidal channel between large seas (see §2.2).

Once a significant number of tidal stream arrays have been built in different locations, there is in addition an important issue from an economic point of view: to what extent can the variability of the power output from a number of sites be combined to reduce overall variability as a function of time? This is considered in §2.6.5.

2.6 UK Tidal energy resource assessments

2.6.1 Early estimates of energy resources

An estimate of tidal stream power in UK waters was provided by Fraenkel and Musgrove (1979) through a simple assessment of the kinetic energy flux through major channels using approximate mean depth and width values. A contemporary study by the then GEC Hirst Research Centre (Wyman and Peachey 1979) produced similar figures, also using Admiralty navigational data. The results of these assessments and others considered below can be found in Table 2.2. A note of caution: the many different assumptions and sources of data used by the studies make direct comparison of results difficult, but there is general downward trend in the estimated size of the resource with time.

A new approach to resource assessment was taken by Evans (1987), where numerical modelling was used to select sites and determine kinetic energy flux in space and time in the sea area around the Channel Islands, known as the Normandy-Brittany Gulf (Cave and Evans 1985, 1986; Cave et al. 1987, see also). A two-dimensional finite difference model was used to simulate tidal currents and elevations from the main semidiurnal harmonic constituent and the results were validated in elevation at three ports within the domain. Grid squares were selected on criteria of minimum depth and average kinetic energy flux density $\frac{1}{2}\rho\overline{U_0^3}$ over a tidal period. Some grid squares were also selected due to their possessing a large phase difference with respect to others with higher output, in order to reduce the variability of the supply (see §2.6.5). The power output of the grid squares was then found from the product of the kinetic energy flux density, the swept area of a generator rotor, the number of generators per unit surface area, the surface area of the grid square and a c_p value. This might be termed a 'per-generator' method of resource assessment as it relies on finding the output of a more-or-less realistic generator under certain operating conditions and then scaling the output by the expected number of generator units in an area. In this case there was no consideration given to back-effect of multiple generators on the flow regime.

2.6.2 Assessments in the 1990s

Two key reports from the 1990s included estimates of exploitable resources and although they have been superseded, subsequent studies have drawn on the methodologies used and findings produced. They were desktop studies for the purpose of providing government and industry with broad estimates of the economic potential for the development of tidal stream power.

The Tidal Stream Energy Review (ETSU 1993) produced by the then Energy Technology Support Unit (hereafter ETSU 93) provided estimates of available tidal stream energy resources in the UK. The ETSU 93 study identified suitable sites around the UK taking into account mean spring peak tidal stream speed (greater than 4 knots or approximately 2 m/s) and depth (greater than 20 m). The exact method of choosing the site boundaries was not stated, but from the diagrams included it appears to have been visual interpolation. Each site was divided into plan areas within depth categories and the number of turbines calculated for each area, based on an appropriate rotor size and spacing in plan. The report identified thirty-three sites in the UK with a total surface area of 1450 km^2. The velocity values were taken from tidal stream 'diamonds' (on navigational charts) and tidal stream atlases and the speeds scaled according to the tidal range variation at Dover over one year. A histogram of time spent

Table 2.2: Tidal stream energy resource assessments around the UK

Study	Year	Geographical scope	Data sources	Average resource (GW)	Notes
Energy flux onto NW European continental shelf					
Flather (1976)	1976	Continental shelf	Numerical model	215	Total average net energy flux along closed boundary
Cartwright et al. (1980)	1980		Pressure/current data	250	
Egbert and Ray (2001)	2001		Satellite altimetry	219 ± 31	
Resource assessments					
Fraenkel and Musgrove (1979)	1979	British Isles	Navigational	14.7	Approximate kinetic energy (KE) flux through major channels
Wyman and Peachey (1979)	1979	British Isles	Navigational	18.7	KE flux averaged over sea areas
ETSU (1993)	1993	UK waters	Navigational	6.9	per-generator method, no back effect of generators
European Commission (1996)	1996	Continental shelf	Navigational	3.9	As above
Black and Veatch Consulting Ltd (2004)	2004	UK waters	ETSU 93; EC 96	2.5	20% KE flux through site
Black and Veatch Ltd (2005)	2005	UK waters	ETSU 93; EC 96; MEA 2004	2.1 ± 0.6	As above, but some sites eliminated or reduced to 10–15% KE flux
Alderney Race only					
Evans (1987), A7.25	1987	Alderney Race	Numerical model	0.20	per-generator method, no back effect of generators
ETSU (1993)	1993		Navigational	0.59	As above
European Commission (1996)	1996		Navigational	0.74	As above
Bahaj and Myers (2004)	2004		Navigational	0.84	per-generator method, empirical reduction per row of generators
Black and Veatch Consulting Ltd (2004)	2004		ETSU 93; EC 96	0.19	20% KE flux through Race
Black and Veatch Ltd (2005)	2005		ETSU 93; EC 96; MEA 2004	0.04	As above, but reduced energy extraction to 12% KE flux
Black and Veatch Ltd (2005), A3	2005		Navigational	0.08	Digital interpolation of data; 20% KE flux through Race

Table 2.3: Ratio of swept area of rotor to plan area occupied by turbine in ETSU 93 and EC 96 reports

Study Ref.	**Depth range (m)**	**Surface area $(\mathbf{km})^2$**	**Rotor area/ surface area** $\times 10^{-3}$
ETSU 93	20–25	125.6	35.34
	25–40	219.5	6.44
	> 40	1106.4	11.94
	Weighted average:		13.13
EC 96		1330	8.73

in 0.5 knot (0.26 m/s) bins was then created. For each bin, the annual energy yield was found using a similar, 'per-generator' method to that described above.

A European Commission (EC) funded study as part of the JOULE II Non-nuclear energy programme (European Commission (1996), hereafter EC 96) produced a database of tidal stream energy resources around Europe, including sites in the UK, using a similar methodology to ETSU 93 above. Forty-two sites were identified in the British Isles with a total surface area of 1330 km^2. The criterion for site selection (in most cases) was peak tidal stream speed greater than 1.5 m/s and the tidal stream speeds were summed into 0.25 m/s bins over a year.

Both the ETSU 93 and EC 96 reports relied on tidal stream values taken from navigational charts, which apply to discrete points. No spatial interpolation between points was used in either study; only one set of speeds was used for each site. This is a weakness of the assessments, as there may be considerable variation in tidal stream speed and direction across the sites, which are on the scale of kilometers. A more general problem with using the cube of the flow speed is that it multiplies the relative error in the quantity by a factor of approximately 3. For $U = 2$ m/s with an error bound ± 0.1 m/s, the relative error in U, $\epsilon_r \approx 5\%$, so this is a significant effect. The histograms used in ETSU 93 and EC 96 to produce distributions of speed and hence estimates of power, were linear in speed, rather than using the cube. This means that there was lower resolution (and potentially accuracy) at the higher values of cubed speed. This issue was addressed by Batten et al. (2006), where bins of cubed speed were used.

In addition to issues of site selection and accuracy of velocity values described above, the studies inevitably made a number of assumptions about the performance and configuration of the turbines installed. Neither of the studies attempted to optimize the rated power for the turbines used. In configuring the layout of turbine arrays the ETSU 93 study took a conservative approach, for example only allowing up to 10 m diameter rotors in sites of depth less than 40 m. It also assumed that depths greater than 25 m would require anchored vessels rather than jack-up barges and hence require much greater surface area per-generator unit. The barge used in the Seaflow project stood in 25 m of water, close to the limit of its capabilities, but new barges recently developed for offshore wind farms can work in depths of up to 30 m and it is envisaged that they will be further developed for use in future deployment of tidal stream generators (Thake 2005). The EC 96 study was less prescriptive, arguing that rotor 'footprint' is directly proportional to swept area of turbine, again taking the constant of proportionality from wind turbine experience. A comparison of the rotor densities is included in Table 2.3 and it can be seen that the density used in EC 96 was a third less than the average used in ETSU 93, which goes some way in explaining the discrepancy between the average resource figures (43%) given in Table 2.2.

2.6.3 Recent assessments

2.6.3.1 Assessments based on energy flux

The most recent estimates of tidal stream energy resources in the UK to date are found in (Black and Veatch Consulting Ltd 2004) and (Black and Veatch Ltd 2005) (hereafter BV 2004 and BV 2005) . Like the ETSU 93 and EC 96 reports described above, these were desktop studies produced using secondary material. The authors criticized the methodology used in the former reports for not considering the effect of extracting energy on flow conditions. In this way, it was argued, the power estimates from large arrays of turbines envisaged in ETSU 93 and EC 96 were far higher than physically possible.

In place of this array-based methodology, a 'significant impact factor' was established, which was the proportion of kinetic energy flux through a particular cross-section in a site in the undisturbed state, that could be extracted without significant impact. Based on a 1-D channel with steady flow and a fixed drop in elevation between the ends, significant impact was defined in terms of an acceptable percentage decrease in upstream flow-rate when energy extraction was applied. This raises the question of what acceptable means in this context, apart from simply that which maximizes the power output for a given site; until field data on the environmental impact of turbine arrays becomes available, it will remain a matter for debate.

The application of the results of a steady flow model to the case of time-varying tidal streams is questionable, given that it was found by Bryden and Melville (2004) that there was far less effect on the flow regime when moving from a steady flow model to a quasi-steady time-varying model. In addition, it was shown by Garrett and Cummins (2005) that the relationship between kinetic energy flux and maximum extractable power was specific to a particular channel, so from the point of view of maximizing power extraction there is no reason to assume a global fraction of kinetic energy flux, applicable to all sites. In BV 2004, surface dimensions of sites were taken from the ETSU 93 and EC 96 reports and a constant value of 20 % maximum extraction of kinetic energy was used across all sites in the UK.

The second report BV 2005 was restricted to the ten most energetic sites identified in BV 2004 as containing 80% of the exploitable resource. This removed a number of sites that though small, might prove economically attractive for tidal stream power development. The navigational data were reviewed and some new data included from the Marine Renewable Energy Atlas (see §2.6.3.2 below). Some sites were removed where they were perceived to be affected by adjacent sites. For some sites the significant impact factor was reduced to 8–12%, but the values were still based on 1-D steady flow analysis. Except in one case, the site widths were not updated and single values for site depth were taken to apply to a whole site. The authors of the report cited an uncertainty in the results of ±30%, though not how this figure was arrived at; they admitted that in the absence of site specific modelling, values for both kinetic energy flux at the site and the significant impact factor were approximate.

2.6.3.2 Marine renewable energy atlas

An independent tidal energy resource assessment has been undertaken for the UK Department of Trade and Industry, as part of the Strategic Environmental Assessment of natural resources on the UK continental shelf. Continental shelf tidal modelling data from Proudman Oceanographic Laboratory (with finest grid resolution of approximately 1.8 km) was used to create an atlas of marine energy resources (ABPmer et al. 2004, known hereafter as MEA 2004). The purpose of the atlas was to provide a coarse-resolution distribution of tidal kinetic energy density on the continental shelf, for use by government in strategic decisions on renewable energy policy. Due to constraints of grid size, high-energy localized flows around headlands and through narrow straits were not resolved, meaning that the atlas is unlikely to be useful for detailed resource assessments of particular sites.

2.6.4 Effect of fixed and variable orientation

One characteristic of tidal streams close to coasts, which sets them apart from atmospheric flows, is that at many locations the flow is approximately rectilinear due to the pressure gradients set up at the coast, i.e. the flow direction is always 0 ° or 180 ° with respect to a particular orientation. This corresponds to Kelvin waves progressing at right angles to a coast (Taylor 1920). Consequently, some proposed marine current turbines are designed to have a fixed orientation to the flow and invert the blades in order to operate the turbine in the reverse direction (Marine Current Turbines Ltd 2007; Lunar Energy 2007). The closer the flow is to rectilinear the more efficient these turbine designs will be. However, some sites can have a swing upon flow reversal of 20 ° or more away from 180 ° such as flows around islands and headlands.

In previous assessments of tidal energy, in general the assumption was made that any deviation from rectilinearity of the flow would have no effect on the energy extractable by tidal generators at the site, as would be the case for vertical axis turbines or yawing horizontal axis turbines. One report (ETSU 93) did include a simple correction, but it was not based on yawed rotor theory or experimental results. Blunden et al. (2008) applied curve-fits derived from the experimental results documented by Bahaj et al. (2007a) to tidal stream data at three sites in the English Channel: the Race of Alderney between the Island of Alderney (Channel Islands) and Normandy (France) and St. Catherine's Point to the south of the Isle of Wight (UK) and has been based on publicly available tidal stream data, rather than model results. These results are discussed further in §7.4 and the full paper is included in Appendix H. The energy yield calculations presented there strictly apply to isolated turbines, widely spaced and in small enough numbers not to interact significantly with other units or the tidal flow regime.

2.6.5 Variability of the energy resource in time and space

Tidal streams are predictable in phase, magnitude and direction to a reasonable degree of accuracy for decades ahead, given accurate records or simulation results of a long enough duration to satisfy frequency resolution criteria; at least a month and ideally a year in most cases (see §3.7). Moreover, due to the periodic nature of tidal streams, with the driving frequencies known precisely, errors in amplitude and phase are well-bounded and once estimated are essentially stationary with time. Stationary, that is, unless there are external changes to the tidal dynamics in the locality. In estuaries this could result from dredging; more generally, large tidal power schemes could alter tidal range or tidal stream velocities in a region (see §10). Sea-level rise resulting from climate change is unlikely to have a significant effect in the foreseeable future on tidal range (and therefore tidal streams), at least in the English Channel (Flather and Williams 2000).

Currents driven by a slope in sea surface caused by storm surges (as distinguished from localized upper-layer wind-driven currents) are much less predictable and can result in depth-averaged extreme currents of similar magnitude to tidal streams, for example 0.6 m/s has been quoted for the English Channel (UK Health & Safety Executive 2001). The dynamics of storm surges are linked non-linearly to those of tides on the continental shelf through the continuity equation and the mechanism of dissipation. Interest in tide-surge interaction has been mainly confined to coastal flooding and thus to *total* sea-level rather than *total* currents; the success of numerical models in predicting total elevations at coastal gauges has not been matched in predicting total currents (Jones and Davies 2003). The effect of tide-surge interaction on tidal power generation predictions is not considered further here except to say that it is an area that may require further research.

The predictability of tidal streams is in contrast to wind-driven forms of renewable energy which can only be forecast hours ahead in the case of wind (Bathurst et al. 2002) to a few days ahead in the case of waves (Roulston et al. 2005). Despite this advantage of tidal stream power generation, there remains a potential mismatch between peaks in generation and demand for power. It would be desirable for developers of tidal stream generation to reduce this mismatch as much as possible (House Of Lords Science And Technology Committee 2004; House of Commons Science and Technology Committee 2001). To a certain extent the mismatch is inevitable as tides are dominated by lunar periods whereas electricity demand is dominated by solar periods. Tidal stream generators do not offer the possibility of energy storage, unlike tidal barrage schemes. By 'consolidating' the hourly variation in power output of tidal stream energy generation around the UK (due to differences in phase between sites), the combined likelihood of generating at an economically favorable time would be increased.

The variability of tidal stream power generation in the UK on a regional and national basis, under different development scenarios, was considered in (Sinden 2005). The aim was to investigate how the different phases of maximum tidal stream speed at different sites could reduce the overall hourly variability of the output of all the sites. The hourly variability was defined as the average hourly variation in power output as a percentage of the maximum output. The total yearly energy outputs of the thirty-six sites considered were taken from (Black and Veatch Ltd 2005) (so the comments in 2.6.3.1 apply), whereas the cubed tidal stream speed as a function of time (normalized by the average) was taken from numerical model results produced by Proudman

Oceanographic Laboratory. It was found that the hourly variability tended to increase with the amount of generation in a region, as the phase of one or two large sites dominated the variability. The study considered development scenarios with and without the inclusion of Channel Islands sites; it is not clear whether power generated around the Channel Islands would be exported to the UK distribution network or that of mainland Europe (Myers and Bahaj 2005). It was found that at the level of 80% development of the maximum power output estimated in (Black and Veatch Consulting Ltd 2004), the hourly variability of the total output of all the sites was 15% if the Channel Islands sites were included and 21% if they were not. In general, regions with large spatial variations in tidal phase, such as the Channel Islands and the south-west of England, gave more scope for reductions in hourly variability than other sites.

2.7 Chapter conclusions

Analytical models have provided insights into tidal stream power generation in tidal channels—for example in the case of an enclosed basin connected to the sea—showing that tidal stream generation can extract a significant proportion of the power that a tidal barrage scheme would generate, with far less environmental impact. A general expression for the maximum power that can be generated by turbines in a tidal channel has been derived in (Garrett and Cummins 2005), which can in principle can be evaluated given knowledge of the discharge and surface elevations at the ends of the channel.

Recent assessments of tidal stream energy resources around the UK have estimated the exploitable resource, when averaged over a year, in the range 2–7 GW, which may be compared to an average electrical power consumption in the UK for 2005 of 46 GW (UK Department of Trade and Industry 2006). There is considerable uncertainty attached to these resource estimates, however; all of the assessments to date have either ignored the change in flow conditions due to the effect of the generating devices, or have been based on more or less arbitrary proportions of kinetic energy flux through a site.

A number of issues relating to tidal energy assessment and requiring further research have been raised in this review. Analytical and numerical models of energy extraction by tidal stream generators require scale and field data for comparison, particularly in the area of turbulence quantities; the rate at which a wake mixes with the free stream affects the extent of interaction between a number of generators in an array. Velocity profiles across the rotor may result in differences from expected loads and power output. On the larger scale, there needs to be assessment made of the uncertainty in power predictions as a result of data issues (sparsity and length of records); altered boundary conditions due to the back-effect of generators; and the combined effects of surge and tide.

Chapter 3

Tidal theory

3.1 Introduction

In this chapter, the core theory behind tides and tidal power generation is explained, telescoping from the planetary scale where tides are driven by gravitational forces, to the scale of continental shelves where tidal energy is absorbed, further to the coastal scale where tidal currents are locally amplified by topography and finally to the level at which tidal energy extracting devices may operate.

The chapter begins with the derivation of expressions for the tide-generating forces, which cause the acceleration of fluid particles in the earth's oceans, setting up systems of tidal waves. The progression of tidal energy onto the shallow continental shelves is then described, followed by the analysis methods used to break down tidal signals into frequency components. The focus then switches to the hydrodynamic equations used to model coastal flows with a typical horizontal extent of 100 km. The various assumptions used to make the equations useful for computation are stated, along with the boundary conditions imposed and the form of the solution methods. Finally, some models of tidal power extraction are considered.

This section has been largely informed by the treatise of Cartwright (1977) and Pugh (1987, Chs. 3 and 4).

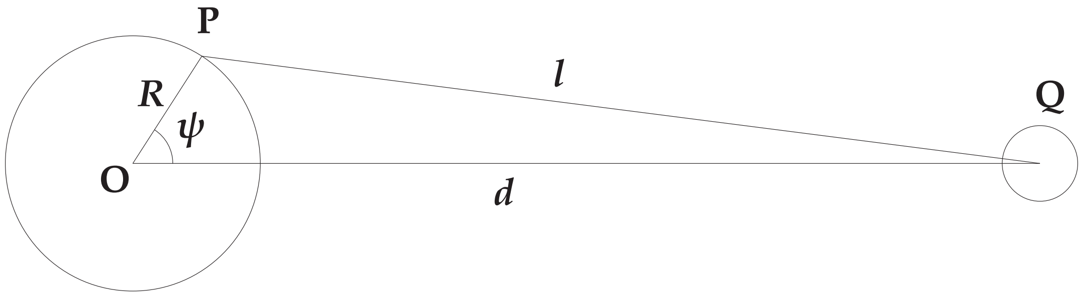

Figure 3.1: Definition of points and lines described in the text. O is at the centre of mass of the earth and P is a general point on the surface of the earth. Q is at the centre of mass of the sun or moon.

3.2 The tide-generating forces

Gravitational fields as predicted by Newton's theory of gravitation are conservative, that is to say that the work done against the field when moving from one point to another is independent of the path taken between the points. In mathematical terms, this means that the force experienced by a unit mass may be described as the negative of the gradient of a scalar potential energy field. Analysis of scalar fields is simpler than that of vector fields as there is only one variable, rather than two separate components. The forces can be retrieved when required by finding the gradient of the potential at that location. The scalar potential fields due to various masses can be simply superimposed to give the total potential, providing that there is a consistent definition of zero potential. The arbitrary reference chosen here is the centre of mass of the earth, located at O in Figure 3.1. Consider the potential V_m at a point on the earth's surface P, solely due to the gravitational field of the body with mass m located at Q:

$$V_m = \frac{Gm}{d} - \frac{Gm}{l} \tag{3.1}$$

where l is the distance PQ and d is the distance OQ. The definition is such that V_m represents the work done on a unit mass in moving it from O to P due to the gravity of m. It is clear that l will increase with rotational symmetry (about OQ) as ψ increases from 0–π radians. Using the cosine rule to express l in terms of the angle ψ and the radius of the earth R, gives:

$$l^2 = R^2 + d^2 - 2Rd\cos\psi \tag{3.2}$$

Eliminating l from (3.1):

$$V_m = \frac{Gm}{d}\left\{1 - \frac{1}{\sqrt{1 - 2\frac{R}{d}\cos\psi + \frac{R^2}{d^2}}}\right\} \tag{3.3}$$

The second term in the outer braces may be recognized as a generating function of the Legendre polynomials (Kreyszig 1999, page 209):

$$\frac{1}{\sqrt{1 - 2tx + x^2}} = \sum_{n=0}^{\infty} \mathcal{P}_n(x)t^n \tag{3.4}$$

Where $\mathcal{P}_n$ are the Legendre polynomials, the first few of which are:

$$\mathcal{P}_0 = 1 \tag{3.5}$$

$$\mathcal{P}_1 = x \tag{3.6}$$

$$\mathcal{P}_2 = \frac{1}{2}(3x^2 - 1) \tag{3.7}$$

$$\mathcal{P}_3 = \frac{1}{2}(5x^3 - 3x)\cdots \tag{3.8}$$

Hence substituting $x = \cos\psi$ and $t = R/d$ into (3.5–3.5) and then into (3.3) gives:

$$V_m = \frac{Gm}{d}\left\{\frac{R}{d}\cos\psi - \left(\frac{R}{d}\right)^2 \frac{1}{2}(3\cos^2\psi - 1) + O\left(\frac{R}{d}\right)^3\right\} \tag{3.9}$$

where $R/d \approx 1/60$ for the moon and $\approx 1/23500$ for the sun, so the third and higher order terms in the series may be reasonably neglected. The physical interpretation of the terms in the brackets of (3.9) is a sum of zonal spherical harmonic terms, with the axis of symmetry OQ. The magnitude of the gradient of the first term in the radial direction is always Gm/d^2 and the direction of the gradient vector is always parallel to OQ, regardless of the position of P on the earth's surface. The first term thus represents the force causing the centripetal acceleration of the point P about the common centre of mass of the two bodies, known as the barycenter (earth-moon or earth-sun). The third term of (3.9) is therefore the source of the tide-generating forces:

$$V_t = -\frac{1}{2}Gm\frac{R^2}{d^3}(3\cos^2\psi - 1) \tag{3.10}$$

A qualitative observation at this point is that the tide generating forces are a second order effect, due to the finite size of the earth in comparison with distance between the earth and other astronomical bodies. Consider the magnitude of the component of the tide-generating forces in the radial (vertical) direction on a unit mass at point P:

$$\mathbf{F}_t \cdot \mathbf{e}_r = -\frac{\partial V_m}{\partial r} = 2Gm\frac{R}{d^3}(3\cos^2\psi - 1) \tag{3.11}$$

where the force is positive in the direction of increasing R, i.e. away from the earth's surface. By comparison, the force (in the radial direction) on a unit mass at the earth's surface, due to the gravitational field of the earth is:

$$\mathbf{F}_M \cdot \mathbf{e}_r = -\frac{GM}{R^2} = -g \tag{3.12}$$

assuming that the earth is a sphere of radius R—a good approximation as the difference between equatorial and polar radii is approximately 0.3%. Then:

$$\left|\frac{\mathbf{F}_t \cdot \mathbf{e}_r}{\mathbf{F}_M \cdot \mathbf{e}_r}\right| = 2\frac{m}{M}\left(\frac{R}{d}\right)^3 (3\cos^2\psi - 1) \tag{3.13}$$

For the moon, $m/M \approx 1/81$ and $R/d \approx 1/60$ so it can be seen that the magnitude of the tide-generating force at the earth's surface in the vertical direction is $O(10^{-8}g)$. For the sun, with $m/M \approx 332900$, the vertical forces turn out to be of the same order of magnitude. As a consequence, only the horizontal components of the tide-generating forces, known as tractive forces, are of significance and *the vertical forces will be subsequently neglected.*

The earth is rotating, in addition to orbiting around its common centre of mass with the moon and sun. Consequently point P on the surface has an additional centripetal acceleration $\Omega^2 R\cos\phi$ directed towards the axis of rotation and perpendicular to it. This acceleration must be provided by the gravitational attraction of the earth and horizontal forces at the earth's surface. The maximum vertical value of the acceleration is approximately $g/291$ at the equator, going to zero at the poles. The azimuthal component is zero at the equator and poles, and reaches a maximum magnitude of $g/582$ at $\pm 45°$N, several orders of magnitude greater than the tide-generating forces. However, the centripetal acceleration varies only with latitude, not time, so does not generate any tides but does result in a constant bulge of the potential towards the equator. It may therefore be considered as a small correction to the magnitude and direction of the acceleration due to gravity.

The position of a general point P on the earth's surface may be expressed relative to the centre of mass of the earth by its longitude λ (positive east of the

Greenwich meridian) and its latitude ϕ (positive north of the equator). The position of the distant body, moon or sun, may be also expressed by a range, in addition to equatorial coordinates of right ascension α and declination δ, as a function of time. The reference longitude is however not taken as the Greenwich meridian, but the direction of the sun vertically overhead at the equator at the March equinox, with respect to the stars (♈), which varies only slightly from year to year (unlike the Greenwich longitude, which varies through 360° every 24 hours). Figure 3.2 describes the relative angles, as projected from a point at the centre of the earth onto a sphere far away (the 'celestial sphere'). It should be noted that the distance d is also a function of time as the orbits of the moon about the earth and the earth about the sun are elliptical.

What is now required to be found is the angle ψ subtended by OQ and OP. This may be obtained from the positions of P and Q and from a spherical triangle identity:

$$\cos c = \cos a \cos b + \sin a \sin b \cos A \tag{3.14}$$

hence,

$$\cos\psi = \cos(90-\phi_P)\cos(90-\delta_Q) + \sin(90-\phi_P)\sin(90-\delta_Q)\cos(\lambda_P - \alpha_Q - \Upsilon) \tag{3.15}$$

simplifying and substituting for the relative equatorial longitude $\lambda_{PQ} = \lambda_P - \alpha_Q - \Upsilon$,

$$\cos\psi = \sin\phi_P \sin\delta_Q + \cos\phi_P \cos\delta_Q \cos\lambda_{PQ} \tag{3.16}$$

Therefore, the tide-generating potential may be expressed in coordinates of latitude and longitude as:

$$V_t = \frac{GmR^2}{d^3}\left\{3\left(\sin\phi_P \sin\delta_Q + \cos\phi_P \cos\delta_Q \cos\lambda_{PQ}\right)^2 - 1\right\} \tag{3.17}$$

Expression 3.17 may be expanded and factorized using trigonometric

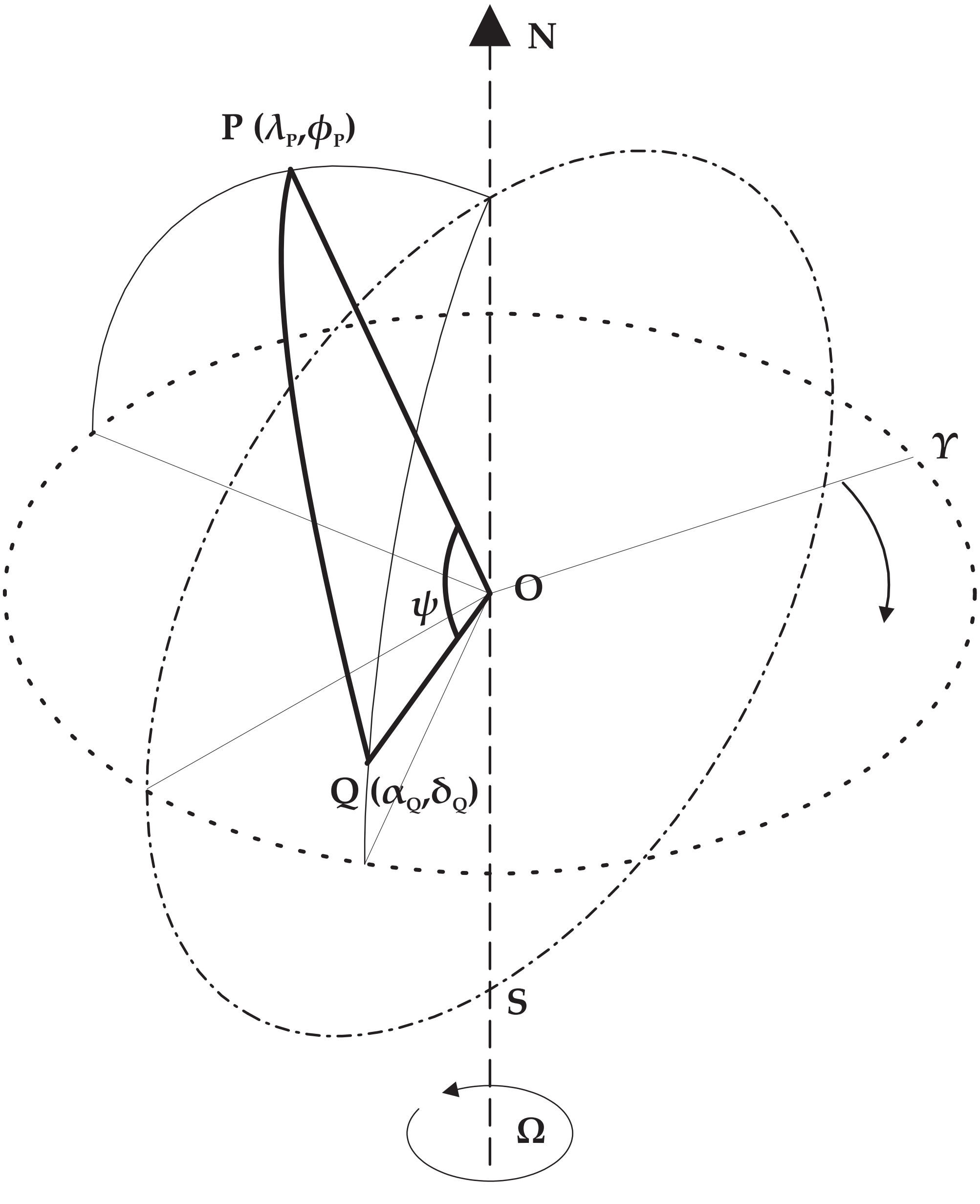

Figure 3.2: Definition of angles described in the text, all lines projected onto a celestial sphere. Dashed line (– –) is the axis of rotation of the earth, with arrow pointing North. Dash-dot line (— ·) is the Prime meridian; dotted line (· · ·) is the equator.

identities to give the tide-generating potential as:

$$V_t = \tfrac{GmR^2}{d^3}\left[\underbrace{\frac{3}{2}(\sin^2\phi_P - \frac{1}{3})(\sin^2\phi_Q - \frac{1}{3})}_{\text{I}} + \underbrace{\frac{1}{2}\sin 2\phi_P \sin 2\phi_Q \cos\lambda_{PQ}}_{\text{II}} + \underbrace{\frac{1}{2}\cos^2\phi_P\cos^2\phi_Q\cos 2\lambda_{PQ}}_{\text{III}}\right] \tag{3.18}$$

The tidal potential has been plotted in Figure 3.3 for two separate instants in time, both close to the October equinox, but one at conjunction (new moon) and a week later at quadrature. The right ascension, declination and range of the sun and moon have been obtained from the HORIZONS database (Jet Propulsion Laboratory 2008). Note the colour scale (in m) varies between the two plots. The horizontal forces resulting from the negative of the gradient of the potential have also been plotted; the scale of the vectors is the same in both plots.

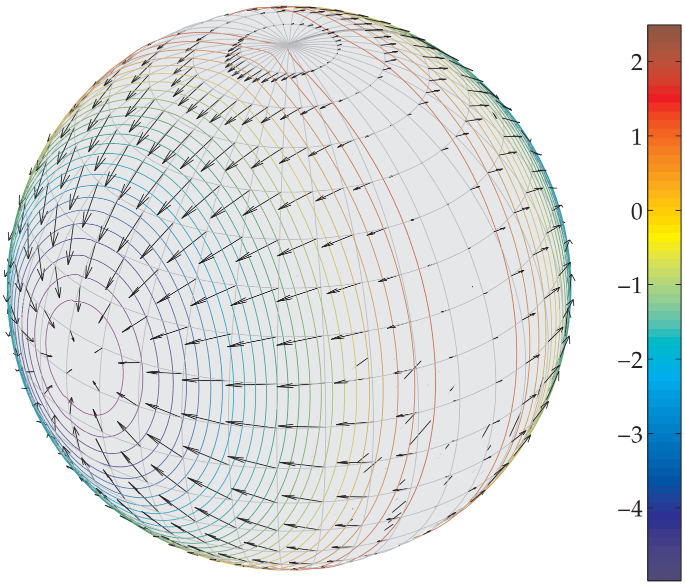

(a) New moon, 29 September 2008, 08:12 (UT).

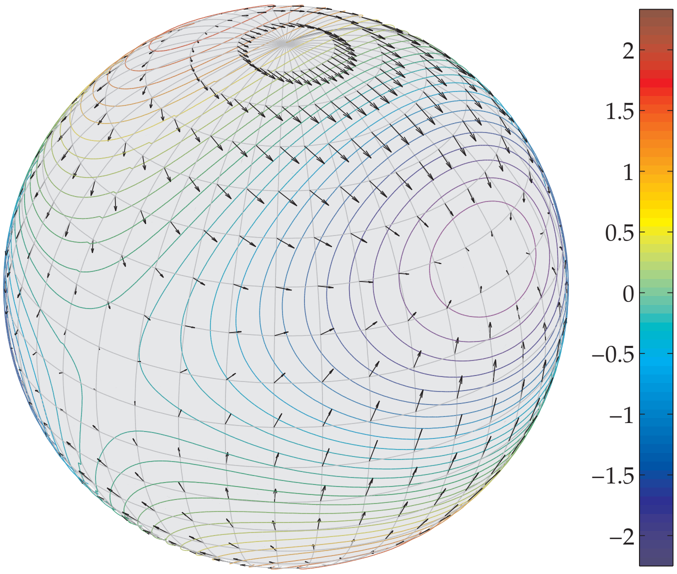

(b) First quarter, 7 October 2008, 09:04 (UT).

Figure 3.3: Tidal potential (m, note different colour scale) and tidal force vectors (to scale)

3.3 Characteristics of the tidal forcing spectrum

The three terms in the square brackets of (3.18) represent the three main species or frequency bands of tidal forcing of the oceans. All the terms are modulated by the distance d and by terms varying in different senses with the latitude of Q:

I Long period tides. These terms do not depend on relative longitude, so vary only very slowly with the fundamental periods of the forcing body. These terms make their maximum contribution to the tidal potential when the body has zero declination with respect to the equator (or in other words, is directly overhead at the equator).

II Diurnal tides. These terms have a period of around 24 hours and contribute tidal potential varying in space from zero at the equator to a maximum at 45° north or south of the equator, then decreasing to zero at the poles. In time they are at a maximum when the sun or moon is at its maximum declination above or below the equator, as the maximum declinations are $\pm 23.45°$ and $\pm 28.35°$, respectively ($< 45°$). In fact the diurnal tides only arise due to the inclination of the earth's axis of rotation to its orbit around the sun, and the obliquity of the moon's orbit about the earth.

III Semi-diurnal tides. These tides have a period of around 12 hours and generate maximum potential at the equator, decreasing monotonically to zero at the poles. In time, they make maximum contribution to the tidal potential when the sun or moon have zero declination.

In order to obtain the tidal forcing as a function of time, λ_{PQ}, δ_Q and d must be found as functions of the astronomical orbital parameters of the earth, moon and sun. In general, this results in complicated expressions for the position of the sun and moon, as the rotational plane of the earth and the orbital planes of the earth and moon are all inclined with respect to one another. In decreasing order of frequency, the important periodicities in the earth-moon-sun system, with respect to distant stars, are:

- The earth is rotating about an axis inclined to its orbital plane.
  $T_0 = 23.934$ h
- The moon is in an elliptical orbit around the centre of mass of the earth-moon system. Same sense of rotation as the earth;
  $T_1 = 27.321661$ days (of 86400 seconds)
- The earth is revolving around the sun in an elliptical orbit. With the earth's rotation; $T_2 = 365.2422$ days
- The moon's orbital ellipse is rotating slowly in its own plane. With the earth's rotation; $T_3 = 5.997$ Julian years (of 365.25 days)
- The moon's orbit around the earth is inclined at an angle of approximately 5.15° with respect to the earth's orbital plane and the points of intersection of the moon's orbit are rotating slowly in that plane. Against the earth's rotation; $T_4 = 18.600$ years
- The earth's orbital ellipse is revolving very slowly about the sun in its plane. $T_5 = 111361$ years (the rate of change is irrelevant, but the phase of the perihelion occurs in a small number of tidal constituents)

From these fundamental periodicities are derived geocentric phases and frequencies, which appear in the tidal forcing and response spectra and are summarized in Table 3.1.

Even this is a simplified view, as the moon's orbit around the earth is not independent of the sun's gravity and is perturbed as a consequence. In addition there are small perturbations of the earth's axis of rotation due to the sun and moon. These effects are not considered further here. The distance, declination and longitude of the moon and the sun can be found by adding or subtracting the relative angular positions as functions of the six periods above, using spherical trigonometry. The eccentricity of the orbits results in approximate expressions for the lunar or solar distance, longitude and declination, containing terms of the form $1 + k \cos x$. When substituted into

Table 3.1: Phase and rate of change of phase of the components of tidal frequencies. Source: Bell et al. (1999). A year is defined in this table as a common year, e.g. 365 days. Angular frequencies $> 180°$/year have been wrapped. The reference phase is in the 1900 epoch.

Angle		Mean rate of change of angle			
	(1) (°)		°/year	°/day	°/hour
Mean right ascension of the Greenwich meridian					
β	0	$\Omega = \omega_0 - \omega_2$	0	0	15.000000
—Moon					
s	277.0247	$\dot{s} = \omega_1$	129.38481	13.17639	0.549016
—Sun					
h	280.1895	$\dot{h} = \omega_2$	-0.23872	0.98565	0.041069
—Lunar perigee					
p	334.3853	$\dot{p} = \omega_3 - \omega_4$	40.66249	0.1114	0.004642
—Lunar ascending node					
N	259.1568	$\dot{N} = -\omega_4$	-19.32818	-0.05295	
—Perihelion					
p'	281.2209	$\dot{p}' = \omega_5 + \omega_3$	0.17192		

Equation 3.18 and expanded, these result in side-bands around the principal diurnal and semidiurnal frequencies of tidal forcing. A high-order expansion of the forcing expression results in hundreds of terms, but the relative amplitude of most are very small and only a few leading terms account for the major part of the energy in the response spectrum.

3.4 Tidal energy and the rotation of the Earth

The earth rotates about its own axis in 23.934 hours. The moment of inertia I of the earth is approximately 8.034×10^{37} kg m^2 (Lambeck 1980), therefore the earth has an energy of rotation of $E_r = I\omega^2/2 = 4.27 \times 10^{29}$ J. From measurements of the moon's orbit, the moon's mean radius of orbit is increasing at a rate of approximately 4 cm/year, meaning that it is 'climbing out' of the earth's gravitational potential 'well'. Consequently, the moon's mean longitude relative to the earth-moon barycenter (centre of mass) is decelerating at a rate of 25 arcseconds/(century)^2 (Christodoulidis and Smith 1988). Applying the chain rule, the total rate of gain of energy by the moon, treated as a point mass (potential plus kinetic, but neglecting small changes in rotational energy), is as follows:

$$\frac{dE_{\mathrm{t}}}{dt} = GMm\frac{dd}{dt}\frac{1}{d^2} + md^2\omega\frac{d\omega}{dt} + md\omega^2\frac{dd}{dt} \tag{3.19}$$

This corresponds to a rate of gain of energy at the expense of the earth's rotation of 160 GW. Simultaneously, the earth's rotation is decelerating at a rate of approximately 6×10^{-22} rad/s^2 (Wu et al. 2003). The rate of change of rotational energy of a body undergoing accelerating rotation is:

$$\frac{dE_r}{dt} = I\Omega\frac{d\Omega}{dt} \tag{3.20}$$

which corresponds to a constant average loss of energy by the earth of 3.5 TW. If this rate of deceleration remained constant, then the earth's rotational period would slow from one day to two days in approximately four billion years. However it is believed that the earth will become uninhabitable in around one billion years due to increases in solar irradiance (Schröder and Connon Smith 2008), so the figure is somewhat academic. The difference in rotational energy lost by the earth and total energy gained by the moon must be dissipated by the tides of the solid earth, the oceans and the atmosphere. Note that this is a tiny rate of dissipation in comparison to the radiated solar energy intercepted by the earth (around 174000 TW*). What makes tidal power worth considering for power generation, along with solar forms such wind, wave, hydroelectric and direct solar conversion, is the way in which tidal energy is concentrated in the shallow continental shelves around the earth's oceans. Taking wave energy for comparison, the total amount of energy transmitted by wind-generated waves is vast, but the exploitable resource within a reasonable distance of the earth's populated coastlines has been estimated at around 100 GW, of the same order of magnitude as the exploitable tidal resource (Pontes et al. 2003).

There are other sinks of tidal energy apart from than in the oceans. The solid earth responds almost instantaneously to tidal forcing, over all forcing frequencies, so is far from resonance. The main effect of the earth tides is to deform elastically and do work against the oceans, which modifies the oceanic response to tidal forcing. By contrast, the inelastic dissipation of energy in the solid earth due to tidal forcing is estimated at only 32 GW (Platzman 1984).

---

[*] see http://www.ngdc.noaa.gov/stp/SOLAR/ftpsolarirradiance.html

Atmospheric gravitational tidal dissipation is estimated to be of the order of 10 GW and principally driven by the ocean surface, rather than by direct forcing. The daily cycle of solar heating has a much greater effect on the atmosphere (Platzman 1991). A simplified *mean* energy-flow diagram showing the coupled solid earth-ocean-atmosphere tidal energy transfers is included in Figure 3.4.

In conclusion, the earth is continually losing rotational energy, but on a timescale comparable with the habitable lifetime of the earth. Even if it were possible to devise a scheme whereby tidal dissipation in the oceans would be increased by an order of magnitude, e.g. by bringing continental shelves closer to resonance, the earth's rotation would not be significantly altered. Consequently, it is safe to categorize tidal energy as a renewable resource. The major part of the rotational energy lost is dissipated in the fluid tide i.e. the global ocean.

3.5 Tidal dissipation in the oceans

There is a net flux of potential and kinetic energy from the deep oceans, where tide-raising forces are significant, to the shallow shelf seas where direct gravitational forcing is a small effect (Cartwright 1977). The energy propagates in the form of very long waves, influenced by the rotation of the Earth. The rate of dissipation of tidal energy in the Earth's shelf seas is on average about 2.5 TW out of a total dissipation of 3.5 TW (Egbert and Ray 2003). This figure is less than originally thought, as previous estimates failed to take into account dissipation due to internal waves in the deep ocean (Wunsch 2000; Jayne and St. Laurent 2001; St. Laurent et al. 2002), but nonetheless represents a large concentration of tidal energy in relatively small areas of continental shelf.

At the edge of a continental shelf, some of the incident tidal energy is reflected back into the deep ocean and the remainder is transmitted onto the shelf, where the energy is eventually dissipated in turbulence. When a continental shelf is close to resonance, the amplitude of the reflected wave at the shelf edge is reduced and the transmitted wave onto the shelf increased in amplitude towards a maximum; the extent to which an area of shelf can resonantly

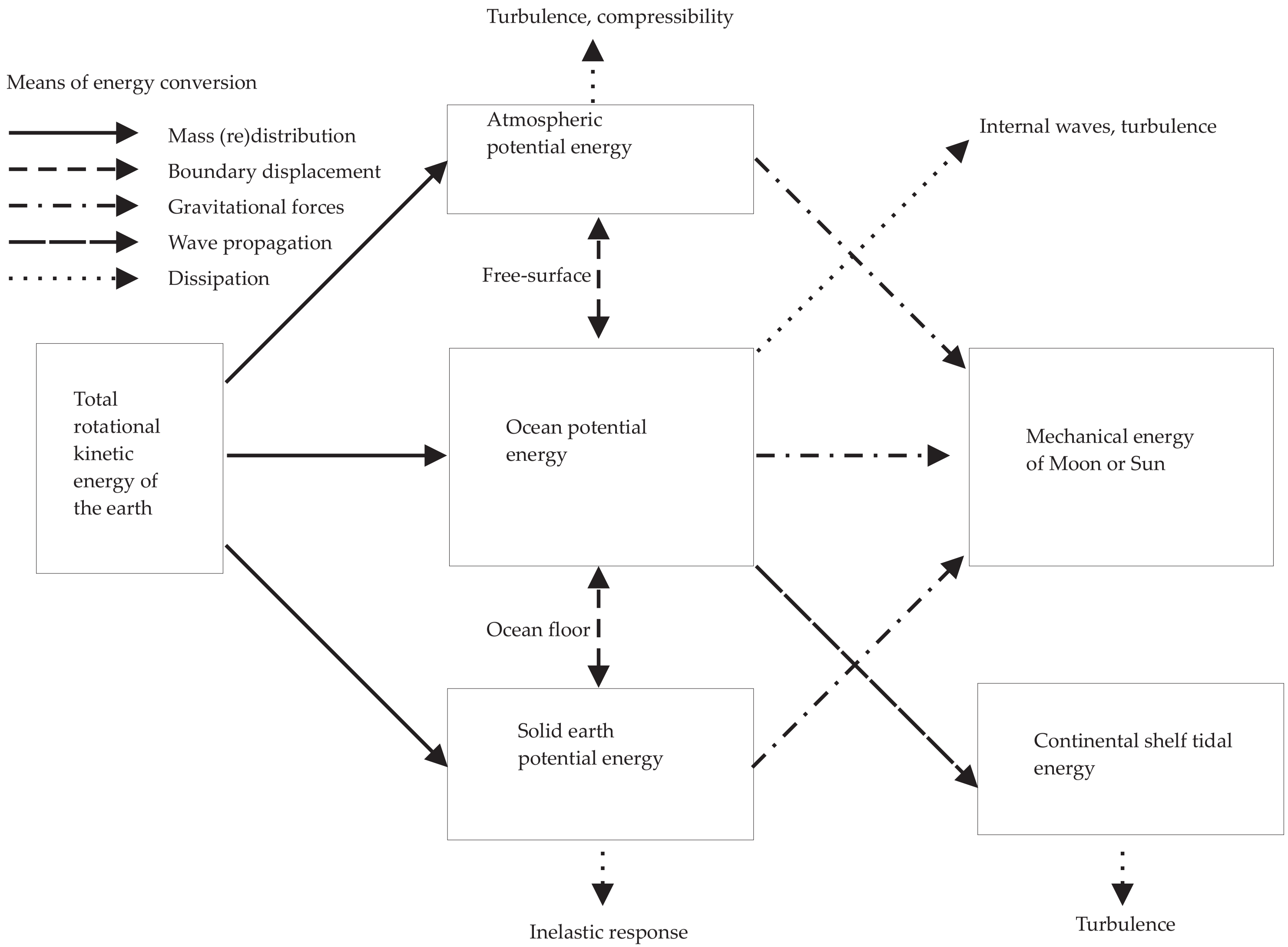

Figure 3.4: Energy flow diagram showing the *average* transfers of tidal energy from the earth's rotation to the moon's orbit

absorb energy is governed by its geometry and frictional damping (Webb 1982). It is not clear whether large-scale introduction of tidal power could significantly affect the absorption of energy by the continental shelf at its boundary. A study on the effect of the proposed Bay of Fundy tidal barrage scheme (Garrett and Greenberg 1977) on the boundary conditions of a numerical model representing the area found that there would be small but significant downward corrections in mass flux ($< 5\%$) at the continental shelf boundary when compared to results assuming no back-effect of the scheme on the boundary conditions. A difficulty found in this analysis was dealing with the part of the boundary lying on the continental shelf, where a change in mass flux would create a far larger change in elevation than in the deep ocean.

3.5.1 Dissipation of tidal energy around the British Isles

In an early piece of work by G. I. Taylor (1920) expressions were derived for the tidal energy flux through a cross-section of a tideway (area of sea or tidal channel) and the dissipation of energy within a region bounded by such cross-sections. From conservation of energy, the divergence of energy flux was equated with the rate of dissipation integrated over the bounded region. These expressions were applied approximately to the Irish Sea where it was found that there was a net flux of 64 GW into the Sea, agreeing well with an estimate for dissipation of 60 GW. The total tidal energy flux onto the north-west European continental shelf derived from two-dimensional numerical model results was estimated by Flather (1976) at 215 GW. A subsequent estimate based on data from moored current meters and bottom pressure transducers put the figure at 250 GW (Cartwright et al. 1980). A more recent estimate using an inverse model constrained by satellite altimetry data (Egbert and Ray 2001) was 219 ± 31 GW and the authors concluded that the uncertainty in their results was of similar magnitude to that of the 250 GW estimate. It can be confidently stated that currently on average over 200 GW of tidal energy is being dissipated in the waters around the British Isles. Questions arising for those interested in tidal energy generation are what proportion of this could be extracted economically and indeed whether the figure could alter significantly due to changes in the impedance of the continental shelf as a result of energy extraction.

3.6 Tidal dynamics

In certain cases, some of the terms in equations (4.58) may be small compared to others and neglected to produce a simpler set of equations. The Rossby number:

$$Ro = \frac{U}{2L\Omega \sin\lambda} \tag{3.21}$$

where L is a characteristic length scale, indicates the importance of the Coriolis acceleration in comparison to inertial acceleration. It is important to note that the Coriolis acceleration is always at right angles to the streamwise acceleration. Where $Ro < 1$, the Coriolis term may not be neglected; at $50\,\mathrm{deg}$N, for a velocity $U = 1$ m/s, this would imply that the Coriolis term is significant for length scales greater than 9 km. If it maintained a constant speed of 1 m/s along its path, a fluid parcel would travel 11 km in a quarter of the period of the principal M_2 tide ($T/4 = 3.1\ hr$), indicating that Coriolis effects are very likely to be important in modelling of tidal flows in localities of interest to tidal stream power generation, possibly also down to the scale of a large array of turbines although certainly not at the level of individual generators.

At larger spatial scales e.g. a continental shelf sea or the deep ocean, if L is taken as a characteristic dimension of the basin then $Ro \ll 1$. As a consequence the inertial acceleration terms become negligible and the flow is said to be in geostrophic balance between the Coriolis acceleration, the pressure gradient and the gradient of the tidal potential.

On the right hand side of the momentum equation, the tidal forces arising from the gradient of the tidal potential may be compared to the other force terms. As mentioned in §4.10, sea-surface slopes of 4×10^{-6} may be expected in the English Channel, which corresponds to an average specific force of approximately $4 \times 10^{-6} g$ N/kg. The tidal forcing at 50°N in the horizontal plane has maximum amplitude $7 \times 10^{-8} g$ N/kg, indicating that in this shallow sea area, almost all the forcing is external, with only a very small contribution from the tide-generating forces. In the deep ocean, the wavelengths are an order of magnitude larger (as the shallow water approximation still holds i.e. $c = \sqrt{gh}$ and h is two orders of magnitude larger) and the amplitudes are smaller, indicating that direct tidal forcing plays an important role.

3.6.1 Propagation of tidal waves onto the continental shelf

When a train of tidal-waves generated in the deep ocean encounters an abrupt decrease in depth at the shelf edge, interesting effects occur, illustrated in one-dimensional form in Figure 3.5. It can be shown for the one-dimensional case (Dean and Dalrymple 1991, page 145) that based on matching the free-surface elevation and flow rate on either side of the shelf break,

1. The waves are partially reflected, with the reflected wave being of a similar amplitude to the incident wave, creating a standing wave pattern.
2. The wave is partially transmitted, with approximately double the amplitude and with decreased wavelength and celerity.

In contrast, when a wave travels from the shelf sea towards the deep ocean:

1. The wave is almost completely reflected, with similar amplitude to the incident wave
2. The wave is partially transmitted, with much reduced amplitude

These effects ensure that once tidal energy has propagated onto a continental shelf, it tends to remain trapped there until dissipated.

3.6.2 Continental shelf tides

In reality, tidal wave propagation onto the continental shelf is more complex than the one-dimensional model would suggest. Observations in the Atlantic Ocean (Cartwright et al. 1980) show that tidal waves in the semi-diurnal band progress in a direction almost parallel to the edge of the continental shelf, rather than directly incident. If the Coriolis term is included (but neglecting

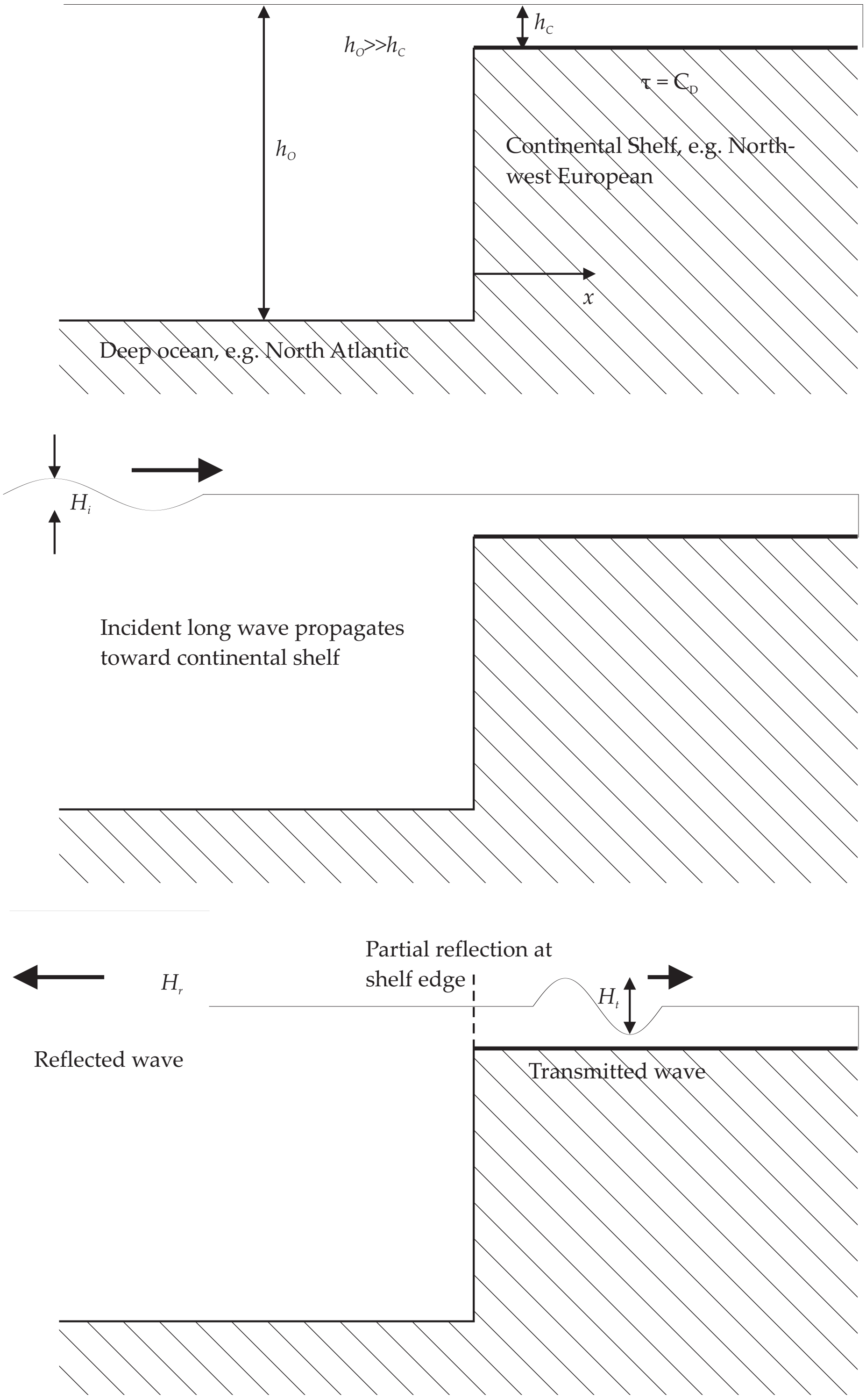

Figure 3.5: Tidal wave propagation onto a continental shelf

tide-generating force, advection, friction and diffusion) in addition to pressure gradient and lateral boundaries (i.e. coastline), then solution is in general complicated, requiring a Green's function approach (Webb 1974). However, for very simple boundary conditions, some analytical solutions have been found. For an infinite coastline with zero flow normal to it, the solution is known as a Kelvin wave, propagating along the coastline with the shallow water celerity $\sqrt{gd}$ and with elevation amplitude decreasing exponentially from the coastline. Taylor (1922) found a solution for the case of a rectangular basin, open at one end, in terms of two Kelvin waves following one another around the basin, in the same sense as the rotation of the earth. The superposition of these waves results in cancellation at a point known as an amphidrome, from which emanate lines of equal phase. Amphidromes have been observed in real seas, notably the southern North Sea. This model was extended to include friction by subsequent authors (Rienecker and Teubner 1980), demonstrating that the amphidrome is displaced landward from the centre of the channel as the attenuation of the waves by friction becomes more important, eventually becoming virtual (or 'degenerate') when it appears to be on land. The English Channel fits this model reasonably well, although the large tidal current amplitudes midway along the Channel and the large elevation amplitudes on the French Coast have lead to suspicions of the presence of a damped half-wave resonance in conjunction with the Kelvin wave-type dynamics (Pugh 1987, 5:4:2). Webb (1976) found that resonance on continental shelves was in theory possible but difficult to identify due to the broad resonant peaks and very narrow tidal forcing bands.

3.7 Analysis of tidal signals

The origin of constituent frequencies that occur in the tidal spectrum was discussed in §3.3. In order to provide a compact representation of the tidal response at a location, whether for tidal elevations or streams, the set of basis functions for a non-linear least squares regression are taken as a truncated set of the terms from the expansion of the forcing potential, along with some higher (and in one case, lower) harmonic 'shallow-water' frequencies. The frequencies are calculated from a combination of the periodicities specified in

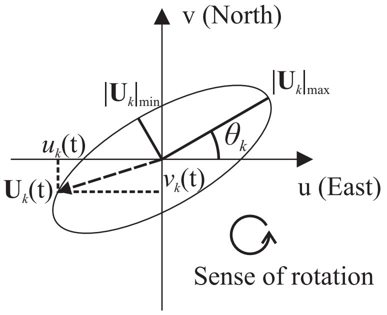

Figure 3.6: Definition of tidal stream ellipse parameters for constituent k.

Table 3.1 according to:

$$\omega_k = i_{\beta k}\dot{\beta} + i_{sk}\dot{s} + i_{hk}\dot{h} + i_{pk}\dot{p} + i_{Nk}\dot{N} + i_{p'k}\dot{p}' \tag{3.22}$$

The reference phase at Greenwich for a particular constituent is similarly:

$$V_k = i_{\beta k}\beta + i_{sk}s + i_{hk}h + i_{pk}p + i_{Nk}N + i_{p'k}p' \tag{3.23}$$

The tidal constituents that are relevant in the English Channel are listed in Table 3.2, ordered by origin and frequency. In other locations, a different set of constituents might be more appropriate, for example more diurnal constituents and less shallow-water constituents included. The constant offset is in order that terms of the form $\sin x$, $-\sin x$ and $-\cos x$ may be expressed as cosine terms.

The velocity of the tidal stream at a point can be represented in complex form U as the sum of N constituent ellipses,

$$U_k = \sum_{k=0}^{N} \alpha_k \exp^{i\omega_k t} + \beta_k \exp^{-i\omega_k t} \tag{3.24}$$

where α_k and β_k are complex. The constituent frequencies are integer combinations of the fundamental astronomical frequencies and $\omega_0 = 0$ rad/s. The properties of the kth ellipse defined in Figure 3.6 on a polar diagram can be readily calculated from A_k and B_k: the semi-major axis (3.25), semi-minor axis (3.26), the inclination (3.27) and the phase of the major axis relative to the equilibrium phase V (3.28).

$$|U_k|_{\max} = |\alpha_k| + |\beta_k| \tag{3.25}$$

$$|U_k|_{\min} = |(|\alpha_k| - |\beta_k|)| \tag{3.26}$$

$$\theta_k = \frac{1}{2}\left[\arg(\alpha_k) + \arg(\beta_k)\right] \tag{3.27}$$

$$\phi_k = V_k - \frac{1}{2}\left[\arg(\alpha_k) - \arg(\beta_k)\right] \tag{3.28}$$

Table 3.2: Description of tidal constituents referred to in the text

Name	σ **(°/h)**	i_a	i_b	i_c	i_d	i_e	i_f	**Offset (°)**	**Origin**
Non-tidal									
S_a	0.0410686	0	0	1	0	0	0	0	Solar radiation
Gravitational - diurnal									
O_1	13.9430356	1	-2	1	0	0	0	270	Inclination of earth's rotation and moon's orbit
K_1	15.0410686	1	0	1	0	0	0	90	Inclination of earth's rotation (sun and moon)
Gravitational - semi-diurnal									
$2N_2$	27.8953548	2	-4	2	2	0	0	0	Eccentricity of moon's orbit (2nd order)
N_2	28.4397295	2	-3	2	1	0	0	0	Eccentricity of moon's orbit (larger)
ν_2	28.5125831	2	-3	4	-1	0	0	0	Sun's effect on moon's perigee (larger)
M_2	28.9841042	2	-2	2	0	0	0	0	Principal lunar
λ_2	29.4556253	2	-1	1	0	0	0	180	Sun's effect on moon's perigee (smaller)
L_2	29.5284789	2	-1	2	-1	0	0	180	Eccentricity of moon's orbit (smaller)
S_2	30.0000000	2	0	0	0	0	0	0	Principal solar
K_2	30.0821373	2	0	2	0	0	0	0	Inclination of earth's rotation (sun and moon)
Mixed gravitational and shallow water									
M_{sf}	1.0158960	0	2	0	0	0	0	0	Sun's effect on moon's mean orbit
μ_2	27.9682084	2	-4	4	0	0	0	0	Sun's effect on moon's mean orbit
Shallow water - continuity and friction									
$2SM_2$	31.0158958	2	2	-2	0	0	0	0	
MN_4	57.4238337	4	-5	4	1	0	0	0	
M_4	57.9682084	4	-4	4	0	0	0	0	
MS_4	58.9841042	4	-2	2	0	0	0	0	
Shallow water - frictional									
M_6	86.9523127	6	-6	6	0	0	0	0	
$2MS_6$	87.9682084	6	-4	4	0	0	0	0	

When U_k is purely real, corresponding to a scalar tidal signal such as pressure or elevation, or a component of velocity, α and β are complex conjugate, and expression 3.24 reduces to the more familiar real form:

$$\zeta = Z_0 + \sum_{n=1}^{N-1} f_n H_n \cos(\omega_n t - \phi_n + V_n + u_n) \tag{3.29}$$

where H_n is the amplitude of the constituent, ω_n the angular speed, ϕ_n phase relative to astronomical argument and V_n astronomical argument (or equilibrium phase). The reference phase is usually taken as the phase of the tidal forcing at a particular longitude, usually the Prime (or Greenwich) meridian. The reason for using this reference rather than the local forcing phase is partly so that the progression of tides can easily be followed on a co-tidal chart and partly because the spatial pattern of phase response in the earth's oceans bears no resemblance to that of the tidal forcing. Z_0 represents mean sea level with respect to a vertical datum. In this case, ζ represents sea-surface elevation, but the same analysis can be used for U and V components of tidal stream velocity.

The choice of the set of N constituents is determined partly by the dynamics of the region in question: whether shallow water constituents are likely to be required; the importance of radiational tides; whether semi-diurnal or diurnal tides are dominant and any local resonant effects resulting in unusually large response amplitudes at certain frequencies. Due to noise present in tidal spectra due to meteorological and other effects, certain constituents may not be separable from each other, particularly when a smaller constituent is close in frequency to another larger constituent. This is particularly critical for record lengths shorter than approximately 29 days. For records between 29 days and one year, there is only one constituent of significant amplitude that cannot be resolved, K_2, which in practice in a harmonic analysis is set to be a certain fraction of the amplitude of, and phase offset to, S_2. The amplitude ratio and phase offset are taken from analysis of the records (greater or equal too a year in length) of a nearby tide gauge. This is justified in general by reference to spatial distributions of amplitude and phase that are similar for constituents with closely spaced frequency. The response spectra of tidal streams, while related directly to that of tidal elevations, is not the same and the application of amplitude ratios and phase offsets derived from tide gauges to current meter records (almost always of less than a year's duration) is questionable, but no better alternative is available.

The terms f and u are small corrections for spectral lines too finely separated to be resolved by one year of data, given the typical level of noise in the spectrum. The spectral lines are separated either by the 18.6-year cycle of the lunar ascending node or the 8.85 year cycle of regression of the lunar apsides and are therefore one and zero respectively for all purely solar constituents Pugh (1987). The corrections are cumbersome to use as they must be calculated separately for each constituent frequency containing a different multiple of i_b and i_c. Typically the terms are only calculated once for analysis of a year of data, as they themselves are cosine terms with a frequency of ω_N. They are assumed to be in phase with the astronomical argument.

Once the set of N tidal constituents are decided upon, a tidal signal may be analyzed as a non-linear least-squares problem with N unknown amplitudes and N unknown phases (in the case of a vector, there are $4N$ unknowns) which requires the inversion of a $2N \times 2N$ matrix.

Chapter 4

Hydrodynamic equations

4.1 Reference frame

In this section, the equations of motion for fluid on the surface of the earth will be derived in Cartesian coordinates, taking into account the rotation of the earth to maintain generality. The equations will be derived by applying the principle of conservation of mass and Newton's Second Law to a small fluid cube $\delta V = \delta x \, \delta y \, \delta z$, with mass $\delta m = \rho \, \delta V$ centred on (x, y, z), as defined in Figure 4.1. The origin of the reference frame is a point fixed on the earth's surface, with $\mathbf{i}, \mathbf{j}, \mathbf{k}$ forming a right-handed set aligned with the local east, north and vertical directions.

The x-y plane of this Cartesian frame of reference is tangent at its origin to a sphere representing the earth. However, bathymetric data input to numerical models are given in projections of spherical coordinates. As the finite element method is to be used to solve the equations (§5.1.2), consistency of co-ordinates is only required at the local level; with elements of length scale 1 km, the curvature of the earth has a negligible effect. The angular velocity vector of the reference frame with respect to the fixed stars is:[*]

$$\boldsymbol{\Omega} = \Omega \cos \phi \mathbf{j} + \Omega \sin \phi \mathbf{k} \tag{4.1}$$

---

[*] The angular frequency of the earth Ω with respect to the fixed stars is slightly greater (0.27%) than the frequency of a solar day, due to the orbit of the earth around the sun.

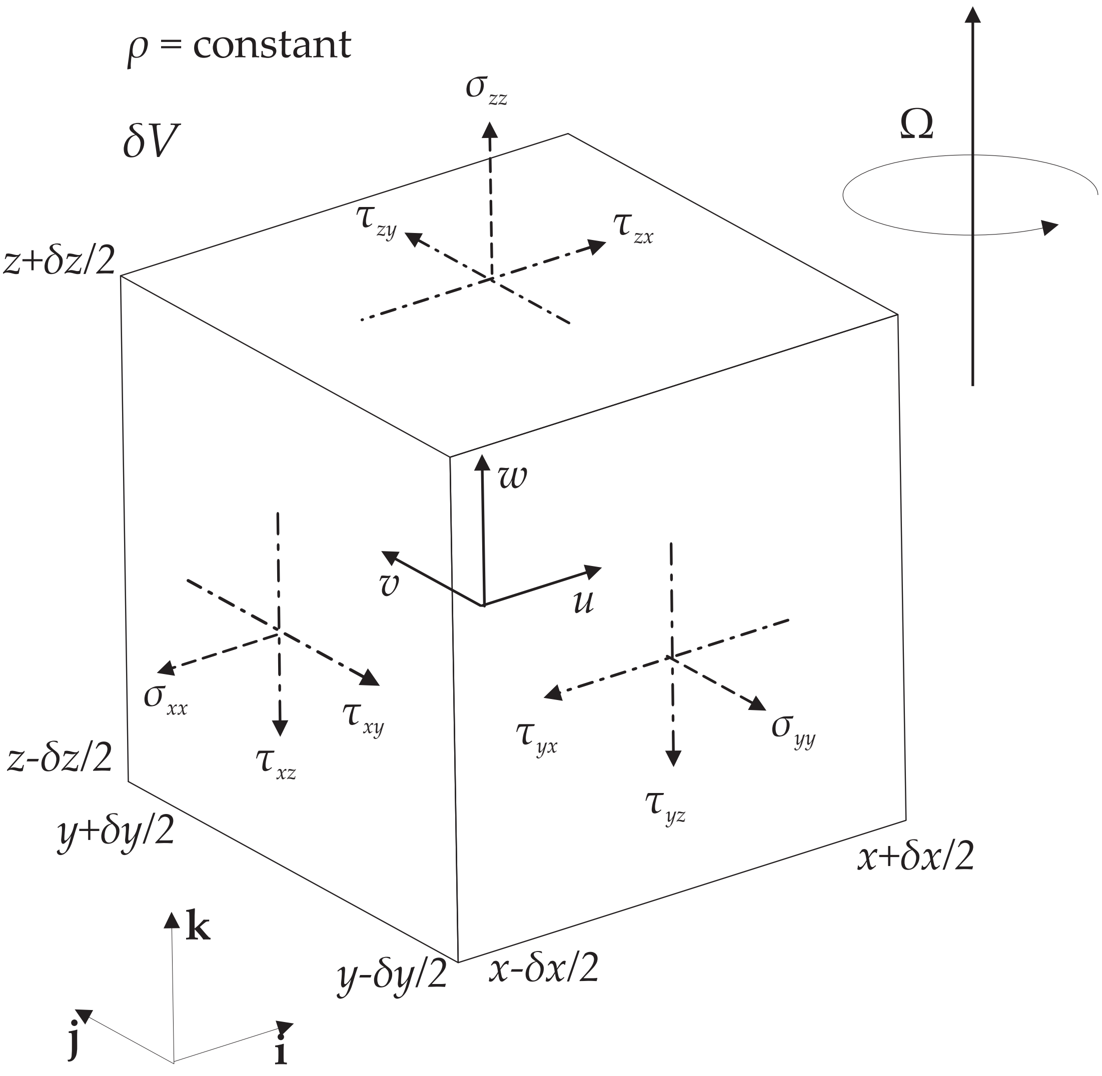

Figure 4.1: Definition sketch for Navier-Stokes equations. Control volume δV centred on (x, y, z)

4.2 Properties of sea-water

Water is practically incompressible, with a bulk modulus of approximately 2×10^9 Pa. As an illustration, consider moving a fluid parcel from the sea surface to the sea-bed at 100 m depth, where the hydrostatic pressure is approximately 10^6 Pa; this would result in a volume change of 0.05%. As a consequence it is assumed here that the density is not a function of pressure. A further assumption is that the fluid is of uniform density. This eliminates fluid density from the equations, excluding the variation of density with temperature and salinity, which lead to phenomena such as stratification, internal waves and fronts between mixed and stratified regions; all of which are observed in the oceans and coastal seas. However, the density of water in the oceans varies only for the global ocean, it has been shown that the first mode of oscillation arising in the solution to the equations of motion allowing variation of density in the vertical, converges to the solution of the equations when constant average density is assumed (Cartwright 1977). At the coastal scale, in regions of strong tidal currents on the continental shelf there is vigorous mixing throughout the water column even through the summer months where solar heating is high and wind-driven mixing is low (Webb 1982). As a consequence the approximation of constant density is valid in these regions.

4.3 Derivation of the continuity equation

Applying conservation of mass within volume δV and taking the first term of the Taylor series expansion of (u, v, w) about (x, y, z):

$$\begin{aligned}
\left(u - \frac{\partial u}{\partial x}\frac{\delta x}{2} + O(\delta x)^2\right)\delta y \delta z - \left(u + \frac{\partial u}{\partial x}\frac{\delta x}{2} + O(\delta x)^2\right)\delta y \delta z &\quad + \\
\left(v - \frac{\partial v}{\partial y}\frac{\delta y}{2} + O(\delta x)^2\right)\delta x \delta z - \left(v + \frac{\partial v}{\partial y}\frac{\delta y}{2} + O(\delta x)^2\right)\delta x \delta z &\quad + \\
\left(w - \frac{\partial w}{\partial z}\frac{\delta z}{2} + O(\delta x)^2\right)\delta x \delta y - \left(w + \frac{\partial w}{\partial z}\frac{\delta x}{2} + O(\delta x)^2\right)\delta x \delta y &= 0
\end{aligned} \tag{4.2}$$

Simplifying:

$$\frac{\partial u}{\partial x}\delta x\,\delta y\,\delta z + \frac{\partial v}{\partial y}\delta x\,\delta y\,\delta z + \frac{\partial w}{\partial z}\delta x\,\delta y\,\delta z + O(\delta x)^4 = 0 \tag{4.3}$$

In the limit of $\delta V \to 0$, the $O(\delta x)^4$ terms approach zero more quickly than the terms in $O(\delta x)^3$, hence:

$$\frac{\partial u}{\partial x} + \frac{\partial v}{\partial y} + \frac{\partial w}{\partial z} = 0 \tag{4.4}$$

which is the continuity equation for a fluid of constant density.

4.4 Acceleration terms

In order to apply Newton's second law, it is required to find the acceleration $\mathbf{a}$ of the fluid particle in an inertial reference frame. Now $\mathbf{a} = \frac{d^2\mathbf{r}}{dt^2}$ where $\mathbf{r}$ is defined in the inertial reference frame . However, if $\mathbf{r}$ is redefined in a rotating reference frame R, such as with respect to a fixed point on the earth's surface, the rotation operator must be applied (Weisstein 2008c):

$$\left[\frac{d\mathbf{x}}{dt}\right]_{\mathrm{A}} = \left[\frac{d\mathbf{x}}{dt}\right]_{\mathrm{R}} + \mathbf{\Omega} \times \mathbf{x} \tag{4.5}$$

Where $\mathbf{x}$ is a general vector, A denotes the inertial reference frame and R the rotating reference frame. The rotation vector in Cartesian co-ordinates is:

$$\mathbf{\Omega} = \Omega \cos\phi\mathbf{j} + \Omega \sin\phi\mathbf{k} \tag{4.6}$$

where the conventions are defined in Figure 4.1. Hence the relative velocity of the small fluid mass with respect to the origin:

$$[\mathbf{u}]_{\mathrm{A}} - [\mathbf{u}_P]_{\mathrm{A}} = \left[\frac{d\mathbf{r}}{dt}\right]_{\mathrm{A}} = \left[\frac{d\mathbf{r}}{dt}\right]_{\mathrm{R}} + \mathbf{\Omega} \times \mathbf{r} \tag{4.7}$$

Where $\mathbf{u}_P = \mathbf{\Omega} \times R\mathbf{k}$, the velocity of the origin with respect to the centre of mass of the earth. Applying (4.5) again in order to differentiate with respect to time and using the chain rule as $\mathbf{u} = \mathbf{u}(\mathbf{r}, t)$:

$$[\mathbf{a}]_{\mathrm{A}} = \left[\frac{d^2\mathbf{r}}{dt^2}\right]_{\mathrm{A}} = \frac{d\mathbf{u}_P}{dt} + \left[\frac{d^2\mathbf{r}}{dt^2}\right]_{\mathrm{R}} + 2\mathbf{\Omega} \times \left[\frac{d\mathbf{r}}{dt}\right]_{\mathrm{R}} + \mathbf{\Omega} \times (\mathbf{\Omega} \times \mathbf{r}) \tag{4.8}$$

Simplifying:

$$\mathbf{a} = \Omega \times (\Omega \times R\mathbf{k}) + \frac{\partial \mathbf{u}}{\partial t} + \frac{\partial \mathbf{u}}{\partial \mathbf{r}}\frac{d\mathbf{r}}{dt} + \frac{d\mathbf{\Omega}}{dt} \times \mathbf{r} + 2\mathbf{\Omega} \times \mathbf{u} + \mathbf{\Omega} \times (\mathbf{\Omega} \times \mathbf{r}) \tag{4.9}$$

The first term on the RHS represents the centripetal acceleration of the rotating reference frame towards the axis of rotation of the earth, where R is the radius of the earth. It was shown in §3.2 that this acceleration is small compared to the acceleration due to the gravitational attraction of the earth, and may be considered as a small latitude-dependent correction to g, independent of longitude. The final term representing variations in centripetal acceleration may also be neglected by extension from the first term, provided that magnitude of the relative displacement vector **r** is small in comparison to the radius of the earth. Both the first and last terms are always much smaller than the Coriolis (fifth) term, due to Ω^2 dependence. The fourth term may also be neglected as the changes in the magnitude and direction of the angular velocity vector Ω over the course of a year are of the order of 10^{-3} s/solar day and 1 arcsec in direction. Therefore the remaining acceleration terms are:

$$\mathbf{a} = \frac{\partial \mathbf{u}}{\partial t} + \frac{\partial \mathbf{u}}{\partial \mathbf{r}}\frac{d\mathbf{r}}{dt} + 2\boldsymbol{\Omega} \times \mathbf{u} \tag{4.10}$$

in Cartesian coordinates:

$$a_x = \frac{\partial u}{\partial t} + \frac{\partial u}{\partial x}\frac{dx}{dt} + \frac{\partial u}{\partial y}\frac{dy}{dt} + \frac{\partial u}{\partial z}\frac{dz}{dt} + 2\left(\boldsymbol{\Omega} \times \mathbf{u}\right) \cdot \mathbf{i} \tag{4.11}$$

$$a_y = \frac{\partial v}{\partial t} + \frac{\partial v}{\partial x}\frac{dx}{dt} + \frac{\partial v}{\partial y}\frac{dy}{dt} + \frac{\partial v}{\partial z}\frac{dz}{dt} + 2\left(\boldsymbol{\Omega} \times \mathbf{u}\right) \cdot \mathbf{j} \tag{4.12}$$

$$a_z = \frac{\partial w}{\partial t} + \frac{\partial w}{\partial x}\frac{dx}{dt} + \frac{\partial w}{\partial y}\frac{dy}{dt} + \frac{\partial w}{\partial z}\frac{dz}{dt} + 2\left(\boldsymbol{\Omega} \times \mathbf{u}\right) \cdot \mathbf{k} \tag{4.13}$$

It has been implicitly assumed in the application of Newton's Second Law that the coordinates (x, y, z) track the particle δm, so it follows that:

$$\mathbf{u} = \left(\frac{dx}{dt}, \frac{dy}{dt}, \frac{dz}{dt}\right) \tag{4.14}$$

Substituting and expressing the Coriolis terms with the latitude ϕ and East longitude λ:

$$\begin{aligned}
a_x &= \frac{\partial u}{\partial t} &+& \quad u\frac{\partial u}{\partial x} + v\frac{\partial u}{\partial y} + w\frac{\partial u}{\partial z} &+& \quad 2\Omega w \cos\phi - 2\Omega v \sin\phi \\
a_y &= \frac{\partial v}{\partial t} &+& \quad u\frac{\partial v}{\partial x} + v\frac{\partial v}{\partial y} + w\frac{\partial v}{\partial z} &+& \quad 2\Omega u \sin\phi \\
a_z &= \frac{\partial w}{\partial t} &+& \quad u\frac{\partial w}{\partial x} + v\frac{\partial w}{\partial y} + w\frac{\partial w}{\partial z} &-& \quad 2\Omega u \cos\phi
\end{aligned} \tag{4.15}$$

Using the gradient operator to contract the advection terms, the acceleration components are finally:

$$
\begin{aligned}
a_x &= \frac{\partial u}{\partial t} + \mathbf{u}\cdot\nabla u + 2\Omega w\cos\phi - 2\Omega v\sin\phi \\
a_y &= \frac{\partial v}{\partial t} + \mathbf{u}\cdot\nabla v + 2\Omega u\sin\phi \\
a_z &= \frac{\partial w}{\partial t} + \mathbf{u}\cdot\nabla w - 2\Omega u\cos\phi
\end{aligned}
\tag{4.16}
$$

4.5 Normal, shear and body forces

Having defined the acceleration terms, the forces on the mass δm, are considered. These consist of the normal and shear stresses on the faces of the cube $\delta x\,\delta y\,\delta z$ as defined in Figure 4.1. The normal and shear stresses considered as a whole are a rank-2 tensor field; for each of the three spatial dimensions there is a resultant stress vector with three components. This may be compared to a rank-1 tensor (i.e. vector) field such as velocity, where there is only one speed component for each spatial dimension. The double subscript for the stresses reflects the two vectors required to determine the tensor field: the first indicates the orientation of the surface on which the stress is acting and the second the direction of the stress. There are also body forces acting on δm due to the gravitational fields of the earth, moon and sun (as discussed in

§ 3.2). Once again taking the first two terms of the Taylor expansion:

$$\begin{aligned} F_x &= \left(\sigma_{xx}+\frac{\partial\sigma_{xx}}{\partial x}\frac{\delta x}{2}\right)\delta y\delta z-\left(\sigma_{xx}-\frac{\partial\sigma_{xx}}{\partial x}\frac{\delta x}{2}\right)\delta y\delta z+ \\ &\quad \left(\tau_{yx}+\frac{\partial\tau_{yx}}{\partial y}\frac{\delta y}{2}\right)\delta x\delta z-\left(\tau_{yx}-\frac{\partial\tau_{yx}}{\partial y}\frac{\delta y}{2}\right)\delta x\delta z+ \\ &\quad \left(\tau_{zx}+\frac{\partial\tau_{zx}}{\partial z}\frac{\delta z}{2}\right)\delta x\delta y-\left(\tau_{zx}-\frac{\partial\tau_{zx}}{\partial z}\frac{\delta z}{2}\right)\delta x\delta y \\ &\quad -\frac{\partial V_t}{\partial x}+O(\delta x)^4 \qquad (4.17) \\ & \qquad (4.18) \\ F_y &= \left(\sigma_{yy}+\frac{\partial\sigma_{yy}}{\partial y}\frac{\delta y}{2}\right)\delta x\delta z-\left(\sigma_{yy}-\frac{\partial\sigma_{yy}}{\partial y}\frac{\delta y}{2}\right)\delta x\delta z+ \\ &\quad \left(\tau_{xy}+\frac{\partial\tau_{xy}}{\partial x}\frac{\delta x}{2}\right)\delta y\delta z-\left(\tau_{xy}-\frac{\partial\tau_{xy}}{\partial x}\frac{\delta x}{2}\right)\delta y\delta z+ \\ &\quad \left(\tau_{zy}+\frac{\partial\tau_{zy}}{\partial z}\frac{\delta z}{2}\right)\delta x\delta y-\left(\tau_{zy}-\frac{\partial\tau_{zy}}{\partial z}\frac{\delta z}{2}\right)\delta x\delta y \\ &\quad -\frac{\partial V_t}{\partial y}+O(\delta x)^4 \qquad (4.19) \\ & \qquad (4.20) \\ F_z &= \left(\sigma_{zz}+\frac{\partial\sigma_{zz}}{\partial z}\frac{\delta z}{2}\right)\delta x\delta y-\left(\sigma_{zz}-\frac{\partial\sigma_{zz}}{\partial z}\frac{\delta z}{2}\right)\delta x\delta y+ \\ &\quad \left(\tau_{xz}+\frac{\partial\tau_{xz}}{\partial x}\frac{\delta x}{2}\right)\delta y\delta z-\left(\tau_{xz}-\frac{\partial\tau_{xz}}{\partial x}\frac{\delta x}{2}\right)\delta y\delta z+ \\ &\quad \left(\tau_{yz}+\frac{\partial\tau_{yz}}{\partial y}\frac{\delta y}{2}\right)\delta x\delta y-\left(\tau_{yz}-\frac{\partial\tau_{yz}}{\partial y}\frac{\delta y}{2}\right)\delta x\delta y \\ &\quad -\rho g\delta x\,\delta y\,\delta z+O(\delta x)^4 \qquad (4.21) \end{aligned}$$

noting the body forces due to the tide-generating potential in the **i** and **j** directions and the earth's gravitational field in the $-\mathbf{k}$ direction. In the absence of body-couples (applied torque per unit volume) the shear forces on the volume are of $O(\delta x)^3$, but the moment of inertia goes as $O(\delta x)^5$. This implies that as the side length is shrunk towards zero, the angular velocity will accelerate to infinity if the shear forces are out of balance. This is unphysical, so in the limit $\delta V \to 0$, opposing shear forces must be equal e.g. $\tau_{xy} = \tau_{yx}$. Hence, simplifying once more:

$$\begin{aligned} F_x &= \left(\frac{\partial\sigma_{xx}}{\partial x}+\frac{\partial\tau_{xy}}{\partial y}+\frac{\partial\tau_{xz}}{\partial z}-\rho\frac{\partial V_t}{\partial x}\right)\delta x\,\delta y\,\delta z+O(\delta x)^4 \qquad (4.22) \\ F_y &= \left(\frac{\partial\tau_{xy}}{\partial x}+\frac{\partial\sigma_{yy}}{\partial y}+\frac{\partial\tau_{xz}}{\partial z}-\rho\frac{\partial V_t}{\partial y}\right)\delta x\,\delta y\,\delta z+O(\delta x)^4 \qquad (4.23) \\ F_z &= \left(\frac{\partial\tau_{xz}}{\partial x}+\frac{\partial\tau_{xy}}{\partial y}+\frac{\partial\sigma_{zz}}{\partial z}-\rho g\right)\delta x\,\delta y\,\delta z+O(\delta x)^4 \qquad (4.24) \end{aligned}$$

It is convenient to express the forces acting on the faces of the fluid cube as the divergence operator acting on a tensor. In the same way that the divergence operator acting on a vector field (rank-1 tensor field) results in a scalar field (rank-0 tensor field), the divergence operator acting on a rank-2 tensor field results in a vector field, in this case force:

$$\mathbf{F} = \nabla . \begin{bmatrix} \sigma_{xx} & \tau_{xy} & \tau_{xz} \\ \tau_{xy} & \sigma_{yy} & \tau_{yz} \\ \tau_{xz} & \tau_{yz} & \sigma_{zz} \end{bmatrix} \tag{4.25}$$

Pressure gives rise to normal stresses that, at a point, are equal in all directions and only act to reduce the fluid cube in volume (although the fluid here is assumed incompressible), not to distort its shape. Therefore, the pressure can be expressed as the average of the diagonal (normal stress) terms of the matrix in (4.25):

$$p = -\frac{\sigma_{xx} + \sigma_{yy} + \sigma_{zz}}{3} \tag{4.26}$$

the negative sign arising from the direction convention in Figure 4.1. The residual normal stresses, for completeness, are:

$$\begin{aligned} \tau_{xx} &= \sigma_{xx} + p \\ \tau_{yy} &= \sigma_{yy} + p \\ \tau_{zz} &= \sigma_{zz} + p \end{aligned} \tag{4.27}$$

Therefore the stresses acting on the faces of the cube may be expressed as:

$$\mathbf{F} = \nabla . \left(\begin{bmatrix} \tau_{xx} & \tau_{xy} & \tau_{xz} \\ \tau_{xy} & \tau_{yy} & \tau_{yz} \\ \tau_{xz} & \tau_{yz} & \tau_{zz} \end{bmatrix} - p\mathbf{I} \right) \tag{4.28}$$

where $\mathbf{I}$ is the 3×3 identity matrix. The expression may be further simplified to:

$$\mathbf{F} = -\nabla p + \nabla . \mathbb{T} \tag{4.29}$$

where the stress tensor field,

$$\mathbb{T} = \begin{bmatrix} \tau_{xx} & \tau_{xy} & \tau_{xz} \\ \tau_{xy} & \tau_{yy} & \tau_{yz} \\ \tau_{xz} & \tau_{yz} & \tau_{zz} \end{bmatrix} \tag{4.30}$$

4.6 Derivation of the momentum equation

Applying Newton's second law to the control volume:

$$\delta m\,\mathbf{a} = \sum \mathbf{f} \tag{4.31}$$

Substituting (4.29) into (4.22) and dividing by the mass of the fluid cube $\rho\,\delta x\,\delta y\,\delta z$, then equating with the acceleration terms (4.15) gives, after allowing $\delta V \to 0$:

$$\frac{\partial u}{\partial t} + \mathbf{u}\cdot\nabla u - 2\Omega\left\{w\cos\phi + v\sin\phi\right\} = -\frac{1}{\rho}\frac{\partial p}{\partial x} + \frac{1}{\rho}\left(\nabla\cdot\mathbb{T}\right)\cdot\mathbf{i} - \frac{\partial V_t}{\partial x} \tag{4.32}$$

$$\frac{\partial v}{\partial t} + \mathbf{u}\cdot\nabla v + 2\Omega u\sin\phi = -\frac{1}{\rho}\frac{\partial p}{\partial y} + \frac{1}{\rho}\left(\nabla\cdot\mathbb{T}\right)\cdot\mathbf{j} - \frac{\partial V_t}{\partial y} \tag{4.33}$$

$$\frac{\partial w}{\partial t} + \mathbf{u}\cdot\nabla w - 2\Omega u\cos\phi = -\frac{1}{\rho}\frac{\partial p}{\partial z} + \frac{1}{\rho}\left(\nabla\cdot\mathbb{T}\right)\cdot\mathbf{k} - g \tag{4.34}$$

These, together with the continuity equation (4.4) are the Navier-Stokes equations describing the motion of the fluid. The first thing to note is that while there are effectively nine unknown variables (three velocity components and six stresses) there are only four equations, meaning that in this form the Navier-Stokes equations are intractable. Even when the equations are closed by including extra information, the convective acceleration terms are non-linear, making analytical solution practically impossible. Some progress can be made by assuming that the fluid is Newtonian, i.e. that the deviatoric stresses are proportional to the rate of strain of the fluid, with the constant of proportionality (known as the dynamic viscosity) μ being independent of direction:

$$\mathbb{T} = \mu\begin{bmatrix} \frac{\partial u}{\partial x} & \frac{\partial u}{\partial y} & \frac{\partial u}{\partial z} \\ \frac{\partial v}{\partial x} & \frac{\partial v}{\partial y} & \frac{\partial v}{\partial z} \\ \frac{\partial w}{\partial x} & \frac{\partial w}{\partial y} & \frac{\partial w}{\partial z} \end{bmatrix} \tag{4.35}$$

By substituting (4.35) into (4.32–4.34), the unknown variables are reduced to four (three velocity components and pressure) so the equations can in theory be solved. However, in practice the damping provided by the viscous terms is small compared to the inertial acceleration, so instability—turbulence—is generated in the flow and the velocity appears to be stochastic at time-scales and length-scales relevant to most flows. This is the motivation for the time-averaging procedure described in the next section. Equations (4.32–4.35) form the basis for the time-averaging and spatial-averaging procedures described in §4.7 and §4.9.

4.7 Reynolds-averaged Navier-Stokes (RANS) equations

To make the Navier-Stokes equations useful for numerical computation of real flows, a time-averaging procedure is adopted. The essential idea is that the flow at every point can be separated into the sum of a mean velocity $(\overline{u}, \overline{v}, \overline{w})$ that is quasi-steady compared to an averaging period and a stochastic fluctuating velocity (u', v', w) which has zero mean over the averaging period, e.g.:

$$\begin{aligned} u &= \overline{u} + u' \\ p &= \overline{p} + p' \end{aligned} \tag{4.36}$$

These decompositions may be substituted into (4.32–4.34) and then the resulting equations averaged themselves. Terms linear in the fluctuating quantities disappear as the time-average is zero by definition. Similarly, terms in averaged quantities stay the same and therefore:

$$\frac{\partial \overline{u}}{\partial x} + \frac{\partial \overline{v}}{\partial y} + \frac{\partial \overline{w}}{\partial y} = 0 \tag{4.37}$$

$$\frac{\partial \overline{u}}{\partial t} + \overline{\mathbf{u}} \cdot \nabla \overline{u} + \overline{u' \frac{\partial u'}{\partial x}} + \overline{v' \frac{\partial u'}{\partial y}} + \overline{w' \frac{\partial u'}{\partial y}} + 2\Omega \overline{v} \sin\phi = -\frac{1}{\rho}\frac{\partial \overline{p}}{\partial x} + \frac{1}{\rho}\left(\nabla \cdot \overline{\mathbb{T}}\right) \cdot \mathbf{i} - \frac{\partial V_t}{\partial x} \tag{4.38}$$

$$\frac{\partial \overline{v}}{\partial t} + \overline{\mathbf{u}} \cdot \nabla \overline{v} + \overline{u' \frac{\partial v'}{\partial x}} + \overline{v' \frac{\partial v'}{\partial y}} + \overline{w' \frac{\partial v'}{\partial y}} + 2\Omega \overline{u} \sin\phi = -\frac{1}{\rho}\frac{\partial \overline{p}}{\partial y} + \frac{1}{\rho}\left(\nabla \cdot \overline{\mathbb{T}}\right) \cdot \mathbf{j} - \frac{\partial V_t}{\partial y} \tag{4.39}$$

$$\frac{\partial \overline{w}}{\partial t} + \overline{\mathbf{u}} \cdot \nabla \overline{w} + \overline{u' \frac{\partial w'}{\partial x}} + \overline{v' \frac{\partial w'}{\partial y}} + \overline{w' \frac{\partial w'}{\partial y}} + 2\Omega \overline{u} \sin\phi = -\frac{1}{\rho}\frac{\partial \overline{p}}{\partial z} + \frac{1}{\rho}\left(\nabla \cdot \overline{\mathbb{T}}\right) \cdot \mathbf{k} - g \tag{4.40}$$

However, the terms non-linear in the fluctuating quantities remain and introduce unknown quantities into the equations. Recognizing that

$\overline{2u'\dfrac{\partial u'}{\partial x}} = \dfrac{\partial \overline{u'^2}}{\partial x}$, etc. allows the terms to be written in the form of a stress tensor, which is simply added to the RHS of (4.32–4.34):

$$\mathbb{R} = -\frac{1}{2}\begin{bmatrix} \overline{u'^2} & \overline{u'v'} & \overline{u'w'} \\ \overline{u'v'} & \overline{v'^2} & \overline{v'w'} \\ \overline{u'w'} & \overline{v'w'} & \overline{w'^2} \end{bmatrix} \tag{4.41}$$

where the terms in the brackets are known as Reynolds stresses and represent the loss of information due to the averaging process. These terms are generally much larger than the viscous terms, so $\mathbb{T}$ is absorbed into $\mathbb{R}$. Some means of relating the Reynolds stresses to the mean flow variables is necessary to close the equations again, one of which is to derive more transport equations for the Reynolds stresses. An alternative and more widely used method is partly provided by the turbulence viscosity concept of Boussinesq. This makes an analogy with transfer of momentum in Newtonian fluids under laminar flow conditions and assumes that the stress tensor will go to zero as the mean strain-rate tensor goes to zero. Under this assumption, the Reynolds stress tensor is set equal to the mean strain-rate tensor multiplied by a variable, but scalar turbulence viscosity:

$$\mathbb{R} = \mu_t \begin{bmatrix} \dfrac{\partial u}{\partial x} & \dfrac{\partial u}{\partial y} & \dfrac{\partial u}{\partial z} \\ \dfrac{\partial v}{\partial x} & \dfrac{\partial v}{\partial y} & \dfrac{\partial v}{\partial z} \\ \dfrac{\partial w}{\partial x} & \dfrac{\partial w}{\partial y} & \dfrac{\partial w}{\partial z} \end{bmatrix} - \frac{1}{3}\left(\overline{u'^2} + \overline{v'^2} + \overline{w'^2}\right)\mathbf{I} \tag{4.42}$$

Whereas μ is a property of the fluid, a function only of temperature, the turbulence viscosity μ_t in general varies with space and time and is affected by the flow variables and boundary conditions. This is because the analogy with molecular viscosity is not an exact one and turbulent eddies do not physically transfer momentum in the same way as molecules colliding in a fluid. Dimensionally, the turbulence viscosity can be expressed as the product of the fluid density, a length and a velocity. There is wide variety of choices of length and velocity, depending on the situation. The second term on the right hand side of (4.42) is analogous to pressure in (4.26); a new scalar variable is therefore introduced:

$$k = \frac{1}{2}\left(\overline{u'^2} + \overline{v'^2} + \overline{w'^2}\right) \tag{4.43}$$

where k is known as the turbulence kinetic energy and is used later on to estimate the velocity scale for calculating μ.

There is no set of equations for finding appropriate length and velocity scales that has been shown to be universally applicable to all types of flow. A large number of methods exist of varying complexity, each with tune-able parameters for fitting to experimental data. The aim of such models is to be flexible enough to apply to a large range of flows while not entailing excessive computational cost (Launder and Spalding 1972). One closure model, used widely in engineering software such as the TÉLÉMAC system, is the k-ε model. The model is so called due to the two quantities from which ν_t is calculated, requiring two extra equations. The velocity scale is provided by k, introduced above. A transport equation for the total derivative of k can be found by subtracting Equation 4.32 from Equation 4.38 to give the fluctuating momentum balance, then multiplying through by u', v' and w' respectively and summing to give the kinetic energy of the fluctuations and finally time-averaging the sum. Einstein notation is introduced at this point to compactly represent the terms; the indices $i = \{1, 2, 3\}$ and $j = \{1, 2, 3\}$ stand for any dimension and a repeated subscript indicates summation of terms over the three dimensions, e.g. $\overline{u_i'u_i'} = \overline{u'^2} + \overline{v'^2} + \overline{w'^2}$. As there is no change of co-ordinate system, subscripts only will be used. Hence:

$$\frac{\partial k}{\partial t} + \overline{\mathbf{u}} \cdot \nabla k = \frac{\partial}{\partial x_j}\left\{-\frac{1}{\rho}\overline{pu_j} - \overline{ku_j} + \nu\frac{\partial}{\partial x_j}k\right\} - \overline{u_iu_j}\frac{\partial U_i}{\partial x_j} - \nu\overline{\frac{\partial u_i}{\partial x_j}\frac{\partial u_i}{\partial x_j}} \tag{4.44}$$

k is thus a scalar quantity that is convected along with the flow. This is physically intuitive, as turbulent eddies can be visualized as convecting along with the mean flow. The final term (nine terms when expanded) that is subtracted from the right hand side of (4.44) is always positive and is consequently known as the dissipation ε, i.e.

$$\varepsilon = \nu\,\overline{\frac{\partial u_i'}{\partial x_j}\frac{\partial u_i'}{\partial x_j}} \tag{4.45}$$

ν is the molecular kinematic viscosity. ε is a less intuitive quantity than k and more difficult to measure directly; it provides the length scale required to calculate ν_t. It is equivalent to the true dissipation of k only in the case of homogeneous turbulence, which is only ever approximately true. The penultimate term in (4.44) is equivalent to the Reynolds stresses, which have already been approximated by the Boussinesq assumption in the momentum equation. The convection-type terms in the curly braces of (4.44) are approximated by a diffusion term, with a tunable coefficient, in order to eliminate the unknown fluctuating quantities.

A similar semi-empirical transport equation is derived for ε. In this case there is not only an experimentally-tuned coefficient to model the diffusion terms, but also two extra coefficients for the production and dissipation terms. The two quantities k and ε are then used to calculate the value of ν_t used in the momentum equation:

$$\nu_t = c_\mu \frac{k^2}{\varepsilon} \tag{4.46}$$

where c_μ is a constant. The values of the constants in the model have been established in a number of classic experiments (Rodi 1980).

From this point forward, *the overbar indicating time-averaging will be dropped for the time-mean variables.*

4.8 The hydrostatic approximation

If the hydrodynamics are assumed to be dominated by long waves, further simplifications can be made using the asymptote of small-amplitude wave theory for long wavelengths. Making this assumption excludes all waves with wavelengths less than $\approx 20h$, where h is the depth; this means the equations so-simplified cannot describe wind-generated wave phenomena. As the major periods for tidal oscillations are 4–24 hours, and the asymptotic wave speed for a long wave is $\sqrt{gd}$, the wavelength will be much greater than $20h$, even in the deepest parts of the ocean (e.g. 10^4 m). It can be shown that the ratio of vertical to horizontal velocity amplitudes for the long wave limit is $2\pi h/L$ where L is the wavelength, and as previously stated, this h/L is very small (Dean and Dalrymple 1991, page 132). The same ratio applies for accelerations and spatial derivatives; the ratio of the maximum vertical acceleration amplitude to g is $4\pi^2 \eta h/L^2$ where η is the free surface elevation amplitude, clearly very small regardless of the depth of the water column.

Considering the vertical momentum equation (4.40), the terms comprise:

terms in w and its spatial and temporal derivatives (inertial accelerations and turbulent stresses); a term in u (Coriolis acceleration); the pressure gradient, and g. Noting u is of the order 1 m/s and $\Omega = 7.3 \times 10^{-5}$ rad/s; ν_t is of the order 10 m^2/s; w and its derivatives are small compared to g (see above); then cancelling the small terms:

$$0 = -\frac{1}{\rho}\frac{\partial p}{\partial z} - g \tag{4.47}$$

So the vertical profile of pressure is simply hydrostatic under these assumptions. Neglecting terms in w for the continuity equation gives:

$$\frac{\partial u}{\partial x} + \frac{\partial v}{\partial y} = 0 \tag{4.48}$$

and for the horizontal momentum equations:

$$\frac{\partial u}{\partial t} + \mathbf{u} \cdot \nabla u - 2\Omega v \sin\phi = -\frac{1}{\rho}\frac{\partial p}{\partial x} + \nu_t \left\{ \frac{\partial^2 u}{\partial x^2} + \frac{\partial^2 u}{\partial y^2} + \frac{\partial^2 u}{\partial z^2} \right\} - \frac{\partial V_t}{\partial x} \tag{4.49}$$

$$\frac{\partial v}{\partial t} + \mathbf{u} \cdot \nabla v + 2\Omega u \sin\phi = -\frac{1}{\rho}\frac{\partial p}{\partial x} + \nu_t \left\{ \frac{\partial^2 v}{\partial x^2} + \frac{\partial^2 v}{\partial y^2} + \frac{\partial^2 v}{\partial z^2} \right\} - \frac{\partial V_t}{\partial y} \tag{4.50}$$

4.9 Depth-averaged RANS equations

If assumptions are made about the vertical profile of velocity and the stresses at the bed and free surface, the equations may be averaged over the vertical, converting the problem from three-dimensional to two-dimensional, reducing computing requirements and replacing the variable pressure with the more useful free-surface co-ordinate. In order to integrate the differential terms, the limits of which are functions of x and y, use is made of the Leibniz integral rule (Weisstein 2008b):

$$\frac{\partial}{\partial x}\int_{a(x)}^{b(x)} f(x,z)\,dx = \int_{a(x)}^{b(x)} \frac{\partial f}{\partial x}\,dz + f(b(x),x)\frac{\partial b}{\partial x} - f(a(x),x)\frac{\partial a}{\partial z} \tag{4.51}$$

which, after rearrangement, allows the integral sign to be taken inside the differential sign, giving the differential equation in terms of averaged quantities. Hence integrating (4.48) from the bed with vertical elevation z_b to the free surface at z_s and dividing through by the depth $h = z_s - z_b$ gives:

$$\frac{1}{h}\left\{ \frac{\partial Uh}{\partial x} - u_s\frac{\partial z_s}{\partial x} + u_b\frac{\partial z_b}{\partial x} + \frac{\partial Vh}{\partial y} - u_s\frac{\partial z_s}{\partial y} + u_b\frac{\partial z_b}{\partial y} \right\} = 0 \tag{4.52}$$

Where the use of capital letters for u and v indicates averaging over the vertical, i.e.

$$U = \int_{z=z_b}^{z=z_s} u \, dz \tag{4.53}$$

However, if the usual assumptions made about the kinematic boundary conditions are made —that the sea-bed is impermeable and static (no normal flow) and that a fluid particle on the free-surface remains there (Dean and Dalrymple 1991, page 44)—then the following relationships apply:

$$(u_b, v_b, 0) \cdot \left(-\frac{\partial z_b}{\partial x}, -\frac{\partial z_b}{\partial y}, 1 \right) = 0 \tag{4.54}$$

$$\frac{\partial h}{\partial t} + (u_s, v_s, 0) \cdot \left(\frac{\partial z_s}{\partial x}, \frac{\partial z_s}{\partial y}, -1 \right) = 0 \tag{4.55}$$

where the normal vectors have not been normalized due to the zero right hand side. Note reversed direction of normal vector at the bed compared to the surface. Combining the two expressions gives:

$$\frac{\partial h}{\partial t} + u_b \left(-\frac{\partial z_b}{\partial x} \right) + u_b \left(-\frac{\partial z_b}{\partial y} \right) + u_s \left(\frac{\partial z_s}{\partial x} \right) + u_s \left(\frac{\partial z_s}{\partial y} \right) = 0 \tag{4.56}$$

Substituting (4.56) into (4.52) and multiplying by h gives the vertically averaged continuity equation:

$$\frac{\partial h}{\partial t} + U\frac{\partial h}{\partial x} + h\frac{\partial U}{\partial x} + V\frac{\partial h}{\partial y} + h\frac{\partial V}{\partial y} = 0 \tag{4.57}$$

It can be seen from (4.57) that the process of vertical averaging has introduced non-linearity into the continuity equation via the depth. This is significant as it may be used to explain the generation of higher harmonics (or 'overtides') in response to tidal wave forcing in shallow areas where the variation in sea-surface elevation is a significant proportion of the depth.

Following a similar procedure for the horizontal momentum equations, eliminating a number of terms by substituting the continuity equation, and then dividing through by h, gives:

$$\frac{\partial U}{\partial t} + \mathbf{U} \cdot \nabla U - 2\Omega V \sin\phi = -\frac{1}{\rho}\frac{\partial p}{\partial x} + \frac{1}{h}\nabla \cdot (\nu_t h \nabla U) - \frac{\partial V_t}{\partial x} \tag{4.58}$$

$$\frac{\partial V}{\partial t} + \mathbf{U} \cdot \nabla V + 2\Omega U h \sin\phi = -\frac{1}{\rho}\frac{\partial p}{\partial x} + \frac{1}{h}\nabla \cdot (\nu_t h \nabla U) - \frac{\partial V_t}{\partial y} \tag{4.59}$$

In a similar manner to taking the time average of the Navier-Stokes equations, spatial averaging of non-linear terms introduces additional unknown terms due to the variation of velocity in the vertical, which are referred to as dispersion. These terms are of analogous form to Reynolds stresses and have been absorbed into the definition of ν_t as additional diffusion of momentum. They find their way back into the system via two constants in the vertically-averaged k and ε transport equations that have been 'optimized' for open channel flow (Hervouet and Van Haren 1994). In addition to the above, (more) non-linearity is introduced into the momentum equation via the diffusion term. The division by depth makes handling of wetting and drying difficult, due to potential division by zero.

4.10 Vertical flow profiles in the sea

In hydraulics terminology, a tidal stream may be described as gradually-varied flow in a very wide, open channel. As a consequence, spatial and temporal gradients are small and locally the flow can be approximated as one-dimensional uniform flow. Flow profiles in open channels are divided into an inner and outer layer. The layers are not distinct, but merge in an overlap layer (or inertial sub-layer; see Figure 4.2).

In the inner layer, it is assumed that the boundary layer thickness does not affect the flow profile. Boundary layers in laboratory-scale flows tend to be defined by the flow reaching 99% of the 'free-stream' velocity, but generally this is not useful in the sea due to near-surface wind-driven currents, wave orbit velocities and—in the case of fast tidal currents in relatively shallow water—the theoretical boundary layer height being well above the surface of the water. Consequently the depth h is a more useful length-scale. The outer layer is affected by the depth, but not the details of what is going on at the bed (the surface length scales). Both the inner and the outer layers are affected by the friction caused by the presence of the boundary. For the inner boundary layer, dimensional analysis suggests:

$$u = f(u_*, \nu, z, h_r, s_i) \tag{4.60}$$

where the friction velocity $u_* = \sqrt{\tau/\rho}$, h_r is the mean height of the roughness elements and s_i are surface length scales such as lateral and longitudinal spacing of roughness elements. Consequently, the non-dimensional velocity can be expressed as:

$$u/u_* = f_{\text{in}}(u_* h_r/\nu,\ z/h_r,\ \sigma_i) \tag{4.61}$$

The first dimensionless group in the brackets is a kind of Reynolds number. It would therefore be expected that when this group is large, u/u_* is no longer dependent upon it. In practice, this has been found to be the case for $u_* h_r/\nu > 70$. For tidal flows of significant amplitude, it can be demonstrated that this requirement is fulfilled; an estimate of the friction velocity for 1-D flow is $u_* = \sqrt{gh\ |\partial h/\partial x|}$. Observations of progressive-wave tidal elevations at coastal gauges in the English Channel indicate typical elevation amplitudes of 1 m, with quarter-wavelengths of around 250 km for the M_2 tide, giving an average $\partial h/\partial x = 4 \times 10^{-6}$. Assuming a depth of 30 m, this would imply a roughness height $h_r > 2$ mm, likely to be fulfilled in all realistic situations. For the outer layer:

$$u/u_* = f_{\text{ou}}(z/h) \tag{4.62}$$

In the overlap layer, both relationships must apply simultaneously:

$$u/u_* = f_{\text{in}}(z/h_r,\ \sigma_i) = f_{\text{ou}}(z/h) \tag{4.63}$$

Differentiating (4.63) implicitly with respect to z and then multiplying through by z to regain non-dimensionality:

$$\frac{z}{u_*}\frac{du}{dz} = \frac{z}{h_r}\frac{df_{\text{in}}}{dz} = \frac{z}{h}\frac{df_{\text{ou}}}{dz} \tag{4.64}$$

As the two right hand terms of (4.64) have no independent variables in common, they must equal a constant, named after Von Kármán $1/\kappa$, where κ has been found to be close to 0.4 in a wide variety of flows in both air and water.

Integrating (4.64) with respect to z

$$\frac{1}{u_*}\int_{z=d}^{z}\frac{du}{dz}\,dz = \int_{z=d}^{z}\frac{1}{\kappa z}\,dz \tag{4.65}$$

leads to a logarithmic velocity profile:

$$\frac{u}{u_*} = \frac{1}{\kappa}\ln(z-d)\ + A \tag{4.66}$$

where A is an unknown function of h_r and σ_i. A is absorbed into the logarithmic term by setting:

$$A = -\frac{1}{\kappa} \ln z_0 \tag{4.67}$$

where z_0 is known as the roughness *length*. Hence:

$$\frac{u}{u_*} = \frac{1}{\kappa} \ln \frac{z-d}{z_0} \tag{4.68}$$

This simple relationship has been observed in the sea over part of the water column on many occasions. It gives rise to a straight line on a log-linear plot of z versus u, sketched in Figure 4.3, which enables the estimation of the quantities u/u_* and z_0 directly from the measured velocity profile. The displacement height d is poorly defined as it lies outside the region of validity of the logarithmic profile; it is adjusted to give best fit in a least squares regression of the data. Due to the large curvature of the profile toward the bed and the interaction with the displacement height, the errors involved in the determination of z_0 in this manner tend to be large, of the order of $\pm 100\%$ (Dyer 1986, page 64). However, as will be shown in §4.11, the mean flow is relatively insensitive to the specification of z_0.

If the logarithmic profile holds over most of the depth i.e. the displacement height, the roughness sublayer and the non-logarithmic part of the outer layer are small in comparison to the depth; then an estimate of the depth-averaged velocity can be found by integrating (4.68) over the water column:

$$U = \frac{1}{h} \int_{z=0}^{z=h} \frac{u_*}{\kappa} \ln \frac{z}{z_0} \, dz = \frac{u_*}{\kappa} \left(\ln \frac{h}{z_0} - 1 \right) \tag{4.69}$$

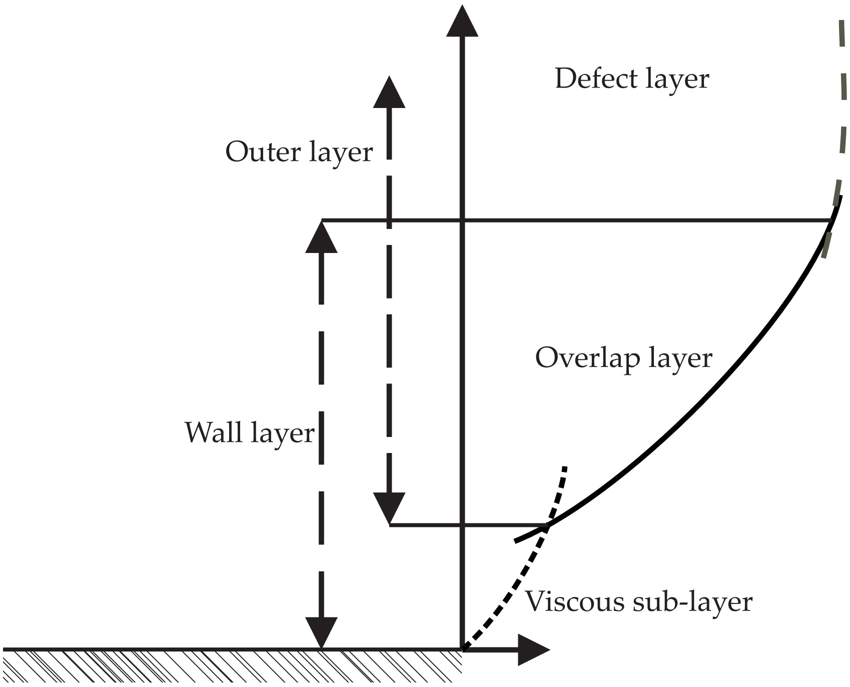

(a) Smooth-wall boundary layer flow profiles

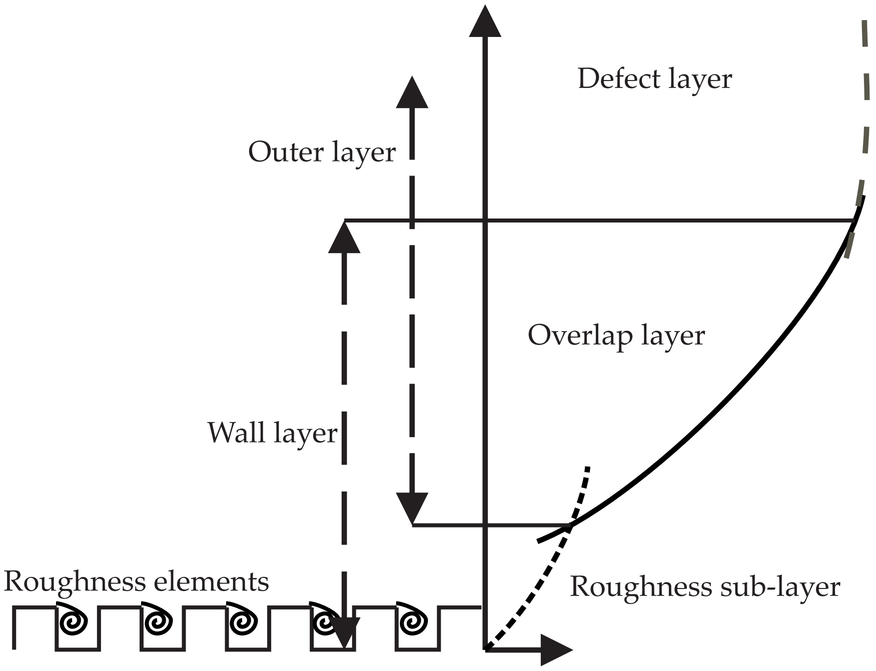

(b) Rough-wall boundary layer flow profiles

Figure 4.2: Diagrams illustrating layers of flow profiles observed over surfaces of varying boundary Reynolds number

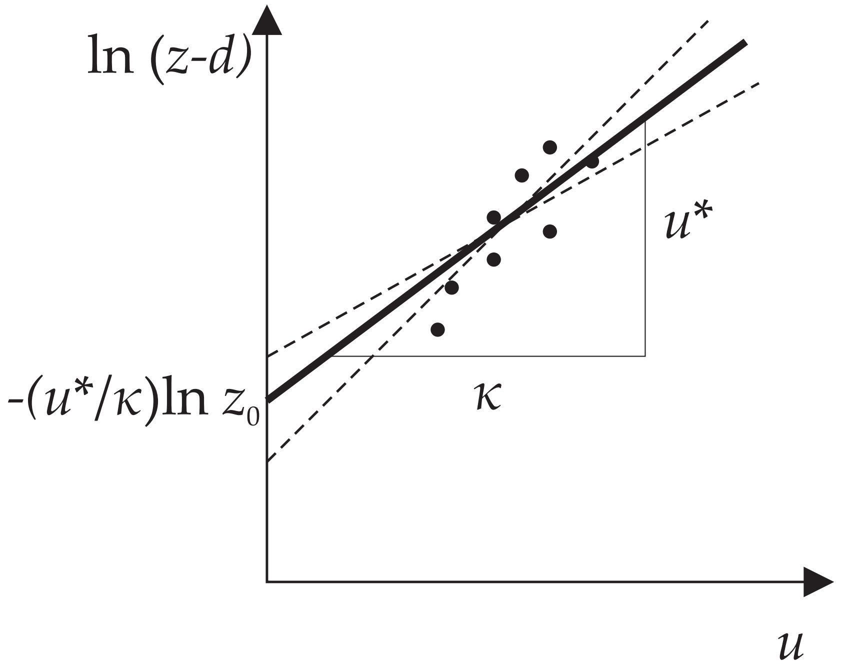

Figure 4.3: Sketch of a logarithmic velocity profile illustrating how friction velocity u_* and roughness length z_0 can be derived from the plot

4.11 Bed friction

While in the deep ocean the dynamics are strongly linear, in continental shelf seas and rivers non-linear frictional processes are usually important and by analogy with flow over a flat plate, a quadratic friction law is used to relate the drag force to the flow velocity, either at a specified depth, or in this case, the depth-averaged value:

$$F_x = -\frac{1}{2}\rho\, c_f\, U\, |\mathbf{U}| \tag{4.70}$$

$$F_y = -\frac{1}{2}\rho\, c_f\, V\, |\mathbf{U}| \tag{4.71}$$

For the case of uniform flow—which in principle cannot occur on a horizontal bed, as there would be no energy input to balance the work against friction—the forces due to the hydrostatic pressure resolved down the bed slope must be balanced by the bed friction, as there is no average rate of change of momentum. In a situation far from lateral boundaries, as in the sea, the area over which the bed friction acts and the projected area on which weight of the water acts are equivalent. Under these conditions, the mean flow velocity is given by:

$$U = C\sqrt{h\, S_0} \tag{4.72}$$

Where C is the Chézy coefficient (m$^{\frac{1}{2}}$/s)

$$C^2 = \frac{2g}{c_f} \tag{4.73}$$

and where $S_0 = -\partial h/\partial x$. Although derived for uniform flow, this relationship has been applied successfully to control volumes with spatially-varied depth-averaged flows due to the slopes at the bed and the surface being generally $\ll 1$. Empirical functions have been developed to relate the Chézy coefficient to parameters which depend only on the surface characteristics of the bed (rather than a combination of the bed and the flow). The most well-used are the equivalent formulae of Manning and Strickler:

$$C = Kh^{1/6} \tag{4.74}$$

Where the Manning $n = 1/K$ and the Strickler K has units of m$^{\frac{1}{3}}$/s.

It is of interest to compare the theoretical vertically-averaged flow speed predicted by (4.69) with that generated by the empirical Strickler law, as the

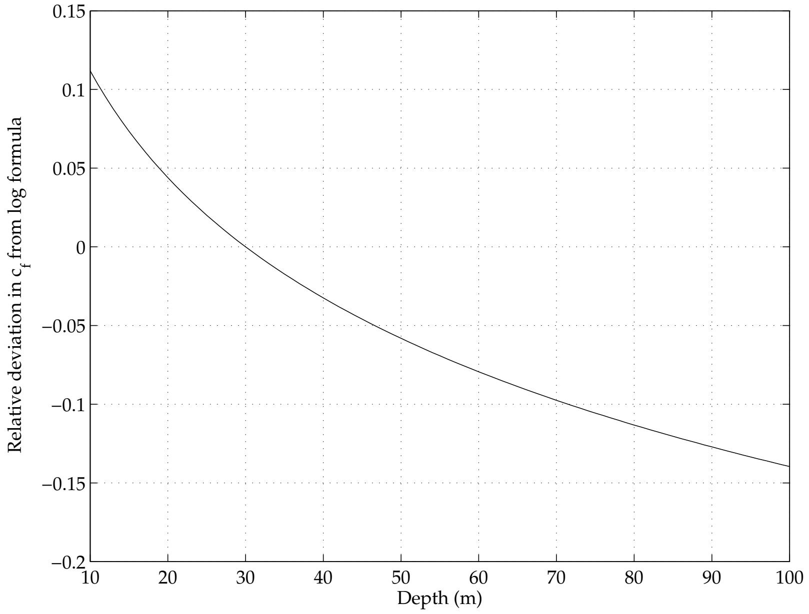

Figure 4.4: Relative deviation of Strickler c_f from logarithmic-profile c_f as depth varies in the case where the formulae are equivalent when $K = 40\ \mathrm{m}^{\frac{1}{3}}/\mathrm{s}$ and depth $h = 30$ m.

latter is what tends to be used in practice to calculate bed friction in numerical modelling. For flow along the x-direction:

$$\frac{U}{u_*} = \sqrt{\frac{2}{c_f}} = \frac{Kh^{1/6}}{\sqrt{g}} = \frac{1}{\kappa}\left(\ln\frac{h}{z_0} - 1\right) \tag{4.75}$$

If, is as is usually the case, K is fixed for all depths h in the model, then there will be a discrepancy between the friction coefficient predicted by the Strickler formula and the logarithmic formula as h varies. As an example, if $K = 40\ \mathrm{m}^{\frac{1}{3}}/\mathrm{s}$ were considered to give the 'correct' friction coefficient $c_f = 0.0039$ in $h = 30$ m depth, i.e $z_0 = 1.4$ mm, then the deviation of the friction coefficient at other depths from the logarithmic formula may be calculated and is plotted in Figure 4.4. It can be seen that the Strickler formula gives a friction coefficient within ±7.5% of the logarithmic formula over the depth range 15–60 m.

If instead z_0 varies while the depth is held constant, the friction coefficient can be seen in Figure 4.5 to vary by a factor of around 3–4, small in comparison to the variation of z_0 through four orders of magnitude.

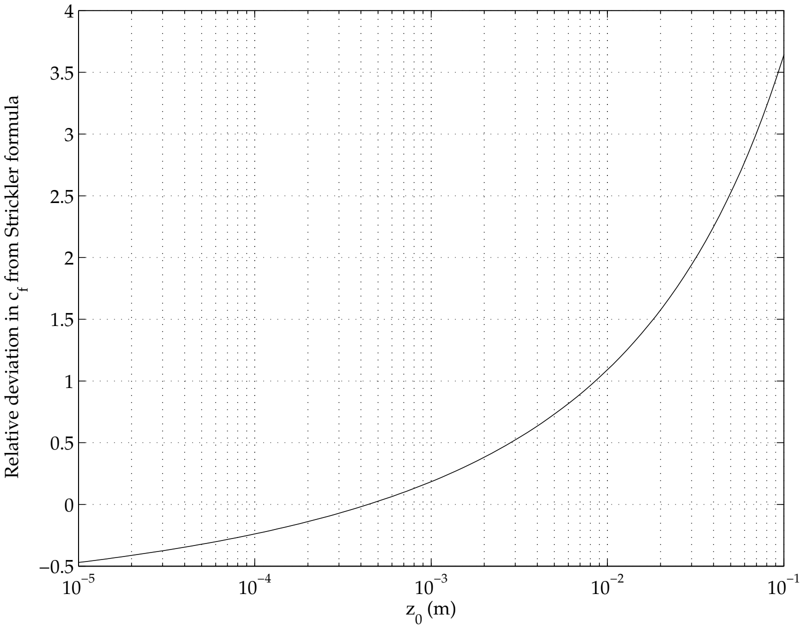

Figure 4.5: Relative deviation of Strickler c_f from logarithmic-profile c_f as roughness length z_0 varies in the case when Strickler $K = 40$ m$^{\frac{1}{3}}$/s and depth $h = 30$ m.

Chapter 5

Numerical solution of the equations of motion

5.1 Principal methods used for coastal applications

There are three principal methods for the spatial discretization of numerical schemes for the solution of partial differential equations: finite difference, finite element and finite volume.

5.1.1 Finite difference method

The finite difference method is the simplest to understand: the domain is divided into increments in each spatial dimension; in practice the grid is usually regular in the coordinate system used, although it may be transformed into curvilinear or non-uniform co-ordinates. The equations are rewritten in difference form using a Taylor expansion about a general grid point. At each time-step, new values of the variables at each point can be calculated, using the boundary conditions and the values of the variables at the previous time step. The error involved in approximating the difference equations is then straightforwardly related to the order of the expansion and the size of the spatial increment. The principal disadvantages of the finite difference method in coastal modelling (and elsewhere) are poor resolution of complex geometry and lack of flexibility in grid resolution resulting in unnecessary computational expense in areas of the domain far from boundaries or topographic gradients.

5.1.2 Finite element method

The finite element method is a more general approach to the problem and is consequently harder to understand and describe. The variables are first approximated as weighted sums of basis functions ψ_i, with a weight for each of the variables at each of the N nodes of the mesh, which may in general be irregular.

$$u = \sum_{i=1}^{N} a_{ui} \psi_i \tag{5.1}$$

The basis functions ψ are simple locally within each element, but globally, the weighted sum can approximate a complicated function such as the velocity field over the domain. The approximations for the variables are then substituted into the equations; the basis functions are chosen to be easy to differentiate and integrate exactly. The continuity and momentum equations written in the form $f(x, y) = 0$ are replaced by $f(x, y) = \epsilon(x, y)$, where ϵ is a residual to be minimized in a global sense. For example, the continuity equation (4.48) becomes:

$$\sum_{i=1}^{N} a_{ui} \frac{\partial \psi_i}{\partial x} + \sum_{i=1}^{N} a_{vi} \frac{\partial \psi_i}{\partial y} = \epsilon \tag{5.2}$$

The Fundamental Lemma of Calculus of Variations (Weisstein 2008a) is applied where if, with certain conditions on the test function $\phi(x, y)$,

$$\int_a^b \epsilon(x, y)\, \phi(x, y)\, dS = 0 \tag{5.3}$$

then $\epsilon(x, y) = 0$, which is what is required. Any suitable ϕ may be used, but a set of functions defined at the nodes already exists in ψ, so these may be re-used. This then reduces the problem to a linear system with N equations, which can be assembled into a matrix expression and solved. The main advantage of the finite element method is the flexibility in mesh generation. When used with a semi-implicit time discretization, the finite element method does not have the strong constraint on stability imposed by the Courant-Fredrichs-Levy condition on finite difference and finite volume methods. This allows larger time-steps to be used; a significant advantage when computing tidal flows in the sea, where wave celerities are high due to the depth. Disadvantages of the method include the need to prescribe boundary conditions at nodes, rather than by fluxes across surfaces. This is partly due to the origins of the finite element method in structural analysis. As a consequence, where boundary conditions involve imposing depths at open boundaries—often the case for tidal models—mass is not conserved at these points and therefore in the domain as a whole.

5.1.2.1 Semi-implicit discretization in time

Terms in the equations involving time derivatives (i.e. acceleration) are discretized in the form:

$$\frac{\partial u}{\partial t} \rightarrow \frac{u_{n+1} - u_n}{\Delta t} \tag{5.4}$$

where Δt is the time increment. However, other terms in the equation contain u. To keep the error in the discrete representation of the continuous equation $O(\Delta t)^2$ (second-order accurate in time) would require these other terms to be written at the centre of the time-step, i.e. $u \rightarrow (u_n + u_{n+1})/2$. In practice, this results in numerical instability; instead u is taken slightly closer to u_{n+1} than u_n resulting in a stable scheme and accuracy less than second order (but better than first order):

$$u \rightarrow \theta u_n + (1 - \theta) u_{n+1} \tag{5.5}$$

where $0.5 < \theta \leq 1.0$. Time-stepping of the non-linear terms is more complicated and involves either sub-iterations or a two-step approach using the method of characteristics.

5.1.3 Finite volume method

In the finite volume method (FVM), variables are not sampled at points but rather averaged over volumes by integration. The averaged quantities change via fluxes of the variables across the faces of the elements. The finite volume method is thus inherently conservative of mass and momentum and allows intuitive handling of boundary conditions at surfaces, both advantages over the finite element method. FVM also allows flexibility in the type and size of elements, an advantage over the finite difference method. A possible disadvantage is that as the averaged values are not known *a priori*, neither are the integrals on the boundary representing the fluxes. Consequently, some arbitrary form of interpolation of the cell-averaged values is required. Second-order interpolation reduces the method to finite differences, but with *simultaneous* conservation of quantities enforced. In practice, more complicated, non-linear methods of interpolation are used.

5.2 Numerical simulation using the TÉLÉMAC system

5.2.1 Rationale for use of the TÉLÉMAC system

The TÉLÉMAC system was chosen as it is well-established for the purpose of coastal hydrodynamic modelling and was available free to academic institutions[*]. In contrast to other commercial hydrodynamic modelling software such as MIKE-21 or MIKE-3, there is considerable access to the source code, which was necessary for the implementation of energy extraction, for example. However, re-compilation and linking is required if changes are made and the graphical user interface is basic in comparison to other packages.

The system was originally developed for Electricité de France—responsible for a large number of hydroelectric and nuclear installations—for the purpose of simulating tides, transport of pollutants, flood waves and river flows. The system has undergone continuous development since the 1980s (Galland et al. 1991) and has been validated in a number of specific cases with analytical solutions (Hervouet 1989; EDF-DRD 2000). Originally written in Fortran-77 code, it has since been updated to Fortran-90. The system is used by several academic institutions around the world, in addition to many commercial users. The system has been cited in seventy-four journal articles and conference papers on the Compendex/Inspec/Geobase bibliographic database, which compares favorably with other equivalent packages (sixty for

---

[*] until October 2007, after which time a charge of £1200 per annum was introduced by the distributors

MIKE-21, twenty-four for RMA-2, twelve for MIKE-3 and four for DELFT-3D) but is significantly less than for the open-source Princeton Ocean Model (POM), with around two hundred citations (Engineering Village 2008).

Real-world applications of TÉLÉMAC-2D, where the model results have been validated against field data, have included flood-plain inundation (Bates et al. 1997); a dam break study (Petitjean et al. 1997) and shelf tidal modelling (Jones and Davies 2005). In the latter case it was found that the TÉLÉMAC-2D solution agreed well with a well-established operational finite difference model of the Irish Sea.

5.2.2 Implementation of a tidal model in TÉLÉMAC

The process of setting up and running a tidal model using TÉLÉMAC-2D is illustrated as a flowchart in Figure 5.1. The processing of raw bathymetry is covered separately in Chapters 9 and 8.

5.2.2.1 Pre-processing

Meshes generated by the TÉLÉMAC pre-processor MATISSE are triangulated, with checks performed on minimum angle of element vertices. There are two kinds of basis function used in TÉLÉMAC, namely linear triangles (also known as P1) and 'quasi-bubble' triangles, both of which are illustrated in Figure 5.2. For quasi-bubble triangles, there is an extra node located at the centroid of each element, resulting in a higher-order approximation for the variables than with the linear triangles.

5.2.2.2 Boundary conditions

A full-slip boundary condition was imposed at solid boundaries, with correction of free-surface gradient for drying of elements. The full-slip boundary is justified as the coastal frictional boundary layer is a sub-grid process when elements of approximate dimension 100 m or larger are used.

In a comprehensive review of coastal and shelf-sea modelling literature in the

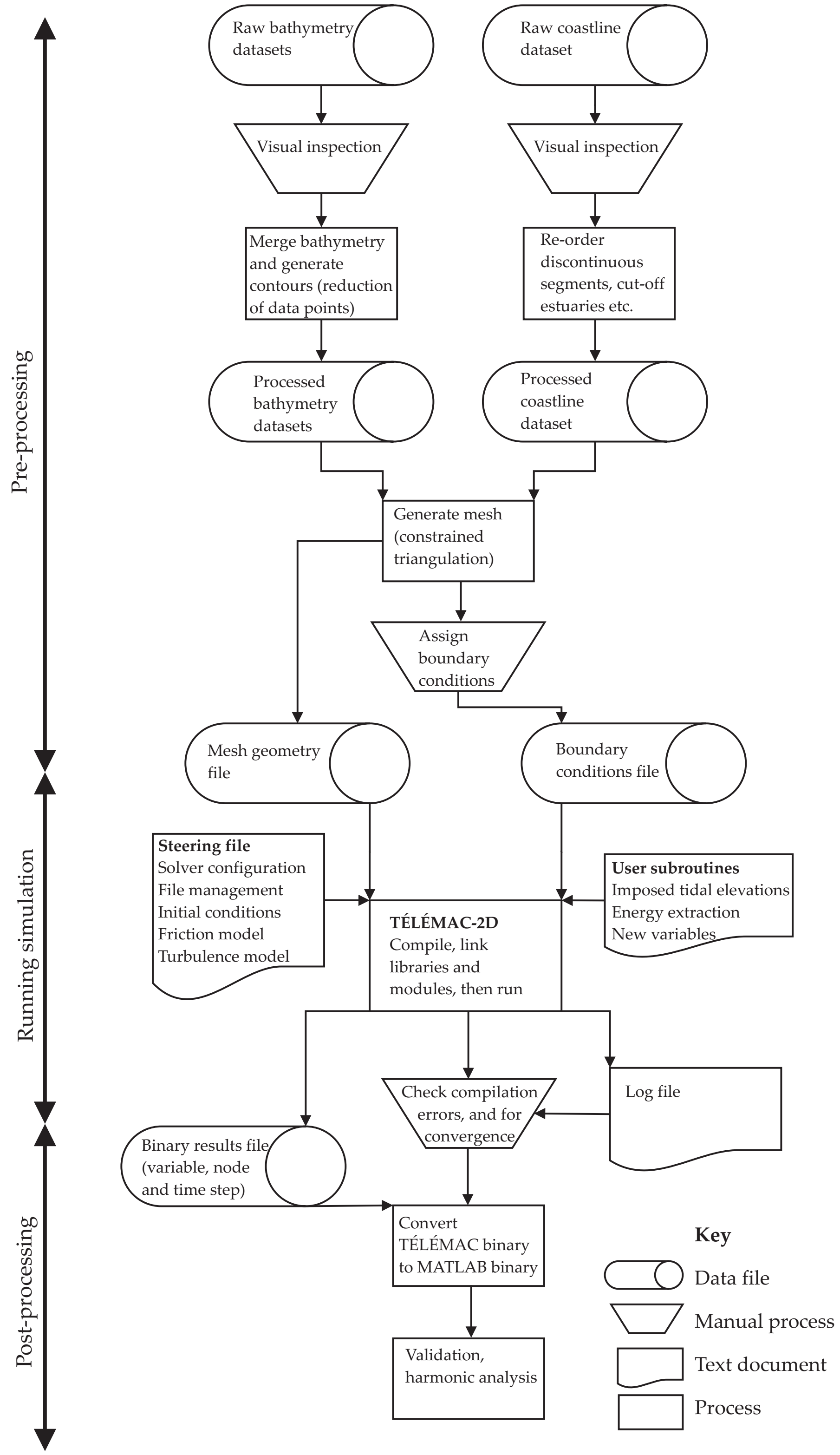

Figure 5.1: Flowchart illustrating stages involved in running a coastal tidal simulation with TÉLÉMAC-2D

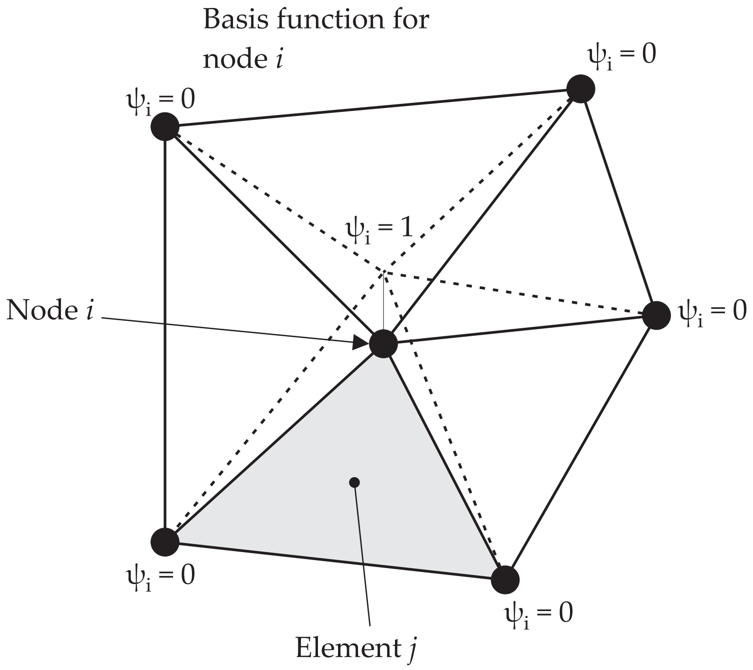

(a) Linear triangles

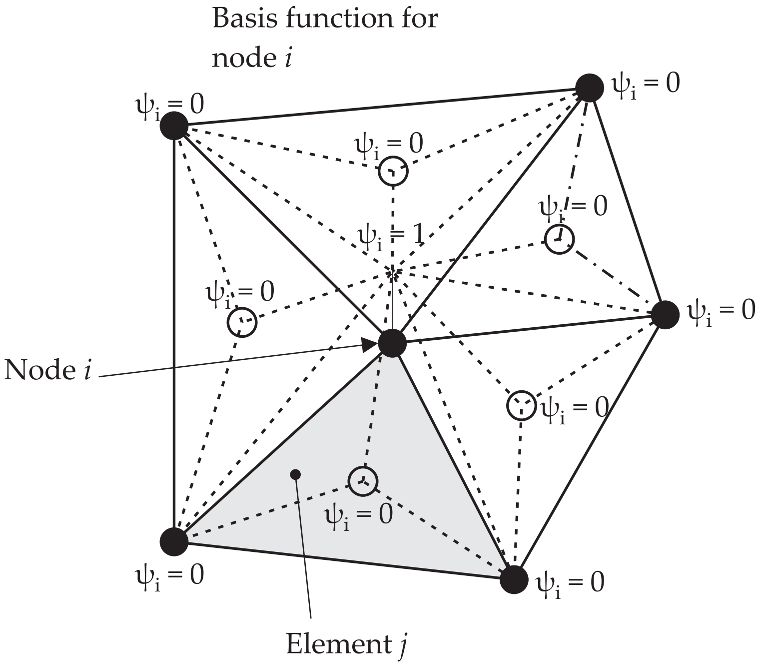

(b) Quasi-bubble triangles

Figure 5.2: Finite element basis functions used in TÉLÉMAC-2D

European context, Jones (2002) found that a number of combinations of open boundary conditions were in use, broadly divided into:

1. Imposed elevation
2. Imposed elevation and velocity
3. Radiation (internally generated waves propagate out of the domain)
4. Sponge (internal fields are relaxed towards external values)

Type-1 boundary conditions are under-constrained in a mathematical sense and without further treatment, allow the solution to 'drift' as not enough information is propagating into the domain. While Type-2 boundary conditions provide complete information, it is difficult to ensure consistency between depth and velocity, particularly as the two variables may not be measured in the field at the same location. Moreover, tidal velocities depend more strongly on local bathymetry and coastline than do tidal elevations. Inconsistencies in the specification of the boundary may lead to instability and lack of convergence in the model. In addition, the availability of velocity data points is limited when compared to widely-available tide-gauge data and co-tidal charts. Type-3 (radiation) boundary conditions prescribe an incident shallow water wave at the boundary, while allowing waves reflected from within the domain to escape. Radiation boundary conditions still require the normal component of velocity at the boundary to be specified. Sponge boundary conditions are not implemented in TÉLÉMAC, but in any case are still reliant on data being available at the boundary. They are useful when coarse-resolution externally generated fields are being used to drive the model.

To overcome the open boundary problem, the TÉLÉMAC-2D code uses a time-varying 'non-reflective' boundary condition (Thompson 1987, 1990). This is designed to allow imposed time-varying values of elevation on the boundary, while minimizing reflection of outgoing waves. The method uses the method of characteristics, convecting the h, u and v variables normal to the boundary and adjusting the imposed elevations to match. In practice this boundary condition is only truly non-reflective when waves are exiting the domain normal to the boundary; at other angles some partial reflection may occur (Tsynkov 1998). A consequence of using this method is that—at least in TÉLÉMAC-2D—parallelization cannot be employed. Jones (2002) also noted that in areas of shallow water with high energy dissipation by friction, errors are smoothed out as they propagate into the domain and therefore that the interior solution is not as sensitive to the external specification as would be the case in deeper water.

5.2.2.3 Running the simulation

The core of TÉLÉMAC-2D is the finite element implementation of the depth-averaged RANS equations in §4.9. The full steering file, with explanatory notes, is included in Appendix D. The finite element mesh used quasi-bubble triangle discretization in space for velocity and a P1 triangle discretization for depth. The time discretization was semi-implicit, with a coefficient of 0.6, i.e. h was discretized in time as $0.6h_{n+1} + 0.4h_n$. The best performance in terms of computation time was found to be using the generalized minimum residual method (GMRES), as advised in the TÉLÉMAC manual (EDF-DRD 2002), with Krylov sub-space of order 5 and a time step of 30 seconds.

Chapter 6

Modelling large arrays of turbines

6.1 Introduction

This chapter lies at the core of this thesis. A new model of a large array of tidal stream turbines has been derived, drawing together ideas from the literature on wind farm modelling; tidal stream field data and flow over general arrays of obstacles. This is the first time that the 'added-roughness' approach to modelling tidal stream turbine arrays has been given a theoretical basis.

The purpose of the new model is two-fold:

1. To provide an equivalent added roughness value for the array, combining the effects of bed roughness, device spacing and drag on devices, suitable for coastal-scale numerical modelling. This is to enable modelling of the impacts of large arrays of tidal stream turbines on the wider flow regime.
2. To estimate the equilibrium velocity deficit in very large array. This is to enable estimation of power generation by the array compared to that of an isolated generator and also to provide an asymptotic value that may feed into future non-equilibrium finite-array models.

The model is later used in Chapter 10 to investigate the impacts of a possible array at Portland Bill, where the added area-averaged drag coefficient derived here for an infinite array is used to model a finite array.

6.2 Modelling multiple-wake interactions

Frandsen et al. (2006) identified three main regimes characterizing wake interactions within a large array of wind turbines, ignoring complicated edge effects and starting from the upwind rows and moving downstream:

Regime 1 Wakes not merged laterally; turbines are only affected by the wakes of turbines directly upstream.

Regime 2 Wakes merged in the lateral direction; combined wake can only expand vertically.

Regime 4 Wakes merged in a very large wind farm; the combined wakes are in balance with the boundary layer and the flow is uniform in a spatially-averaged sense.

The focus in this chapter is on the third regime, as the objects here are the effects and performance of large tidal arrays which have reached a saturation level of momentum and energy extraction.

There are three main families of wake interaction models used to model the interaction of wakes in wind turbine arrays: (Crespo et al. 1999):

6.2.1 Wake superposition models

These are based on the principle of the conservation of momentum-deficit within the wake. The expansion of the far wake is governed by the thrust coefficient of the generator unit and the ambient turbulence intensity (Lissaman 1979). There may also be a small contribution added from rotor-generated turbulence. The momentum deficits from each wake are linearized and superposed and then the performance of each turbine is calculated and summed to give the output of the whole array. Wake interaction with the ground is handled using potential flow theory by a reflection plane with an ‘image’ turbine. These models break down for large arrays as they tend to predict incident velocity on each successive row of turbines tending to zero or even negative values. This is due to the model ignoring the increased rate of momentum transfer from above resulting from the greater shear present in the flow.

6.2.2 Field models

These calculate flow variables at every point in the farm using a numerical model (with spatial discretization). They range from simplified models with self-similar wake expansion, including a algebraic eddy-viscosity turbulence model, such as that of Ainslie (1987). Such models typically neglect longitudinal pressure variations (the ‘parabolic’ approximation). At the other end of the spectrum are computationally-intensive three-dimensional CFD models using general-purpose codes, such as described in Ammara et al. (2002). The simplified models have been widely used as tools to predict wind turbine array performance, whereas CFD models remain computationally expensive (Crespo et al. 1999).

6.2.3 Area-averaged models

These only apply to ‘large’ wind farms, as mentioned above, where it is assumed that there is a spatially-averaged balance between momentum input and drag forces. Observations have shown that velocity deficit at hub height downstream of the first row of turbines in an array rapidly attains a steady value as each successive row is encountered (Frandsen et al. 2006). Consequently, a wind turbine array with more than four rows can be considered a ‘large’ farm. The turbine drag can then in principle be modelled as an additional uniform drag coefficient over the surface area of the array. These models have not been widely used due to the success of the wake superposition and simplified field models above, which give more information about the power output of each successive row than the area-averaged type, and the lack of measurements of sufficient quantity and quality of flow profiles in and above wind turbine arrays. In addition, the impact of arrays of wind turbines on downstream wind speeds is less of a concern than for tidal stream turbines, where the depth and the momentum flux available for recovery of flow speeds is more limited.

6.3 Rationale for using area-averaged modelling approach

In this chapter, the boundary layer approach, taken previously in estimating speed deficit in large wind turbine arrays has been revisited in the context of tidal stream power generation. There are two reasons for considering this type of model. First, it has relevance to the question of maximum power extraction from tidal flow at a particular location, which has been analyzed for the general case of a tidal 'fence' across a well-bounded channel (Garrett and Cummins 2005), but remains an open problem for less well bounded situations, such as flow around headlands. Second, a simplified approach using distributed roughness is attractive from the point of view of modelling the impact of large tidal turbine arrays on tidal flows, using existing coastal modelling software. Individual turbines are too small to be simulated directly in a coastal numerical model with horizontal extent of tens of kilometers, as to resolve the turbines and include the largest scales in the flow would entail excessive computational expense.

A distributed roughness approach has been applied previously to specific geographic locations by Sutherland et al. (2007) in the case of tidal flows in channels, and by Blunden and Bahaj (2007b) (also included in Appendix G) to headland-accelerated tidal flow. In the former, the drag coefficient was increased until the maximum power was dissipated through the increased friction. In the latter, values of drag coefficient and spacing of turbines within the array were assumed prior to modelling, and averaged over the affected elements in the model mesh. In neither case were taken into account the changes in spatially-averaged vertical velocity shear profile due to the change in momentum balance within the array. Bryden et al. (2007) have considered energy extraction in a layered 3-D model for some idealized cases, using

80×80 m grid cells. However, their work was focused on single-row tidal fences in channels rather than representing multi-row arrays.

6.4 Review of rough-wall flow through obstacle arrays

The modelling of wind turbine arrays using distributed roughness has been informed by boundary layer micro-meteorology, which has developed in the context of measuring and predicting flows over crops, forests and urban landscapes. These are classed as rough-wall turbulent boundary layer flows; 'rough-wall' as the Reynolds number based on the characteristic area-averaged height of the roughness obstacles $u_* L_r / \nu$ is high enough to attain similarity and molecular viscosity no longer affects the scaling. For a comprehensive review of rough-wall boundary layer flow, see Raupach et al. (1991).

The parameters of a general regularly-spaced obstacle array are defined in Figure 6.1. The roughness length z_{0+} describes the combined roughness of the obstacles and the underlying surface, as experienced by the flow *above* the obstacles.

According to a classic analysis, introduced in §4.10, the flow profile (whether in the atmosphere or an open channel) is considered to consist of a roughness sublayer, influenced by the friction velocity and the properties of the roughness, and an outer layer, influenced by the friction velocity and the boundary layer thickness, but not the roughness properties. Between the two layers is an overlapping region that follows the well-known logarithmic profile:

$$\frac{u}{u_*} = \frac{1}{\kappa} \ln\left(\frac{z-d}{z_0}\right) \tag{6.1}$$

where the zero-plane displacement d is used as a parameter for adjusting the profile for a better logarithmic fit; physically it is equivalent to the mean level of momentum absorption. The roughness sub-layer extends from the surface up to some multiple of the geometric roughness (obstacle) height. For arrays of bluff-bodies such as cubes, or within forest canopies, measurements of the mean flow profile within the roughness sub-layer have been fitted to an empirical exponential profile, derived assuming a constant mixing length

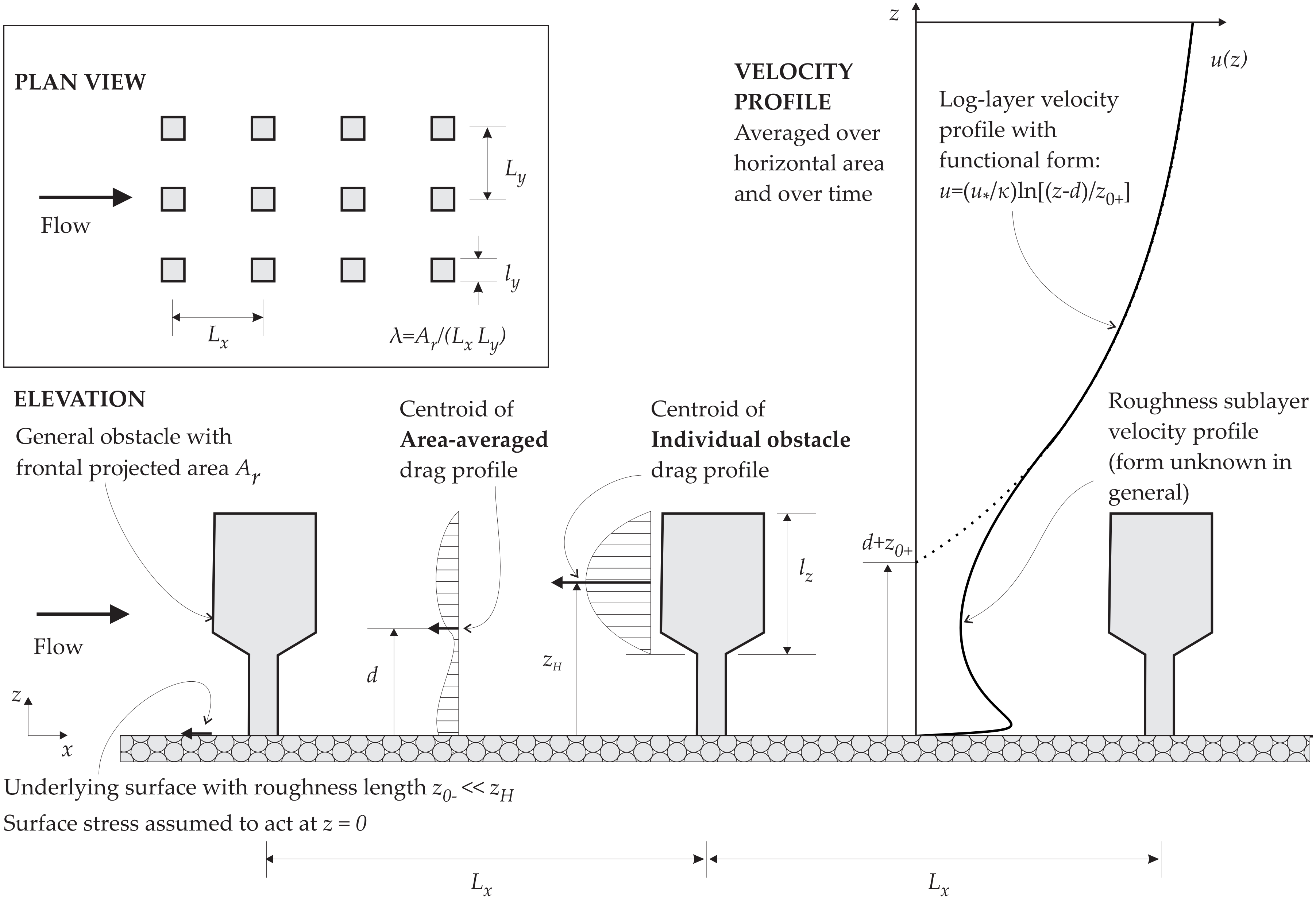

Figure 6.1: Definition of terms used in the text to characterize a general obstacle array in rough-turbulent flow.

Table 6.1: Variation of frontal area to plan area ratio λ with tidal stream turbine size and configuration. n is the number of rotors per generator unit

D (m)	A (m^2)	n	σ_x (L_x/D)	σ_y (L_y/D)	λ ($nA/\sigma_x\sigma_y D^2$)
10	79	1	15	7.5	0.007
16	201	1	15	4	0.013
20	314	2	7.5	4	0.052

throughout the layer. However, flow profiles through comparatively sparse arrays of turbines, where there is no large-scale flow separation, can not necessarily be expected to fit the same function.

The key geometric parameter of an obstacle array has been found to be the ratio of projected frontal area of obstacles to the horizontal array area, λ (Raupach et al. 1991). Values of λ for tidal arrays might be expected to be in the range 0.005–0.05 (see Table 6.1), compared to 0.05–10 for flows over vegetation. It has been observed that in atmospheric flows over arrays of obstacles of various shapes and arrangements, that at low obstacle densities (isolated roughness flow), the ratio of roughness length to roughness height is approximately linearly related to the obstacle density. (Raupach et al. 1991; Stephan and Gutknecht 2002).

6.5 Previous application of approach to large wind turbine arrays

Where boundary layer theory has been applied to wind turbines, in most cases, the velocity profile has been considered logarithmic over the entire planetary boundary layer down to the hub height of the rotor, with a single new roughness length describing the flow through the array compared to the flow in the undisturbed state. The ‘gradient wind’ at height was assumed constant, although the boundary layer thickness was allowed to vary in some cases. A difficulty arises with the momentum approach to this type of model in that the distribution of drag between friction (and possibly form drag if there are large-scale features) at the bed and the turbines is not known (Bossanyi et al. 1980). The energy approach is even more uncertain however as the rotor- and wake-generated turbulence production is also not known. Newman (1977) assumed that the shear stress on the ground was constant i.e. no change from upstream to within the array. The new roughness length could then be calculated from the sum of the shear stress on the ground and the spatially-averaged drag on the turbines.

Frandsen (1992) proposed dual logarithmic velocity profiles matching at hub height, noting that flow below hub height had been observed to be logarithmic within a wind turbine array. The 'gradient wind' was used to eliminate the roughness length in the upper layer. In the inner layer, deep within the outer planetary boundary layer, the bed roughness height was assumed to be known and the lower flow profile matched to the upper by velocity at hub height, resulting in a quadratic expression for hub height velocity.

The model of Frandsen bears similarities to the growth of a new internal boundary layer from the bed due to a change of bed roughness, where the upper layer retains the memory of the upstream roughness, whereas the slowly-growing internal layer is adapted to the new conditions. However, it is not clear why the internal layer would only extend to hub height and not grow to fill the whole external boundary layer. The velocity measurements cited by Frandsen as evidence of a logarithmic profile below hub height were taken within the onshore wind turbine array Nørrakær Enge II, Jutland, Denmark (Højstrup et al. 1993, page 27) where there were two to three points in the vertical below hub height and the measurements were taken at effectively two rows into the array. The measurements do not therefore represent conclusive evidence for the model being correct.

6.6 Similarities and differences with natural rough-wall flows through obstacle arrays

Definition sketches for particular types of flow over obstacle roughness are included in Figure 6.2 and for flow through turbine arrays in Figure 6.3. The

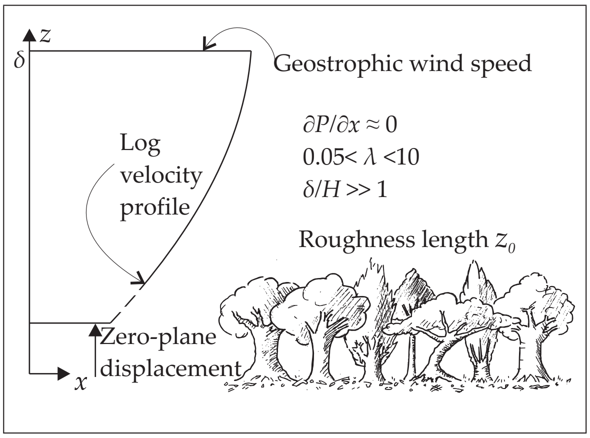

(a) Terrestrial canopy

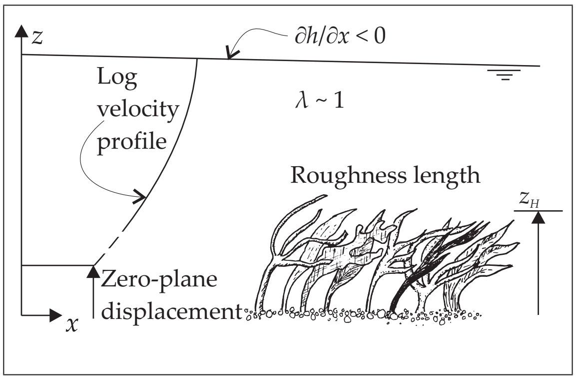

(b) Aquatic canopy

Figure 6.2: Conceptual models for flows over atmospheric and aquatic canopies

differences are apparent in terms of frontal area ratio and fraction of boundary layer or depth occupied by roughness height. Flows through submerged vegetation bear the most resemblance to those in large tidal turbine arrays, in terms of fraction of depth of flow occupied. However, the high frontal area ratio in submerged vegetation results in a large zero-plane displacement in comparison to plant height, with a logarithmic profile above the canopy, observed in the laboratory with synthetic plants (Nepf and Vivoni 2000) and saltmarsh vegetation (Neumeier 2007).

There is little experimental data for flow above and especially below the geometric roughness height of large arrays of obstacles of a similar nature to tidal turbines (low frontal area ratio, large fraction of depth occupied, high porosity, no flow separation) for comparison. MacDonald (2000) investigated flow among and above arrays of cuboid obstacles and derived a semi-empirical exponential expression for the velocity profile below the

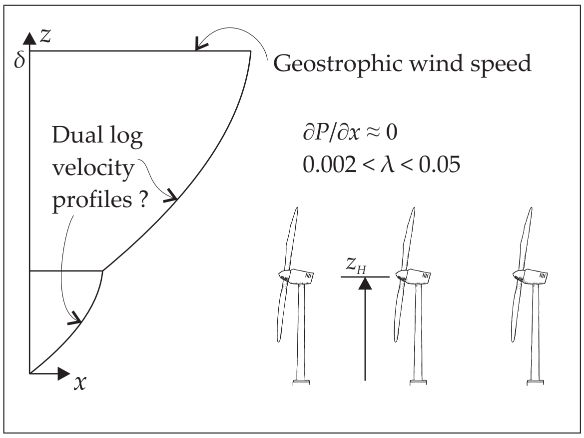

(a) Large wind turbine array after Frandsen (1992) (density exaggerated)

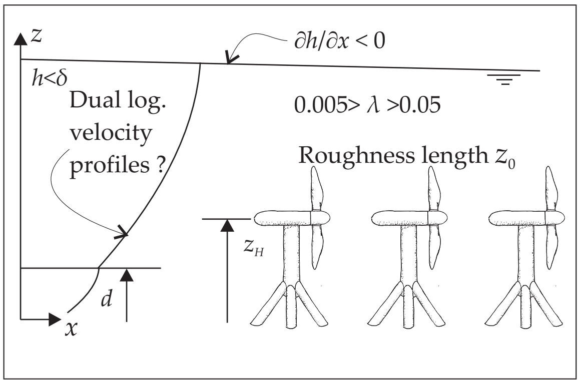

(b) Large tidal turbine array (density exaggerated)

Figure 6.3: Conceptual models for flow through wind and tidal turbine arrays

obstacle height. In doing so, it was assumed that at each height above the surface, the drag coefficient experienced by the flow was constant and that the length scale for the turbulent viscosity was also constant. Moreover, the lowest value of area ratio investigated was at the upper end of the range that might be expected for a tidal turbine array. Bentham and Britter (2003) proposed an even simpler model, with the velocity constant below obstacle height. This gives results similar to MacDonald for low values of area ratio, and was proposed by in the context of modelling flow through and over urban canopies.

6.7 Evidence for logarithmic vertical velocity profiles in fast tidal streams

The vertical velocity profile in a tidal stream varies over the tidal cycle, with phase differences in velocity over the water column as the upper portion is more affected by inertia and the lower by friction at the bed. These effects are most important when the velocities are low and are therefore likely to have little effect on the energy capture of a tidal turbine, which would be generating at low efficiency or not at all (if below cut-in speed). The external balance of forces in the flow during most of a tidal cycle is between longitudinal pressure gradient due to sea-surface slope and frictional stresses on the sea bed (Campbell et al. 1998), which is in contrast to the atmospheric boundary-layer case where the flow is driven by the geostrophic wind from above.

Observations made in a moderately fast tidal stream of amplitude 1.2 m/s in depth of around 50 m (Elliott 2002) indicated a good fit to a logarithmic profile over most or all of the depth sampled (30–40 m above the bed) during the ebb and flood periods. In a fast, unstratified tidal stream, the logarithmic profile may extend all the way to the free surface (Dyer 1986).

The portion of the water column close to the surface is avoided by most designs of full-scale tidal turbines, for many reasons including cavitation or ventilation on the blade tips; hazards to surface vessels and wave action. Consequently the deviation from a logarithmic profile in this region is unlikely to have a large effect on the energy capture of such turbines. Anecdotal evidence from the Seaflow project off Foreland Point near Lynmouth, Devon (Thake 2005, p. 45), with the velocity profile measured using a boat-mounted ADCP, have suggested a more sheared flow profile was observed over the whole depth than would be expected if the usual 1/7 power law or other empirical flow profiles were assumed.

The results of another ADCP survey exercise carried out by Cardiff University were reported at a recent conference (Mason-Jones et al. 2008). The site was located in the inner Bristol Channel, with position 51.3416°N, -3.4931°E, approximately 35 m depth, and was sampled using a boat-mounted ADCP.

The maximum velocity measured was 1.8 m/s. The authors fitted a fourth-order polynomial expression to the filtered ADCP velocity profile $u(z)$ (m/s), with 14 degrees of freedom and $r^2 = 0.986$:

$$u = -2 \times 10^{-6} z'^4 - 2 \times 10^{-5} z'^3 + 0.0006 z'^2 + 0.0215 z' + 1.81 \tag{6.2}$$

Where z' (m) is measured positive upwards from the sea surface, i.e. $z' = z - h$ in the co-ordinate system used in this chapter, where z is measured positive upwards from the sea bed. In terms of z:

$$u = -2 \times 10^{-6} z^4 + 2.60 \times 10^{-4} z^3 - 0.0120 z^2 + 0.249 z - 0.351 \tag{6.3}$$

Here, the polynomial fit has been re-sampled (with the same resolution in the vertical) and instead a logarithmic profile fitted, of the form (6.1). In the literature, d has typically been adjusted graphically to give a straight line on a log-linear plot (Dyer 1986), however this method does not take full account of the non-linearity of the errors for varying z. A more accurate method—robust non-linear least squares—was implemented with the MATLAB curve-fitting toolbox. This led to the problem that the original expression tends to minus infinity at this depth and below this elevation, becomes complex. This proved to be a problem for convergence of the curve-fitting toolbox, as the values of d and z_0 are not known in advance and the lowest re-sampled data points were below the level where $(z - d) = 0$ for a best fit to the other points. As mentioned above, the lower limit of validity of the logarithmic relationship is not well defined as it merges with the roughness sublayer velocity profile. Recognizing that:

$$\ln\left(\frac{z-d}{z_0}\right) \equiv \ln\frac{z}{z_0} - \ln(1 - \frac{d}{z}) \tag{6.4}$$

the expression $\ln(1 - \frac{d}{z})$ was expanded using a Taylor series to make the equation more well-behaved around $(z - d) \rightarrow 0$. The Taylor series expansion ensures that the curve diminishes towards negative velocities without becoming undefined at $(z - d) = 0$, while remaining close to the original curve. This method has not previously been noted in the literature, to the best of the author's knowledge.

$$u = \frac{u_*}{\kappa}\left\{\ln\frac{z}{z_0} - \frac{d}{z} - \frac{1}{2}\left(\frac{d}{z}\right)^2 - \frac{1}{3}\left(\frac{d}{z}\right)^3 - \frac{1}{4}\left(\frac{d}{z}\right)^4\right\} \tag{6.5}$$

The lowest two points on the curve plus the three highest points were excluded from the curve-fit to try due to eliminate free-surface and

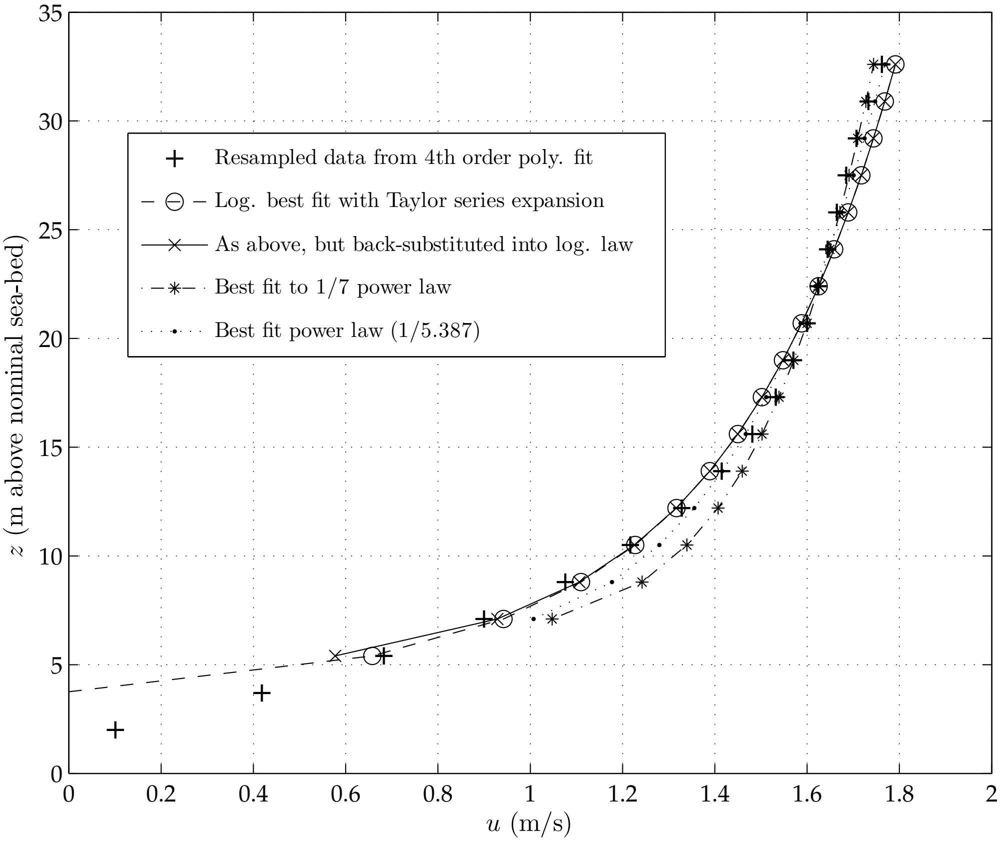

Figure 6.4: Log-law flow profile fitted to polynomial curve-fit of ADCP data given in Mason-Jones et al. (2008)

poorly-resolved near-bed effects. The logarithmic curve-fit ($r^2 = 0.991$, 11 degrees of freedom) is plotted against the empirical curve-fit in Figure 6.4. The plot compares the resampled data points (+) with the two logarithmic profiles with and without expanded terms in order to show that the curves are nearly coincident. It also shows two power law profile fits. For the expanded curve, the 95% confidence intervals for u_*, z_0 and the displacement height d, were as follows:

$$\begin{aligned} \text{CONF}_{95}\,\{0.12 \le u_* \le 0.18\} &\quad \text{m/s} \\ \text{CONF}_{95}\,\{0.035 \le z_0 \le 0.42\} &\quad \text{m} \\ \text{CONF}_{95}\,\{3.2 \le d \le 5.4\} &\quad \text{m} \end{aligned} \tag{6.6}$$

The friction velocity implies a sea-surface slope of approximately 8×10^{-5}, which is large, but plausible; Elliott (2002) estimated friction velocities of up to 0.06 m/s from an ADCP survey in the Irish Sea. The roughness length is extremely large, giving the highly sheared flow profile. It is possible that this is the result of an upstream change of roughness giving a 'kinked' profile due to a slowly-growing internal boundary layer, or simply that the averaging was not over a sufficient period to minimize the effect of random fluctuations. The displacement height is large and reflects the uncertainty in near-bed measurement from a surface vessel. It would be desirable to compare these results with other locations having fast tidal streams and similar bathymetry in order to assess whether such highly sheared profiles are the norm. The 1/7 power law gives a poorer fit to the data in the lower half of the profile; an exponent of 1/5.4 does better, but not as well as the logarithmic profile. Not being derived from physical reasoning, in contrast to the logarithmic velocity profile, the power law profiles can not give information about the bed roughness or friction velocity.

In conclusion, the evidence above implies that it is reasonable to expect that the tidal flow in the natural state is fully rough-turbulent and the mean vertical velocity profile can be described by a logarithmic function over most of the depth (from close to the roughness to close to the surface).

6.7.1 Hub height velocity in the undisturbed case

Using the logarithmic expression for U_0 (4.69) and assuming that upstream, the zero-plane displacement $d_- = 0$:

$$\frac{u_{H-}}{U_-} = \frac{\ln z_{0-}/h - \ln z_H/h}{\ln z_{0-}/h + 1} \tag{6.7}$$

Where all the quantities have been normalized with respect to the depth h. Where subscript H refers to hub height (or the height of the centroid of the flow capture area of the device). The square of this function is plotted against z_H/h in Figure 6.5 for various plausible values of z_0/h. It is interesting to note that if the hub height is near to $e^{-1}h \approx 0.37h$—compare Seaflow, with $z_H/h = 0.38$ where h was mean sea level—then regardless of the bed roughness, the hub height upstream velocity (and hence the thrust coefficient of an isolated turbine) may be robustly estimated using the depth-averaged velocity, regardless of the value of the poorly-determined bed roughness. In areas with lower tidal range than the location of Seaflow (Bristol Channel), z_H/h may be greater, but would be unlikely to be much above 0.5 due to wave

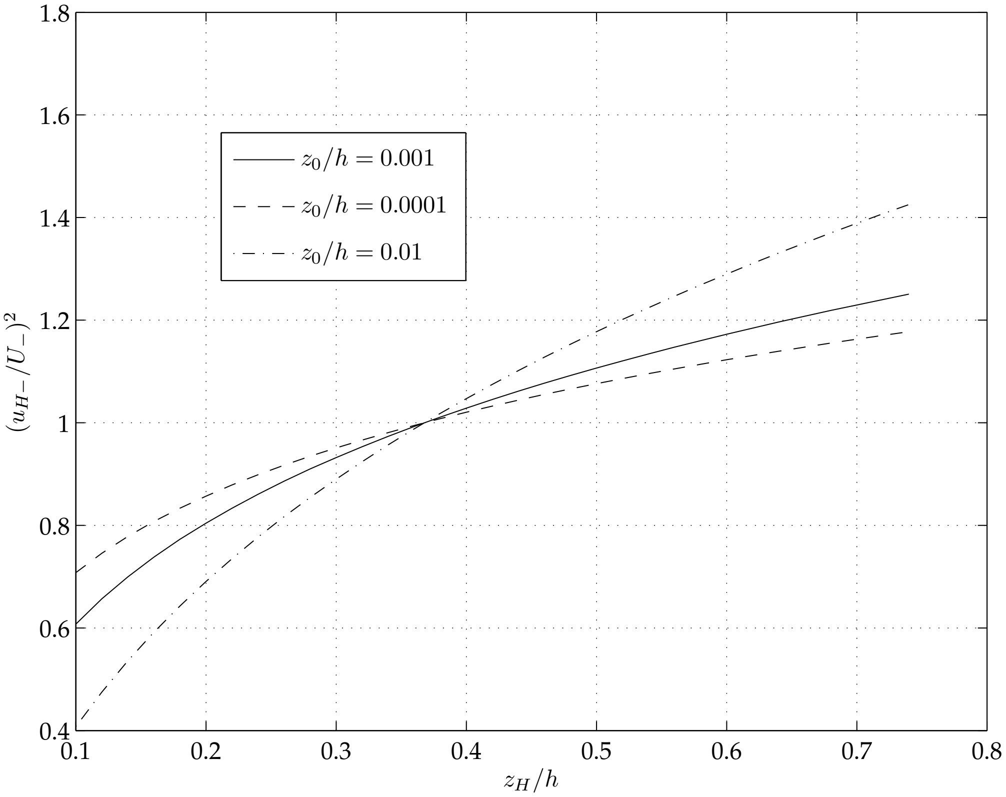

Figure 6.5: Ratio of hub-height flow speed-squared to depth-averaged flow speed-squared against hub-height as a proportion of depth for a variety of bed-roughness values

action, increasing overturning moments on the structure and diminishing flow capture area.

6.8 Development of a new area-averaged model for a large tidal stream turbine array

The following sections detail a new model which extends the methodology previously used for wind turbine arrays, to tidal stream arrays. The ratio of new to old hub height velocity is derived based on a logarithmic profile above hub-height. The equivalent drag coefficient related to the depth-averaged velocity is then found by assuming a matching logarithmic profile below hub-height. In order to develop the new model, two further assumptions need to be made.

Assumption 1 *The force upon and power generated by each unit depends only on the mean incident velocity at the hub height (or at the height of the centroid of the swept area of the turbine).*

This assumption neglects non-linearities in the vertical velocity profile (and its higher moments, u^2 and u^3) upstream of the turbine rotor disk, that would be likely to lead to higher rotor-area-averaged characteristic velocities for drag and power than the centroid velocity. It would be possible to use multiple-streamtubes with varying velocities to integrate the profile across the swept area, but as the upstream velocity profile is not known in advance, this would lead to unjustifiable complication. Moreover, if the velocity profile maintains a similar form, values of c_d and c_P will be out by constant factors that may be established later in the light of experimental velocity profiles.

In reality, there would also be a contribution to the total drag experienced by the flow, caused by the structure providing reaction against the thrust of the turbine. This could be added into the model at a later stage based on the estimated drag on a particular structural configuration.

Assumption 2 *The flow within the array can be considered to be a sum of a mean value plus periodic components with period L_x.*

This assumption relies on the turbulent mixing deep within the array being sufficient that the mean flow adjusts to the new combined roughness of the array and the bed, so that there is no further change in drag on the turbines or friction on the bed with the stream wise co-ordinate, when averaged over subsequent periods of L_x downstream of the leading edge of the array. As previously mentioned in §6.2.3, in the case of wind farms, the velocity deficit has been observed to level out after approximately four rows. In the case of tidal stream turbine arrays, there are no full-scale data, but characterization of such arrays has begun using mesh simulators in the laboratory and extended using CFD (Blunden et al. 2009, in review). A set of experiments were carried out on an array of four porous mesh fences in a channel. Measurements were made of flow velocities and drag on the fences. The results were compared with those of a CFD model with similar geometry and with the fences represented as imposed pressure gradients. Reasonable agreement in velocity

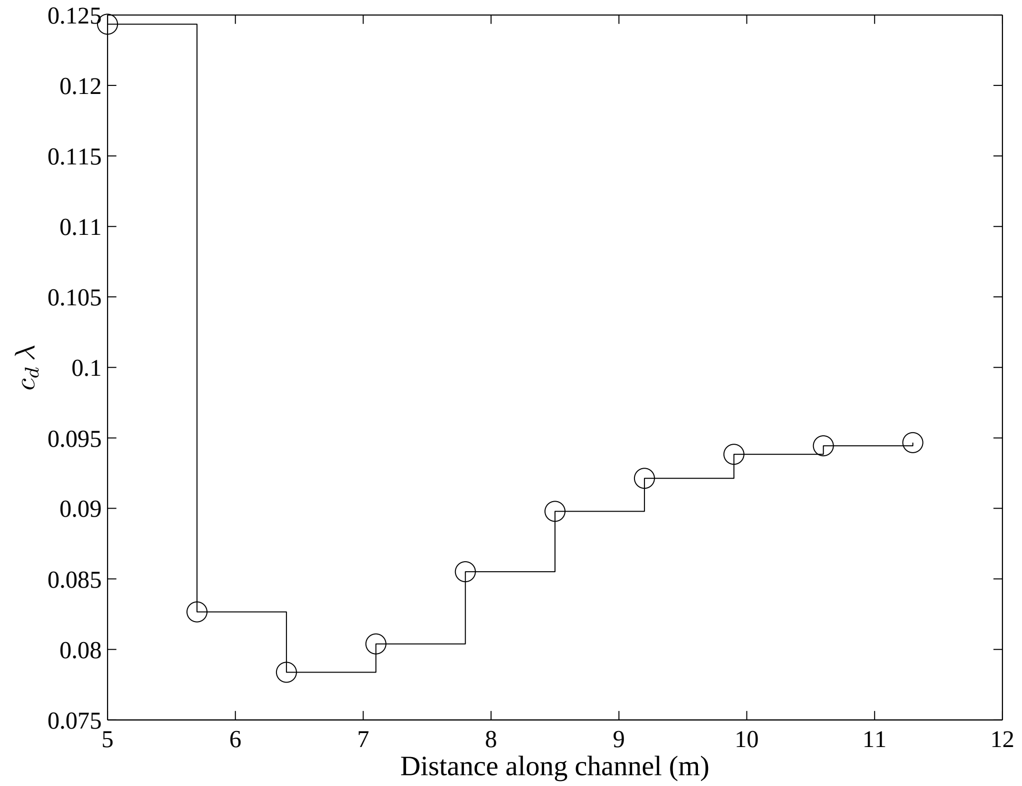

Figure 6.6: Variation of area-averaged fence drag $c_d\lambda$ with distance along channel. Drag coefficient is referred to the local depth-averaged flow speed.

profile was found above and on the centre-line of the fences, but was poorer below. The CFD model was extended to an array of ten fences to examine the degree of convergence on equilibrium values for an array with an infinite number of fences. It can be seen from Figure 6.6 that the area-averaged drag coefficient of the fences $c_d\lambda$ converged to 0.0947 ± 0.0002. The variation of bottom friction coefficient with distance from the first fence was fitted to a build-up exponential curve (Figure 6.7) which predicted an equilibrium value $c_f = 0.00873$ with a 95% confidence interval of 5×10^{-5}. The fence drag was very large in this case when compared to the small bed friction, which explains why a large number of rows (a long fetch) was required to reach a steady state. The main point remains intact however, that an equilibrium is approached as more rows are added to an array.

This assumption also relies on the mean flow remaining quasi-uniform in the horizontal; the slope in the free-surface is not considered to have a significant effect on either the depth or on the depth-averaged velocity. This is a good

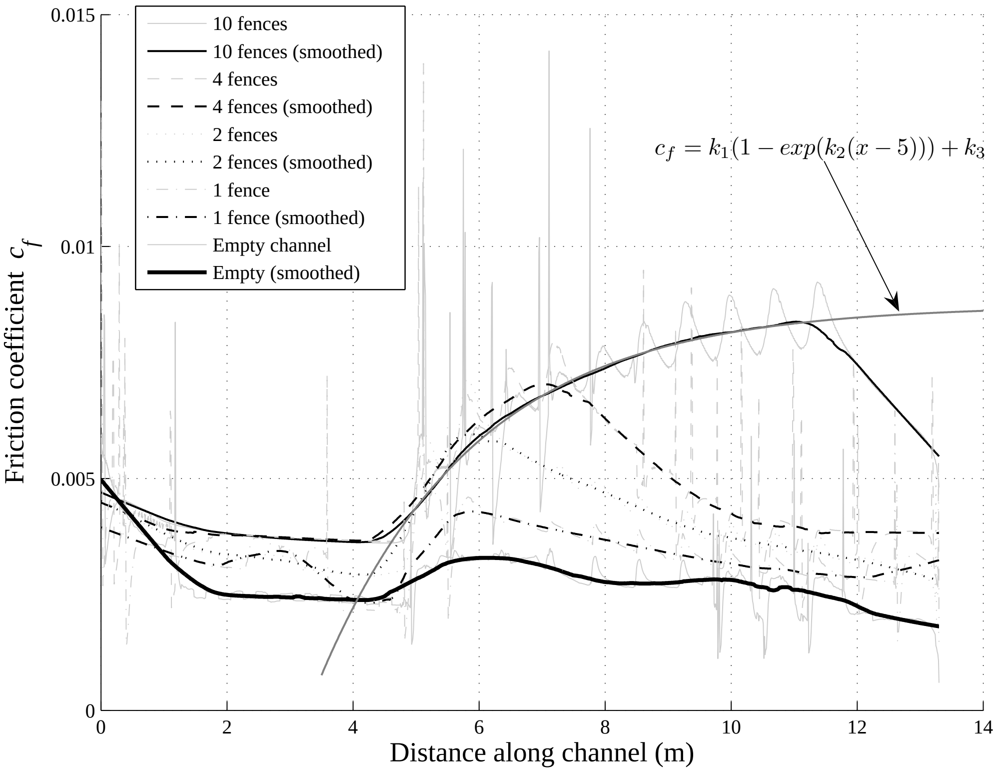

Figure 6.7: Variation of bed friction coefficient with distance along channel. Friction coefficient c_f is referred to the local depth-averaged flow speed.

approximation as the depths are of order 30 m and the sea-surface slopes of order 1×10^{-4}, so a fetch of order 15 km would be required to lead to a change in depth of 5%.

6.8.1 Hub height velocity within the large array

Under these assumptions, the hub height velocity several rows into the turbine array can be expressed as:

$$\frac{u_{H+}}{u_{*+}} = \frac{1}{\kappa} \ln \left(\frac{z_H - d_+}{z_{0+}} \right) \tag{6.8}$$

There are now three unknown independent variables: the friction velocity u_{*+}, the zero-plane displacement d_+ and the roughness length for the large array, z_{0+}. By analogy with flow over submerged vegetation, where it is assumed that $z = d$ is effectively a lower boundary to the flow and $h - d$ is the effective depth (Nepf and Vivoni 2000), the friction velocity can be related to the streamwise free surface slope by:

$$u_{*+} = \sqrt{gS_{0+}(h - d_+)} \tag{6.9}$$

Where $S_{0+} = -\partial h/\partial x$. The sea-surface slope (pressure gradient) S_{0+} is not known; for a finite array, it will be a function of upstream and downstream conditions. In addition it may be affected by the geometry of the array and the proximity of lateral boundaries. For the case of an infinite array (uniform flow), used to derive the equivalent friction coefficient for the turbines, the free-surface slope will be assumed to remain constant, regardless of whether the turbines are present, i.e. $S_{0+} = S_{0-}$.

When the maximum power for an array of finite size is considered, the assumption will be relaxed and the slope allowed to vary up to the point where the depth-averaged current is the same regardless of the presence of the turbines. The fixed free-surface slope gives the most pessimistic estimate (constant voltage source in an electrical analogy) and the fixed flow-rate the most optimistic (constant current source in the electrical analogy). Reality will lie somewhere between these extremes, i.e. the flow is likely to back-up in front of the array resulting in a local steepening of the free-surface slope across the array in the streamwise direction, but there will also be a local decrease in the depth averaged velocity. Define relative steepening in slope:

$$\beta = \frac{S_{0+} - S_{0-}}{S_{\max} - S_{0-}} \tag{6.10}$$

where $S_{\max}$ is the slope that the sea-surface would need to adjust to, to maintain a constant depth-averaged velocity. u_{*+} is also known independently through the sum of the resistive forces, assuming equilibrium:

$$u_{*+} = \frac{1}{\sqrt{2}} \sqrt{c_D \lambda u_{H+}^2 + \alpha c_f U_-^2} \tag{6.11}$$

Where α is an unknown fraction. If $\alpha = 1$, then there is no change in drag on the sea-bed with respect to the undisturbed case. When the sea-surface slope is assumed constant and as $\lambda \to \{0, \infty\}$, $\alpha \to \{1, 0\}$, but for intermediate values of λ, α would depend on the distribution of shear stresses in the flow between the sea-bed and hub-height. For the previous wind turbine array models, authors have taken $\alpha \propto (u_{H+}/u_{H-})^2$ (Bossanyi et al. 1980). This assumes that the ratio of the two velocities squared approximates the degree of shear in the flow profile close to the bed. This would be expected where the lateral spacing of the turbines is large enough that on average the flow is not too constrained in the vertical and a simple monotonic decrease in velocity would occur towards the bed (when spatially-averaged). However in the 2-D case of rows of tidal fences for example (§2.2), the flow must accelerate underneath the fence and the shear at the bed may be subsequently enhanced. This approach is adopted here and in the absence of any better information, the constant of proportionality is taken as unity:

$$\alpha = (u_{H+}/u_{H-})^2 \tag{6.12}$$

The depth-averaged velocity in the natural state U_- is known in terms of u_{H-} from (6.7).

The zero-plane displacement d, as mentioned previously, is the mean level of momentum absorption. It is often ignored for flow over surfaces as it is of the same order as the height of the roughness elements, i.e. $d_- \approx 0$ and consequently small compared to the depth. However, in the case of an obstacle array it may be raised significantly. The wind turbine models considered previously have assumed a zero-plane displacement of zero, presumably either for the sake of simplicity—it introduces awkward algebra into the expressions—or because the turbine hub height was much less than the thickness of the planetary boundary layer.

$$\frac{d_+}{z_H} = \frac{\lambda c_D u_{H+}^2}{\lambda c_D u_{H+}^2 + \alpha c_{f-} U_-^2} \tag{6.13}$$

with the requirement that $(z_H - d_+)/z_{0+} > 1$. Using the expression for α above has the consequence that the zero plane displacement is a function only of the friction/drag coefficients and length scales, not the flow velocity. An equation for u_{H+}/u_{H-} may then be found in terms of $\{c_d,\ z_H/h,\ z_H/z_{0-},\ \kappa,\ \lambda\}$ by combining (6.9), (6.11), (6.13) and (6.7) which was solved by analytical means using the MATLAB symbolic mathematics toolbox:

$$\frac{u_{H+}}{u_{H-}} = \frac{\sqrt{2}\kappa\,\sqrt{\frac{S_{0+}}{S_{0-}}}\sqrt{c_d\,\lambda\,\left(\ln\frac{z_H}{z_{0-}}\right)^2 + 2\,\kappa^2 - c_d\,\lambda\,\frac{z_H}{h}\,\left(\ln\frac{z_H}{z_{0-}}\right)^2}}{c_d\,\lambda\,\left(\ln\frac{z_H}{z_{0-}}\right)^2 + 2\,\kappa^2} \tag{6.14}$$

A MATLAB script for generating the solution is included in Appendix B.1. It is plotted in Figure 6.8 as a function of λ for varying values of z_{0-} in the case

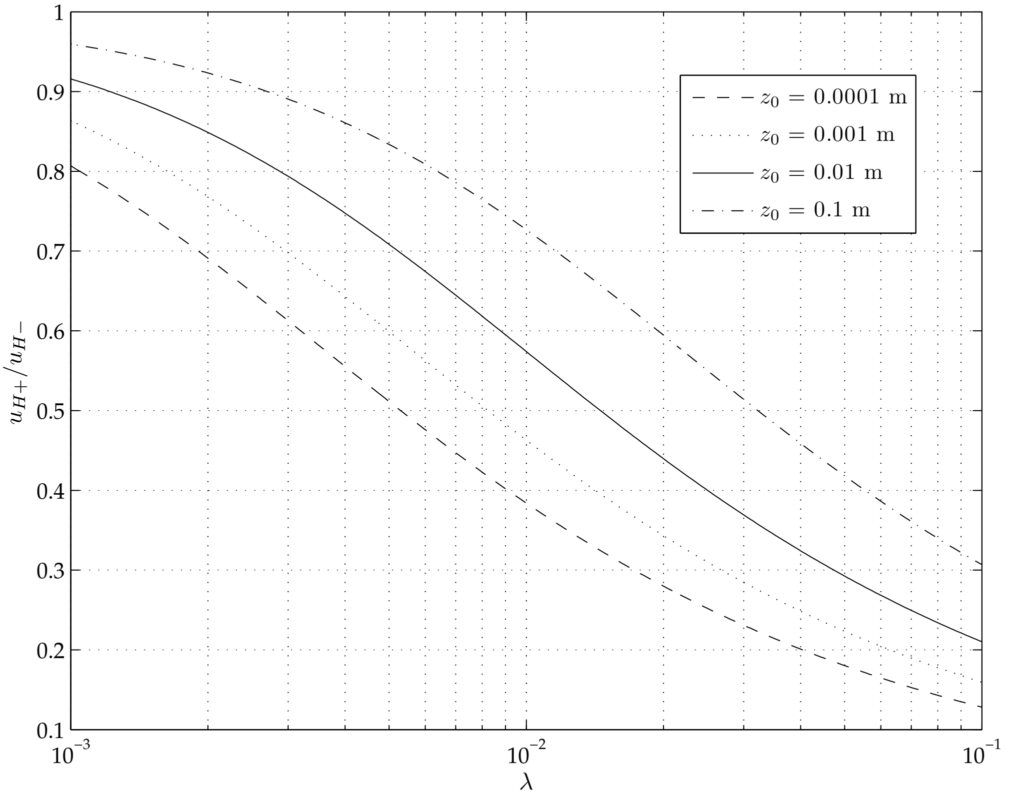

Figure 6.8: Variation in relative decrease in hub-height velocity with area density of turbines, showing sensitivity to sea-bed roughness length in the case where $h = 30$ m and $z_H/h = 0.37$

where $h = 30$ m and $z_H/h = 0.37$. As the free-surface slope has been assumed constant, higher values of roughness length indicate more dissipation by friction in the natural state, and therefore more energy or momentum available for absorption by the turbines in the array.

An expression for the roughness length z_{0+} can also then be found by back-substitution; it is also not a function of the flow parameters.

$$\frac{z_{0+}}{z_H} = \exp\left(-\frac{\sqrt{2}\,\kappa\,\ln\frac{z_H}{z_{0-}}}{\sqrt{c_d\,\lambda\left(\ln\frac{z_H}{z_{0-}}\right)^2 + 2\,\kappa^2}} \right) \tag{6.15}$$

6.9 Development of equivalent roughness for numerical modelling

A true finite-array added roughness model would need to take into account the non-equilibrium growth of an internal boundary layer from the leading edge of the array in Regime 2 (defined in §6.2). Similarly, downstream of the array, the flow will require a certain distance to re-attain equilibrium. Parameters derived for Regime 3 may be applied in Regime 2 in a similar manner to a standard assumption in open channel hydraulics, that a coefficient of friction derived for uniform flow can be applied to spatially-varied flow (Chow 1959, page 217). The greater the number of rows in the array, the less the edge-effects and the better the approximation. For the results of the equilibrium model to be useful for numerical modelling, the results must be transformed into an equivalent added drag coefficient. A difficulty arises at this point, in that the velocity profile below hub height in the array is not specified, so the total frictional drag cannot be directly related to the depth-averaged velocity in the presence of turbines. In order to close the problem, the approximation of Frandsen (1992) will be used, i.e. there is an internal boundary layer below hub-height following a logarithmic profile, with the original roughness length z_{0-} and matching $u = u_{H+}$ at $z = z_H$. While this relationship is not based on firm experimental evidence or theory, it at least ensures that the condition $U_+ < U_-$ is fulfilled, which is not necessarily the case with the constant or exponential flow profiles mentioned above. The velocity profiles for the case where $h = 30$ m, $z_0 = 1.4$ mm, $c_d = 0.9$ and $\lambda = 0.0055$ are plotted in Figure 6.9.

The depth-averaged velocity is then:

$$U_+ = \frac{1}{h}\left(u_{*H+}\int_0^{z_H}\frac{1}{\kappa}\ln\frac{z}{z_{0-}}\,dz + u_{*+}\int_{z_H}^{h}\frac{1}{\kappa}\ln\frac{z-d_+}{z_{0+}}\,dz\right) \tag{6.16}$$

with:

$$\frac{u_{H+}}{u_{*H+}} = \frac{1}{\kappa}\ln\frac{z_H}{z_{0-}} \tag{6.17}$$

and:

$$u_{*+}^2 = \frac{1}{2}\left(c_{f-} + \lambda c_d'\right)U_+^2 \tag{6.18}$$

but U_+ is now known as a function of u_{H+}, so the equivalent added drag coefficient c_d' can be found as a function of the other parameters. It is plotted in

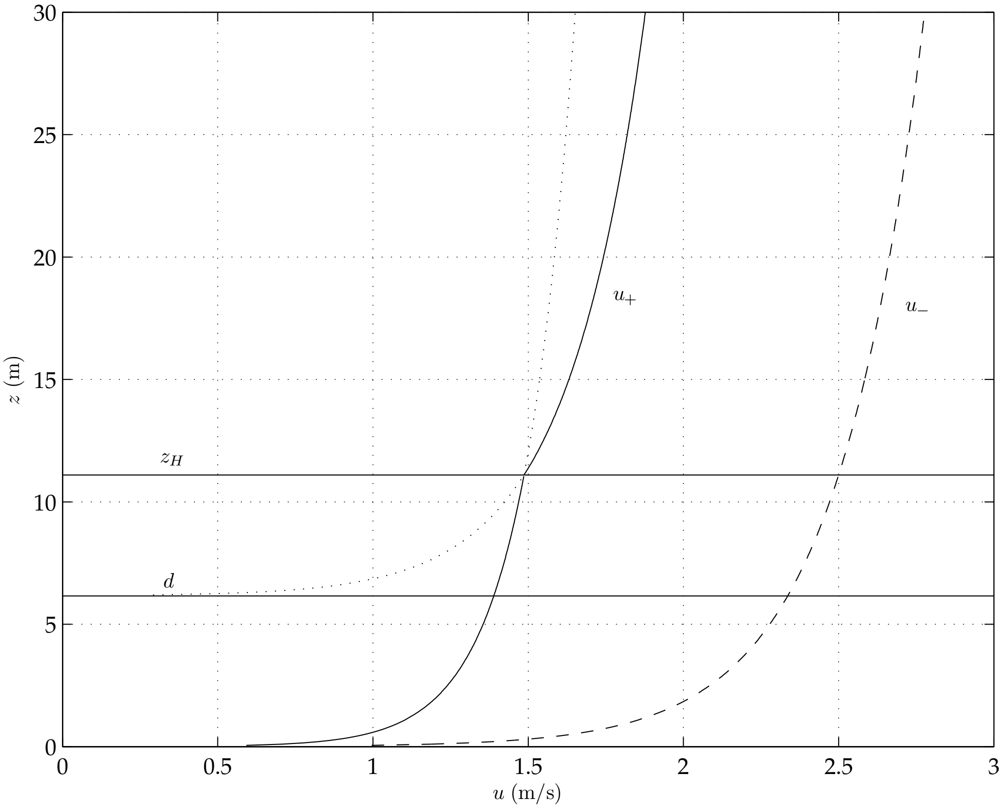

Figure 6.9: Velocity profiles in the undisturbed state and in balance with a large array of turbines, for the case where $c_d = 0.9$, $h = 30$ m, $u_{H-} = 2.5$ m/s, $z_{0-} = 1.4$ mm and $z_H/h = 0.37$

Figure 6.10 against λ for varying values of z_{0-} in the case where $h = 30$ m and $z_H/h = 0.37$. $c_d'\lambda$ is also plotted against λ in Figure 6.11 for convenience as this is the value that is supplied to a numerical model in order to calculate the added drag. It can be seen that in this model c_d' varies only weakly with z_0 in the range of λ of interest, which is reassuring where, as is usually the case, the sea-bed roughness length is uncertain.

6.10 Optimum spacing for maximum power from an array

Typically the area available for a tidal stream turbine array, A_a, will be limited by bathymetric, velocity or licensing constraints. In addition, the rated power of an individual unit will be limited by bathymetry (rotor size) and the power

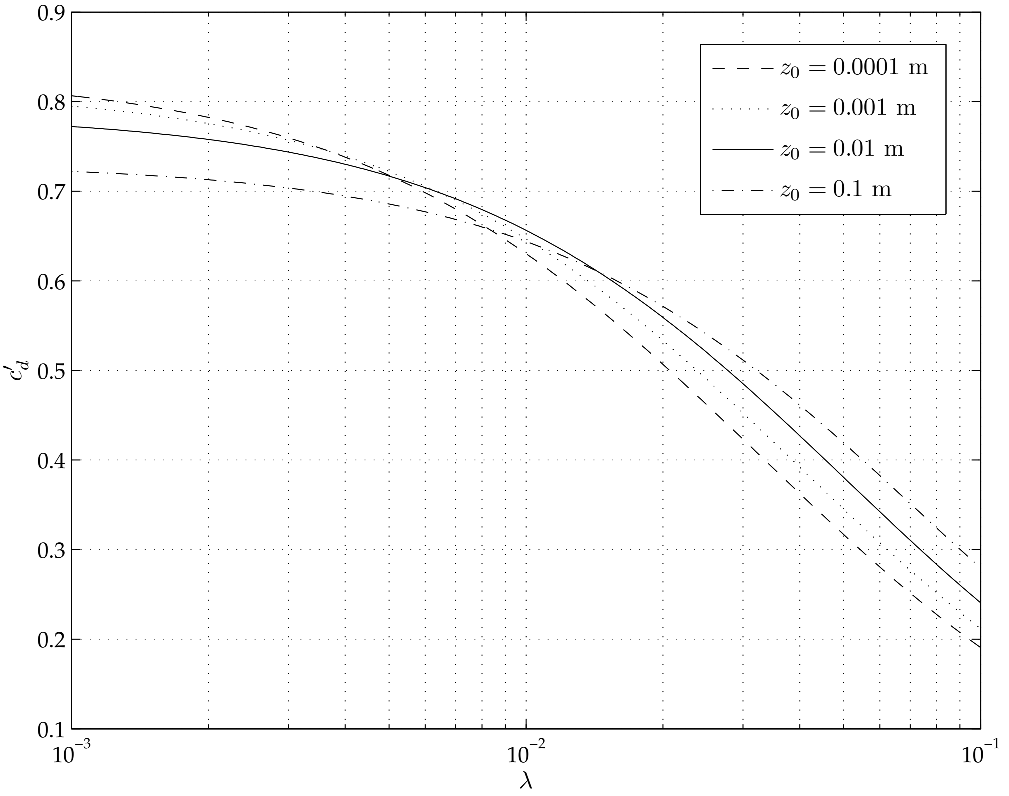

Figure 6.10: Variation of equivalent added drag coefficient with area ratio, for the case where $c_d = 0.9$, $h = 30$ m and $z_H/h = 0.37$, showing sensitivity to variation in sea-bed roughness length.

coefficient, both of which fall in a fairly narrow range. There will then be a trade-off between the number of turbines in the array and the power generated per turbine unit. It is then of interest to find what value of λ maximizes the power generated by the whole array, for a given flow speed in the natural state. If the model described above is applied to some finite area of sea A_a, the capture area of an individual rotor A_r is fixed and all the turbines in the array are generating with the same power coefficient c_p, then

$$P_a/P_- = \lambda \left(A_a/A_r\right) \left(u_{H+}/u_{H-}\right)^3 \tag{6.19}$$

Where the reference power of an isolated turbine $P_- = \frac{1}{2}\rho c_p u_{H-}^3 A_r$. This function is plotted against λ in Figure 6.12 for a range of values of sea-bed roughness length in the case where $h = 30$ m and $z_H/h = 0.37$.

For a concrete example, for the case where $c_P = 0.35$, $u_{H-} = 2.5$ m/s and $z_0 = 1.4$ mm, the model predicts a maximum power output of 3.2 MW/km^2 at an area density $\lambda = 0.0055$, giving $u_{H+} = 1.5$ m/s. For this bed roughness

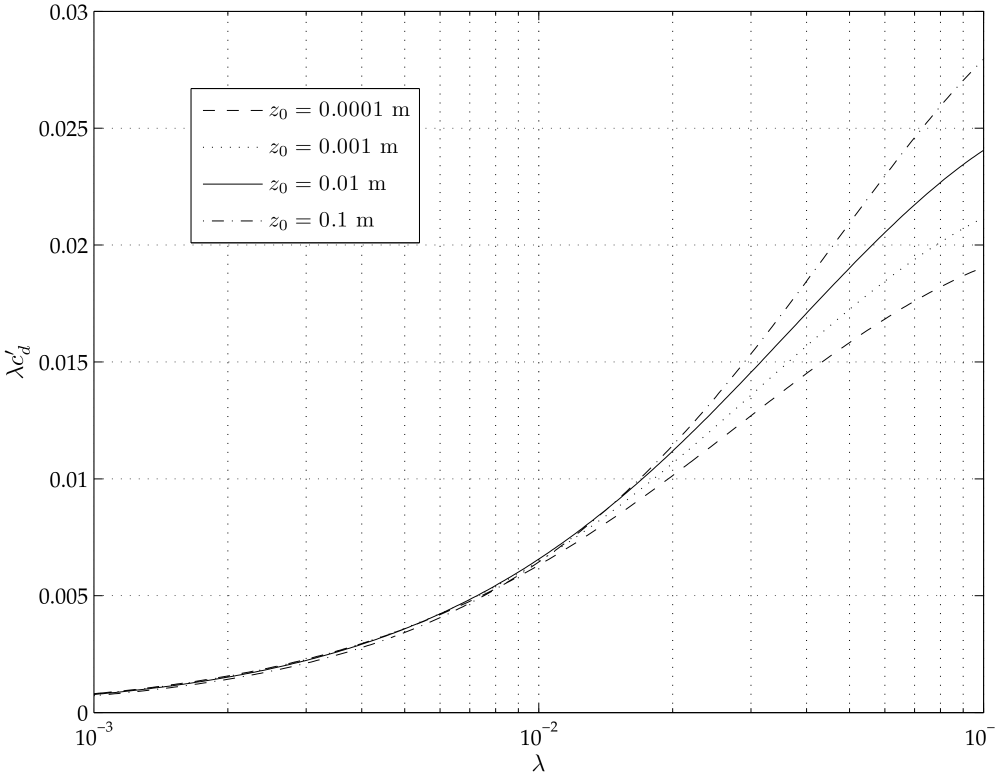

Figure 6.11: Variation of equivalent added area-averaged drag coefficient with area ratio, for the case where $c_d = 0.9$, $h = 30$ m and $z_H/h = 0.37$, showing sensitivity to variation in sea-bed roughness length.

value, the array power output does not vary too strongly with λ. Assuming a twin rotor unit, each rotor of diameter 16 m (equivalent diameter $D = 22.6$ m), this would imply an area of 73×10^3 m^2/unit provided by e.g. an equal ($L_x = L_y$) spacing of $12D$, which would be conservative from wind-turbine experience.

If the free-surface slope is allowed to increase when the array is present, the picture changes. For the case described above, P_a/P_- is plotted against λ for varying β in Figure 6.13. It can be seen that the right hand tail of the curve is pulled up, firstly resulting in a minimum, and then to the point where there are no extrema in the range of λ considered, as $\beta \to 1$.

The safest conclusion to draw is that the maximum power output from an array is sensitive to its coupling to the wider flow dynamics, reinforcing the case for site-specific modelling. It is important to note that the economic optimum will depend on the discounted income from power generation

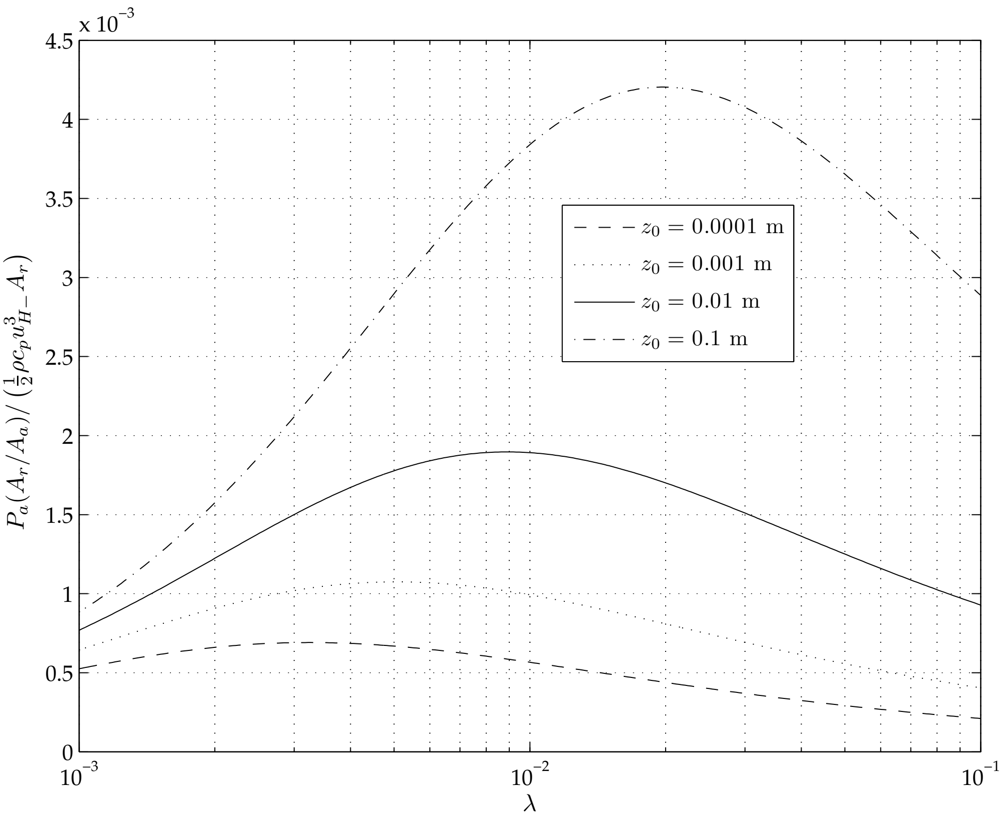

Figure 6.12: Variation in power per unit array area with frontal area ratio of turbines, for the case of constant free-surface slope, showing sensitivity to sea-bed roughness length. for the case where $c_d = 0.9$, $h = 30$ m and $z_H/h = 0.37$

compared to the overall capital expenditure, over a range of generating flow speeds, rather than simply maximizing the power output from the array at a single speed.

6.11 Discussion

This new model has been based on both previous theories applied to wind turbine arrays and analogies with rough-wall boundary layer obstacle flows, in particular that over submerged vegetation. In the latter, obstacle densities are in general much higher and flow separation around obstacles occurs. In the former, arbitrary assumptions are made concerning the distribution of drag in the vertical. Consequently, the new model should be regarded as a first step towards characterizing flow in large tidal arrays, highlighting the need for suitable experimental data for comparison.

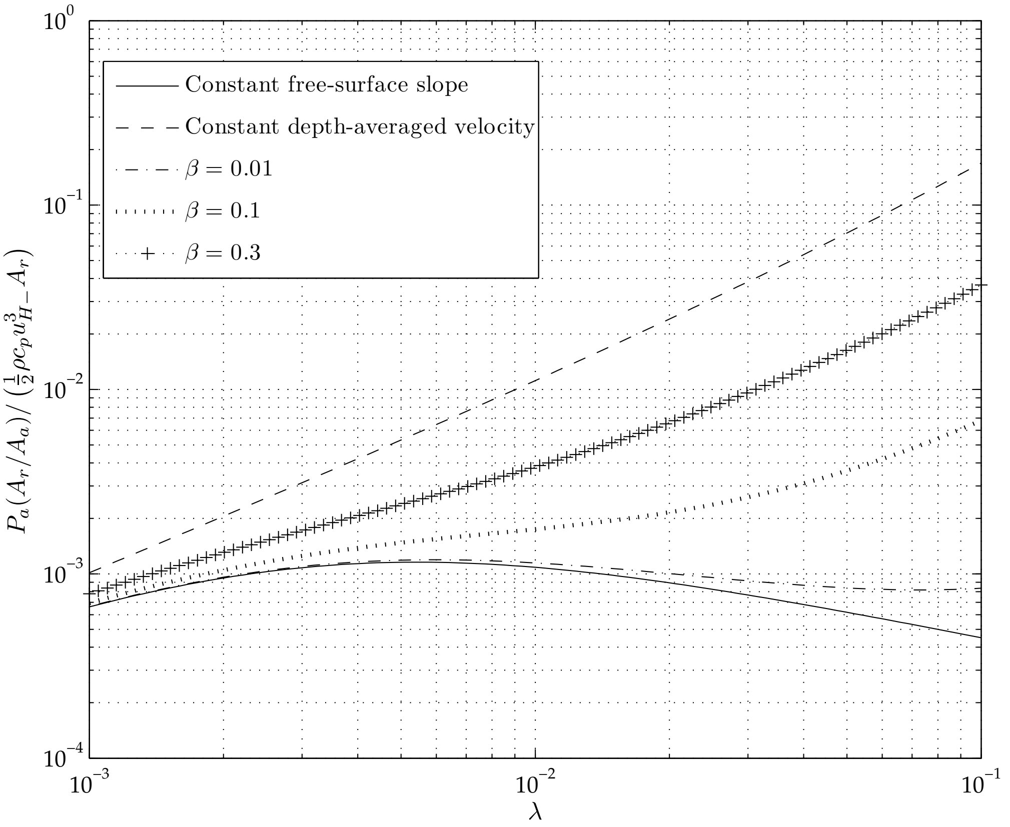

Figure 6.13: Variation in power per unit array area with area ratio, showing sensitivity to variation in sea-surface slope when turbines are present. for the case where $c_d = 0.9$, $h = 30$ m $z_H/h = 0.37$ and $z_{0-} = 1.4$ mm

The results of the previous equilibrium models applied to wind turbine arrays have indicated that they tend to give pessimistic estimates of the array efficiency when compared to experimental data (Milborrow 1980) and empirical finite array models (Builtjes and Milborrow 1980; Bossanyi et al. 1980). The results presented here in terms of hub-height velocity reduction for the case of constant free-surface slope lie at the pessimistic end of the predictions from the equilibrium wind farm models. This is for two reasons; firstly in the wind farm case the geostrophic wind speed is considered fixed whereas in the tidal stream case, the surface velocity may decrease. Secondly, an important difference between this model and previous wind farm models is the inclusion of the upward displacement of the spatially-averaged mean level of the momentum absorption, the zero-plane displacement d/h, significant for plausible array densities and depths. The cost of the inclusion of this parameter is an increase in algebraic complexity, which is justified by the need to take account of the large fraction of the depth taken up by the turbines.

The model highlights the need for more experimental investigation of:

- The flow profile above and below an array of turbines (or turbine simulators); does it maintain a logarithmic form? Or would other functions better represent the profile?
- The distribution of total drag resisting the flow, between the turbines and the bed, as a function of bed roughness and hub height.

The drag profiles may be inferred from the Reynolds shear stress profiles and the mean velocity profiles, measured several rows deep into an array of simulators. The total drag may also be estimated from the free surface slope; this is likely to be very small and in a laboratory may require special head amplification techniques for accurate measurement, for example using a light-oil inverted manometer.

6.12 Conclusions

1. A new model has been proposed for the velocity reduction in a large array of tidal stream turbines. It is the first time that such a model has been applied to tidal stream turbine arrays. An important difference between this model and previous models used for wind farm modelling is the inclusion of the upward displacement of the spatially-averaged mean level of momentum absorption, the zero-plane displacement d/h, which is significant for plausible array densities and depths.
2. An equivalent added drag coefficient, referred to the depth-averaged velocity and suitable for use in 2-D modelling has been derived and found to be insensitive (± 0.1) to the specification of bed roughness length over the plausible range of area density for tidal stream turbine arrays. This indicates that the model is numerically robust.
3. When the model derived here for an infinite-sized array was applied to a finite area, the values of inter-turbine spacing maximizing the power

output of the finite area were at the upper end of that found in wind turbine arrays. This indicates that the model is conservative, from the point of view of giving an upper bound on the magnitude of the effect of a real (finite) array on flow speed.

4. The parameter representing the bed friction coefficient in the array in comparison with the undisturbed case, α, is presently uncertain, but future experiments on arrays of simulators in the laboratory, with varying λ and z_{0-}, could help to determine α as a function of the other variables.
5. Application of the parameterization developed in this chapter within realistic numerical modelling domains of large extent (in comparison to the array), will help to determine whether the parameter β, the relative steepening in free-surface slope, varies significantly from zero. In this way, numerical modelling may feed-back into and constrain the semi-empirical model described here.

Chapter 7

Characteristics of tidal currents at three locations in the English Channel

7.1 Introduction

The work in this chapter relates to the first objective in § 1.2, namely evaluating the available tidal stream data at sites of interest in the English Channel. This involved developing a method of extracting tidal constituent ellipse properties from Admiralty tidal diamond data. For one location, raw current meter data was also available for analysis and the results were compared in terms of tidal constituent ellipse properties.

7.2 Methodology

7.2.1 Tidal data

Tidal stream time series of duration one year were generated using data included on Admiralty navigational charts at three locations in the English Channel: Portland Bill, the Race of Alderney and St. Catherine's Point (Isle of Wight). The locations were chosen to give a range of tidal stream velocities

Table 7.1: Metadata for Admiralty Tidal Diamonds and associated tidal elevation parameters for locations in the English Channel

	Portland Bill	Race of Alderney	St. Catherines Point	
Admiralty Chart diamond	2615 F	2669 E	2045 D	2045 F
Water depth (m)	30	34	30	34
Reference port	Devonport	St. Helier (Jersey)	Portsmouth	
Annual data file	2004	2003	1997	
Mean spring range (m)	4.75	9.75	4.10	
Mean neap range (m)	1.96	3.64	2.01	
Bad/missing data	None	None	None	

and swing upon flow reversal. The chart data, known as 'tidal diamonds' (due to the purple diamond symbol marked on the chart) give tidal stream speeds and directions for ±6 hours with respect to high water (HW) times at a reference port. Information about the tidal diamonds used is included in Table 7.1. For many locations, including Portland Bill and the Race of Alderney considered here, raw current meter records from hydrographic surveys are not publicly available (BODC 2007), so navigational charts (and associated tidal stream atlases) are the only source of field data on tidal streams. The main drawback of using tidal diamonds is that they were likely to be produced using short time series of 13–50 hours (Hydrographic Department 1965), and consequently rely on two sets of information known at the reference port in order to reproduce longer period variations: time of high water (HW) and tidal range (Pugh 1987, chap. 4:4:1).

Tidal ranges and tidal streams are physically connected through horizontal pressure gradients set up by phase differences in tidal elevation over an area of sea. The tidal stream speeds printed on an Admiralty chart give the rates at the times of mean spring and neap tidal range at the reference port. At a general time t, the rate is linearly interpolated between, or extrapolated from these rates using the average tidal range of that day. In this work, the tidal range has been taken at the HW closest to time t, in an attempt to re-introduce diurnal information into the tidal signal. In this case, depending on whether the HW occurs before or after t, the tidal range is calculated by subtracting the following or preceding low water (LW) elevation from the HW elevation.

Tidal stream rates derived from tidal diamonds strictly apply to the top 10 m of the water column; however, without vertical velocity profiles at the location it is not possible to state with certainty how the surface velocity relates to the

Table 7.2: Metadata for current meter records obtained from the British Oceanographic Data Centre for St. Catherine's Point

BODC reference	6369	6382
Year	1974	
Start date	6 August	
End date	4 September	
Duration (days)	29	
Sampling interval (min)	10	
Total number of records	4130	
Bottom depth (m)	32	
Meter type	Impeller	Impeller
Meter depth (m)	9.5	12
Bad/missing records	3	28

incident velocity across the rotor disk. An empirical profile may be chosen, but in the absence of other information, the characteristic velocity at the rotor disk will just be a constant fraction of the surface velocity. At St. Catherine's Point, raw current meter records were available at a point close (65 m nominal separation) to a tidal diamond (see Figure 7.1 for location and Figure 7.2 for a scatter plot of the raw data), which enabled independent comparison of tidal harmonic constituents analyzed at that location. The records were sourced from the BODC inventory (see Table 7.2 for details, also (BODC 2007)) and the measurements originally made by the then Directorate of Fisheries Research of the Ministry of Agriculture, Fisheries and Food (MAFF), Lowestoft, using a string of two impeller-type current meters on a mooring (Bedwell et al. 1975).

7.2.2 Time series reconstruction and analysis

For navigational purposes, HW times and tidal ranges at the reference port would be taken from printed tide tables or commercial software. For this work, it was considered desirable to start from raw sea level elevation data at the reference port, in order to keep track of the variance of the residual signal after tidal analysis. Tidal elevations from tide gauges at the reference ports of Devonport (for Portland Bill), St. Helier (Race of Alderney) and Portsmouth (Isle of Wight) were obtained from the National Tidal Sea-Level Facility (NTSLF) in the form of validated annual data files. The elevation data was analyzed using the TIRA program in the TASK 2000 package (Bell et al. 1999)

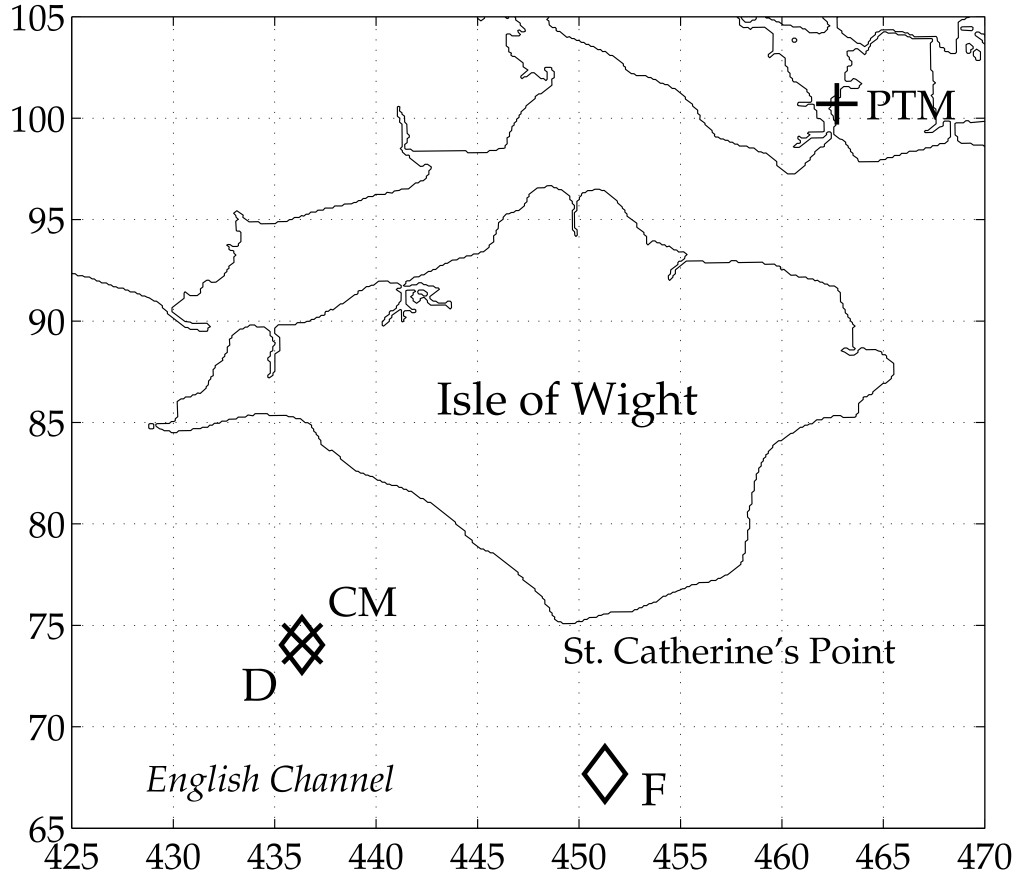

Figure 7.1: Location of current meter deployment (X); Admiralty Tidal Diamonds D and F (◇); and Portsmouth tide gauge (+). Eastings and Northings in km

into harmonic constituents and then the tidal signal for the same year was reconstructed from the constituents, with a smaller time step (one minute). This gave the original signal, with the surge (meteorological) component removed, making the usual assumption that tidal constituent amplitudes and phases are stationary over the period of observation (Pugh 1987, chap. 4:6). Another program in the TASK package (MARIEHL) was then used to pick out HW and LW times and elevations from the reconstructed signal. A smoothing window of 15–35 minutes was applied to ensure each HW/LW was followed by a LW/HW. With this data, it was then straightforward to calculate tidal ranges throughout the year and hence the mean spring and mean neap tidal ranges at the reference port.

The tidal stream speed and direction at the diamond location were then

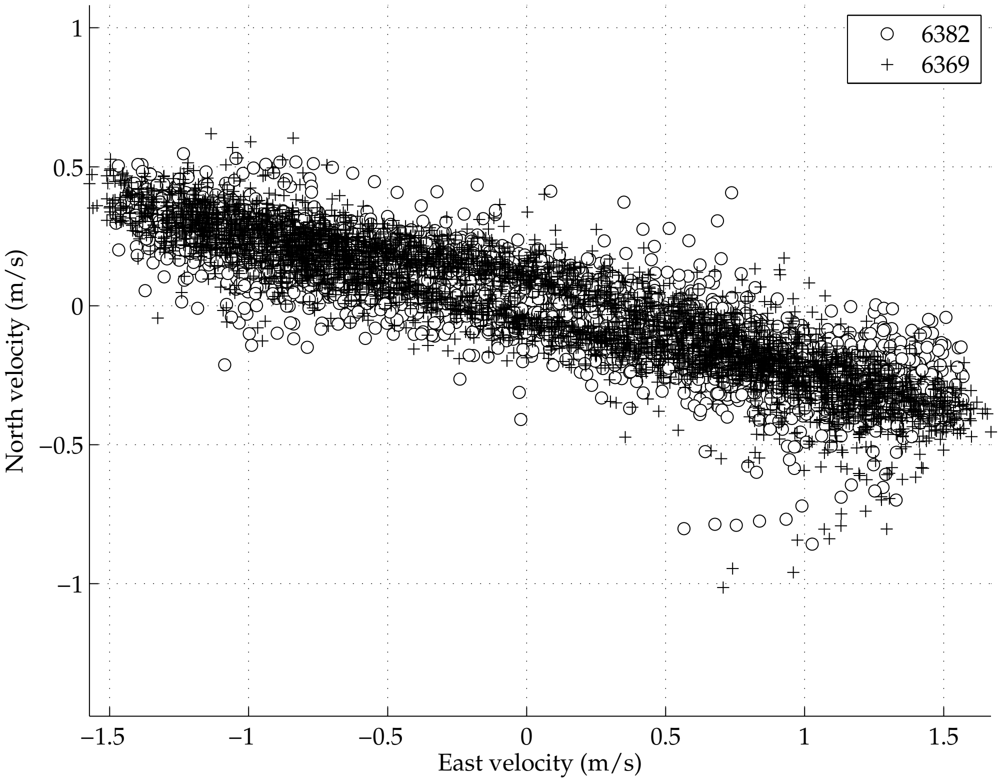

Figure 7.2: Scatter plot of raw current meter data for the two current meters deployed near St. Catherine's Point, Isle of Wight

calculated for each HW ±6 hours. These values were converted into Cartesian components u and v to avoid 360° jumps in direction and then interpolated onto an evenly spaced time vector. The velocity of the tidal stream at that point was then finally represented in complex form, $U = u + vi$. The T_TIDE package for MATLAB (Pawlowicz et al. 2002) was used to determine the constituent ellipse properties by harmonic analysis of the complex time series.

7.3 Results of tidal analysis

Three constituents derived from the analysis are presented in Table 7.3, in addition to the constant current component. The constituents are all semi-diurnal: the principal lunar (M_2), principal solar (S_2) and the larger elliptical lunar (N_2). The inclination is given in polar form, in degrees anticlockwise from East. There are a number of similarities between the analyses evident in Table 7.3. Firstly, reconstructing the signal from the three

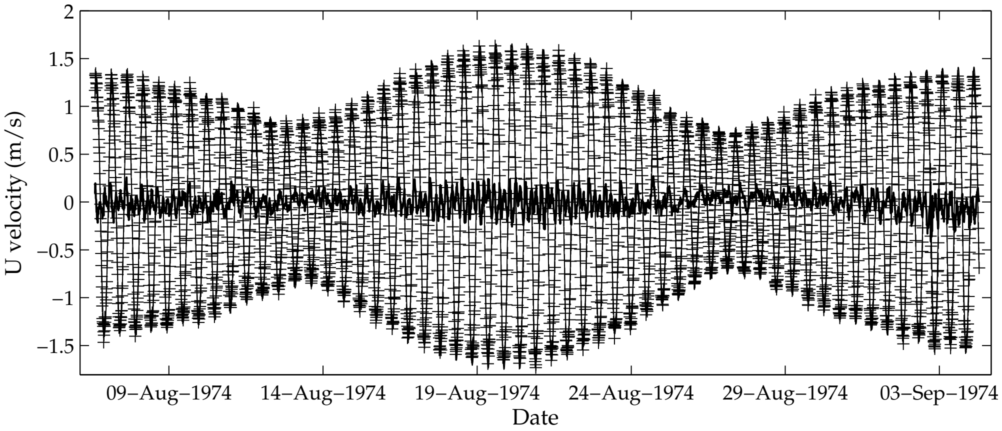

Figure 7.3: Comparison of raw data (+), signal reconstructed from harmonic analysis (thinner line) and residual (bold line) for current meter record 6369 deployed near St. Catherine's Point, Isle of Wight.

constituents mentioned above, plus the constant components, captured over 90% of the variance in the original signal when applied to both the current meter records and the reconstructed tidal diamond time series. Variance capture is defined as:

$$\varrho = \left(1 - \frac{\mathrm{var}(X - X_m)}{\mathrm{var}(X)}\right) \times 100\% \tag{7.1}$$

where X is the original time series of a variable and X_m is the modelled time series of that variable, in this case the sum of the three harmonic constituents and the constant current components. In all cases, the semi-minor axes of the constituent ellipses were always of similar magnitude to the residual signal, around 5% of the semi-major axis. To increase the variance capture to a uniform 97.5% across all the locations, extra constituents were included in the modelled time series, in order of major axis length, until this level was reached. These extra constituents are indicated in Table 7.4, from which it is clear that the most complicated tidal stream signal is at Portland Bill. For the current meter records at the Isle of Wight location, the raw and reconstructed time series for the velocity component resolved along the M_2 axis are included in Figure 7.3, showing the magnitude of the residual signal. The swing observed at Portland Bill was captured in the harmonic analysis by the constant current, a significant southerly flow of 0.8 m/s. This is a result of a well-known phenomena known as tidal rectification (Pingree and Maddock 1980), which results in an average constant circulation pattern around a

Table 7.3: Tidal stream parameters derived from harmonic analysis. AC indicates Admiralty chart, CM current meter measurements

			Portland Bill	**Race of Alderney**	**St. Catherines Point**			
			2615 F	2669 E	2045 F	2045 D	CM 6369	CM 6382
U_0		m/s	-0.17	-0.03	0.03	0.11	0.05	0.05
V_0		m/s	-0.82	-0.01	0.00	0.01	0.00	-0.01
M_2	$U_{\max}$	m/s	2.22	2.06	1.67	0.95	1.13	1.05
	$U_{\min}$	m/s	-0.06	0.10	-0.03	-0.03	-0.07	-0.06
	θ	°	10.0	55.1	171.9	167.8	165.6	167.4
	ϕ	°	194.3	199.3	39.7	35.0	37.5	44.3
S_2	$U_{\max}$	m/s	0.77	0.77	0.51	0.29	0.37	0.37
	$U_{\min}$	m/s	-0.03	0.04	-0.01	-0.01	-0.02	-0.01
	θ	°	10.2	55.2	171.9	167.8	164.9	167.0
	ϕ	°	250.6	248.4	80.9	76.7	83.1	90.6
N_2	$U_{\max}$	m/s	0.43	0.38	0.34	0.19	0.23	0.26
	$U_{\min}$	m/s	-0.01	0.02	-0.01	-0.01	-0.02	-0.02
	θ	°	9.9	54.9	171.9	167.8	168.0	167.8
	ϕ	°	183.2	180.6	18.1	13.4	7.2	7.9
ϱ		%	91.0	96.8	97.3	97.3	96.6	95.7

headland subject to oscillating tidal flow, and separation occurring at the headland. In addition, the presence of a large number of constituents with significant amplitude indicates the non-linear nature of the flows in the vicinity of the headland. At the other two sites, the constant component was very small and in all cases, the inclination of the semi-diurnal ellipses fell within $\pm 5°$ of that of the principal lunar constituent (M_2). The ratios of amplitudes of tidal constituents are observed to remain constant over wide areas of sea (Pugh 1987, 5:4:3), as the tidal forcing falls in narrow bands of frequency and the seas respond smoothly. This can be demonstrated for the English Channel by observing the similarity in spatial distribution of tidal amplitudes in the semi-diurnal band (Howarth 1990).

Consequently, the major axes of the constituents derived from the analysis of the current meter records were plotted in Figure 7.4 against those derived from tidal diamond D (St. Catherine's Point), a nominal distance of 65 m from the

Table 7.4: Extra constituents included to increase variance capture to 97.5%. Values refer to major axis length (m/s). (Isle of Wight (IoW) constituents were selected for inclusion by rank in current meter analysis.)

	μ_2	K_2	M_{sf}	M_4	$2\mathrm{MS}_6$	M_6	$2\mathrm{N}_2$	MS_4	ν_2	L_2	λ_2	M_{m}	$2\mathrm{MN}_6$
PB	0.24	0.23	0.22	0.21	0.19	0.16	0.14	0.14	0.14	0.13	0.10	0.09	0.08
RA		0.22											
IoW	0.05	0.15								0.09			

current meter location (This may have been affected by previous co-ordinate system conversion and rounding prior to obtaining the data set) and 25 km from tidal diamond F. There was a good linear fit (with zero y-intercept), with a slope of 0.86 and 95% confidence interval of ±3% of major axis length. The agreement in phase and inclination was close in both cases (see final three columns of Table 7.3). The causes of the discrepancy in major axes are unknown: possible explanations are local changes in depth due to difference in horizontal position; instrument error; the effect of the meteorological component on the original tidal diamond measurements or the error introduced by the tidal diamond method of predicting tidal streams itself. A conservative estimate of the uncertainty in the constituent major axes derived from tidal diamonds at this location would therefore be ± 14%. If it were assumed that the linear factor of the discrepancy was deterministic, then a more optimistic estimate would be ±3%.

7.4 Conclusions

Tidal stream data has been analyzed from three of the most promising locations for siting turbines in the English Channel. At St Catherine's Point, reasonable agreement was found between a harmonic analysis of current meter records and analysis based on navigational data (tidal diamond) at the same location. A pessimistic estimate of the error in constituent ellipse major axis length was found to be 14%. For all three sites and for both current meter data and navigational data, the variance capture was over 90% when only the three major semi-diurnal constituents were included, in addition to the constant components. The latter were only of significance at Portland Bill, which is subject to flow separation and tidal rectification.

The tidal stream data analyzed in this chapter were subsequently used as

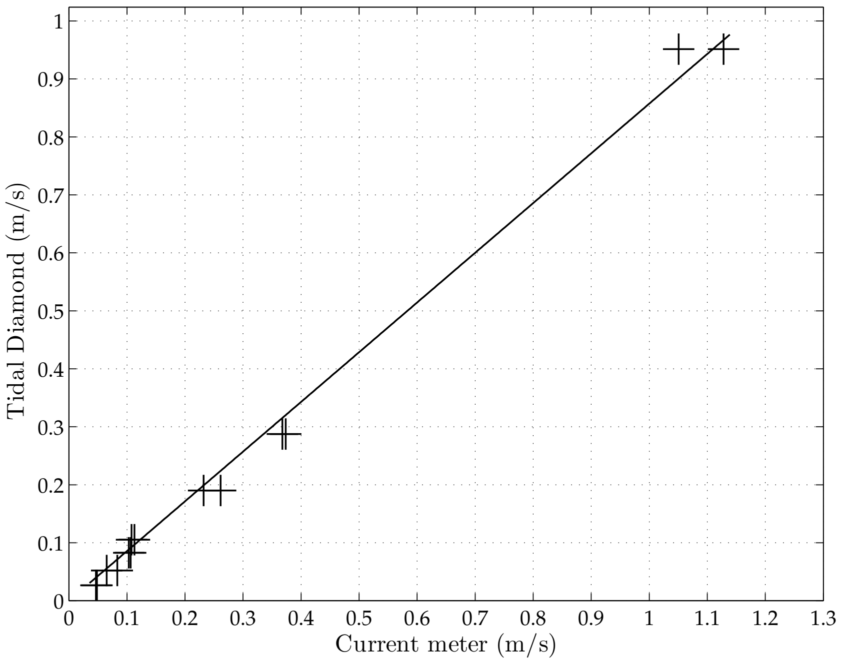

Figure 7.4: Major axes lengths for constituents analyzed from raw current meter data versus analysis of Admiralty tidal diamond D

input for a program written to estimate and compare the energy yield over the 18.6 year nodal cycle at the three sites; the full paper is included in Appendix H (Blunden et al. 2008). Previously-obtained experimental data on the variation of power coefficient with yaw angle (Bahaj et al. 2007a) were used to compare the energy yield from fixed-orientation and yawing turbines. This was in contrast to previous assessments of tidal energy, reviewed in Chapter 2, where in general the assumption was made that any deviation from rectilinearity of the flow would have no effect on the energy extractable by tidal generators at the site, as would be the case for vertical axis turbines or yawing horizontal axis turbines. One report (ETSU 1993) did include a simple correction, but it was not based on theoretical or experimental results and therefore was of limited validity.

Blunden et al. (2008) found that even at Portland Bill, with the most non-rectilinear tidal streams (and additional constant current) the proportion of power lost by fixing the orientation at the optimum (85°) was 15% when compared to a yawing design. For the Race of Alderney and the Isle of Wight, lying in areas with simple rectilinear tidal flows, the power loss at optimum orientation was negligible compared to a varying design. These results imply that the economic benefit gained from a continuously yawing device may be rather small when compared to a simpler fixed-orientation design, either with blade pitch angle rotated through 180° at slack water, or with symmetrical blade profiles.

Chapter 8

Modelling the tidal dynamics of the English Channel

8.1 Introduction

The principal reason for including this chapter in the thesis is to describe the broader context of the tidal dynamics of the English Channel. The results of this model were ultimately not used to input into local sub-models of tidal sites in Channel Islands as originally intended. However, the work may be of use to those intending to model the English Channel and similar shelf sea areas, indicating the difficulties involved and recommending how to improve the model in future.

The purpose of the work undertaken was originally to produce a validated finite element model of the English Channel, primarily to provide input boundary conditions for local models of potential sites for tidal stream power development: the Race of Alderney and Portland Bill.

8.2 Data

The bathymetric data used for mesh generation was abstracted from the digitized 1-minute grid of the General Bathymetric Chart of the Oceans (GEBCO), with a nominal resolution of 1 m in the vertical. Figure 8.1 shows the portion of the GEBCO grid along with the locations of the coastal tide gauges used in the study. The GEBCO grid is primarily intended for study of the deep oceans and the metadata for shelf areas is incomplete; it is not clear whether the depths are with respect to local Chart Data, or corrected to form a seamless data-set. It was assumed that the geographic co-ordinates are with respect to the WGS-84 spheroid. There are a number of anomalous features present in Figure 8.1: the western end of the Solent is closed off; the Channel Islands are poorly resolved; there is a clear artifact at the western end of the Channel where two data-sets have been joined together. The 'dimples' that appear across the data-set are likely to be artifacts introduced by spline interpolation. The coastlines were derived from the World Vector Shoreline (WVS), which claims 90% of shoreline features are located within 500 m of their true geographic position with respect to the WGS-84 datum. Both the GEBCO and the WVS are in the public domain (IOC et al. 2003).

Tidal elevations from tide gauges along the English coast of the English Channel and in the Channel Islands were obtained from the National Tidal Sea-Level Facility (NTSLF) in the form of validated annual data files. Elevations from French tide gauges were obtained from SONEL, also in validated data files, but not necessarily spanning only one year. Quality control information for the records used is included in Table 8.1. This shows that the tidal data used is of high quality and capable of fulfilling both Nyquist and Rayleigh criteria, being able to resolve in the frequency domain all relevant harmonic constituents (Pugh 1987, 4:2:5).

8.3 Pre-processing

8.3.1 Tidal elevation harmonic constituents

The Tidal Analysis Software Kit (Bell et al. 1999) was used to decompose a year of elevation data into a set of 62 harmonic constituents; constituents with amplitude generally greater or equal to 5 cm at Dover, Calais, Newlyn and Le Conquet are included in Table 8.2.

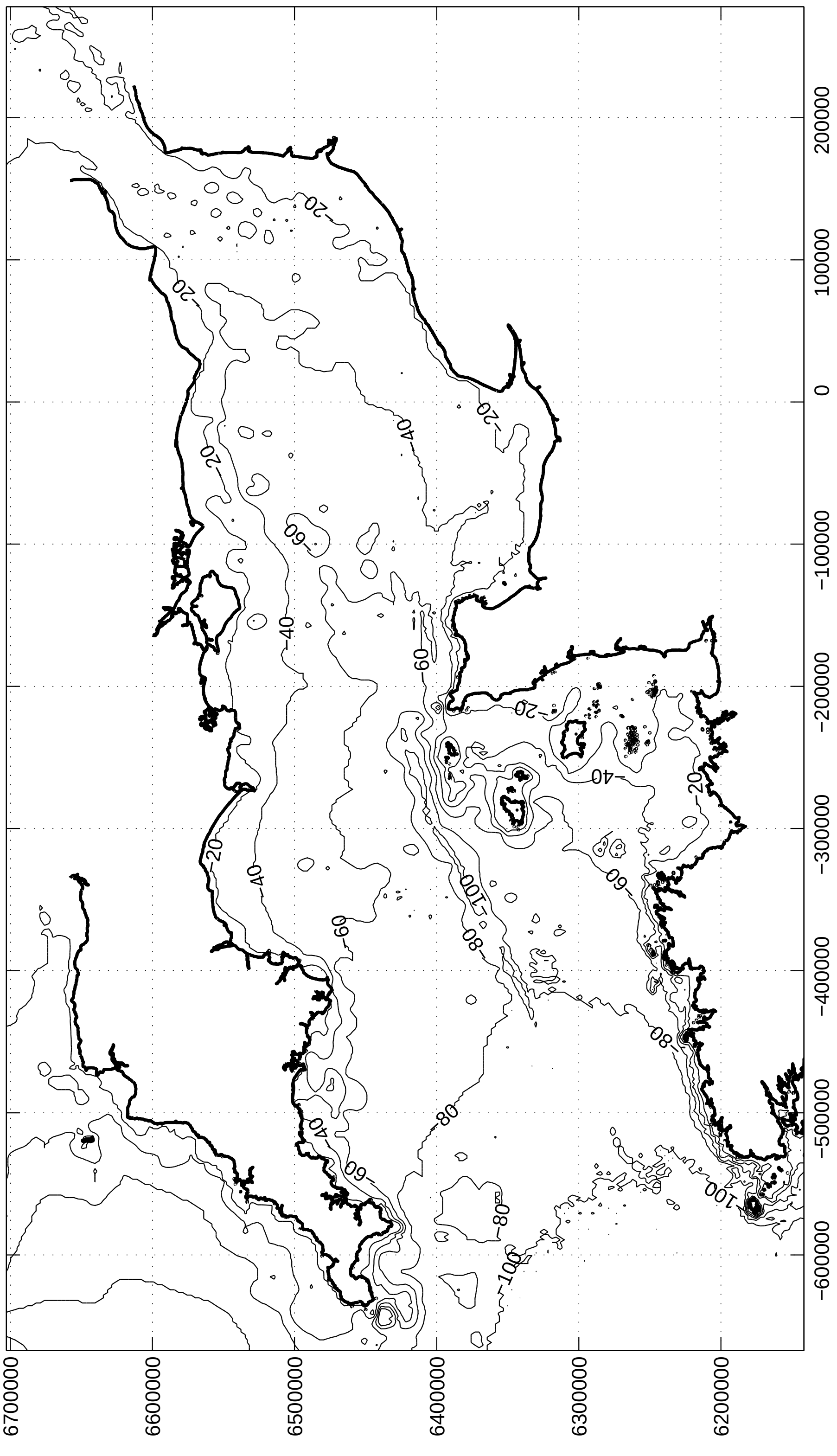

Figure 8.1: Portion of GEBCO one-minute grid used to generate mesh. Depths in m. Figures in brackets next to tide gauge locations refer to mean spring tidal range.

Table 8.1: Quality control data for tide gauge records used in harmonic analysis

Port	Years	Span (days)	Sampling interval (min)	Completeness (%)
Boulogne-sur-Mer	1990–1991	390	60	93.5
Bournemouth	1999	365	15	100
Calais	2002	365	60	97.8
Cherbourg	2003	365	60	100
Devonport	2004	366	15	100
Dover	2004	366	15	100
Le Conquet	2002	365	15	97
Le Havre	2004	366	60	100
Newhaven	2004	366	15	100
Newlyn	2004	366	15	100
Portsmouth	1997	365	15	100
Saint-Malo	2003–2004	356	60	99.6
St. Helier (Jersey)	2003	365	60	100
Weymouth	2004	366	15	100

Table 8.2: Amplitudes (cm) and phases (°) for constituents with amplitude generally greater than 5 cm. See §3.3 for details of tidal constituents.

	Eastern boundary				**Western boundary**			
	Calais		**Dover**		**Le Conquet**		**Newlyn**	
	H (cm)	ϕ (°)	H (cm)	ϕ (°)	H (cm)	ϕ (°)	H (cm)	ϕ (°)
S_a	7.9	258	6.4	214	8.9	252	6.4	197
O_1	5.0	138	5.6	176	6.5	324	5.3	342
K_1	1.4	54	5.0	34	6.6	73	6.5	109
$2N_2$	3.4	347	9.0	268	6.0	80	5.4	76
μ_2	9.6	66	8.7	48	7.8	101	5.3	170
N_2	45.8	317	41.3	309	41.2	91	33.1	114
ν_2	10.9	308	9.9	307	7.7	88	7.2	106
M_2	249.4	340	226.5	331	202.1	110	171.7	133
λ_2	5.9	338	5.9	324				
L_2	19.5	348	9.7	337	7.7	94	5.8	137
S_2	78.4	32	71.5	23	73.6	150	57.9	177
K_2	23.3	31	20.6	20	21.2	147	16.6	175
$2SM_2$	5.1	240	5.1	221				
MN_4	10.1	209	9.1	198				
M_4	25.1	237	26.4	219	7.1	135	11.4	165
MS_4	15.9	291	16.9	272	5.2	191	7.5	218
M_6	6.0	128	6.7	101				
$2MS_6$	5.8	177	6.8	147				

8.3.2 Mesh generation

The bathymetry was initially projected from geographic co-ordinates into regular Mercator co-ordinates. The TÉLÉMAC system requires co-ordinates in this projection for large domains where the curvature of the earth is significant. At the start of a computation, the co-ordinates are multiplied by a local latitude-dependent scale factor.

The triangulated irregular finite-element mesh (Figure 8.2) was created using the TÉLÉMAC pre-processor MATISSE. The element side length varies from 1.9 km at the coastline to 6 km in deeper areas (deepest around 115 m). This enables good reproduction in the mesh of the coastline geometry. Areas with difficult geometry were smoothed and the element side length reduced down to 1 km. The mesh contains approximately 24000 nodes generated from approximately 37000 input gridded bathymetric data points. Five islands are included in the mesh: the Isle of Wight, Jersey, Guernsey, Sark and Alderney. The Channel Island of Herm and other small islands in the domain (<1 km) were too small to be resolved efficiently.

8.4 Numerical model

The TÉLÉMAC system was used to construct a numerical model according to the methodology described in §5.2, where the choice of open boundary conditions are discussed in §5.2.2.2. The model was driven by imposed elevations along the two open boundaries, extending between Le Conquet and Newlyn at the western end ($1 \rightarrow 2$ on Figure 8.2) and Dover and Calais at the eastern end ($3 \rightarrow 4$ on Figure 8.2).

Amplitudes and phases of all harmonic constituents with amplitude greater than or equal to 5 cm were linearly interpolated between the two pairs of tide gauge locations. Nodal factors f and u were calculated at the beginning of the simulation period and the astronomical argument V was recalculated each day. The imposed elevation was implemented by a user-supplied subroutine, included in Appendix C.5.

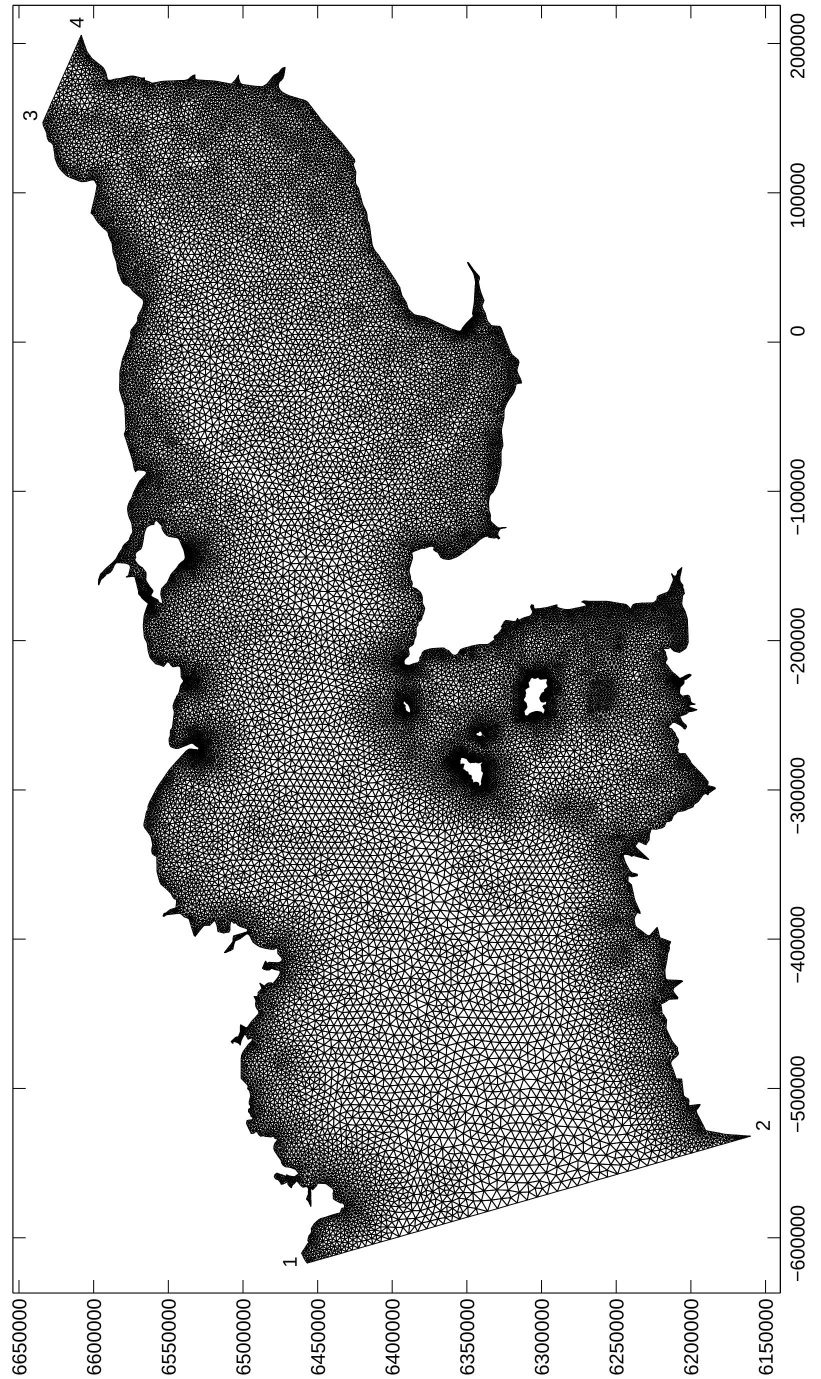

Figure 8.2: Finite element mesh used for English Channel tidal simulations. Regular Mercator coordinates (m)

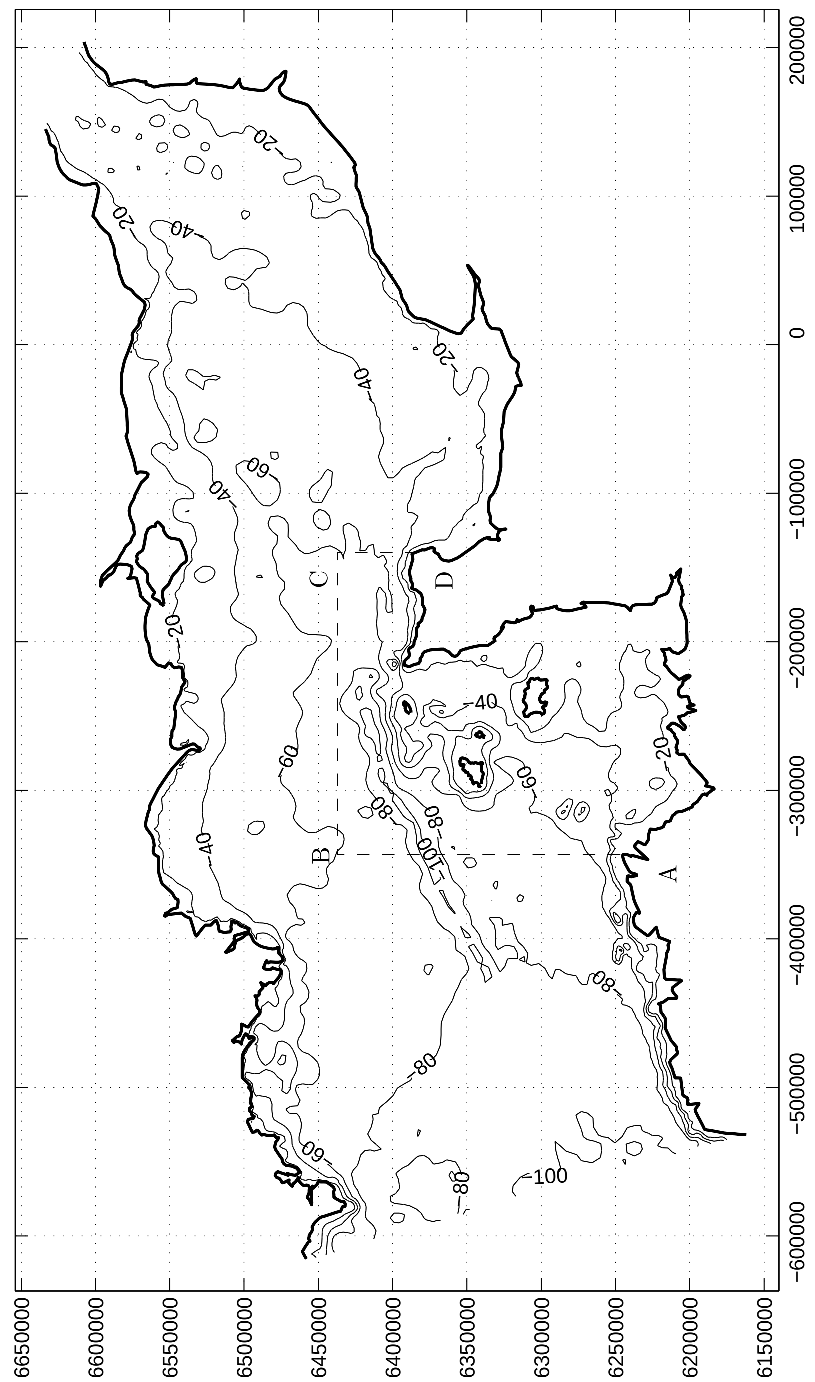

Figure 8.3: Bathymetry of finite element mesh used for English Channel tidal simulations. Regular Mercator coordinates (m)

8.4.1 Model parameters

Bed friction was given by the Strickler formula with a spatially-uniform coefficient of 35 $\mathrm{m}^{\frac{1}{3}}/\mathrm{s}$, and the k-ϵ closure method was used for turbulence modeling. The Coriolis acceleration term was included in the hydrodynamic equations due to the scale of the domain (extent $>> 10$ km). Tide-generating potential was also included in the model; however it was shown in §3.3 that this is a minor effect in this region of the continental shelf.

8.5 Results and discussion

The model was run for a total simulated time of one month - long enough to separate the M_2 and S_2 constituents in the results by harmonic analysis applying the Rayleigh criterion. The harmonic analysis of the results used a 'related constituents' approach (Pugh 1987) to determine the more finely separated constituents: $2N_2$, ν_2, λ_2, K_2. The amplitude ratios and phase lags for these related constituents were derived from the annual analyses of the observed values. Figures 8.4(e)–8.5(b) show the constituents as derived from the tide gauge data (red)—the true values—compared with those derived from the simulation results for the M_2 and S_2 tidal constituents at the closest node locations within the model mesh (blue).

The results are variable in their agreement with the coastal gauges; the errors are generally lower on the French side and most significant in amplitude close to the degenerate amphidrome (near to Bournemouth and Weymouth) where the tidal ranges are very small (<2 m) and non-linear effects dominate. This is similar to that reported in a previous model of the English Channel (Le Provost and Fornerino 1985). The errors in phase increase in the English coast towards the eastern end of the English Channel. The behaviour of the semidiurnal tidal waves is complicated in this area, indicated by the fact that Newhaven is slightly ahead of Portsmouth in phase (Figures 8.5(d) and 8.5(e)). The phase errors imply the eastern forcing boundary is inadequate for reproducing these complex tides. To improve the model, the boundary would be drawn further up into the North Sea, to allow the local dynamics to develop.

The errors at Cherbourg and St. Malo are comparatively low, with this in mind the amplitudes and phases along boundary ABCD (Figure 8.3) for the local model are presented in Figures 8.5(a) and 8.5(b) as an example of how the Channel model could be applied in tidal resource assessment. The M_2 and S_2 parameters for sea-surface elevation, U and V velocity components will be used to drive the local model. Figures 8.5(a) and 8.5(b) also illustrate the smoothness of elevation parameter variation, as a scalar quantity, when compared to the variation of that of the velocity components. A source of error in the model is the linear distribution of tidal constituent amplitudes and phases along the open boundaries. Comparison with co-tidal charts in the literature (Howarth 1990) shows that the distribution is a more complex shape.

Optimization of the friction coefficient as a function of space to minimize error over the simulation period is possible using the TÉLÉMAC system, but has not yet been attempted. This would be likely to yield better results than using a single estimated friction coefficient for the whole domain. This could be given a physical basis if the domain were divided into zones depending on the nature of the sea-bed. However, this has not been attempted in previous models that have still achieved reasonable results; therefore accuracy of bathymetry and tidal forcing at the boundary must be the most important factors in minimizing errors in the domain. The bathymetric data-set could be improved by inclusion of higher resolution data in coastal areas with better documentation of the datum of soundings or process used to create a seamless data-set (in the case of the GEBCO bathymetry).

8.6 Conclusions

A two-dimensional finite-element model of the English Channel has been produced using the TÉLÉMAC system. The model was driven by imposed elevations on its two open boundaries, calculated from harmonic constituents. The results were analyzed by standard harmonic method at the locations of tide gauges within the domain and the results compared with observed data. This indicated a reasonable phase agreement at tide gauges with large tidal range, but poor agreement at gauges with low tidal range.

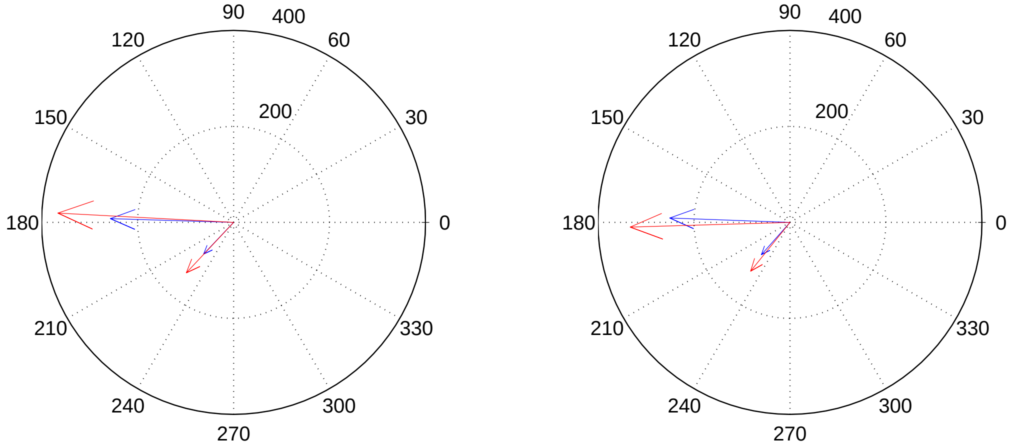

(a) Saint Malo

(b) Jersey

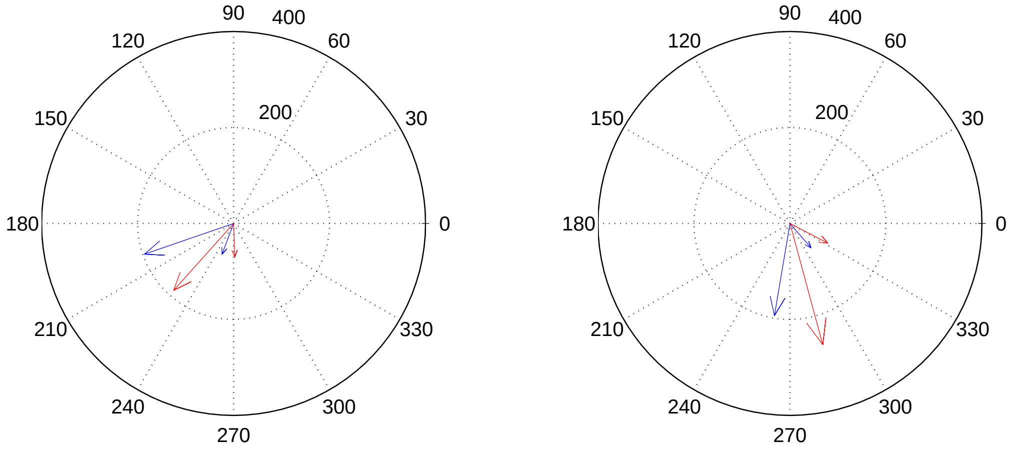

(c) Cherbou

d) Le Havre

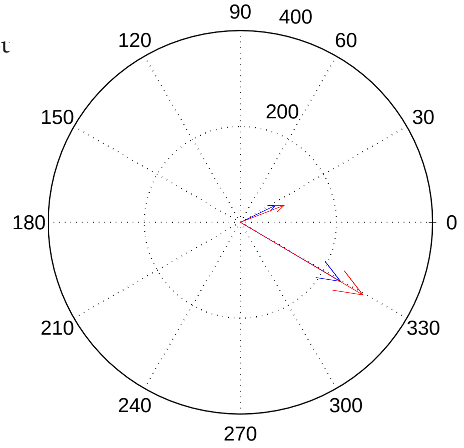

(e) Boulogne

Figure 8.4: Amplitude (cm) and phase (degrees) of M_2 and S_2 elevation constituents at tide gauge locations along French coast of English Channel (Figure 8.1), expressed in polar form and in order of phase progression. Red arrows were analyzed from tide gauge data, model results in blue.

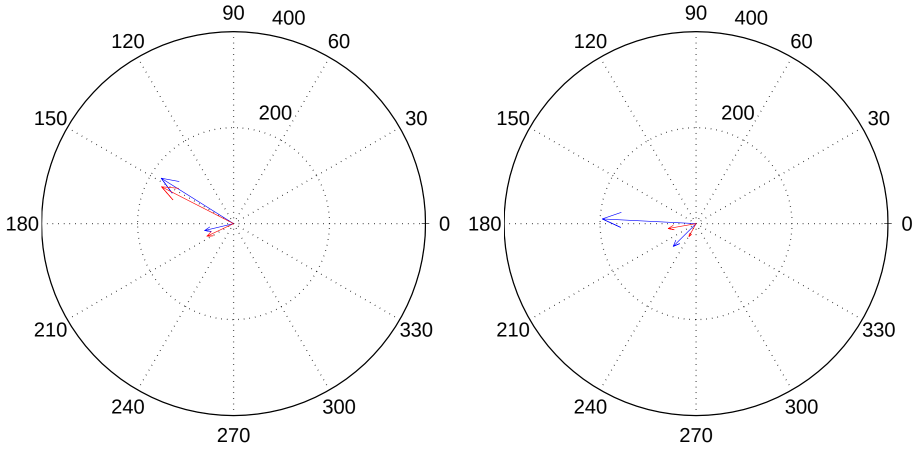

(a) Devonport

(b) Weymouth

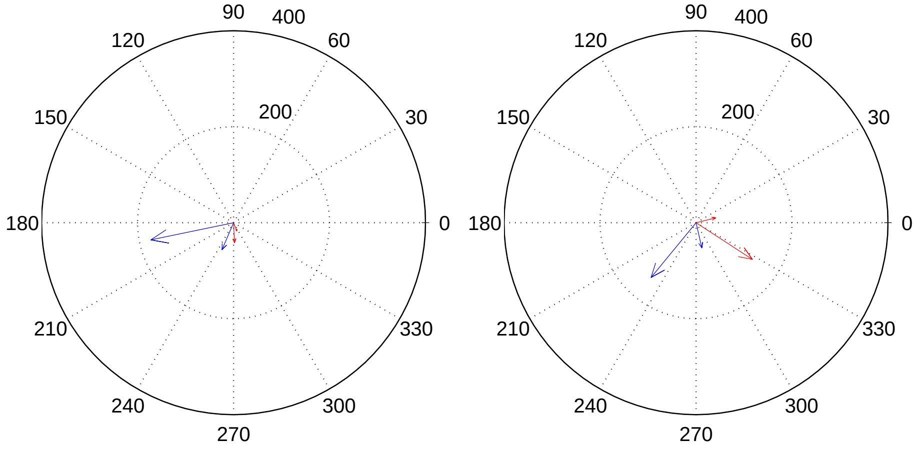

(c) Bour

tsmouth

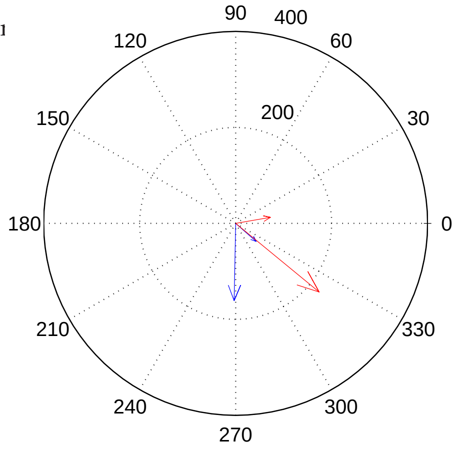

(e) Newhaven

Figure 8.4: Continued; English coast

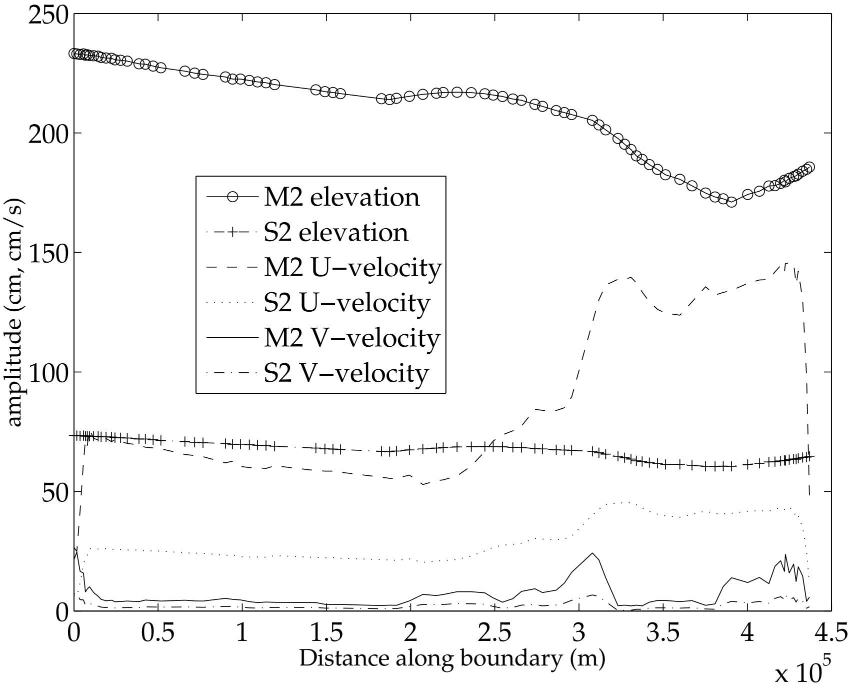

(a) Amplitude

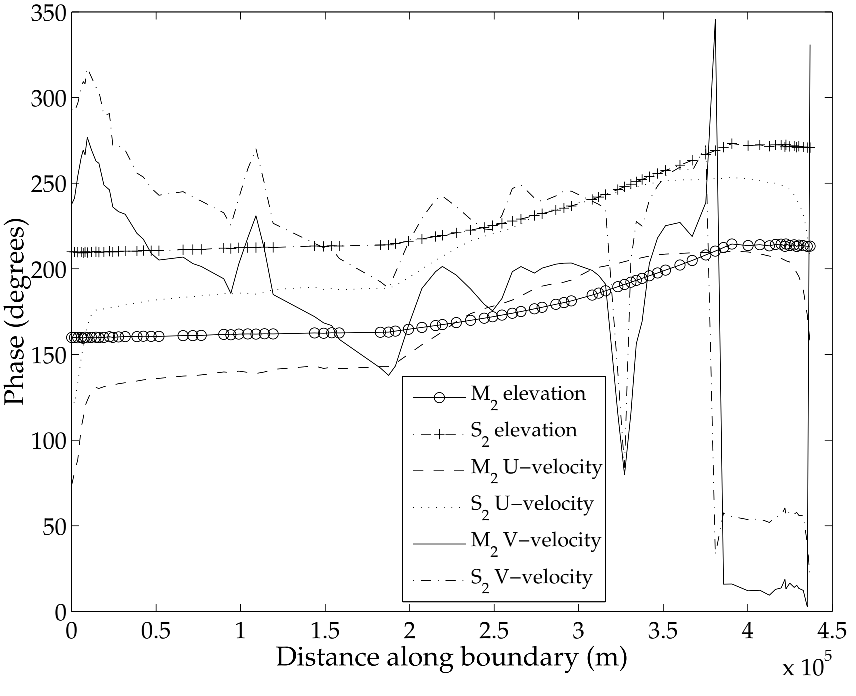

(b) Phase

Figure 8.5: Variation of tidal parameters of the two main semidiurnal harmonic constituents with distance along boundary ABCD

To develop the model further, the western boundary would be extended to the shelf edge and boundary conditions would be taken from a global solution. This would provide a driving boundary independent of the tide gauge data within the domain and inconsistencies in velocity and elevation introduced at the boundary would attenuate as the oscillations propagate into the interior of the modelling domain. The eastern boundary would be extended well into the North Sea for the same reason.

The decision was made not to develop the English Channel model further was made for the following reasons:

1. There was not sufficient time nor bathymetric data available to produce a detailed local model of the Channel Islands region, for which the English Channel model was intended to provide boundary conditions.
2. The bi-linear interpolation between tide gauges applied in the Portland Bill model (§9.2) gave results of satisfactory accuracy, when adjusted to fit elevations at Weymouth. Consequently, the additional effort of re-imposing the boundary conditions externally from the English Channel model was not considered worth spending time on
3. Further improvement of the accuracy of the English Channel model would not justify the time investment required, given that numerical models of the English Channel have been produced previously and that simulation of the Channel tides is not the main focus of the work as a whole.

Nevertheless, the agreement between simulation and tide gauge data was reasonable in the Normandy-Brittany Gulf and the model could be used as basis for future detailed modelling of the complex tidal flows in the region.

Chapter 9

Portland Bill: model development and site selection

9.1 Introduction

Two assessments of the tidal stream energy resource at Portland Bill have been made in the ETSU (1993) and European Commission (1996) reports; both of these estimates involved the selection of a possible area of sea for exploitation. The reports have been discussed previously in Chapter 2 and have been superseded by a more recent assessment (Black and Veatch Consulting Ltd 2004), but the site dimensions used in the earlier reports were carried forward into the new report. The ETSU 93 report selected sites on the basis of peak mean spring tidal stream speed $\overline{U_S}$ greater than 4 knots (2 m/s), as indicated on an Admiralty chart, with minimum water depth 20 m. The EC 96 report did not specify a minimum depth, but stated that sites were selected using four points with $\overline{U_S}$ greater than 1.5 m/s. The purpose of the work described here is to investigate the selection of site boundaries at the Portland Bill site using simulation results of the flow in the natural state (simulation of energy extraction is included in Chapter 10), and compare with the results from these previous reports.

Table 9.1: Finite element meshes used in model

Mesh	**1**	**2**	**3**	**4**	**5**
Nominal node separation (m)	1000	500	400	300	250
Number of nodes ($\times 10^3$)	2.2	8.2	12.6	22.2	31.9
Number of elements ($\times 10^3$)	4.1	16	24.7	43.7	62.9
Wall time for 1 month simulation $\approx$ (hr)	1	6	10	26	34

9.2 Methodology

The bathymetry used in the model was derived principally from two data-sets originally digitized by A. Bastos (Bastos et al. 2003b), from UK Hydrographic Office sounding sheets, having horizontal resolution of approximately 1 km and 50 m, respectively. The raw bathymetry data-sets were overlaid, with higher resolution datasets replacing lower resolution points where required, to provide a master data-set (Figure 9.1). In practice, this proved to be too many input points for the TÉLÉMAC pre-processor to cope with—perhaps due to an integer overflow—and so the master data-set was interpolated onto a grid and then converted to contours, maximizing the information retained in the input points.

To investigate the sensitivity of the results to varying finite element size, meshes of increasing density were used, with a target mesh node separation distance for the triangulation process varying from 1 km in the coarsest mesh down to 250 m in the finest mesh. Information on the meshes are summarized in Table 9.1 and Figure 9.2 shows a close-up view of the portion of the meshes close to the tip of the headland.

The model was forced by imposing elevations at each time step at the open boundary nodes, synthesized from the fourteen most significant harmonic constituents. Tidal elevation data were obtained from the National Tidal Sea-Level Facility (NTSLF 2006) in the form of quality-controlled annual data files. All three files were complete and without any bad or missing data; the years covered were 2004 (Devonport), 2004 (Weymouth) and 1999 (Bournemouth). The sample interval was 15 minutes in all cases. The

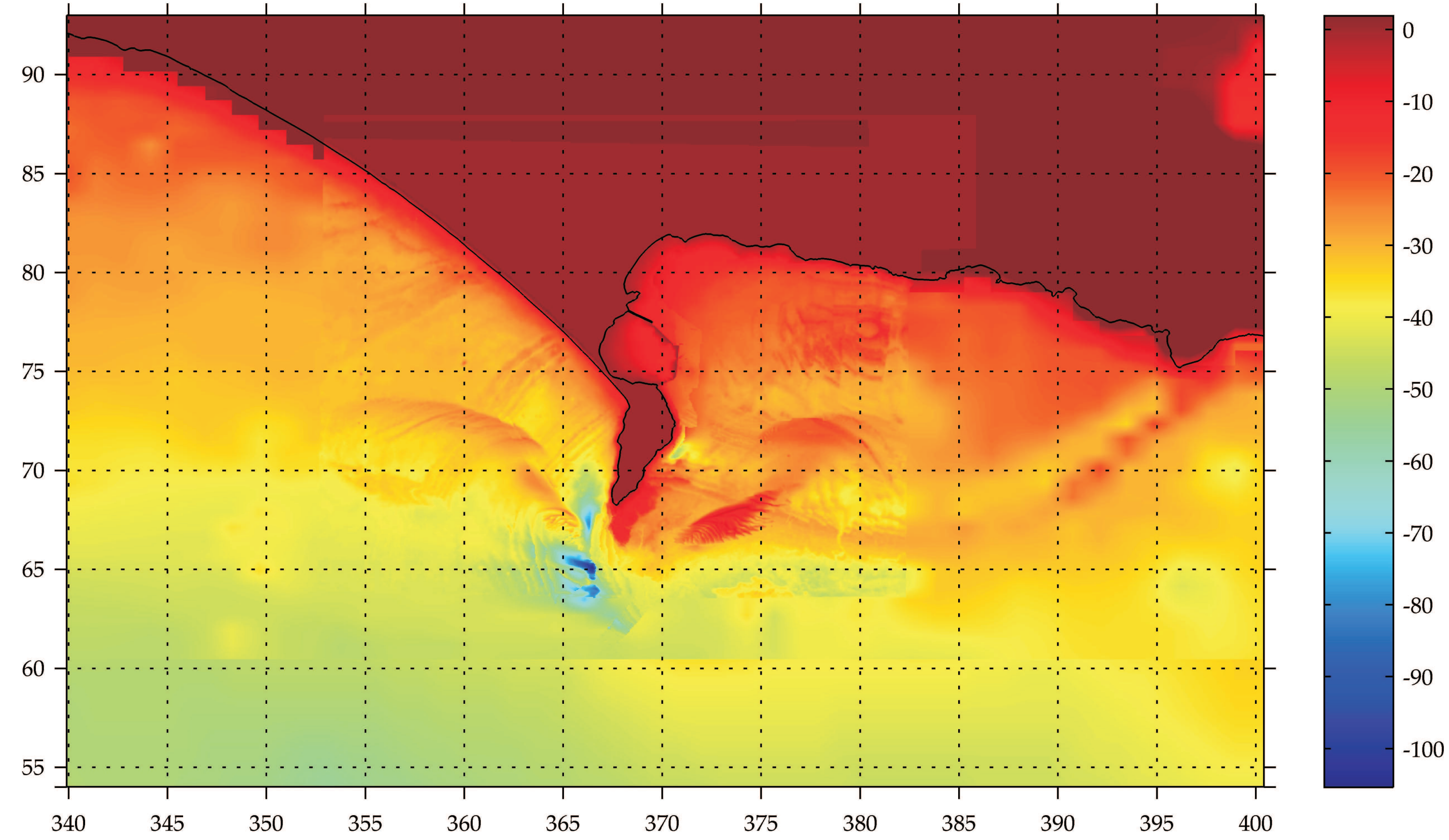

Figure 9.1: Bathymetry of Portland (m ACD)

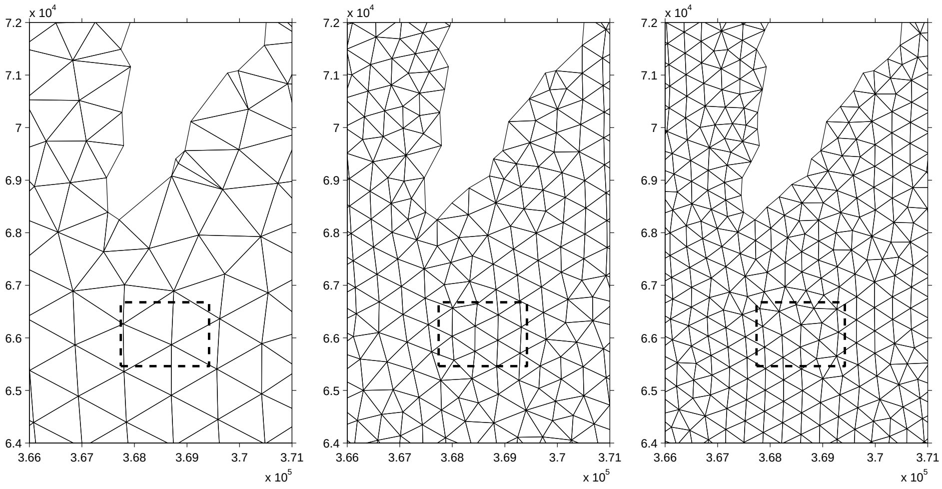

(a) Mesh 1 (b) Mesh 2 (c) Mesh 3

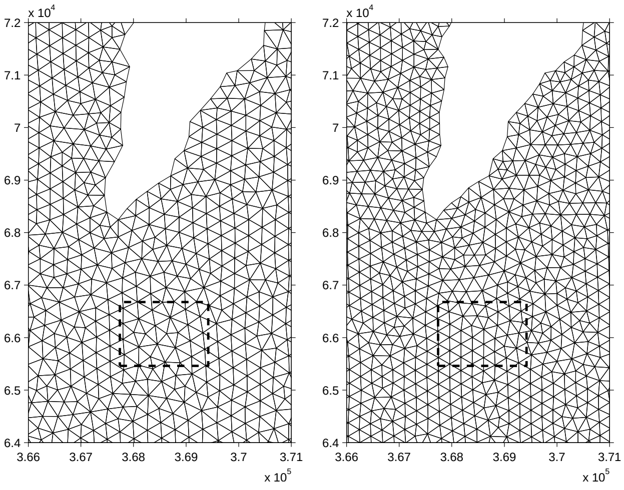

(d) Mesh 4 (e) Mesh 5

Figure 9.2: Detail of part of mesh showing area of energy extraction (dashed line). National Grid co-ordinates.

non-reflecting boundary condition described in §5.2.2.2 was used to try and avoid unphysical reflections at the open boundary in addition to constraining the unspecified velocities at the boundary nodes. The co-ordinates of the mesh boundary nodes were translated and rotated onto axes parallel to lines joining Devonport—Weymouth and Weymouth—Bournemouth tide gauge positions, X_1' and X_2' (see Figure 9.3). The imposed elevations were recalculated at each time step using linear interpolation along the two transformed axes of amplitudes and phases of tidal constituents, analyzed from tidal records at the gauges. The justification for using this method is the Kelvin wave-type dynamics of the tidal flows in the English Channel, with the co-tidal lines (lines of equal phase) progressing at right angles to the coastline from west to east. The amplitude does increase offshore, however, and there is a phase lag associated with rounding the Portland Bill headland towards Weymouth. This in practice led to an adjustment of the M_2 constituent of +69 cm in amplitude and a phase lead of 12.5° in order to best fit those analyzed from tide gauge records at Weymouth.

For all of the meshes, the bed friction was given by the Strickler formula with a spatially-uniform coefficient of 40 $\mathrm{m}^{\frac{1}{3}}/\mathrm{s}$. As discussed in §4.11, in a typical depth at the site of 30 m, this friction law implies a drag coefficient c_d of 0.0039 and roughness length z_{0-} of 1.4 mm. The Coriolis acceleration term was included in the hydrodynamic equations due to the scale of the domain (extent $>$ 10 km) and the k-ϵ closure method was used for turbulence modeling.

The numerical model results used for comparison with the ETSU 93 and the EC 96 reports were generated using the methodology described in §5.2 and are here referred to as LB 07. A harmonic analysis (described in §3.7) of the one month of model results was performed at each node to generate tidal stream ellipse parameters. The ellipses were then used to generate a time series of tidal stream speeds for each node, at intervals of 15 minutes, for a duration of 18.6 years. This was to include the important modulating effect of the lunar nodal cycle (Pugh 1987) on the mean cube speed rather than simply base the results on one average year as the case with the previous reports. Contours of mean cubed speed were generated directly from the triangulated values of $\overline{U^3}$ using the TRICONTOUR function for MATLAB (Engwirda 2006).

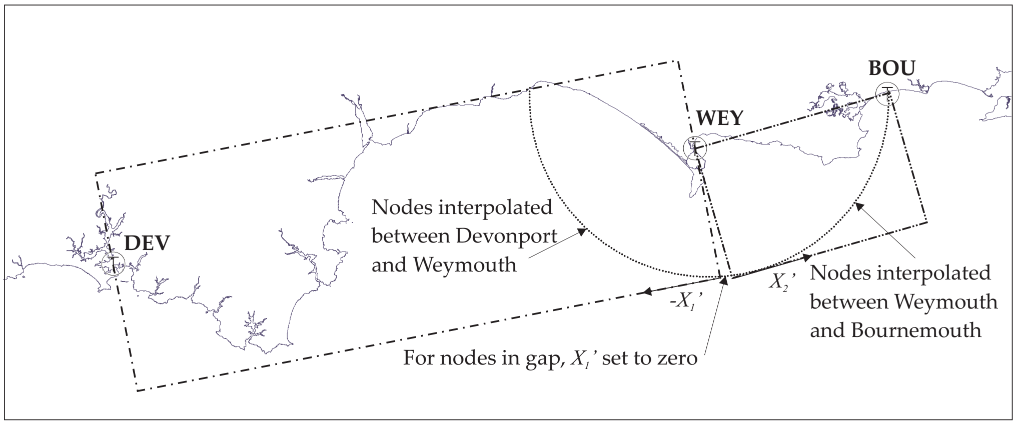

Figure 9.3: Bi-linear interpolation of tidal elevation constituent amplitudes and phases between Devonport (DEV), Weymouth (WEY) and Bournemouth (BOU) tide gauges (marked with 'T' symbol).

In order to compare the model results against the criteria used to select the areas stated in the previous reports, an estimate of the mean spring peak flow speed at each node was made using the tidal parameters derived from the harmonic analysis, thus avoiding a complicated search through a synthesized time series to pick out spring peak flows:

$$\overline{U_S} = U_{\mathrm{max,M_2}} + U_{\mathrm{max,S_2}} \tag{9.1}$$

Where $U_{\mathrm{max,M_2}}$ and $U_{\mathrm{max,S_2}}$ are the major axes of the lunar semi-diurnal (M_2) and the solar semi-diurnal (S_2) tidal stream ellipses. This should be a reasonable estimate providing the inclinations of the ellipses are similar (nearly always the case) and the constant component is not too large (not always true, but the estimate is conservative).

9.3 Results and Discussion

9.3.1 Comparison of simulated and observed elevations

Table 9.2 is a comparison of observed and simulated tidal elevation constituents at the only coastal tide gauge within the domain, at Weymouth. It can be seen that there was little difference between the meshes in terms of sea level elevations; the error in the model was 1–2 cm (1.7–3.4%) in amplitude

Table 9.2: Amplitude and phase with 95% confidence intervals (C.I.) for M_2 elevation constituent at Weymouth. TG refers to analysis of annual tide gauge records.

Results	H_{M_2} (m)	CI_{95} (m)	g_{H,M_2} (deg)	CI_{95} (deg)
TG	0.59	0.01	190.1	0.6
Mesh 1	0.58	0.05	199.1	4.3
Mesh 2	0.58	0.05	199.0	4.3
Mesh 3	0.58	0.05	199.1	5.3
Mesh 4	0.58	0.05	199.1	4.7
Mesh 5	0.57	0.05	199.2	4.3

and 9° in phase in all cases. This is after adjustment of the imposed boundary amplitudes and phases to give a better fit. These error estimates do not translate directly into those for tidal streams however, as currents are highly dependent on bathymetry and Weymouth Bay is only a small area within the domain; errors may be larger further away from the coast and closer to the forcing boundary. The relationship between the imposed elevations at the forcing boundary and the sea-surface elevation parameters at Weymouth is not independent of the non-linear bed friction characteristics. Consequently comparison with observed tidal streams in the domain is required to demonstrate the validity of the model.

9.3.2 Comparison with tidal diamonds

As mentioned in §7.2, there are no primary current-meter data available for areas of interest around Portland. Consequently, the best available data for comparison with the simulated tidal streams were tidal diamonds. The results were analyzed into tidal constituents at each mesh node and interpolated onto the locations of sixteen tidal diamonds in the domain. The tidal diamond data was analyzed according to the procedure laid out in §7.2. The ellipses generated from the results and from the diamonds are plotted to scale in Figure 9.4(a) for the tidal diamonds located in the outer part of the domain, and in Figure 9.4(b) for the region close to the headland. The figures show good agreement in inclination of the tidal ellipses, apart from in one instance close to the tip of the headland. This is likely to be the result of differences between the model and reality in the point of flow separation at the headland during east- and west-going streams. It should be noted that to obtain a simple comparison between the results of the different meshes, mesh density was not increased at the coastline relative to offshore, which would be likely to improve the results there. The best agreement occurs in the area with the fastest streams, which is reassuring from the point of view of resource assessment. The model over-predicts the amplitudes of the tidal stream to the west of the headland and slightly under-predicts on the eastern side.

9.3.3 Mass conservation

As mentioned in §5.1.2, the finite element formulation used does not strictly conserve mass across its inflow/outflow boundary when elevations are imposed at the boundary. The relative error in mass-balance was checked at each time step and at the end of each simulation run; while the out-of-balance at each time-step was small, of order 10^{-6}, the relative error accumulated over the month of simulation time was large, around 0.9. It is therefore important to consider what impact this might have on the results. Sutherland et al. (2007) commented on this shortcoming of finite elements in a similar context, noting that providing the elevations and currents in the region of interest are well-reproduced, then energy flux calculations should be valid within that region. The lack of mass-conservation is a less serious issue when it is the Eulerian (at a fixed point) tidal streams that are object of the simulation, rather than other modelling cases where Lagrangian (following a fluid parcel) currents are required, as in the case of dispersion of pollutants; or where diffusion down concentration gradients occurs.

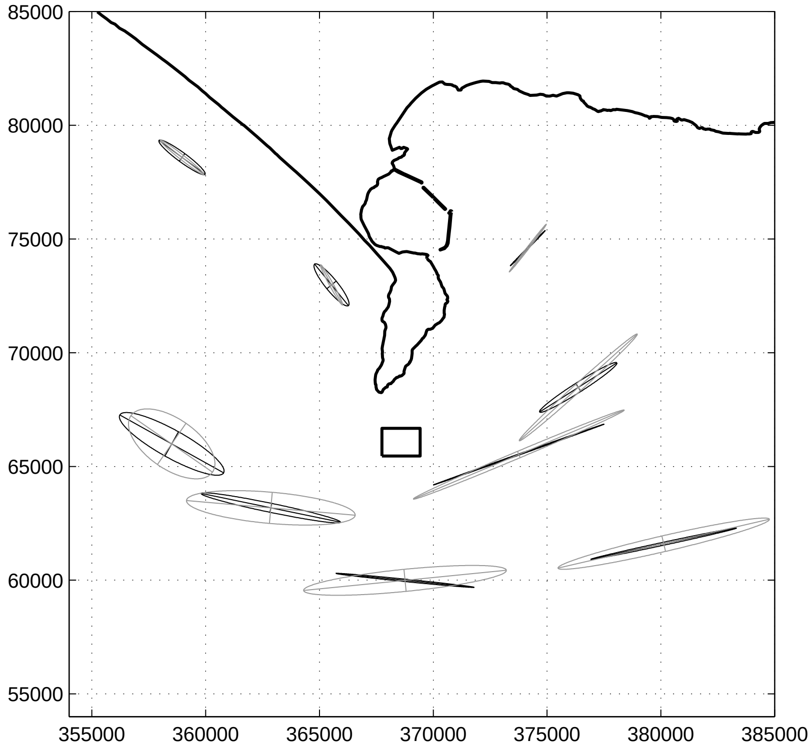

(a) Outer domain

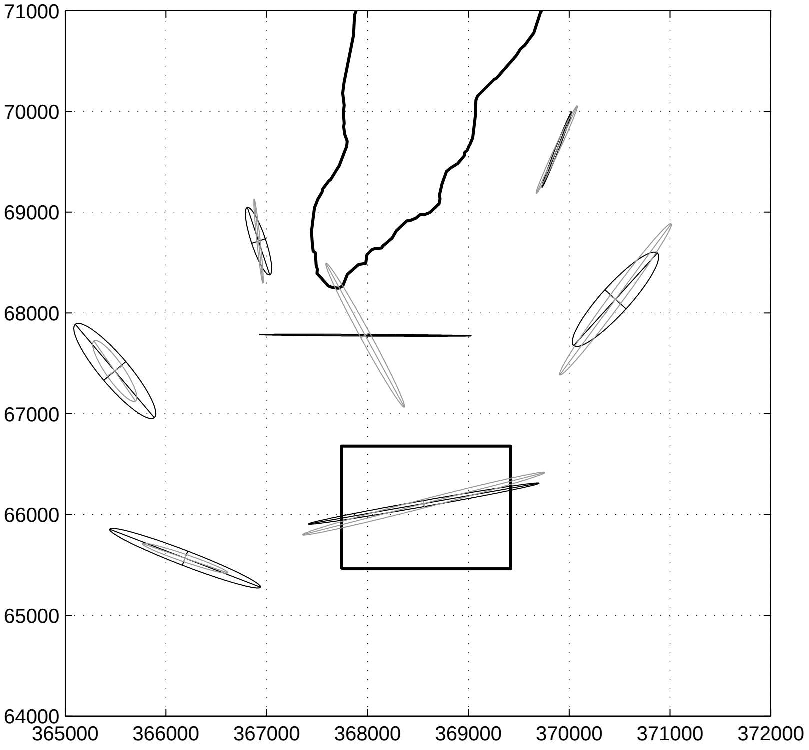

(b) Region close to headland

Figure 9.4: Tidal ellipses for the M_2 tidal constituent plotted to scale. Black ellipses are from tidal diamond data; grey ellipses have been analyzed from the simulation results. Location of each diamond is at the centre of each ellipse. UK National Grid co-ordinates

9.3.4 Selection of potential areas of high resource

New criteria are suggested here for more appropriate site selection than in the previous reports:

1. Mean cube speed over suitable period greater than 5.5 $(\mathrm{m/s})^3$
2. Depth greater than 25 m with respect to Chart Datum.

The energy captured by a tidal stream turbine at a point is related to the time-distribution of cubed speed U^3 through its c_P–U characteristic (see Chapter 2) and while both the full distribution of U^3 and the characteristic are required for assessing the output of a given device, $\overline{U^3}$ gives a good rough metric for characterizing the potential output at that location. If the c_P value were constant over all flow speeds, then $\frac{1}{2}\rho c_p\overline{U^3}$ would give the average power output of the turbine per unit area of rotor. A difficulty arises due to the proportion of time where U is close to zero; all designs of turbine would have some lower speed threshold below which little or no power would be generated. Introducing such a threshold into the calculation of energy yield would make the resource metric design-specific however, so this has been avoided. The first criterion would ensure that, for example, a generator unit with two rotors, each of equivalent diameter of 15 m, is presented with a flow of time-average kinetic power of at least 1 MW. Considering that almost all serious full-scale concepts for tidal stream power generation units are rated at 1 MW or above and given typical c_P values in the range 0.3–0.5, this criterion would ensure a reasonable capacity factor for devices of a reasonable size. This is of course assuming that the mean cube flow velocity has not been significantly reduced by the presence of other turbines in a surrounding array. The validity of this assumption will be examined in Chapter 10.

The second criterion is to ensure adequate submergence of such a rotor. This might be relaxed with some of the more exotic designs of energy converter (for example the Atlantis or Pulse Stream devices), although in the case of Portland Bill, the use of shallower areas would be likely to encroach upon the tidal race with associated highly confused flows and breaking waves generated by the currents (UK Hydrographic Department 1979). These effects are not directly

Table 9.3: Comparison of area selected using model results and new criteria, with ETSU 93 and EC 96 reports.

Data	**Criteria**		**Area in depth range (km^2)**					$\overline{\overline{U^3}}$
	Speed	Depth (m)	0-20	20-25	25-40	> 40 m	Total	(m/s)^3
ETSU 93	$U_{ms} > 2$ m/s	≥ 20	0.0	1.8	7.0	0.0	8.8	6.78
EC 96	$U_{ms} > 1.5$ m/s	—					17.5	6.21
LB 07	$\overline{U^3} > 5.5$ (m/s)^3	> 25	0.0	0.0	12.4	15.4	27.9	6.74

captured in the simulation when using vertically averaged velocities and the long-wave approximation. Navigational advice suggests that average tidal stream flow speeds are *reduced* in such areas (UK Hydrographic Department 1973).

Table 9.3 compares the results from the ETSU 93 and EC 96 reports with the numerical model data. The variable $\left\langle \overline{U^3} \right\rangle$ in the final column is the spatial mean of the temporal mean cube speed over the nodes fulfilling the criteria and is a metric of the available power density of the selected site. This value is similar in all three cases as it reflects similar assumptions made about likely turbine size and performance, whereas the surface area selected varies considerably. This is due to the use in the ETSU 93 and EC 96 reports of sparse data points from one location in or near the site, without consideration of the spatial variation in mean cube speed across the site area. Figure 9.5 shows the variation of $\overline{U^3}$ across the modelling domain. Bathymetric contours are superimposed to show the variability with depth. The area of highest power density is confined to a small area off the tip of the headland, in less than 30 m depth, showing the concentrating effect of cubing the speed on spatial distribution of power density.

9.3.5 ETSU 1993 and EC 1996 selection criteria applied to model results

Figure 9.6 shows contours of the approximated mean spring peak flow speeds. The 1.5 and 2 m/s contours extend out of the domain towards the east, an observation which agrees with the Marine Renewable Energy Atlas (ABPmer et al. 2004, Figure 21). Moreover, the relevant tidal stream atlas (UK

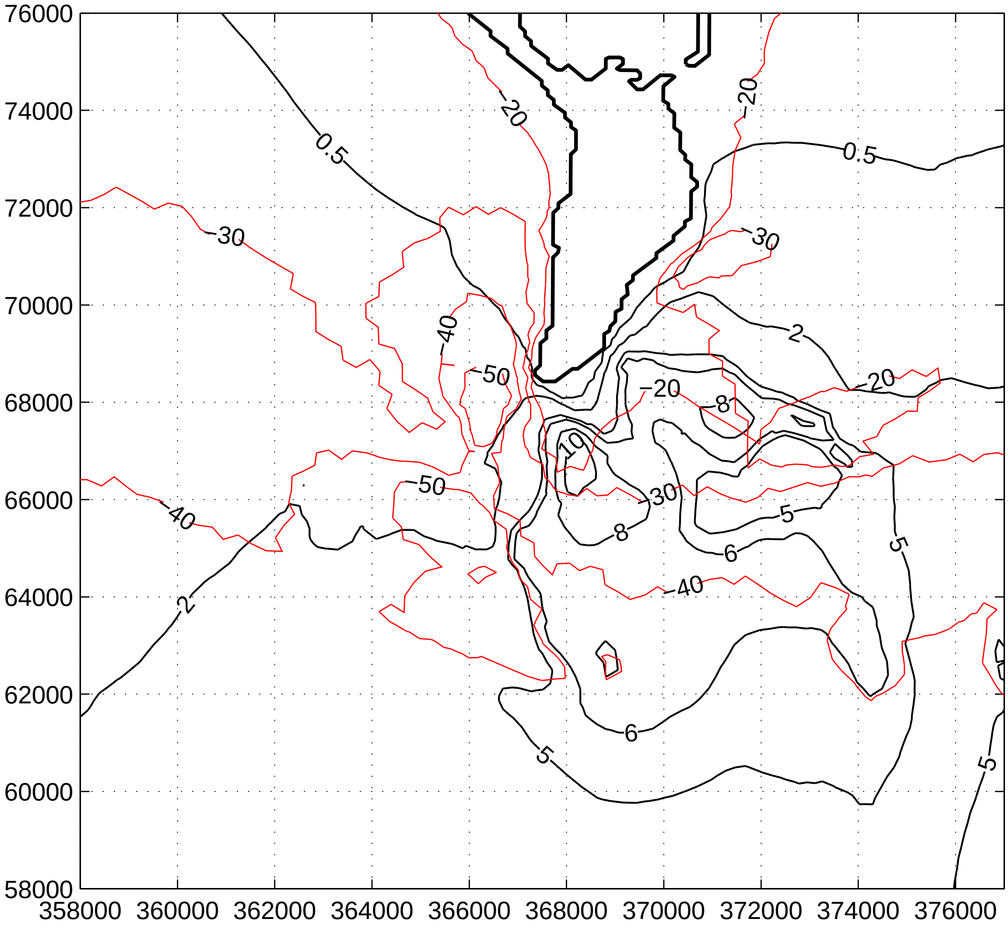

Figure 9.5: Contour plot of mean cube speed of tidal stream around Portland Bill over 18.6 year period derived from model results. Bathymetric contours (red) in m ACD. UK National Grid co-ordinates

Hydrographic Department 1973) shows mean spring peak rates of 4 knots (or 2 m/s, fulfilling the ETSU 93 criteria) at some considerable distance to the south-east of the site boundary as printed on the chart provided in the ETSU 93 report.

Caution should be applied with the model results close to the open boundary, as errors in the forcing elevations may dominate there. The bathymetry is also more sparse toward the open boundary. The results imply that the actual site areas that would be selected if the criteria in the reports were applied to the continuous flow field, rather than individual points, would be far larger than those quoted in the reports.

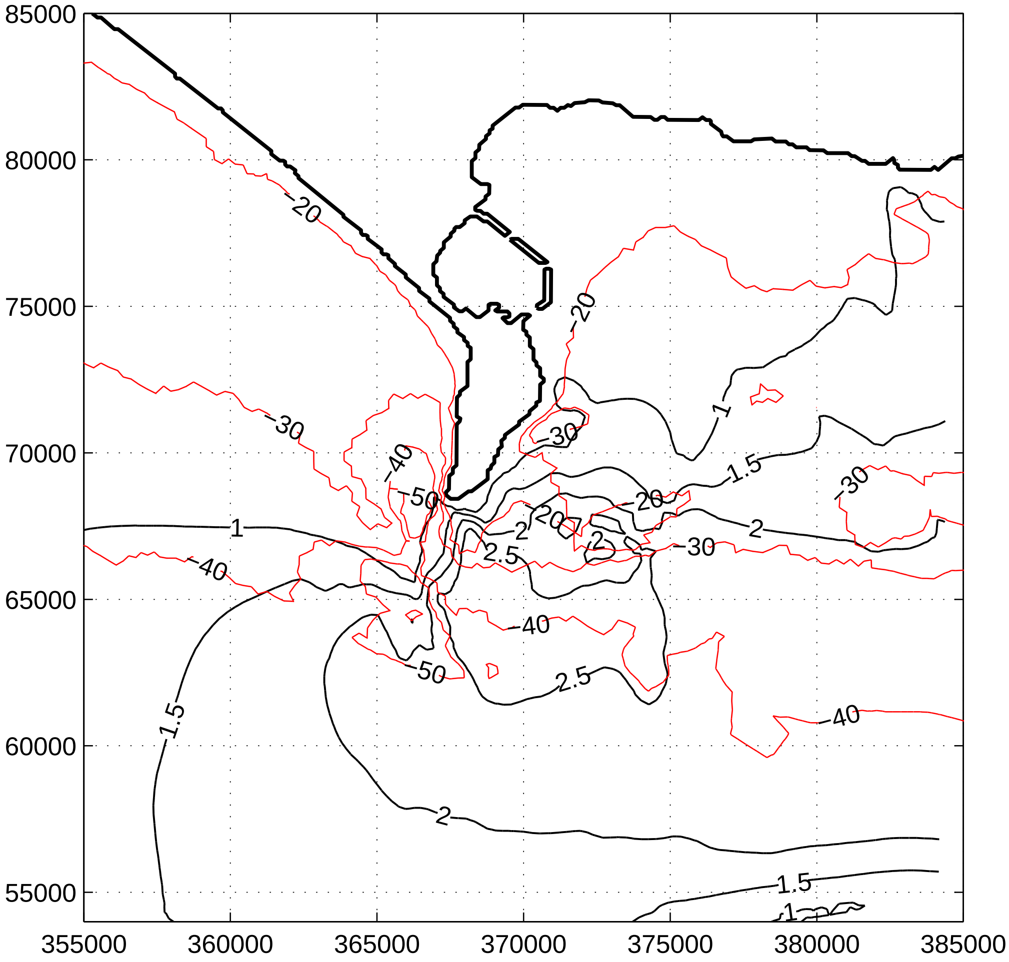

Figure 9.6: Contour plot of sum of M_2 and S_2 tidal stream ellipse major axes (m/s) around Portland Bill derived from model results. Bathymetric contours (red) in m ACD. UK National Grid co-ordinates

9.3.6 New selection criteria

The selected area can be seen in Figure 9.7, and the results included in the third row of Table 9.3. The selected area of 28 km^2 is considerably larger than the other reports. The cube-root-mean-cube speed $\sqrt[3]{\left\langle \overline{U^3} \right\rangle} = 1.89$ m/s is similar, lying between the average values found in the reports. This implies that a larger number of generators could be deployed off Portland Bill than supposed in the other reports. However, this estimate does not take into account the effect that such a large number of generator units would have upon flow conditions, which is the subject of the following chapter.

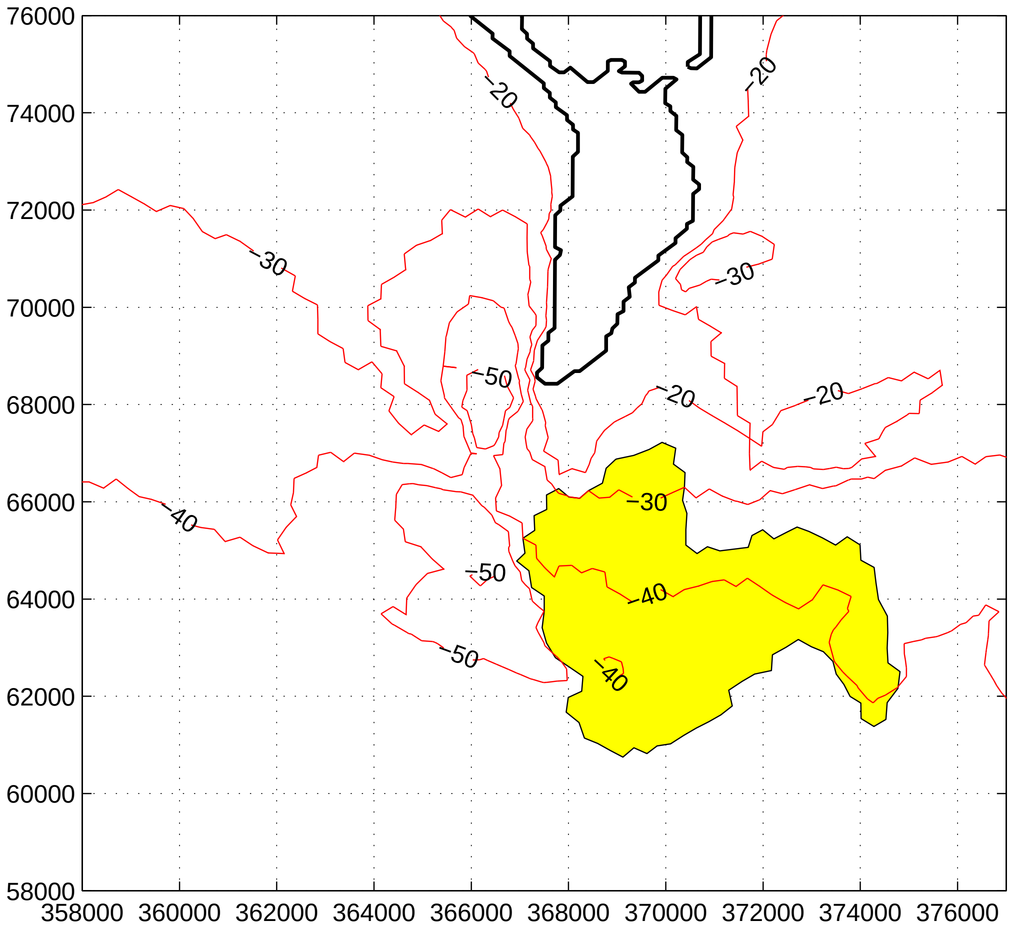

Figure 9.7: Area of site selected according to new analysis criteria. Bathymetric contours (red) in m ACD. UK National Grid co-ordinates.

9.4 Conclusions

1. An area has been selected at Portland Bill as having a high potential for tidal stream generator arrays, using numerical model results and new criteria based on mean cubed speed over an 18.6 year lunar nodal cycle. The area extended over 28 km^2 compared to 9 km^2 and 18 km^2 in the ETSU 93 and EC 96 reports respectively.
2. Mean spring peak flow rates have been calculated approximately from the model results and plotted to show that the areas in the vicinity of Portland Bill headland fulfilling the speed criteria of the previous reports are much larger than stated in those reports.
3. These results imply that the site areas used in tidal stream energy resource assessment at Portland Bill in the ETSU 93 and EC 96 reports

and subsequent reports drawing on their results (see Chapter 2) were too small. This in turn highlights the need for site-specific modelling, combined with reliable tidal stream measurements, to give sufficient spatial resolution and extent to characterize the resource.

Chapter 10

Portland Bill: energy extraction

10.1 Introduction

In this chapter, the new model developed in Chapter 6 to represent large arrays of tidal stream turbines as distributed added-drag, has been applied to the numerical model of Portland Bill described in Chapter 9. Whereas in Chapter 9 the results of the numerical model were used to select an area off the headland of interest for tidal stream development, in this chapter, energy extraction by tidal generators has been included in the model in order to investigate possible effects of a large array of tidal generators on the local tidal dynamics.

The model developed in Chapter 6 introduced a parameter depending on conditions external to the array, β, which describes the steepening of the sea-surface slope (or increase in pressure gradient) in response to extra drag imposed by the array, compared to that in the natural state. The results from the model in this chapter are used to comment on the value of this parameter in a realistic modelling context.

10.2 Methodology

10.2.1 Parameterization of drag due to turbines

The location of the area in the model where energy extraction was to take place was a sub-region of the area selected in §9.3.6. The full area was large and of an irregular concave shape, so it was decided to consider the effects of a more modest and geographically compact rectangular array. For the purposes of simulation, the following assumptions were made, using the theory developed in Chapter 6:

- Array area $A_a = 1.7$ km × 1.2 km = 2.04 km^2
- One generator unit consists of two 16 m rotors, giving a total flow capture area per unit of $A_r = 402$ m^2.
- The drag coefficient of the turbine rotors $c_d = 0.9$, assumed constant.
- Possible realization of the array: 15 units per row, 9 rows deep i.e. 135 units in total with $L_x = 11D = 176$ m and $L_y = 5D = 80$ m spacing. This gives area ratio $\lambda = 0.027$ and lateral tip-to-tip spacing between units of $2.3D$, based on a total width of unit of $2.7D$ (similar to the SeaGen configuration).
- Added drag coefficient $c_d' \lambda = 0.013$ from Figure 6.11 in Chapter 6, assuming $z_0 = 1.4$ mm (based on $K = 40$ in 30 m depth). This lies in the range investigated by Sutherland et al. (2007).

For the purposes of the simulation, a generator unit had an assumed rated speed $U_r = 2.5$ m/s, a value informed by a case study in Batten et al. (2006). The thrust on a unit was limited to rated thrust (1.16 MN) for $U > U_r$. A more realistic model of turbine performance would have limited the power rather than thrust, with the thrust peaking at the rated speed and then falling away; a lower cut-in speed could also be implemented as could variation of c_d with U. In reality the response of the array to incident flow would also be anisotropic, as the relative generator spacing would change with the direction of the flow. This feature was not reproduced in the model, but could be introduced in future work.

10.2.2 Implementation of the array in the finite-element model

In the 2-D finite element model, the vertically-averaged velocity field in the model is approximated by the basis functions of the finite elements, linear in this case (§5.2.2.1). The frictional stress is also linearly interpolated between the nodes of each element and is then integrated across the area of the affected elements to provide a term in the momentum equation.

For a mesh node with index i lying within array area A_a, which has a total of N tidal turbines, the force on the flow due to the thrust of the turbines in the x and y directions per unit volume was given by:

$$F_{ix} = -\frac{1}{2}\rho c_d' |\mathbf{u}_i| u_i \frac{A_r}{h_i}\frac{1}{\cancel{A_i}}\frac{\cancel{A_i}}{A_a}N \qquad (10.1)$$

$$F_{iy} = -\frac{1}{2}\rho c_d' |\mathbf{u}_i| v_i \frac{A_r}{h_i}\frac{1}{\cancel{A_i}}\frac{\cancel{A_i}}{A_a}N \qquad (10.2)$$

c_d' is here distinguished from c_d as it is not the drag coefficient for an isolated turbine, rather it is the equivalent added drag coefficient based on the theory developed in Chapter 6 for a large array, taking into account the changes in the spatially-averaged vertical velocity profile. It can be seen from Equations 10.1–10.2 that A_r/h_i is an equivalent diameter that varies with h, the factor $1/A_i$ transforms the point forces on the generators into a distributed stress, A_i/A_a is the fraction of the array area corresponding to node i and the area A_i cancels from the expression. The nodal forces were then multiplied by the basis functions of the triangular finite elements and integrated element-wise. The subroutine adapted to include (10.1) in the TÉLÉMAC model, may be found in Appendix C.1, along with in-line comments.

10.2.3 Tidal analysis

The T_TIDE package for MATLAB Pawlowicz et al. (2002) was used to determine the constituent ellipse properties at each finite element node by harmonic analysis. T_TIDE applies nodal corrections to constituent amplitudes and phases based on the central time of the input time series. In addition, T_TIDE was used to produce estimates of signal-to-noise ratio (SNR) for the constituent ellipses by using a nonlinear bootstrap method adding Gaussian

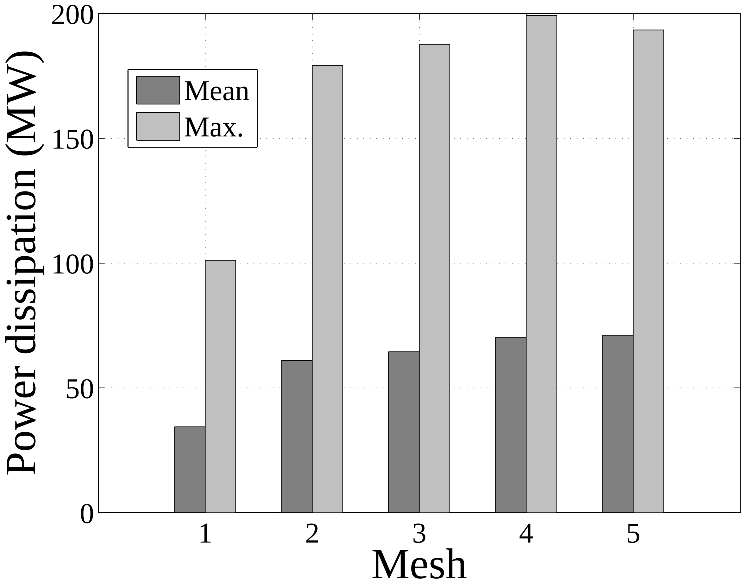

Figure 10.1: Mean and maximum power dissipated by added friction within the meshes over period of simulation (MW)

noise with variance derived from the spectrum of the residual values, to the signal reconstructed from the constituents. Using these constituents, time series of tidal stream velocity can be predicted with any time step and start date.

10.3 Results and discussion

10.3.1 Effects of mesh resolution on power dissipation by added drag

Figure 10.1 compares the mean power dissipated by the energy extraction within the five meshes over the one month period. The values converge as the mesh density increases; the difference in mean power dissipation between meshes 4 and 5 was +1.2% and the difference in maximum power dissipation was -2.9%. The values converge as both the array area and the velocity field are better resolved. The results used for analysis in the following sections were all taken from the second most refined mesh (Mesh 4) as a compromise between convergence and computational expense.

10.3.2 Changes to the local tidal regime as a result of the array

Figures 10.2(a) and 10.2(b) present co-tidal and co-amplitude (tidal elevation) lines for the largest harmonic constituent, M_2. The co-tidal lines are not at equal intervals of phase, for clarity; the rate of propagation of the eastward going wave decreases sharply on passing the headland, so the co-tidal lines bunch up. In the model, this is the result of the interpolated phase distribution on the boundary; in reality it is a result of the wider tidal dynamics of the English Channel. The distortion of the contours at the bottom right hand corner of Figure 10.2(b) is an artifact introduced by the bi-linear approximation of the phase distribution, resulting in a step in phase gradient with respect to distance along the boundary.

The tides in the English Channel are well explained by a combination of an eastward going Kelvin wave travelling up the Channel with highest amplitudes on the French coast and a much weaker reflected westward travelling wave with highest amplitudes on the English coast. The combination of these waves results in the co-tidal lines in the Channel radiating outwards from an apparent point inland of the English coast, known as a degenerate amphidrome, which is situated to the east of Portland Bill, inland of Christchurch. (Pugh 1987, 5:4:2). The position of the co-tidal lines in the model results agrees to about 10 degrees of phase with those produced from observations and models of the English Channel, which have the 180 degree contour slightly to the west of the headland Pingree and Maddock (1978); Le Provost and Fornerino (1985); Howarth (1990). This error in the model is explained by the phase distribution used along the boundary, which is derived from the coastal gauges and applied to ≈20 km offshore. The effect of adding extra roughness is to locally decrease the wavelength and consequently the speed of the progressive wave (Dean and Dalrymple 1991, 5.6.2). This effect can be seen in Figure 10.2(b) as the co-tidal lines are ‘pulled in’ towards the headland. Figures 10.3 and 10.5 show a reduction in major axis for the M_2 tidal stream ellipses in and around the area of energy extraction of around 0.25 m/s. This represents a reduction in maximum speed cubed of 30%, indicating a significant reduction in available power at the location. The change predicted in ellipse orientation is generally small (see Figure 10.5(b)),

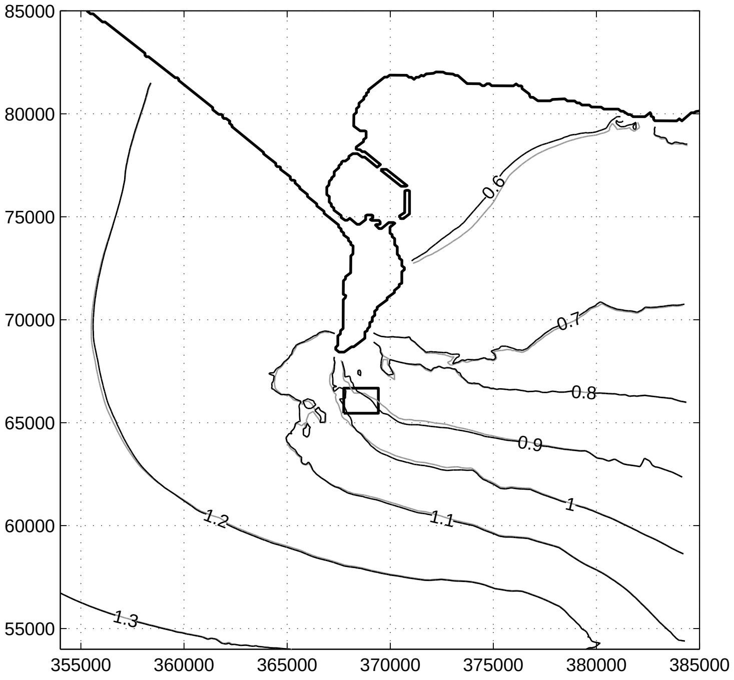

(a) Co-amplitude lines for the M_2 elevation constituent (m)

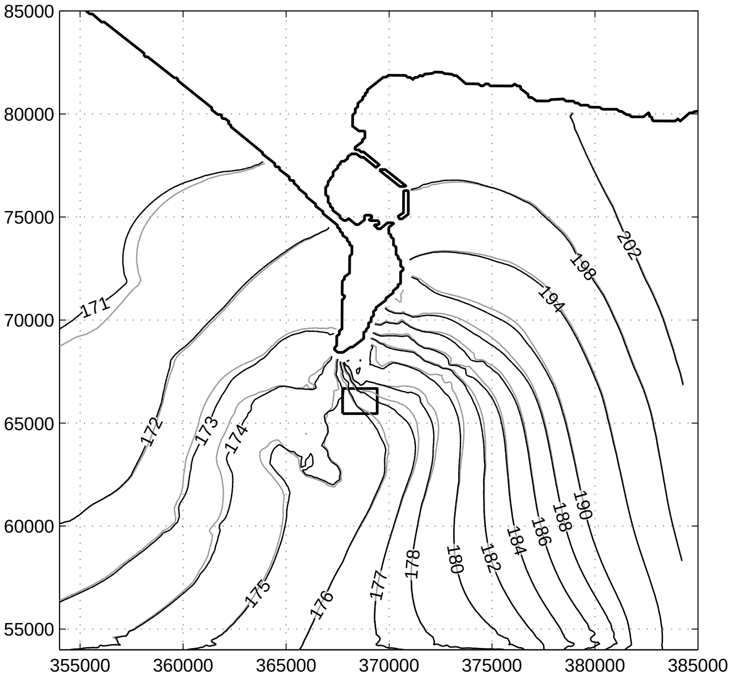

(b) Co-tidal lines for the M_2 elevation constituent (°)

Figure 10.2: Contours of parameters for tidal elevation for the M_2 constituent. Grey: natural state; black: with energy extraction applied

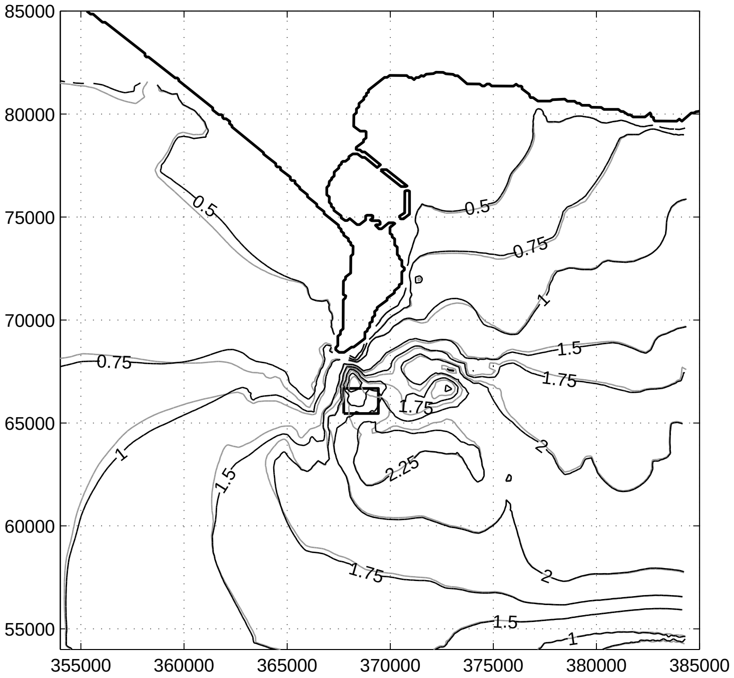

(a) M_2 tidal ellipse major axis (m/s)

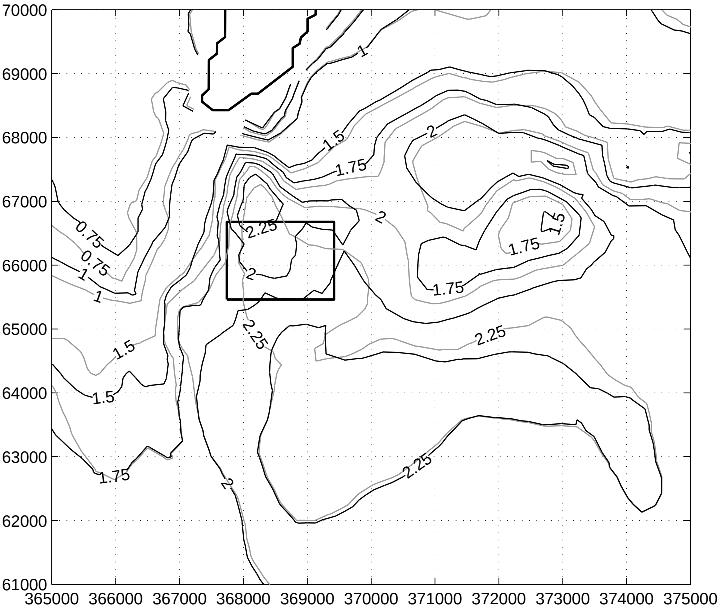

(b) M_2 tidal ellipse major axis (m/s); detail of the area of energy extraction

Figure 10.3: Contours of parameters for tidal stream ellipse for the M_2 constituent. Grey: natural state; black: with energy extraction applied

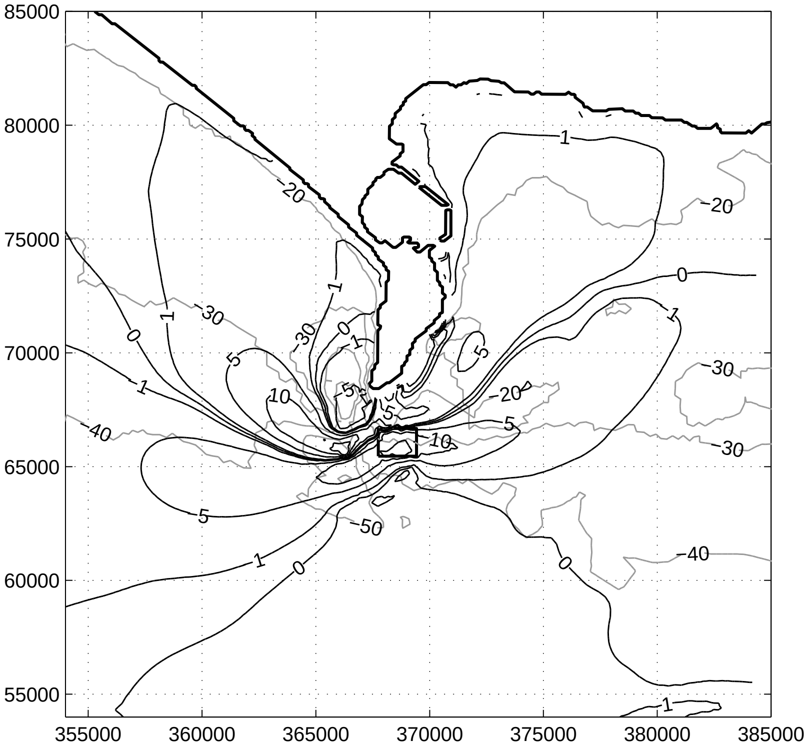

(a) Percentage change in major axis. Grey lines indicate bathymetric contours (m ACD)

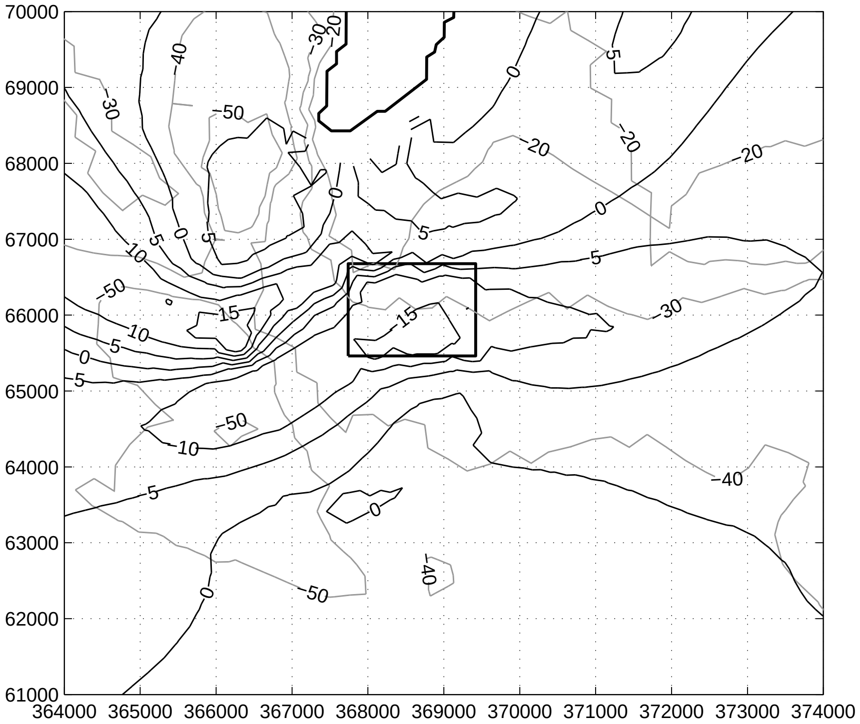

(b) Percentage change in major axis; detail

Figure 10.4: Change in major axis length for the M_2 tidal constituent.

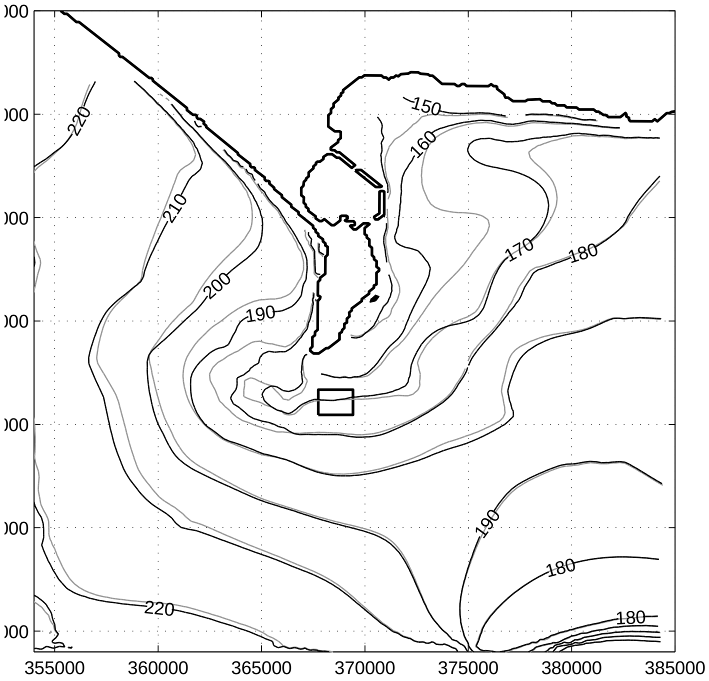

(a) M_2 tidal ellipse phase of major axis (°). Grey: natural state; black: with energy extraction applied. Grey lines indicate bathymetric contours (m ACD)

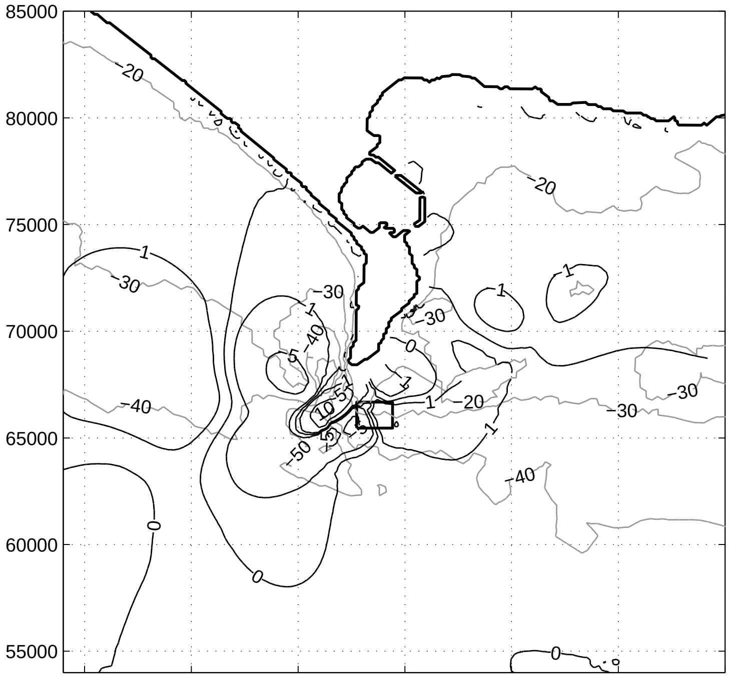

(b) Change in inclination of major axis (° ACW from horizontal) Grey lines indicate bathymetric contours (m ACD)

Figure 10.5: Change from natural state in tidal stream ellipse parameters for the M_2 constituent when energy extraction is applied

less than 1 degree, apart from close to area of energy extraction where variations of up to 10 degrees are found.

10.3.3 Power density in the array area compared to natural state

For a long wave, the total energy flux per unit width normal to U is given by:

$$\dot{E} = \frac{1}{2}\rho g h |Z|_{\max} |U|_{\max} \cos(\phi_H - \phi_U) \tag{10.3}$$

It can be seen by comparison of Figures 10.2(b) and 10.5(a) that the phase difference between elevation and currents in the area concerned is less than 15 degrees, so the cosine term in (10.3) is close to unity and is relatively insensitive to small changes in phase difference. Physically, this indicates that friction is dominant over inertial acceleration. One way of estimating the energy dissipation—equivalent to the divergence of energy flux—within a bounded area is to apply Green's theorem in the plane and find the closed line integral of the energy flux normal to the boundary (Taylor 1920). Over a long enough period the total energy flux due to a number of constituents is simply the sum of the individual energy fluxes (Pugh 1987, A4:1). This would in principle enable the average energy dissipation in a region to be calculated analytically from the tidal harmonic constituents around the boundary. Unfortunately, this was found to result in a poorly conditioned problem due to the subtraction of large numbers to find a relatively small difference, therefore the dissipation was calculated directly. It is possible to use the binomial expansion to generate an analytical approximation to the energy dissipation from the harmonic constituents (Pugh 1987, 7:9:1). However, given that there were number of constituents with significant amplitude, it was considered more straightforward to calculate the average dissipation numerically from a time series of cubed speeds.

For each node, a time series of quarter-hourly velocity components was generated for 18.61 years, the period of the lunar nodal cycle. This allowed the full variation of tidal streams to be captured, rather than simply that over the simulation period of one month, as in the author's previous work (Blunden and Bahaj 2006), or over one year, as in published reports (ETSU

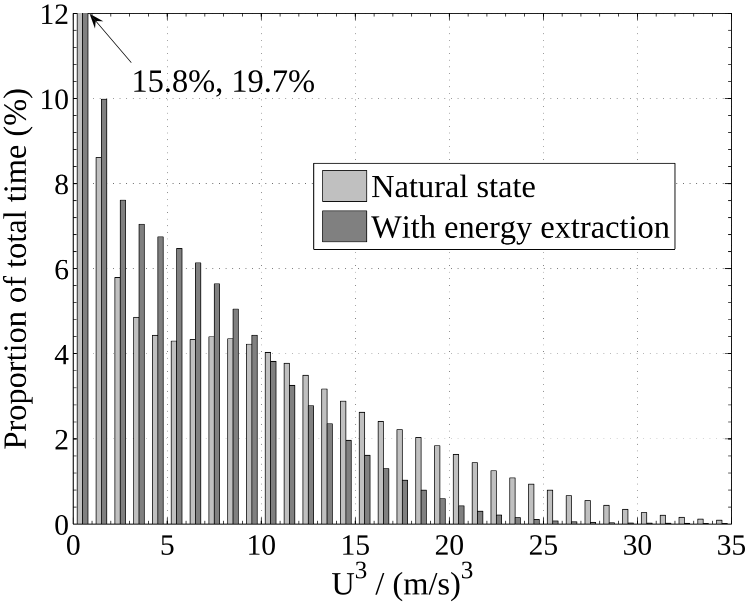

Figure 10.6: Histograms of cubed speeds averaged over area of energy extraction and derived from 18.6 year predicted currents for cases with and without energy extraction.

1993; European Commission 1996). The time series was then used to create a histogram of cubed speeds, with hourly data sorted in bins of 1 (m/s)^3 in the range 0–35 (m/s)^3. For Mesh 3, the distribution of cubed speeds was spatially averaged over the area of energy extraction and compared for the cases with and without energy extraction. The histogram is shown in Figure 10.6. In the bin that was closest to the rated speed chosen for the array in this case, 15–16 (m/s)^3, there was a reduction in available energy of approximately one third. This implies that there could be a large impact upon individual generator design criteria in this case.

10.3.4 Change in free-surface slope compared to the natural state

As stated in 9.2, for the average depth in the array of 30 m, the bed friction coefficient c_d imposed by the model was 0.0039. Consequently, the sea-surface slope required in the model to drive the flow at a constant speed of e.g. 2.5 m/s across a flat bed was -4.2×10^{-5}. The area-averaged added drag coefficient $c'_d\lambda$ imposed in the model to represent the array was chosen to be 0.013 (§10.2.1). Therefore if the local sea-surface slope were to adjust to the combined drag coefficient, $c_d + c'_d\lambda$, so that the flow speed remained constant, the slope $S_{\max}$ would need to change to -17.9×10^{-5}. Comparing the model results with and without the array present gave values of difference in sea surface slope, $S_{0+} - S_{0-}$ for each node and time step, allowing the calculation of β for the array (β was first defined in 6.8.1):

$$\beta = \frac{S_{0+} - S_{0-}}{S_{\max} - S_{0-}}$$

Values of $S_{\max}$ and S_{0-} were calculated based on the flow speed and depth at each node. The parameter β was then calculated node-wise and averaged over the array area. In Figure 10.7, values of array-area-averaged β at 15-minute intervals are plotted against the flow speed at the location of tidal diamond F on Admiralty Chart 2615 (§7.2) for the two highest resolution meshes. While there is scatter, the value of β falls into the range $0.2 \leq \beta \leq 0.4$ for 90% of the time when the flow speed was greater than 1.5 m/s (excluding values of $0 \leq \beta \leq 1$). At values of flow speed greater than 2.5 m/s, there is less scatter and the values of β calculated from both meshes converge to around 0.35. The implication of these results is that the assumption in Chapter 6 that $\beta = 0$, i.e. that there is no change in free-surface slope (pressure gradient) when the array is present, is a pessimistic one. Consequently the power output per unit area at 2.5 m/s flow speed from Figure 6.12 in §6.10 is nearly ten times larger than that assuming constant free surface slope, at a more useful 25 MW/km^2.

10.4 Conclusions

For all four meshes, when extra roughness simulating a generator array was applied, the simulation results predicted measurable changes in tidal stream ellipse major axes in the domain. These were mainly in the form of decreases but increases in speed also occurred where the flow was constrained between the array and the headland. These increases imply that there is case for optimizing the layout of an array or arrays deployed at the headland to exploit the blocking effect. There may also be implications for the accumulations of sand on either side of the headland, (described in Bastos et al. (2003a)) as small changes in tidal stream speed and direction may have a significant impact on sediment transport (Brown et al. 1997, 4.3). The model results predicted no significant change in elevation amplitude and phase for largest harmonic constituent at Weymouth.

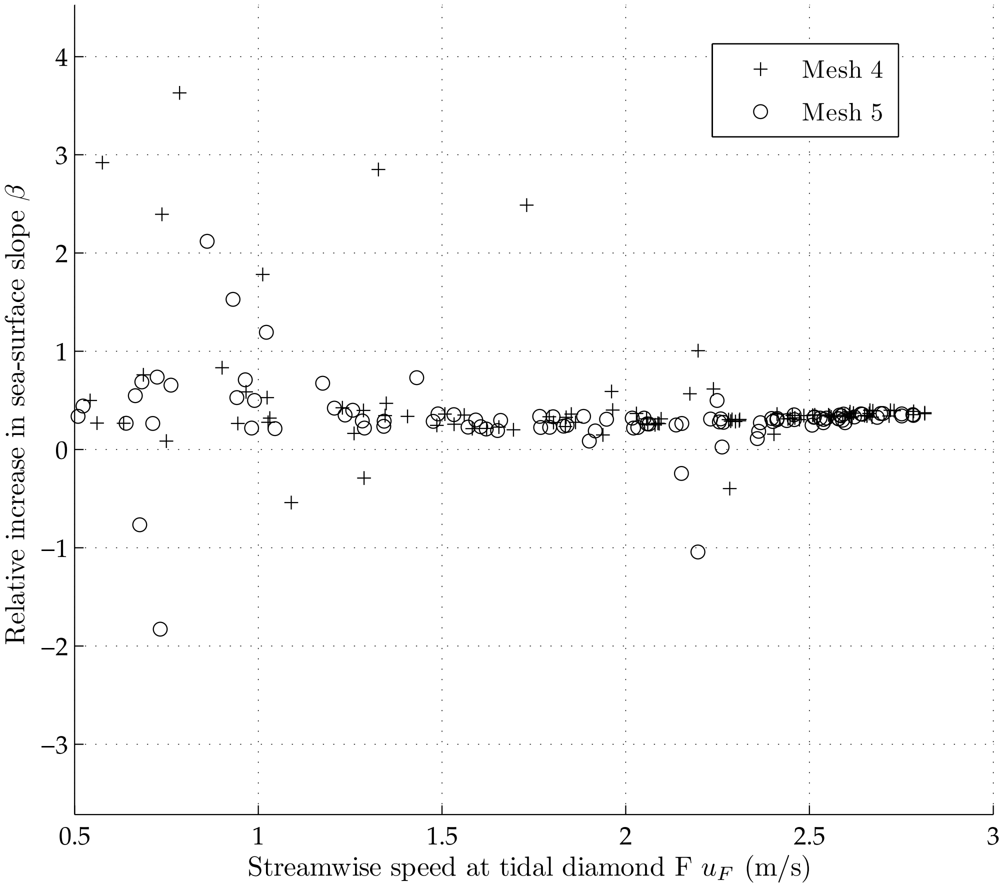

Figure 10.7: Distribution of β from numerical modelling results over a 24-hour period at conditions of medium tidal range. Values have been averaged over the array area.

Chapter 11

Overall conclusions and recommendations for further research

11.1 Overall conclusions

The work described in the previous chapters should be of interest to tidal stream developers, renewable energy consultants and coastal physical oceanographers. It has brought together elements of wind-power resource assessment, tidal theory and analysis, boundary layer theory and coastal numerical modelling techniques in order to develop a new methodology for investigation of the tidal stream resource. The methodology has the twin aims of flexibility and simplicity; to be flexible enough to reproduce complex tidal flows in a variety of locations but with a simple parameterization of a tidal stream array that does not require simulation of individual turbines.

A large proportion of the material included in the previous chapters has been published in journal and conference publications, most recently in Blunden and Bahaj (2008), which was awarded Best Paper in the Marine category of the World Renewable Energy Congress X (included in Appendix I). A complete list of the publications has been included in Appendix A.

In Chapter 6, a new model was developed for momentum extraction by a large array of tidal turbines, in balance with the driving pressure gradient (slope in sea-surface) and the friction on the sea bed. Though similar models have been proposed for wind turbine arrays, this is–to the best of the author's knowledge—the first time that they have been applied to tidal turbine arrays. There are significant differences between the wind turbine array models and the proposed model; the inclusion of the zero-plane displacement is one; another is the difference in the driving mechanism for the flow. The model was used to infer relative velocity decreases deep inside the array in order to determine an equivalent added drag coefficient, suitable for use in coastal numerical modelling. The spacing required for maximum power output from an array was also estimated and found to be sensitive to the bed roughness and very sensitive to assumptions about the coupling with the wider flow dynamics. While work has begun on characterizing the far wakes of individual turbines using mesh simulators (Bahaj et al. 2007b) and similarly for multiple row arrays of mesh fences for (see §6.8), there has not yet been sufficient data to constrain the parameter α representing the change in bed friction inside the array compared to in the natural state. Requirements for further work to experimentally measure α are discussed in §11.2.

High-resolution bathymetry data was obtained for the Portland Bill location, but not for the Channel Islands so work has been focused on the former location. Portland provides an interesting test case for the resource assessment methodology as it represents the most challenging conditions for the numerical simulation of tidal streams that are likely to be experienced. The region is one where non-linear tidal constituents are of significant amplitude; there is complex topography; a poorly constrained open boundary and flow separation at the tip of the headland.

No raw current meter records were available in the areas of Portland Bill or the Race of Alderney, so the best available data on tidal streams was found to be that printed on Admiralty charts. For the Isle of Wight location, some raw current meter records were available of sufficient duration for direct analysis. It was found (See Chapter 7) that the analysis results agreed with that of a method using a Admiralty tidal diamond—located close to the current meter position—to within 14% of major axis length of the constituent tidal stream ellipses. This indicated that analysis of the Admiralty tidal diamonds could give reasonable estimates of tidal stream ellipse properties, at least for that location.

A hydrographic survey off Portland carried out for a third party in October 2006 resulted in further enhancements to the bathymetric data-set, but unfortunately planned ADCP measurements of currents off the headland did not go ahead due to poor weather within the available window fixed by time and budget constraints. A record of the related correspondence is included in Appendix E. This was a salutary reminder of the difficulty of working in exposed locations with fast tidal currents.

In Chapter 8, the development of a numerical model of the English Channel for the purpose of providing boundary conditions for interior models was described. The errors in the modelled tidal elevations in terms of amplitude and phase were in the acceptable range at some tide gauges within the Channel, but not at others, particularly toward the eastern end of the Channel and along the English coast. Further development of the model was not pursued due to time constraints, lack of bathymetric data for the Channel Islands region and good results from the Portland Bill model without the use of an external model to provide boundary conditions. Nevertheless, it would be of interest to investigate the coupling of a hypothetical, very large tidal scheme to the wider shelf dynamics, and this could only be accomplished with a regional-scale model.

A numerical model of Portland Bill was developed, tuned and then the results compared against independent tidal diamond velocity data. The results were then used to select an area of high potential for development (Chapter 9). The open boundary condition was imposed tidal elevations, with amplitudes and phases adjusted to reduce the error at a coastal tide gauge in the domain. After adjustment of boundary conditions, the error in the largest tidal elevation harmonic constituent was 1 cm in amplitude and 9 degrees in phase at the tide gauge location in the domain. The agreement with independent tidal stream amplitudes derived from Admiralty chart tidal diamonds was good in fifteen out of sixteen cases. Simple criteria based on bathymetry and mean cubed speed over a complete 18.6 year tidal cycle were applied to simulation results to select areas of high potential for development at Portland Bill. It was found that an area of 12.4 km^2 had depths in the range 20–40 m and mean cube speed greater than 5.5 (m/s)^3.

The model was then further enhanced through implementation of momentum extraction within the domain to simulate a large tidal stream turbine array (Chapter 10). Momentum extraction was implemented in the numerical model using an area-averaged added drag coefficient approach, to tie-in with Chapter 6. This was the first time that a large tidal array has been simulated in a realistic coastal domain of large extent, with a parameterization that takes into account the interaction of the turbines with the rough-wall flow in the natural state. It was found that there was a significant effect on the tidal ellipse major axis length in the area of energy extraction, the largest (M_2) reduced by 10–15%. There was a corresponding decrease in mean cube speed in the area of energy extraction, altering the time distribution of cubed speeds from higher-value bins to lower. The time spent in the cubed speed bin at the simulated rated speed was reduced by a third.

In Chapter 10, maps of tidal stream parameters around the site of simulated momentum extraction at Portland Bill were produced to indicate the predicted local changes in amplitude and phase of both the tidal elevation and the tidal stream ellipse major axes. They suggest that there is a region downstream of the array extending approximately 5–10 km around the simulated tidal stream turbine array in which the tidal stream ellipse major axis is reduced by at least 5%. The eddies occurring on either side of the headland—due to flow separation and influenced by the Coriolis acceleration—play a role in advecting the reduced-velocity wake of the array away from the axis of orientation of the array.

The model developed in Chapter 6 introduced a parameter depending on conditions external to the array, β, which describes the local steepening of the sea-surface slope (or increase in pressure gradient) across the array in response to extra drag imposed by the array, compared to that in the natural state. The results of Chapter 10 were used to calculate β over a tidal cycle and it was found that while there was scatter in the results, $beta$ mainly fell in the range $0.2 \leq \beta \leq 0.4$. This indicates that for this site, the assumption of constant free-surface slope would give pessimistic (or conservative) estimates of array power output. The parameter β is clearly affected by the wider characteristics of the domain: the open boundary conditions, bed friction and proximity of coastline; it would therefore be necessary to model several sites before drawing general conclusions about appropriate values of the parameter to use in resource assessment.

11.2 Suggestions for further research

11.2.1 Velocity and shear stress profiles in large arrays of turbines

In developing the new theory described in Chapter 6, a number of assumptions were made which have not been experimentally validated and have raised the following specific questions:

1. Can fast tidal flows be well-characterized by a logarithmic profile over most of the water column, for most of the time (when velocities are high enough to be of interest)?
2. Can tidal boundary layers of a nature experienced in sites of interest for tidal stream development be reproduced in a laboratory setting?
3. After how many rows of an array are equilibrium conditions approached, as the bed roughness varies?
4. When equilibrium conditions are approached, does the flow above the array tend to a logarithmic profile? If so down to what height above the bed?
5. Is it reasonable to assume that the drag on the turbine/turbine-simulators is concentrated at the centroid of the swept area of the rotor disk?
6. What type of function best fits the flow profile beneath the turbines/turbine simulators (e.g. log-law, exponential, power law, or constant)?

7. What is the distribution of total drag resisting the flow, between the turbines and the bed, as a function of bed roughness, 'hub height' and row spacing?

ADCP data from the European Marine Energy Centre may help to answer Question 1. The remaining questions would require a dedicated set of physical model tests using a wide but comparatively shallow circulating water channel. Bed roughness would need to be simulated e.g. using cuboid obstacles, along with a large array of turbines e.g. using mesh disks. Measurements would ideally be conducted with Laser Doppler Velocimetry, enabling high resolution in the vertical. Drag profiles may be inferred from the Reynolds shear stress profiles and by using the mean velocity profiles, measured several rows deep into an array of simulators. To answer Question 7 would require at least one turbine simulator to be instrumented for drag force and in addition, the total drag (bed friction plus turbines) could be determined independently from the free-surface slope: likely to be very small and may require special head amplification techniques for accurate measurement.

The work above has not considered how the altered velocity and turbulence intensity profiles might impact upon the dispersion terms resulting from vertical-averaging in 2-D numerical models, which are absorbed into turbulence models (see §4.9), e.g. on the empirical coefficients used in the k-ϵ model. Reynolds stress and turbulence intensity profiles would enable, for example, a modified mixing-length or other turbulence model to be fitted to the data for modelling purposes.

11.2.2 Non-tidal residual currents

It was mentioned in §2.6.5 that the prediction of *total* currents, including storm-surge induced currents, via numerical simulation, is an active area of research. In order to predict extreme loads on tidal turbines, the joint probability of extreme tidal currents in conjunction with extreme *depth-average* storm surge currents needs to be estimated. Including meteorological effects in the model would require wind and air pressure fields to be included and would probably require a move to a multi-layered 3-D approach.

11.2.3 Modelling sediment transport

The sandbanks on either side of Portland Bill headland exist in a location where the general magnitude of the tidal streams (and hence the bed shear stress) suggests they should not. They are held in place in kind of dynamic equilibrium related to spatial- and time-varying rates of sediment transport (Bastos et al. 2003a). The sensitivity of the sandbanks to perturbations in velocity potentially caused by a large tidal stream turbine array off the headland has not been investigated. A sediment transport module could be coupled to the existing model of tidal streams to assess the possible impacts of such an array.

11.2.4 Software for extended modelling

Changing from one software package to another brings with it a cost in terms of time. There are inevitable problems and delays associated with installing, configuring, running and de-bugging the code. However, moving to open source hydrodynamic software would bring significant potential advantages in terms of reduced costs and more flexibility to extend source code and therefore should be used for further work.

Appendix A

Publications by the author

[*]L. S. Blunden and A. S. Bahaj. Flow through large arrays of tidal energy converters: is there an analogy with depth limited flow through vegetation? In A. A. M. Sayigh, editor, *Tenth World Renewable Energy Congress*, Glasgow, 2008. Elsevier.

L. S. Blunden, W. M. J. Batten, and A. S. Bahaj. Comparing energy yields from fixed and yawing horizontal axis marine current turbines in the English Channel. In B. Leira, editor, *27th International Conference on Offshore Mechanics and Arctic Engineering*, Estoril, Portugal, 2008. American Society of Mechanical Engineers.

L. S. Blunden and A. S. Bahaj. Effects of tidal energy extraction at Portland Bill, southern UK predicted from a numerical model. In A. Falcão, editor, *Seventh European Wave and Tidal Energy Conference*, Porto, Portugal, 2007.

L. Blunden and A. Bahaj. Tidal energy resource assessment for tidal stream generators. *Proceedings of the Institution of Mechanical Engineers, Part A: Journal of Power and Energy*, 221(2):137–146, 2007.

L. S. Blunden and A. S. Bahaj. Comparison of different approaches to site selection for tidal stream energy resource assessment. In *Second International Conference on Renewable Energy in Maritime Island Climates*, Dublin, Ireland, 26–28 April 2006. The Solar Energy Society.

---

[*] Awarded Best Paper in the Marine category

[†]L. S. Blunden and A. S. Bahaj. Initial evaluation of tidal stream energy resources at Portland Bill, UK. *Renewable Energy*, 31(2):121–132, 2006.

L. S. Blunden and A. S. Bahaj. A high resolution model of the English Channel for tidal stream resource assessment. In C. Johnstone and A. D. Grant, editors, *6th European Wave and Tidal Energy Conference*, Glasgow, UK, 29 August–2 September 2005.

[†] Part of the work for this article was completed by the author prior to starting this PhD

Appendix B

MATLAB functions

B.1 Function NEW_LOG_PROFILE

This MATLAB function was written to process the algebra outlined in §6, solving for u_{H+} in terms of z_{0-} and λ. The variable names are intuitive, for example `uHminus` represents u_{H-}.

```
function new_profile
% Added roughness model for tidal turbines
% Luke Blunden 2009

% clear Maple kernel
maple restart

% Define variables as elements of R+
syms b cD cDprime dprime F g h S0 S0minus S0plus T tau...
     uHminus uHplus ustarminus ustarplus ustarplusL...
     z z0minus z0prime z0plus zHprime zH0prime Zprime...
     alpha kappa lambda positive

% Dimensionless variables
z0minus=z0prime*h;
zHprime=zH0prime*z0prime;
zH=zHprime*h;


% In the absence of turbines:

%- log profile flow velocity
uminus=ustarminus*(1/kappa)*log(z/z0minus)

%- free surface slope
ustarminus1=uHminus/((1/kappa)*log(zH/z0minus));
ustarminus2=sqrt(g*S0minus*h);
e=ustarminus1-ustarminus2;
S0minus=solve(e,S0minus)

% - depth averaged velocity
Uminus=int(uminus,z,0,h)
Uminus=Uminus/h

%- friction coefficient
cfminus = 2*ustarminus1^2/Uminus^2;
cfminus = simplify(cfminus)


% With turbines present
% fraction of upstream drag on bed when turbines are present
Alpha = (uHplus/uHminus)^2

%- area-averaged thrust on turbines
T=(1/2)*cD*uHplus^2*lambda

%- frictional stress on bed
F = (1/2)*Alpha*cfminus*Uminus^2

```

```
%- zero-plane displacement
dplus=T*zH/(T+F);
dplus=simplify(dplus)
pretty(dplus)

%- friction velocity 1
ustarplus1=sqrt(g*S0plus*(h-dplus));
ustarplus1=subs(ustarplus1,S0plus,b*S0minus);
ustarplus1=simplify(ustarplus1)
findsym(ustarplus1)

%- friction velocity 2
ustarplus2=sqrt(T+F)
ustarplus2=simplify(ustarplus2)
findsym(ustarplus2)

%- solve for uHplus and z0plus
e=ustarplus1-ustarplus2;
uHplus=solve(e,uHplus)
findsym(uHplus)

%- roughness length
uHplus2=ustarplus1/kappa*log(zH/z0plus)
e=uHplus-uHplus2;
z0plus=solve(e,z0plus)
findsym(z0plus)

%- upper velocity profile
uplusU=ustarplus1/kappa*log((z-dplus)/z0plus)

%- lower velocity profile
uplusL=ustarplusL/kappa*log(z/z0minus);

%- hub height velocity 3
uHplus3=subs(uplusL,z,zH);

%- lower profile friction velocity
e=uHplus3-uHplus;
ustarplusL1=solve(e,ustarplusL);
ustarplusL=subs(ustarplusL1)
findsym(ustarplusL)


% vertical average of velocity with turbines present
%- lower profile
UplusL=int(uplusL,z,0,zH)
findsym(UplusL)

%- upper profile
UplusU=int(uplusU,z,zH,h)
findsym(UplusU)

%- vertical average
Uplus=(UplusL+UplusU)/h
findsym(UplusU)

% Equivalent drag coefficient
tau=(1/2)*(cfminus+lambda*cDprime)*Uplus^2;
% e=tau-ustarplus2^2;
% cDprime=solve(e,cDprime);
% findsym(cDprime)

% case of constant free-surface slope
uHplus_CS=subs(uHplus,b,1)
% cDprime_CS=subs(cDprime,b,1)

% case of constant depth-averaged velocity
% e=Uminus-Uplus;
% e=simplify(e);
% b_CV=solve(e,b)
% uHplus_CV=subs(uHplus,b,b_CV)
% cDprime_CV=subs(cDprime,b,b_CV)
% findsym(uHplus_CV)

save('symbolic_expressions')
```

B.2 Function EVAL_NEW_LOG_PROFILE

This MATLAB function was written to numerically evaluate the expressions solved in §B.1

```
function [uHplus_val,Uplus_val,Uminus_val,...
    dplus_val,z0plus_val,ustarplus_val,b_CV]=eval_new_profile(...
    B,cD_val,h_val,lambda_val,uHminus_val,zH_val,z0minus_val)
maple restart

```

```
load symbolic_expressions.mat
kappa_val=0.4;
digits(6)

% re-dimensionalize
zH0prime_val=zH_val./z0minus_val;
z0prime_val=z0minus_val/h_val;

% upstream friction velocity
ustarminus_val=ustarminus1;
ustarminus_val=subs(ustarminus_val,{kappa,uHminus},...
    {kappa_val,uHminus_val});
ustarminus_val=subs(ustarminus_val,'zH0prime',zH0prime_val);
ustarminus_val=double(ustarminus_val);

% upstream depth average velocity
Uminus_val=Uminus;
Uminus_val=subs(Uminus_val,{kappa,uHminus,'zH0prime','z0prime','h','ustarminus'},...
    {kappa_val,uHminus_val,zH0prime_val,z0prime_val,h_val,ustarminus_val});
Uminus_val=double(Uminus_val);

% downstream displacement height
dplus_val=subs(dplus,{cD,h,kappa,lambda,uHminus,'zH0prime','z0prime'},...
    {cD_val,h_val,kappa_val,lambda_val,uHminus_val,zH0prime_val,z0prime_val});
dplus_val=double(dplus_val);

% downstream lower profile friction velocity
ustarplusL_val=subs(ustarplusL1,{cD,h,kappa,lambda,uHminus},...
    {cD_val,h_val,kappa_val,lambda_val,uHminus_val});
ustarplusL_val=subs(ustarplusL_val,zH0prime,zH0prime_val);
ustarplusL_val=subs(ustarplusL_val,z0prime,z0prime_val);
ustarplusL_val=subs(ustarplusL_val,ustarminus,ustarminus_val);

% downstream roughness height (upper profile)
z0plus_val=subs(z0plus,{cD,h,kappa,lambda,uHminus,'zH0prime','z0prime','ustarplusL'},...
    {cD_val,h_val,kappa_val,lambda_val,uHminus_val,zH0prime_val,z0prime_val,ustarplusL_val});
z0plus_val=double(z0plus_val);

% downstream depth averaged velocity
Uplus=subs(Uplus,{cD,h,kappa,lambda,uHminus,'zH0prime','z0prime','ustarplusL'},...
    {cD_val,h_val,kappa_val,lambda_val,uHminus_val,zH0prime_val,z0prime_val,ustarplusL_val});

% value of b for constant flow velocity
e=Uminus_val-Uplus;
b_CV=solve(e,b);
b_CV=double(b_CV);
b_val=1+B*(b_CV-1);

% downstream upper friction velocity
ustarplus_val=subs(ustarplus2,{cD,h,kappa,lambda,uHminus,'zH0prime','b'},...
    {cD_val,h_val,kappa_val,lambda_val,uHminus_val,zH0prime_val,b_val});

% downstream depth-average velocity
Uplus_val=subs(Uplus,'b',b_val);
Uplus_val=double(Uplus_val);

% hub height velocity - case of variable slope
uHplus_val=subs(uHplus,{cD,h,kappa,lambda,uHminus},...
    {cD_val,h_val,kappa_val,lambda_val,uHminus_val});
uHplus_val=subs(uHplus_val,'zH0prime',zH0prime_val);
uHplus_val=subs(uHplus_val,'z0prime',z0prime_val);
uHplus_val=subs(uHplus_val,'ustarplusL',ustarplusL_val);
uHplus_val=subs(uHplus_val,ustarminus,ustarminus_val);
uHplus_val=subs(uHplus_val,'b',b_val);
uHplus_val=double(uHplus_val);

% back substitute for new friction velocity
ustarplus_val=subs(ustarplus_val,'uHplus',uHplus_val);
ustarplus_val=double(ustarplus_val);




% cDprime
% cDprime_val=subs(cDprime,{cD,h,kappa,lambda,uHminus,'zH0prime','z0prime','b'},...
%     {cD_val,h_val,kappa_val,lambda_val,uHminus_val})
% cDprime_val=vpa(cDprime_val)
% cDprime_val=subs(cDprime_valzH0prime_val)
% cDprime_val=subs(cDprime_val,,z0prime_val)

% double(cDprime_val)


% vpa(b_CV)
% vpa(uHplus_CV)
%save('evaluated_expressions')
```

Appendix C

Fortran-90 user subroutines

This appendix includes subroutines which were either created or substantially re-written for the work described in the thesis and relate to important aspects of the numerical models therein. The full user Fortran source files used in the compilation of the various models, are included on the accompanying disk.

C.1 Subroutine DRAGFO

This subroutine is part of the TÉLÉMAC distribution and can be modified by the user to impose forces in the mesh. It is called from the main program to calculate and return the nodal forces due to the simulated turbines. It also calculates the power dissipation by the forces, which are stored in variables and written to file.

```
SUBROUTINE DRAGFO(FUDRAG,FVDRAG)

   !**********************************************************************
   ! TELEMAC 2D VERSION 5.2            01/03/90      J-M HERVOUET
   ! Edited by Luke Blunden (LB) 14/01/05
   !                              10/11/06 sorted out area problem.
   !                              17/11/06 minor changes to output
   !                              01/12/06 sorted another problem with area
   !                              07/10/06 included power calculation
   !**********************************************************************
   !
   !  USER SUBROUTINE DRAGFO
   !
   !  FUNCTION   : ADDING THE DRAG FORCE OF VERTICAL STRUCTURES IN THE
   !               MOMENTUM EQUATION.
   !
   !  FU IS THEN USED IN THE EQUATION AS FOLLOWS :
   !
   !  DU/DT + U GRAD(U) = - G * GRAD(FREE SURFACE) +..... + FU_IMP * U
   !
   !  AND THE TERM FU_IMP * U IS TREATED IMPLICITLY.
   !
   !----------------------------------------------------------------------
   !  ARGUMENTS
   ! .----------------.----.---------------------------------------------
   ! |       NOM      |MODE|                    ROLE
```

```
!  |----------------|----|--------------------------------------------
!  |      FU,FV     |<-->| COEFFICIENTS WHERE TO ADD THE FRICTION TERM.
!  |----------------|----|--------------------------------------------
! MODE : -->(DONNEE NON MODIFIEE), <--(RESULTAT), <-->(DONNEE MODIFIEE)
!-----------------------------------------------------------------------
!
! PROGRAMME APPELANT : fricti (in turn called by moment, propag, thomps)
! PROGRAMMES APPELES : RIEN EN STANDARD
!
!***********************************************************************

use BIEF
use DECLARATIONS_TELEMAC2D

implicit none

! Create a new data structure for a turbine array
! in this case for East-West principal orientation
type turbine_array

    integer :: n_lon=1 ! number of longitudinal rows (x-direction)
    integer :: n_lat=1 ! number of lateral rows (y-direction)
    integer :: n_pos=160 ! turbines per grid point
    real(8) :: d_lon=80. ! longitudinal spacing (m)
    real(8) :: d_lat=32. ! lateral spacing (m)
    real(8) :: bottom_left_x=368580. ! x coordinate of most SW turbine/s  (m)
    real(8) :: bottom_left_y=66070. ! y (m)
    integer :: n_box=4 ! number of vertices of polygon surrounding turbines.

    ! Co-ordinates specifying polygon surrounding turbine/s (at 0,0 m)
    real(8) :: box_x(4)=(/-840.,840.,840.,-840./)
    real(8) :: box_y(4)=(/-608.,-608.,608.,608./)

end type turbine_array

! New turbine array
type(turbine_array) :: ta

integer LNG,LU
common/INFO/LNG,LU

! These are the variables returned to the main program
type(BIEF_OBJ), intent(INOUT) :: FUDRAG,FVDRAG

! General variables
integer IELEM,I,I4,j,k,dragfo_called,m,idx(1000),n_inpoly
real(8) UNORM,AIRE,SOM,XSOM(4),YSOM(4),X4,Y4,UDRAG,SOM11,depth
real(8), parameter :: C_D=0.8, & ! Drag coefficient
      A_turbine=201.06, & ! Turbine swept area m**2
      U_design=2.5 ! Rated speed m/s

! Initialize counters
dragfo_called=dragfo_called+1; m=0

! Integrate basis functions
call VECTOR (T1,'=','MASBAS␣␣␣␣␣␣␣␣␣␣',UN%ELM,1.D0,S,S,S,S,S,S,MESH,.false.,S)

! Copy vector UN onto vector FUDRAG
call CPSTVC(UN,FUDRAG)
call CPSTVC(VN,FVDRAG)

! If this is the first time the subroutine has been called
if(dragfo_called.eq.1) then

    ! Allocate new vectors (not declared in header)
    call allvec(1,fdrag,'fdrag',UN%ELM,1,2)
    call allvec(1,pdrag,'pdrag',UN%ELM,1,2)
    call allvec(1,pvdrag,'pvdrag',VN%ELM,1,2)
    call allvec(1,pudrag,'pudrag',UN%ELM,1,2)

!!$      call allvec(1,PRIVE%ADR(1)%P,'PRIVE1',UN%ELM,1,2)

    ! AIRE is the total area of elements with nodes in the polygon
    ! Initialize AIRE to zero
    AIRE=0.D0

    ! Output rows times columns for the array
    write(LU,*) 'along',ta%n_lon,'␣␣␣␣␣␣down',ta%n_lat

    ! For each component of the array
    do j=1,ta%n_lon

        do k=1,ta%n_lat

            ! Calculate co-ordintes of polygon of influence for component
            XSOM = ta%box_x + ta%bottom_left_x + ta%d_lon*(j-1)
            YSOM = ta%box_y + ta%bottom_left_y + ta%d_lat*(k-1)
            write(LU,*) 'XSOM',XSOM
            write(LU,*) 'YSOM',YSOM

            ! NBPTS returns number of points in domain for the discretization in the argument
            ! 11 corresponds to P1 triangles
            do I=1,NBPTS(11)

                ! If P1 point is in polygon
                ! uses undocumented subroutine INPOLY in BIEF
                if(INPOLY(X(I),Y(I),XSOM,YSOM,ta%n_box)) then
                  m=m+1
                  idx(m)=I
```

```

                        ! Increment AIRE by the integral of the basis function for node I
                        AIRE = AIRE + T1%R(I)

                        ! Ouput some information
                        if(m.eq.1) then
                            write(LU,*) 'No.␣Node␣XCoord␣YCoord␣ElementArea(m)'
                        end if

                        write(LU,fmt='(I6,I7,1X,2(F7.0,1X),F9.0)') m,I,X(I),Y(I),T1%R(I)

                    end if

                end do

                ! calculate reciprocal of P1 area
                SOM11=1.D0/AIRE
                write(6,*) 'total␣area␣P1', AIRE
                n_inpoly=m

                ! If the element type is actually 'quasi-bubble' (4-node triangle), rather than P1
                if(FU%ELM.eq.12) then
                    write(LU,*) 'Q.B.␣called'

                    ! For each element
                    do IELEM = 1 , NELEM

                        ! N.B. absolute subscript.  I4 is the index of the 4th node of q-b triangle
                        I4=IKLE%I(IELEM+3*NELMAX) !

                        ! Average x and y positions (centroid)
                        X4=(X(IKLE%I(IELEM          ))+ &
                               X(IKLE%I(IELEM+  NELMAX))+                  &
                               X(IKLE%I(IELEM+2*NELMAX)))/3.D0
                        Y4=(Y(IKLE%I(IELEM          ))+ &
                               Y(IKLE%I(IELEM+  NELMAX))+                  &
                               Y(IKLE%I(IELEM+2*NELMAX)))/3.D0

                        ! If the extra node is in the polygon
                        if(INPOLY(X4,Y4,XSOM,YSOM,ta%n_box)) then

                            ! Add extra area belonging to 4th node
                            AIRE = AIRE + T1%R(I4)

                        end if

                    end do

                end if

                ! Avoid division by zero
                if(.not.(AIRE.lt.1.)) then

                    ! Calculate reciprocal of total area
                    SOM = 1.D0 / AIRE

                end if

            end do

        end do

        ! Compare q-b total area with P1 total area
        ! SUM is a function in BIEF, hence convoluted expression for array sum
        write(LU,*) 'AIRE␣',AIRE, 'sum␣',dot_product(spread(1,1,n_inpoly),T1%R(idx))

    end if

    ! Copy vectors into new ones
    call CPSTVC(UN,fdrag)
    call CPSTVC(VN,pdrag)
    call CPSTVC(UN,pudrag)
    call CPSTVC(VN,pvdrag)

    ! Initialize new vectors to zero
    call OS('X=C␣␣␣␣␣',FUDRAG,FUDRAG,FUDRAG,0.D0)
    call OS('X=C␣␣␣␣␣',FVDRAG,FVDRAG,FVDRAG,0.D0)
    call OS('X=C␣␣␣␣␣',fdrag,fdrag,fdrag,0.D0)
    call OS('X=C␣␣␣␣␣',pdrag,pdrag,pdrag,0.D0)

    ! Initialize power 'components' vectors to UN and VN respectively
    call OS('X=Y␣␣␣␣␣',pudrag,UN,pudrag,1.D0)
    call OS('X=Y␣␣␣␣␣',pvdrag,VN,pvdrag,1.D0)

    ! Loop over nodes selected as being in the polygon at first time-step
    do m=1,n_inpoly

        ! Calculate normal flow speed, leaving residual to avoid dividing by zero
        UNORM = max(sqrt(UN%R(idx(m))**2+VN%R(idx(m))**2), 0.01)

        ! Find speed to use in calculating drag force (<=rated)
        UDRAG = min(UNORM, U_design)

        ! Find depth, avoid division by zero
        depth = max(H%R(idx(m)), 0.01)

        ! Calculate drag force for given speed, with prescribed turbine drag coefficient
        ! Multiply by number of turbines
        ! fdrag will be used later on
```

```

        fdrag%R(idx(m))  =  0.5 * A_turbine * C_D * UDRAG**2 * ta%n_pos

        ! Calculate values that are passed back to main program
        ! Divide by normal speed (will be multiplied by velocity components)
        ! Divide by depth (depth-averaged)
        FUDRAG%R(idx(m)) = (-1D0)*fdrag%R(idx(m))/(UNORM*depth)
        FVDRAG%R(idx(m)) = FUDRAG%R(idx(m))

        ! Write some output at 24h elapsed (simulation time)
        if(dragfo_called.eq.2880) then
            if(m.eq.1) then
                write(LU,*)  'No.␣X␣Y␣␣U_norm(m/s)␣U_drag(m/s)␣Depth(m)␣DragForce(m^3s^-2)'
                write(LU,fmt='(I4,1X,2(F7.0,1X),2(F5.2,1X),F5.1,1X,F13.5)') &
                  m,X(idx(m)),Y(idx(m)),UNORM,UDRAG,H%R(idx(m)),FUDRAG%R(idx(m))
            end if
        end if

    end do

    ! If q-b elements, change discretization of FUDRAG etc from P1 (11) to q.b. (12)
    if(FU%ELM.eq.12) then
        call CHGDIS(FUDRAG,11,12,MESH)
        call CHGDIS(FVDRAG,11,12,MESH)
        call CHGDIS(fdrag,11,12,MESH)
        call CHGDIS(pudrag,11,12,MESH)
        call CHGDIS(pvdrag,11,12,MESH)
        call CHGDIS(pdrag,11,12,MESH)
    end if

    ! Divide through by total area related to selected nodes to give force per unit area
    call OS('X=CX␣␣␣␣',FUDRAG,T1,T1,SOM)
    call OS('X=CX␣␣␣␣',FVDRAG,T1,T1,SOM)
    call OS('X=CX␣␣␣␣',fdrag,T1,T1,SOM)

    ! Write some output at 24h (simulation time)
    if(dragfo_called.eq.2880) then ! 24 hr
        write(LU,*)  'No.␣X␣Y␣Depth(m)␣fdrag'
        write(LU,fmt='(I4,1X,2(F7.0,1X),F5.1,1X,F13.5)') 1,X(idx(1)),Y(idx(1)),H%R(idx(1)),fdrag%R(idx(1))
    end if

    ! Multiply by force by velocity components, nodewise, to get power
    call OS('X=XY␣␣␣␣',pudrag,fdrag,pudrag,1D0)
    call OS('X=XY␣␣␣␣',pvdrag,fdrag,pvdrag,1D0)

    ! Find the norm of the power 'components'
    call OS('X=N(Y,Z)␣␣',pdrag,pudrag,pvdrag,1D0)

    if(dragfo_called.eq.2880) then ! 24 hr
        write(LU,*)  'No.␣X␣Y␣Depth(m)␣pdrag'
        write(LU,fmt='(I4,1X,2(F7.0,1X),F5.1,1X,F13.5)') 1,X(idx(1)),Y(idx(1)),H%R(idx(1)),pudrag%R(idx(1))
    end if

    ! Multiply nodal power values by basis functions and integrate nodewise
    ! Gives rate of working of all the forces
    call VECTOR(PRIVE%ADR(1)%P,'=','MASVEC␣␣␣␣␣␣␣␣␣␣',12,rho,pdrag,S,S,S,S,S,MESH,.false.,S)

    ! Output the sum of all the powers (with q-b discretization)
    if(FU%ELM.eq.12) then
        if(mod(dragfo_called,120).eq.0) then
            write(LU,fmt='("TOTAL␣POWER␣q.b.␣␣",F7.3,"␣␣MW")') sum(PRIVE%ADR(1)%P)/1.D6
        end if
    end if

    ! Change discretization from q-b to P1 for output to file
    call CHGDIS(PRIVE%ADR(1)%P,12,11,MESH)

    ! Check power values are OK
    if(mod(dragfo_called,120).eq.0) then
        write(LU,fmt='("TOTAL␣POWER␣P1␣␣",F7.3,"␣␣MW")') sum(PRIVE%ADR(1)%P)/1.D6
    end if

    return
end subroutine DRAGFO
```

C.2 Module TIDAL_HARMONIC_DATA

This module defines data structures and values of constants that are used to specify prescribed tidal elevations in both the English Channel and Portland Bill TÉLÉMAC models.

```
module tidal_harmonic_data ! Luke Blunden 2006

  ! This module defines variables and structures required for imposed tidal elevations

  implicit none

  integer,parameter :: n_con=19 ! number of constituents defined in module
  real(8),target :: V_eq(n_con) ! astronomical argument of constituents
  real(8) N,per ! equilibrium phase of lunar ascending node, perihelion
  real(8) time_h ! time in hours

  ! Declare year, day
  integer,parameter :: YEAR = 2003, DAY = 1
  ! years, days elapsed since 1900 (including leap days)
  integer,parameter :: YEARS     = YEAR - 1900, DAYS_0 = (DAY - 1) + (YEARS - 1)/4

  ! Define new data structure for tidal constituent
  type con
     integer i_con
     character*8 name
     real(8) frequency
     integer i_b ! Doodson integers
     integer i_c
     integer i_d
     integer i_f
     real(8) constant
  end type con

  ! New data structure for a single tidal elevation
  type har
     real(8) :: amplitude
     real(8) :: phase
     logical :: present
  end type har

  ! Data structure for tidal elevation at a point in space
  type point
     character(len=32) :: name
     real(8) :: x
     real(8) :: y
     type(har) harmonics(n_con)
  end type point

  ! Structure defining limits of boundary
  type boundary
     type(point) start
     type(point) end
  end type boundary

  ! Specify an array of tidal elevation constituents
  type(con),target :: constituents(n_con) = (/&
       ! number    name     frequency (deg/hr)  i_b  i_c  i_d  i_f  constant (deg)
       con(1,        'Z0',       0.0000000,       0,0,0,0,            0), &
       con(2,        'SA',       0.0410686,       0,1,0,0,            0), &
       con(3,        'O1',      13.9430356,      -2,1,0,0,          270), &
       con(4,        'K1',      15.0410686,       0,1,0,0,           90), &
       con(5,       '2N2',      27.8953548,      -4,2,2,0,            0), &
       con(6,        'MU2',     27.9682084,      -4,4,0,0,            0), &
       con(7,        'N2',      28.4397295,      -3,2,1,0,            0), &
       con(8,        'NU2',     28.5125831,      -3,4,-1,0,           0), &
       con(9,        'M2',      28.9841042,      -2,2,0,0,            0), &
       con(10,       'LAMBDA2',29.4556253,       -1,1,0,0,          180), &
       con(11,       'L2',      29.5284789,      -1,2,-1,0,         180), &
       con(12,       'S2',      30.0000000,       0,0,0,0,            0), &
       con(13,       'K2',      30.0821373,       0,2,0,0,            0), &
       con(14,      '2SM2',     31.0158958,       2,-2,0,0,           0), &
       con(15,       'MN4',     57.4238337,      -5,4,1,0,            0), &
       con(16,       'M4',      57.9682084,      -4,4,0,0,            0), &
       con(17,       'MS4',     58.9841042,      -2,2,0,0,            0), &
       con(18,       'M6',      86.9523127,      -6,6,0,0,            0), &
       con(19,      '2MS6',     87.9682084,      -4,4,0,0,            0)/)

  ! Create an array for amplitude and phase corrections due to the nodal cycle
  type(har),target,dimension(n_con) :: nodal_corrections

  ! Specify tidal constituents at tide gauge locations
  ! Regular Mercator co-ordinates (m) except where specified OSNG
  type(point),target :: &

       DOV=point('Dover',147022.D0,6634105.D0, (/&
       !              H/cm          phase/deg        present?
       har(       376.4,            0.0,    .false.),& !        ZO
       har(         6.4,          214.0,    .false.),& !        SA
       har(         5.6,          175.8,    .false.),& !        O1
```

```
    har(     5.0,      33.6,  .false.),& !       K1
    har(     9.0,     267.7,  .false.),& !      2N2
    har(     8.7,      48.1,  .false.),& !      MU2
    har(    41.3,     309.0,  .false.),& !       N2
    har(     9.9,     306.6,  .false.),& !      NU2
    har(   226.5,     331.3,  .true. ),& !       M2
    har(     5.9,     323.6,  .false.),& !  LAMBDA2
    har(     9.7,     337.3,  .false.),& !       L2
    har(    71.5,      22.8,  .true. ),& !       S2
    har(    20.6,      20.4,  .false.),& !       K2
    har(     5.1,     220.9,  .false.),& !     2SM2
    har(     9.1,     198.1,  .false.),& !      MN4
    har(    26.4,     219.5,  .false.),& !       M4
    har(    16.9,     271.9,  .false.),& !      MS4
    har(     6.7,     101.0,  .false.),& !       M6
    har(     6.8,     146.5,  .false.) & !     2MS6
    /)), &

   CAL=point('Calais',205558.D0,6608325.D0, (/&
    !          H/cm         phase/deg      present?
    har(   404.7,       0.0,  .false.),& !       ZO
    har(     7.9,     258.2,  .false.),& !       SA
    har(     5.0,     138.3,  .false.),& !       O1
    har(     1.4,      53.6,  .false.),& !       K1
    har(     3.4,     347.3,  .false.),& !      2N2
    har(     9.6,      65.6,  .false.),& !      MU2
    har(    45.8,     317.3,  .false.),& !       N2
    har(    10.9,     308.0,  .false.),& !      NU2
    har(   249.4,     340.4,  .true. ),& !       M2
    har(     5.9,     337.6,  .false.),& !  LAMBDA2
    har(    19.5,     348.1,  .false.),& !       L2
    har(    78.4,      32.2,  .true.),& !        S2
    har(    23.3,      30.6,  .false.),& !       K2
    har(     5.1,     240.0,  .false.),& !     2SM2
    har(    10.1,     209.0,  .false.),& !      MN4
    har(    25.1,     237.4,  .false.),& !       M4
    har(    15.9,     290.6,  .false.),& !      MS4
    har(     6.0,     128.4,  .false.),& !       M6
    har(     5.8,     176.7,  .false.) & !     2MS6
    /)), &

   LCQ=point('Le_Conquet',-531989.D0,6160036.D0, (/&
    !         H/cm         phase/deg      present?
    har(   402.4,       0.0,  .false.),& !       ZO
    har(     8.9,     252.3,  .false.),& !       SA
    har(     6.5,     323.7,  .false.),& !       O1
    har(     6.6,      73.1,  .false.),& !       K1
    har(     6.0,      80.4,  .false.),& !      2N2
    har(     7.8,     101.3,  .false.),& !      MU2
    har(    41.2,      90.6,  .false.),& !       N2
    har(     7.7,      88.1,  .false.),& !      NU2
    har(   202.1,     110.2,  .true. ),& !       M2
    har(     2.1,      86.3,  .false.),& !  LAMBDA2
    har(     7.7,      93.7,  .false.),& !       L2
    har(    73.6,     149.7,  .true. ),& !       S2
    har(    21.2,     147.3,  .false.),& !       K2
    har(     1.4,     335.4,  .false.),& !     2SM2
    har(     2.2,     101.8,  .false.),& !      MN4
    har(     7.1,     134.8,  .false.),& !       M4
    har(     5.2,     190.9,  .false.),& !      MS4
    har(     1.4,     328.3,  .false.),& !       M6
    har(     1.0,      28.5,  .false.) & !     2MS6
    /)), &

   NEWL=point('Newlyn',-616231.D0,6456761.D0, (/&
    !         H/cm         phase/deg      present?
    har(   321.3,       0.0,  .false.),& !       ZO
    har(     6.4,     197.3,  .false.),& !       SA
    har(     5.3,     342.5,  .false.),& !       O1
    har(     6.5,     108.6,  .false.),& !       K1
    har(     5.4,      76.1,  .false.),& !      2N2
    har(     5.3,     169.9,  .false.),& !      MU2
    har(    33.1,     113.6,  .false.),& !       N2
    har(     7.2,     106.3,  .false.),& !      NU2
    har(   171.7,     133.0,  .true. ),& !       M2
    har(     3.4,     119.5,  .false.),& !  LAMBDA2
    har(     5.8,     137.4,  .false.),& !       L2
    har(    57.9,     177.2,  .true. ),& !       S2
    har(    16.6,     174.8,  .false.),& !       K2
    har(     2.3,      20.9,  .false.),& !     2SM2
    har(     4.1,     138.8,  .false.),& !      MN4
    har(    11.4,     165.0,  .false.),& !       M4
    har(     7.5,     217.5,  .false.),& !      MS4
    har(     0.9,     324.5,  .false.),& !       M6
    har(     1.0,      23.4,  .false.) & !     2MS6
    /)), &

   WEY=point('Weymouth',368537., 78794., (/&       ! OSGB
    !     H/cm         phase/deg      present?
    har(     116.2,       0.0,  .true.),& !        ZO
    har(       6.5,     198.5,  .false.),& !       SA
    har(       4.7,     351.3,  .true.),& !        O1
    har(       8.7,     109.6,  .true.),& !        K1
    har(       1.0,      38.7,  .true.),& !       2N2
    har(      10.9,     193.8,  .true.),& !       MU2
    har(      13.3,     184.6,  .true.),& !        N2
    har(       1.6,     144.4,  .true.),& !       NU2
    har(      59.0,     190.0,  .true. ),& !       M2
    har(       2.9,      99.2,  .true.),& !   LAMBDA2
```

```
      har(       2.6,       120.1,  .true.),&  !        L2
      har(      30.6,       241.2,  .true. ),& !        S2
      har(       8.6,       236.8,  .true.),&  !        K2
      har(       2.3,       356.8,  .true.),&  !      2SM2
      har(       4.9,         0.5,  .true.),&  !       MN4
      har(      14.7,        24.0,  .true.),&  !        M4
      har(       9.0,        80.7,  .true.),&  !       MS4
      har(       6.3,        61.4,  .true.),&  !        M6
      har(       6.8,       104.4,  .true.)&  !       2MS6
      /)), &

      BOU=point('Bournemouth',409486., 90384., (/&    ! OSGB
      !     H/cm          phase/deg       present?
      har(     158.3,         0.0,  .true.),&  !        ZO
      har(       6.6,       215.1,  .false.),& !        SA
      har(       3.8,       343.6,  .true.),&  !        O1
      har(       8.8,       115.4,  .true.),&  !        K1
      har(       2.3,       246.4,  .true.),&  !       2N2
      har(       7.1,       190.8,  .true.),&  !       MU2
      har(      10.8,       246.3,  .true.),&  !        N2
      har(       1.4,       276.5,  .true.),&  !       NU2
      har(      41.7,       272.6,  .true. ),& !        M2
      har(       1.1,        53.7,  .true.),&  !   LAMBDA2
      har(       1.6,        30.8,  .true.),&  !        L2
      har(      18.4,       291.6,  .true. ),& !        S2
      har(       5.3,       292.4,  .true.),&  !        K2
      har(       1.0,       307.1,  .true.),&  !      2SM2
      har(       6.5,         0.4,  .true.),&  !       MN4
      har(      18.4,        20.8,  .true.),&  !        M4
      har(      11.4,        76.8,  .true.),&  !       MS4
      har(       6.9,        78.1,  .true.),&  !        M6
      har(       7.2,       123.0,  .true.)&  !       2MS6
      /)), &

      DEV=point('Devonport',244778., 54293., (/&      ! OSGB
      !     H/cm          phase/deg       present?
      har(     338.9,         0.0,  .true.),&  !        ZO
      har(       6.5,       202.7,  .false.),& !        SA
      har(       5.6,       348.1,  .true.),&  !        O1
      har(       7.6,       111.0,  .true.),&  !        K1
      har(       5.2,        78.2,  .true.),&  !       2N2
      har(      12.1,       192.0,  .true.),&  !       MU2
      har(      31.9,       137.5,  .true.),&  !        N2
      har(       6.9,       118.1,  .true.),&  !       NU2
      har(     168.7,       152.9,  .true. ),& !        M2
      har(       4.9,       120.1,  .true.),&  !   LAMBDA2
      har(       6.5,       139.3,  .true.),&  !        L2
      har(      61.2,       205.2,  .true. ),& !        S2
      har(      17.6,       202.1,  .true.),&  !        K2
      har(       3.9,        17.5,  .true.),&  !      2SM2
      har(       5.0,       110.6,  .true.),&  !       MN4
      har(      14.0,       132.7,  .true.),&  !        M4
      har(       9.6,       188.5,  .true.),&  !       MS4
      har(       2.4,       169.5,  .true.),&  !        M6
      har(       2.3,       220.4,  .true.)&  !       2MS6
      /))

  ! Define some boundaries
  type(boundary),target :: DovCal,  LCqNew, WeyDev, WeyBou

end module tidal_harmonic_data
```

C.3 Subroutine SET_ASTRONOMICAL_ARGUMENT

Given a day of a particular year, this subroutine calculates the phases of the five main astronomical cycles, in order to give the reference phase for each constituent, at the Greenwich meridian. The formulae are derived from Pugh (1987) and Bell et al. (1999).

```
subroutine set_astronomical_argument(DAYS)

  ! Luke Blunden 2006.  Data from TASK-2000 package.

  use tidal_harmonic_data
  implicit none

  ! Astronomical parameters
  ! sel is the time integral of the angular frequency of a sidereal month
  ! hel " " tropical year " "
  ! pprime " " perihelion rotation " "

  real(8) sel, hel, pprime

  ! DAYS is the input argument to the subroutine and is the number
  ! of days elapsed since the start of the year
  integer DAYS

  ! Pointers to Doodson integers
  integer,pointer :: i_b(:), i_c(:), i_d(:), i_f(:)
  real(8),pointer :: constant(:)
  i_b => constituents%i_b
  i_c => constituents%i_c
  i_d => constituents%i_d
  i_f => constituents%i_f
  constant => constituents%constant

  ! Calculate longitudes
  ! Assume linear equation of time
  sel= 277.0247D0 + 129.38481D0*YEARS + 13.17639D0*DAYS
  hel= 280.1895D0 -    0.23872D0*YEARS +  0.98565D0*DAYS
  pprime= 281.2209D0 + 0.17192D0*YEARS

  ! N declared in module tidal_harmonic_data
  ! Time integral of the angular frequency of the lunar ascending node rotation
  N=    259.1568D0 - 19.32818D0*YEARS +  0.05295D0*DAYS

  ! per declared in module tidal_harmonic_data
  ! Time integral of the angular frequency of the lunar perigee rotation
  per= 334.3853D0 +  40.66249D0*YEARS +  0.11140D0*DAYS

  ! V declared in module tidal_harmonic_data
  ! unwrap angles > 360 degrees
  V_eq = dmod(i_b*sel + i_c*hel + i_d*per + i_f*pprime + constant    ,    360.)

end subroutine set_astronomical_argument
```

C.4 Subroutine SET_NODAL_CORRECTIONS

Once subroutine SET_ASTRONOMICAL_ARGUMENT has calculated the value of the phase of the lunar ascending node for that particular day, this subroutine can calculate the necessary corrections to amplitude and phase for each constituent. The formulae are derived from Pugh (1987) and Bell et al. (1999).

```
subroutine set_nodal_corrections(channel)

! Luke Blunden 2006

  use tidal_harmonic_data
  implicit none

  ! M2 nodal corrections
  real(8) fM2,uM2

  ! Terms in nodal modulations for M1 and L2
  real(8) fu1,fu2

  ! Array of pointers
  real(8),pointer,save :: f,udeg
  character(len=8),pointer,save :: constituent_name
  integer i,channel

  ! Calculate nodal amplitude and phase corrections for M2 constituent
  fM2 = 1.0004 - 0.0373*dcosd(N) + 0.0002*dcosd(2*N)
  uM2 = 0.0 - 2.14*dsind(N)

  ! Loop over all the constituents
  do i=1,n_con

     ! Assign internal variable names
     constituent_name => constituents(i)%name
     f => nodal_corrections(i)%amplitude
     udeg => nodal_corrections(i)%phase

     ! Go through each constituent and calculate nodal factors

     ! Diurnal declinational tides strongly influenced
     if(constituent_name.eq.'O1') then
        f= 1.0089 + 0.1871*dcosd(N) - 0.0147*dcosd(2*N) + 0.0014*dcosd(3*N)
        udeg= 10.8*dsind(N) - 1.34*dsind(2*N) + 0.19*dsind(3*N)

     else if(constituent_name.eq.'K1') then
        f= 1.006 + 0.115*dcosd(N) - 0.0088*dcosd(2*N) + 0.0006*dcosd(3*N)
        udeg= -8.86*dsind(N) + 0.68*dsind(2*N) - 0.07*dsind(3*N)

        ! Lunar semi-diurnal tides generally follow M2
     else if(constituent_name.eq.'M2') then
        f=fM2
        udeg=uM2

     else if(constituent_name.eq.'N2') then
        f=fM2
        udeg=uM2

     else if(constituent_name.eq.'2N2') then
        f=fM2
        udeg=uM2

     else if(constituent_name.eq.'MU2') then
        f=fM2
        udeg=uM2

     else if(constituent_name.eq.'NU2') then
        f=fM2
        udeg=uM2

     else if(constituent_name.eq.'LAMBDA2') then
        f=fM2
        udeg=uM2

        ! L2 is complicated by dependence on per as well as N
     else if(constituent_name.eq.'L2') then
        fu1 = 1.0-0.2505*dcosd(2*per)-0.1102*dcosd(2*per-N)-0.0156*dcosd(2*(per-N))-0.037*dcosd(N)
        fu2 = -0.2505*dsind(2*per)-0.1102*dsind(2*per-N)-0.0156*dsind(2*(per-N))-0.037*dsind(N)
        f=dsqrt(fu1**2 + fu2**2)
        udeg=datand(fu2/fu1)

        ! None of the purely solar tides are affected by changes in N
     else if(constituent_name.eq.'S2'.or.constituent_name.eq.'Z0'.or.constituent_name.eq.'SA') then
        f=1.0
        udeg=0.0

        ! Declinational semi-diurnal tide strongly influenced
```

```
     else if(constituent_name.eq.'K2') then
        f= 1.0241 + 0.2863*dcosd(N) + 0.0083*dcosd(2*N) + 0.0015*dcosd(3*N)
        udeg= -17.74*dsind(N) + 0.68*dsind(2*N) - 0.07*dsind(3*N)

     else if(constituent_name.eq.'2SM2') then
        f=fM2
        udeg=uM2

        ! Shallow water tides follow M2 raised to power of number of M2 terms
     else if(constituent_name.eq.'M4') then
        f=fM2**2
        udeg=2*uM2

     else if(constituent_name.eq.'MS4') then
        f=fM2
        udeg=uM2

     else if(constituent_name.eq.'MN4') then
        f=fM2**2
        udeg=2*uM2

     else if(constituent_name.eq.'M6') then
        f=fM2**3
        udeg=3*uM2

     else if(constituent_name.eq.'2MS6') then
        f=fM2**2
        udeg=2*uM2

     else
        write(channel,fmt='(1x,"BORD:␣unidentified␣constituents")')
        stop
     end if
  end do
end subroutine set_nodal_corrections
```

C.5 Subroutine ASSOCIATE_BOUNDARIES_ECHAN

This subroutine is necessary because the pre-processor for TÉLÉMAC MATISSE, re-numbers boundaries and boundary nodes when changes are made to the mesh. There is no guarantee that the relationship between the two will stay the same when the boundary conditions file is re-written. This subroutine ensures that the correct boundaries and nodes are associated with the tide gauges used for interpolation of the amplitudes and phases of tidal elevations, regardless of changes to the boundary conditions file.

```fortran
subroutine associate_boundaries_echan(n_boundary,nodes,liquid_boundary_number,boundaries,channel)

  ! Luke Blunden 2006

  use tidal_harmonic_data

  implicit none

  integer n_boundary,i,a,b,channel
  type(boundary), dimension(n_boundary) :: boundaries
  type(point), dimension(n_boundary) :: nodes
  integer, dimension(n_boundary) :: liquid_boundary_number
  real(8),parameter :: tol=10000.D0

  ! Assign start and end tide gauges to boundary structure
  DovCal=boundary(DOV, CAL);   LCqNew=boundary(LCQ, NEWL)

  ! Loop over all the boundary nodes
  do i=1,n_boundary

     ! Find a node within tol of the start point for first boundary and get the boundary number
     if(dabs(nodes(i)%x - DovCal%start%x).le.tol.and.dabs(nodes(i)%y - DovCal%start%y).le.tol &
          .and.liquid_boundary_number(i).ne.0) then
        a=liquid_boundary_number(i)

        ! Do the same for the second boundary
     else if(dabs(nodes(i)%x - LCqNew%start%x).le.tol.and.dabs(nodes(i)%y - LCqNew%start%y).le.tol &
          .and.liquid_boundary_number(i).ne.0) then
        b=liquid_boundary_number(i)

     end if

  end do

  ! Here the boundaries are associated
  where(liquid_boundary_number.eq.a.and.a.ne.0)
     boundaries = DovCal
  elsewhere(liquid_boundary_number.eq.b.and.b.ne.0)
     boundaries = LCqNew
  elsewhere
     boundaries%start%name = 'not_liquid_boundary'
  end where

end subroutine associate_boundaries_echan
```

C.6 Subroutine ASSOCIATE_BOUNDARIES_PBILL

This subroutine is similar to C.5 above, but is slightly more complicated in that the interpolation is bi-linear, defined by three points. Consequently nodes on a single free boundary, as defined in the boundary conditions file, may belong to one of two interpolation lines. There is a cross-over region where the boundary nodes are arbitrarily assigned to one line. An adjustment is made to the M_2 amplitude and phase at the midpoint in order to bring the simulated amplitudes in the model at Weymouth into line with the actual values.

```fortran
subroutine associate_boundaries_pbill(n_boundary,nodes,liquid_boundary_number,boundaries,channel)

  use tidal_harmonic_data

  implicit none

  integer n_boundary,i,channel
  real(8) A,B,angle
  type(boundary), dimension(n_boundary) :: boundaries
  type(point), dimension(n_boundary) :: nodes
  type(point) WEY_mod
  integer, dimension(n_boundary) :: liquid_boundary_number

! Adjust M2 amplitude and phase at intermediate point
  WEY_mod=WEY
  WEY_mod%harmonics(9)%amplitude=WEY_mod%harmonics(9)%amplitude + 69.
  WEY_mod%harmonics(9)%phase=WEY_mod%harmonics(9)%phase - 12.5

  ! Assign boundaries
  WeyDev=boundary(WEY_mod, DEV);   WeyBou=boundary(WEY_mod, BOU)

  ! Loop over boundary nodes
  do i=1,n_boundary

    ! If the node is on a free boundary
    if(liquid_boundary_number(i).ne.0) then

      ! Subroutine ANGLE returns included angle given three side lengths
      A=angle(nodes(i),WEY,BOU)
      B=angle(nodes(i),WEY,DEV)

      ! If node is on WEY - BOU side of the domain
      if(A.le.90..and.B.gt.90.) then
        boundaries(i)=WeyBou

        ! If node is on DEV - WEY side of the domain
      else if(B.le.90..and.A.gt.90.) then
        boundaries(i)=WeyDev

        ! If node is in crossover region
      else if((A.ge.90..and.B.ge.90.).or.(A.lt.90..and.B.lt.90.)) then

        ! set crossover nodes' coordinates to those of WEY
        boundaries(i)=WeyDev
        nodes(i)%x=WeyDev%start%x
        nodes(i)%y=WeyDev%start%y

      end if

    else

      boundaries(i)%start%name = 'not_liquid_boundary'

    end if

  end do

end subroutine associate_boundaries_pbill
```

C.7 Subroutine INTERPOLATE_HARMONICS

This subroutine receives the data structure containing the co-ordinates of the nodes of the various boundaries defined in the boundary conditions file. The nodes on these mesh boundaries have been previously been associated with the (separate) boundaries defined by tide gauge locations, by subroutine ASSOCIATE_BOUNDARIES_*x*. This subroutine linearly interpolates the amplitudes and phases of the tidal elevation harmonic constituents, according to the distance of the point along a line joining the start and end points (tide gauges).

```fortran
subroutine interpolate_harmonics(n_boundary,bdy_points,bdy,channel)

  ! Luke Blunden 2006

  use tidal_harmonic_data

  implicit none

  integer i, channel
  integer n_boundary ! Number of boundaries defined in domain
  type(boundary),target,dimension(n_boundary) :: bdy
  type(point),target,dimension(n_boundary) :: bdy_points
  real(8),pointer,save :: x1,y1,x2,y2,x,y,H1(:),H2(:),G1(:),G2(:),H(:),G(:)
  real(8) coords(2,3),primed_coords(3),x1prime,x2prime,xprime,alpha,rotat(2)

  ! For each defined boundary
  do i=1,n_boundary

     ! If the boundary is a sea boundary
     if(bdy(i)%start%name.ne.'not_liquid_boundary') then

        ! Set some pointers
        x1 => bdy(i)%start%x
        y1 => bdy(i)%start%y
        x2 => bdy(i)%end%x
        y2 => bdy(i)%end%y
        H1 => bdy(i)%start%harmonics%amplitude
        G1 => bdy(i)%start%harmonics%phase
        H2 => bdy(i)%end%harmonics%amplitude
        G2 => bdy(i)%end%harmonics%phase
        x => bdy_points(i)%x
        y => bdy_points(i)%y
        H => bdy_points(i)%harmonics%amplitude
        G => bdy_points(i)%harmonics%phase

        ! Find out which harmonics are defined at both ends of the boundary
        bdy_points(i)%harmonics%present=(bdy(i)%start%harmonics%present.and.bdy(i)%end%harmonics%present)

        ! 2-D co-ordinate vectors
        coords=reshape(source=(/x1,y1,x2,y2,x,y/), shape=(/2,3/))

        ! Find rotation coefficients
        alpha=DATAN((y2 - y1)/(x2 - x1))
        rotat(1)=DCOS(alpha); rotat(2)=DSIN(alpha)

        ! Transform coordinates to lines between tide gauges
        ! Multiply by rotation matrix
        primed_coords = MATMUL(rotat, coords)
        x1prime=primed_coords(1)
        x2prime=primed_coords(2)
        xprime=primed_coords(3)

        ! Check for jumps in phase > 180 degrees and correct
        where((G2-G1).ge.180.)
           G1=G1+360
        elsewhere((G1-G2).ge.180.)
           G2=G2+360
        end where

        ! Linearly interpolate amplitudes and phases along primed axis
        H  = H1 + (H2-H1)*(xprime-x1prime)/(x2prime-x1prime)
        G  = G1 + (G2-G1)*(xprime-x1prime)/(x2prime-x1prime)

     end if

  end do

end subroutine interpolate_harmonics
```

C.8 Subroutine BORD

This subroutine is part of the TÉLÉMAC distribution and can be modified by the user to apply boundary conditions as a function of time. In this case the subroutine was modified to impose elevations at the boundary, while leaving the velocities undefined. Only the modified part of the subroutine is shown below.

```
  ! Declare additional variables
  integer        DAYS, bord_called, i, err
  type(point),target :: boundary_nodes(NPTFR)
  type(point),pointer,save,dimension(:) :: ptr_to_boundary_nodes
  type(boundary),target,dimension(NPTFR) :: which_boundary
  type(boundary),pointer,save,dimension(:) :: ptr_to_which_boundary

  ! increment each time subroutine called, initializes to 0 at start of run
  bord_called=bord_called+1

  ! calculate time since beginning of day in decimal hours
  time_h = (dmod(TEMPS,86400.)/3600.)


  ! If second time step, or the first time step of a day
  ! (first call to BORD is at second time step)
  if(time_h.lt.(1./36000.).or.bord_called.eq.1) then

     ! Recalculate number of days
     DAYS        = DAYS_0 + idint((TEMPS)/86400.)

     ! Find astronomical argument for each constituent based on time elapsed since 1900
     ! (recalculated each day)
     call set_astronomical_argument(DAYS)

  end if

  !
  if(bord_called.eq.1) then

     ! Calculate nodal factors. Derived from TASK 2000 code and with reference to D Pugh (1987)
     ! (calculated at start of simulation)
     call set_nodal_corrections(lu)

     ! assign boundary point x and y coordinates
     boundary_nodes%x = MESH%X%R(NBOR)
     boundary_nodes%y = MESH%Y%R(NBOR)

     ! associate boundaries
     call associate_boundaries_pbill(NPTFR,boundary_nodes,NUMLIQ,which_boundary,lu)

     ptr_to_which_boundary => which_boundary

     ! calculate interpolated harmonics for boundary points
     call interpolate_harmonics(NPTFR,boundary_nodes,ptr_to_which_boundary,lu)

     ! Allocate pointers
     ptr_to_boundary_nodes => boundary_nodes

 end if


  !-----------------------------------------------------------------------------------------------
  !
  !  INITIALISATION DE YADEB - integer array of size 100 (max number of liquid boundaries)
  !
  IF(NFRLIQ.GE.1) THEN
     DO K=1,NFRLIQ
        YADEB(K)=0
     END DO
  ENDIF
  !
  !  BOUCLE SUR TOUS LES POINTS FRONTIERE        -         Loop over boundary points
  DO K=1,NPTFR
     ! i.e. if point has imposed H boundary condition and at least 1 liquid boundary exists
     IF(LIHBOR(K).EQ.KENT.AND.NCOTE.NE.0) THEN
        ! i.e. if enough liquid boundaries exist
        IF(NCOTE.GE.NUMLIQ(K)) THEN


           !---------------------------------------------------------------------------

           !                                   LB

           ! Calculate sea surface elevation from sum of constituents and convert from cm to m
           call calculate_z(ptr_to_boundary_nodes(K),time_h,Z,lu)
           Z = Z/100.

           !----------------------------------------------------------------------------
```

Appendix D

Example steering file for TÉLÉMAC-2D

This appendix includes an example of a steering file (formatted file) used for running the simulations described in this thesis for Portland Bill and the English Channel. Comments on the various options are included inline, between pairs of forward slashes. Comment lines begin with a forward slash and strings are delimited by single quotes.

```
TITLE = 'Example␣steering␣file'          /32 characters maximum                                          /


/Compilation
RELEASE : 'V5P4,V5P4,V5P4,V5P4,V5P4,V5P4,V5P4,V5P4,V5P4'         /Libraries linked against              /
PARALLEL PROCESSORS : 0                                          /Number of parallel processes          /
                                                                 /        (invokes MPI if > 0)          /

/File management
STEERING FILE: './example.str'                     /This file                                             /
FORTRAN FILE: '../src/fortran.f90'                 /Contains all user subroutines                         /
BOUNDARY CONDITIONS FILE: '../mesh/boundary.bc'    /Formatted boundary conditions file                    /
GEOMETRY FILE: '../mesh/mesh.geo'                  /Binary mesh file                                      /
RESULTS FILE: '../res/example/example.res'         /Binary results file                                   /
LISTING PRINTOUT PERIOD = 120                      /Interval between listing file output (time steps)     /
GRAPHIC PRINTOUT PERIOD = 30                       /Interval between output to results file (time steps)  /
VARIABLES FOR GRAPHIC PRINTOUTS : 'U,V,S,K,E,N'    /Velocities; free-surface co-ordinate;                 /
                                                   /        TKE; dissipation; user variable               /

/Reference frame
ORIGINAL DATE OF TIME : 2003;01;01      /Only matters when tide-generating potential is included          /
ORIGINAL HOUR OF TIME : 00;00;00        /Of day (As previous)                                             /
TIME STEP = 30.                         /(seconds)                                                        /
DURATION = 2678400                      /Total duration of simulation (seconds)                           /
CORIOLIS = YES                          /Includes Coriolis acceleration                                   /
CORIOLIS COEFFICIENT = 1.122E-4         /Constant in this case (for coastal scale)                        /
SPHERICAL COORDINATES : NO              /Regular Mercator co-ordinates                                    /
TIDE GENERATING FORCE : NO              /Semi-diurnal tidal potential                                     /
LATITUDE OF ORIGIN POINT = 0.0          /For spherical coordinates and variable Coriolis coefficient      /
LONGITUDE OF ORIGIN POINT = 0.0         /For implementation of tide-generating potential                  /


/Initial conditions
INITIAL CONDITIONS : 'CONSTANT␣ELEVATION'          /Across entire domain                                  /
INITIAL ELEVATION = 2.0                            /(metres)                                              /


/Boundary conditions
LAW OF BOTTOM FRICTION: 3               /Strickler's law                                                  /
FRICTION COEFFICIENT = 40               /Strickler K (m^(3^-1)s^(-1))                                     /
PRESCRIBED ELEVATIONS = 100.0;100.0     /dummy value, indicates error in calling BORD user subroutine     /
OPTION FOR LIQUID BOUNDARIES = 2        /Thompson method to find unknown boundary velocities              /
TIDAL FLATS : YES                       /Possibility of wetting and drying                                /


/Turbulence model
TURBULENCE MODEL = 3            /k-epsilon model                                                          /
VELOCITY DIFFUSIVITY = 1.0E-6   /Molecular kinematic viscosity for k-epsilon model                        /


/Energy extraction
VERTICAL STRUCTURES : YES       /Invokes user subroutine DRAGFO to impose momentum sinks                  /


/Finite element scheme
/                               U,V     Depth   TKE     Dissipation
TYPE OF ADVECTION  =            1;      5;      2;      1       /Advection scheme:                        /
                                                                / 1: Method of characteristics            /
                                                                / 2: 'Upwind' Petrov-Galerkin (SUPG)      /
                                                                / 5: SUPG with mass conservation          /
SUPG OPTION :                   1;      2;      1;      1       /For SUPG method,                         /
                                                                / 1: SUPG upwinding = 1                   /
                                                                / 2: SUPG upwinding = Courant number      /
DISCRETIZATIONS IN SPACE =      12;     11;     11;     11      /Type of basis function                   /
                                                                /        11: Linear tiangle               /
                                                                /        12: Quasi-bubble                 /
IMPLICITATION FOR DEPTH = 0.6                                   /1.0 is fully explicit,                   /
IMPLICITATION FOR VELOCITY = 0.6                                /        0.5 is centred in time           /


/Solution of the linear system
INFORMATION ABOUT SOLVER  = YES                         /Print convergence information in listing file   /
MAXIMUM NUMBER OF ITERATIONS FOR SOLVER = 30            /Iterative solver for linear system              /
NUMBER OF SUB-ITERATIONS FOR NON-LINEARITIES = 1        /For non-linear terms                            /
SOLVER ACCURACY = 1.E-4                                 /Tolerance for iterative solver                  /
C-U PRECONDITIONING : YES                               /Replace depth with wave celerity                /
SOLVER : 7                                              /Generalized Minimum RESidual method             /
SOLVER FOR K-EPSILON MODEL : 7                          /GMRES method (for turbulence model)             /
SOLVER OPTION : 4                                       /Dimension of Krylov subspace for GMRES          /
OPTION FOR THE SOLVER FOR K-EPSILON MODEL : 2           /Dimension of Krylov subspace for GMRES          /
MASS-LUMPING ON H : 1.0                                 /Degree of diagonalization for depth matrices    /
                                                        /        0.0--1.0 none---full                    /
INITIAL GUESS FOR H = 2                                 /Extrapolate from values at previous time steps  /
INITIAL GUESS FOR U = 2                                 /        (in order to accelerate convergence)    /
H CLIPPING = NO                                         /Allows -ve depth for mass-balance               /
MASS-BALANCE : YES                                      /check mass balance at each time step            /


&ETA
&FIN
```

Appendix E

Correspondence related to hydrographic survey at Portland

E-mail received 2 October 2006

```
-----Original Message-----
From: Neil Kenyon [mailto:nhk@noc.soton.ac.uk]
Sent: 02 October 2006 10:04
To: a.s.bahaj@soton.ac.uk
Subject: Portland

Dear Professor Bahaj,
        It was good to hear that you have an interest in offshore tidal
power. I am involved in a DTI sponsored study of Portland  as an example of
the sedimentary and benthic biological problems that may be encountered in
tidal power schemes near headlands. We are trying, though hindered by the
poor weather, to complete a survey of the bathymetry and sediments just
south of Portland. It would be very interesting to us to try to measure
currents but there will be logistical difficulties. It would be useful to
meet with your student, Luke Blunden?, and discuss this, as soon as
possible. I am in the NOC today and if not reachable by phone or e-mail
will switch my mobile on (07780662347).
Best regards, Neil


Dr Neil Kenyon, DSc, CGeol
National Oceanography Centre, Southampton
Empress Dock,
Southampton SO14 3ZH,
United Kingdom
```

Coordinator: UNESCO-IOC "Training Through Research" Project, "The Floating University"
website: http://ioc.unesco.org/ttr
Tel +44-(0)2380 596570 (office)
-(0)2380 596555 (secretary)
Fax +44-(0)23 80596554
Email N.Kenyon@noc.soton.ac.uk

E-mail sent 2 October 2006

Date: Mon, 2 Oct 2006 12:05:57 +0100 (GMT Daylight Time)
From: Luke Blunden <lsb1@soton.ac.uk>
To: N.Kenyon@noc.soton.ac.uk
Subject: FW: Portland (fwd)

Dear Dr Kenyon,

Prof. Bahaj forwarded your e-mail onto me, I'm his tidal power student. Your project sounds very interesting and I would certainly like to meet up. I could drop in to the NOC this afternoon, or some time tomorrow, or we could discuss it over the phone.

A powerpoint show of some recent work on energy extraction at Portland can be downloaded from:

http://www.soton.ac.uk/˜lsb1/BlundenWREC06.zip

Regards,

Luke Blunden

E-mail received 10 October 2006

Date: Tue, 10 Oct 2006 11:05:02 +0100
From: Neil Kenyon <nhk@noc.soton.ac.uk>
To: Luke Blunden <lsb1@soton.ac.uk>
Subject: Re: FW: Portland (fwd)

Dear Luke,

Geotek, the company managing the Portland Bill study, are prepared to fund the hire of an ADCP and engineer for a day or two. It would have to be the kind that measure while the boat is underway. It is suggested that as we have missed the Spring tides that we wait for two weeks or so. Would such data be of use to you?

Best wishes, Neil

E-mail sent 10 October 2006

```
Date: Tue, 10 Oct 2006 16:55:24 +0100 (GMT Daylight Time)
From: Luke Blunden <lsb1@soton.ac.uk>
To: Neil Kenyon <nhk@noc.soton.ac.uk>
Cc: A S Bahaj <A.S.Bahaj@soton.ac.uk>
Subject: Re: FW: Portland (fwd)
Parts/Attachments:
   1 Shown     38 lines  Text
   2   OK     992 KB     Application
----------------------------------------
```

Dear Neil,

Yes, the data would be very useful for my work. Even though the record length would be too short for a full harmonic analysis, I could run my model for the measurement days, and then do a validation exercise. It might also be possible to extract some data on turbulence quantities in the flow, which would be of interest - see attached paper.

Best regards,

Luke

E-mail received 25 October 2006

```
Date: Wed, 25 Oct 2006 12:46:45 +0100
From: Neil Kenyon <nhk@noc.soton.ac.uk>
To: LSB1@soton.ac.uk
Subject: Portland
```

Dear Luke,

The survey ended last Friday without much new bathymetry since the previous week and with no video or sampling. The weather was awful. I hope that I can wrote something that will persuade the DTI to give more funds for next year. Dr Quentin Huggett of Geotek, who is the manager of the project for DTI, asks if you or Professor Bakhar Bahaj, would send him a brief e-mail about the value of the current measurements and he will look into whether to fund the measurements.

His e-mail address is Quentin@geotek.co uk

I will provide you with the bathymetry when it is processed.

Best wishes, Neil

E-mail sent 2 November 2006

Date: Thu, 2 Nov 2006 16:15:34 +0000 (GMT Standard Time)
From: Luke Blunden <lsb1@soton.ac.uk>
To: Quentin@geotek.co.uk
Cc: A S Bahaj <A.S.Bahaj@soton.ac.uk>, nhk@noc.soton.ac.uk
Subject: Current measurements at Portland Bill

Dear Dr. Huggett,

I understand from Neil Kenyon that you would like an e-mail outlining the value of current measurements at Portland Bill.

I am a PhD student and part of the Sustainable Energy Research Group in the School of Civil Engineering at the University of Southampton. Our interest in Portland Bill arises from our research into predicting tidal stream energy resources, using numerical modelling techniques. As part of this work, we are trying to assess what effect a large number of tidal stream turbines would have on the flow at the site, which is still an open question.

There are two reasons why current data would be valuable for our work. Firstly, it would provide a means of validation for numerical models of tidal flows around the headland; at the moment data is lacking and we are using Chart Diamonds, which are limited in number and simplified for navigational purposes. Secondly, depending on the method of sampling, the data could be used to derive turbulence quantities in the flow, which are again of interest for validation and also for predicting how the flow would respond to the presence of tidal stream turbines.

Please do not hesitate to contact me if you require further information.

Regards,

Luke Blunden

No further correspondence on this subject

Appendix F

REMIC-2 conference paper

Conference paper presented at the Second International Conference on Renewable Energy in Maritime Island Climates, Dublin, Ireland, 15–20 June 2008 with reference Batten et al. (2006). It is included here as an appendix due to this author's role as a co-author in the paper. The findings are referenced in Chapter 10, §10.2.1.

Yawed Performance of Horizontal Axis Marine Current Turbines

William MJ Batten[*+], AbuBakr S Bahaj[*], Anthony F Molland[**] and Luke S Blunden[*]
Sustainable Energy Research Group, www.energy.soton.ac.uk
[*] School of Civil Engineering and the Environment, University of Southampton, UK,
[**] School of Engineering Sciences, Ship Science, University of Southampton, UK.
[+] Corresponding Author

Abstract

In order to assess the performance horizontal axis marine current turbines in direction varying flows, measurements of a model rotor have made in a towing tank. The model is 1/20th scale of a possible 16m rotor. Results of power and thrust measurements for four yaw angles and two hub pitch angles are presented. Curve fits have been calculated as a function of the cosine of the yaw angle squared and the thrust as cosine of the yaw angle. The curve fits are in good agreement and have been used to compare annual energy output for various designs of fixed orientation and yawed rotors at Portland Bill (Dorset, UK).

Introduction

The oceans around the world offer a large energy source that is yet to be tapped. Although the power from waves and ocean thermal currents are larger, tidal or marine currents with peak flows over five knots (~2.5 m/s), caused by constrained topography, offer an exciting proposition for the extraction of predictable energy [1-3]. Several devices are being studied for marine current energy conversion and many are designed using wind turbine principles.

To an extent, much can be transferred from the design and operation of wind turbines [4] as discussed in [5]. There are however, a number of fundamental differences, which will require further investigation, research and development, such as cavitation [6, 7].

One other unique difference is that many tidal sites are relatively bi-directional. Consequently, some proposed marine current turbines are designed for a fixed orientation to the flow and invert the blades in order to operate the turbine in the reverse direction [8, 9]. The closer the flow is to bi-directional the more efficient theses turbine designs will be. However, some sites around the UK can have flow reversal of 20° or more away from 180°, such as flows around islands [10] and headlands [11].

In order to investigate this flow variation, a 1/20th scale model of a possible 16m diameter horizontal axis tidal turbine has been tested in a towing tank to determine its hydrodynamic characteristics under yawed flow conditions.

This paper presented results that show the impact of various yaw angles on energy capture and rotor thrust. Furthermore, in order to assess the viability of using fixed orientation compared to a yawing device, around Portland Bill, which has a swing upon flow reversal of around 35° from rectilinearity. Curve fitted experimental results have been applied to predictions of the tidal flow [11] and designs chosen to compare annual energy differences.

Experimental Procedure

Measurements of the torque and thrust characteristics of an 800mm rotor in yaw were carried out in a towing tank at Southampton Institute, which a length of 60m, breadth, 3.7m and a depth of, 1.8 m. The maximum carriage speed of 4.5 m/s, but due to design loads, tests were carried out at 1.5 m/s.

The tank has a manned carriage with various computer and instrumentation facilities, which was used to log the carriage speed to an accuracy of 1 per cent. The test rig was mounted from a pair of aluminium channel beams mounted aft of the carriage as shown in Fig 1.

The blades were developed from the profile shape of a NACA 63-8xx and with a chord (*c*), thickness (*t*) and pitch distribution presented in Table 1, where (*R*) is the overall radius (*r*) is the local radius. These were milled on a 5-axis CNC machine from aluminium alloy to an order of accuracy of ±0.05mm. The hub pitch is defined at 20% radius.

The rotor is attached to a main shaft, which drives a DC generator from a pulley though a belt carried up through the vertical support tube (Fig 2). The electrical power is absorbed with rheostats, which also allowed regulation of the rotor speed.

An in-line strain gauge dynamometer mounted next to the turbine was used to measure the thrust and torque. This dynamometer was designed to run wet so measurements could be made before any bearing or seal losses. The strain gauge bridge circuit is connected via a slip-ring assembly to conditioners and output signals were acquired on a computer. Full details of the experimental test rig, models and results are presented in Refs. [6, 12]. The experimental results are

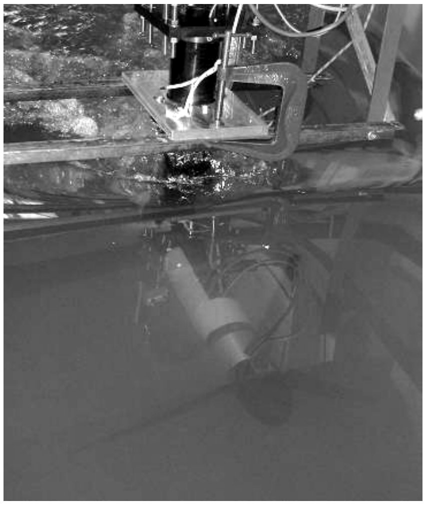

Fig. 1 Photograph of the assembled test rig in the towing tank [12].

Table 1. Particulars of turbine blades [6, 12].

***r*(mm)**	***c*/*R***	**Pitch (deg)**	***t*/*c* %**
80	0.125	20.0	24.0
120	0.116	14.5	20.7
160	0.106	11.1	18.7
200	0.097	8.9	17.6
240	0.088	7.4	16.6
280	0.078	6.5	15.6
320	0.069	5.9	14.6
360	0.059	5.4	13.6
400	0.050	5.0	12.6

corrected for the tank blockage [6, 12] and presented in the established coefficient forms:

$$\text{Tip Speed Ratio,}\quad TSR = \frac{\Omega R}{U_0}, \tag{1}$$

$$\text{Power Coefficient,}\quad C_P = \frac{Q\Omega R}{0.5\rho\pi R^2 U_0^3}, \tag{2}$$

$$\text{Thrust Coefficient,}\quad C_T = \frac{T}{0.5\rho\pi R^2 U_0^2}, \tag{3}$$

where: U_0 is the tidal speed (m/s), Ω the rotation speed (rad/sec), ρ the density of water (kg/m^3) Q the rotor torque (Nm) and T the rotor thrust (N). The blockage corrections when $C_T = 0.8$ amounted to 8% for C_P and 5% for C_T.

Experimental Results

The influence of inflow yaw angle on rotor performance, as tested in the towing tank, is shown in Fig. 3 and 4 for hub pitch angles of 20º and 25º. Both cases show a consistent decrease in power and thrust with increasing yaw angle. For example, for both the 20º and 25º hub pitch angles, a 30º yaw angle reduced the power coefficient by about 30%, whilst the thrust coefficient was reduced by about 15% for the 20º pitch angle and 25% for the 25º pitch angle.

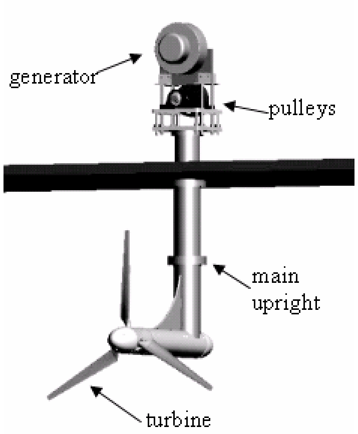

Fig. 2 Visualisation of the experimental rig in the towing tunnel [6].

Momentum theory suggests that the power is proportional to the square of the cosine of yaw angle (γ) and the thrust as a cosine of the yaw angle [6]:

$$C_P = 4a(\cos\gamma - a)^2, \tag{4}$$

$$C_T = 4a(\cos\gamma - a), \tag{5}$$

were a is an axial flow factor.

In order to curve fit the data $a = f(TSR)$ is assumed, therefore the power coefficient was assumed to be of the form:

$$C_p = 4A(\cos\gamma - B)^2, \tag{6}$$

where: $A = c_1 + c_2 TSR$ and $B = c_3 + c_4 TSR$. The thrust coefficient was assumed to be of the form:

$$C_T = 4A(\cos\gamma - B)c_5 + c_6 TSR\ . \tag{7}$$

The coefficients c_1 to c_6 have been found from curve fitting the experimental data points. These are presented in Table 2. All the data was used except the 22.5º pitch angle, which was kept as a check. The fits are presented in Fig. 3 against the experimental data and show good agreement with the data, along with the 22.5º test. This demonstrates that the data fits to the momentum equations and the cosine square rule. These curve fits can therefore be used confidently to compare the effect of fixed and yawing turbines at different locations.

Table 2 Solved constants from curve fitting the yaw experimental data.

Constant	**20º hub pitch**	**25º hub pitch**
c_1	-0.0479	-0.113
c_2	0.0249	0.0634
c_3	-0.765	-0.159
c_4	0.119	0.100
c_5	1.370	1.100
c_6	0.0318	-0.0177

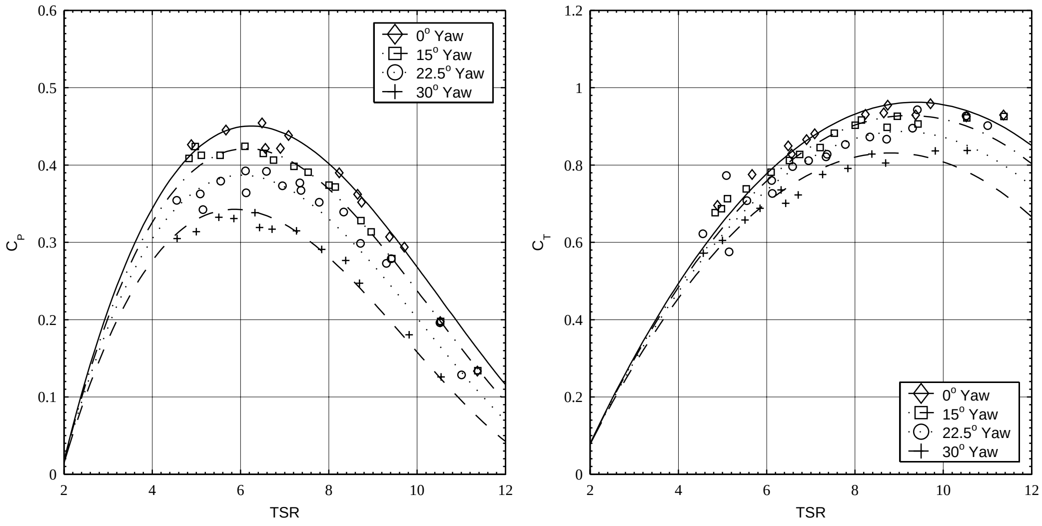

(a) Power Coefficient - 20º hub pitch (b) Thrust Coefficient - 20º hub pitch

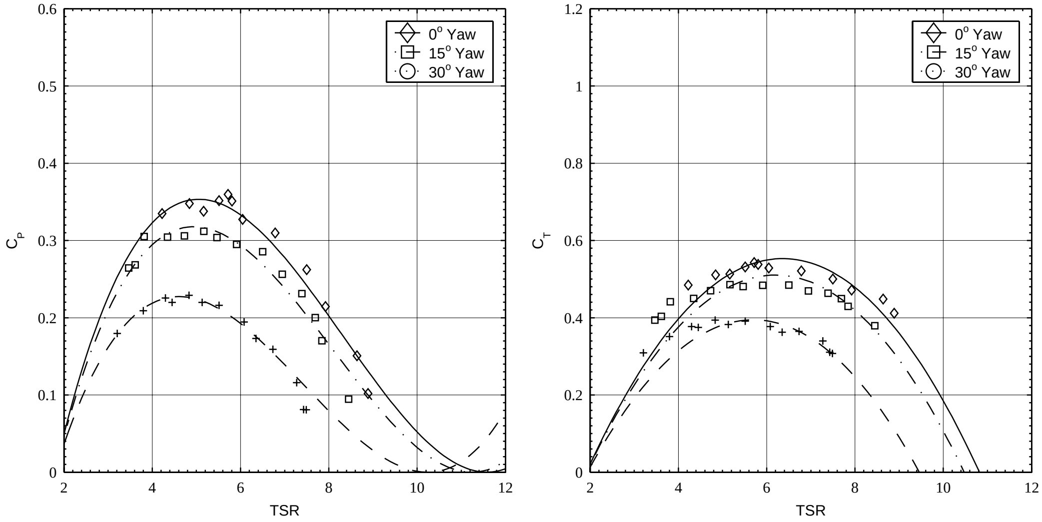

(c) Power Coefficient - 25º hub pitch (d) Thrust Coefficient - 25º hub pitch

Fig. 3 Comparison of the effect of yaw with 20º and 25º hub pitch at towed speed of 1.4 m/s. The symbols are the experimental points [6, 12] and the lines from the curve fits using Eqs. (6) & (7).

Tidal Data Analysis

For example tidal data, simulation results around Portland Bill have been used, this site has a significant swing from the 180º flow reversal, allowing comparisons between fixed orientation and yawing devices. The variation of depth-averaged speed over 28 days from the simulation is shown in Fig. 4. This data has been validated with sea-level elevations and Admiralty chart tidal velocity data. [11]

The velocity of the tidal stream at a point can be represented in complex form *U* as the sum of *N* constituent ellipses, where A_k and B_k are complex (Eq. 8) [14].

$$U(t) = \sum_{k=0,\ldots,N} A_k \mathrm{e}^{\mathrm{i}\sigma_\mathrm{k} t} + B_k \mathrm{e}^{-\mathrm{i}\sigma_\mathrm{k} t} \qquad (8)$$

The constituent frequencies σ are integer combinations of the fundamental astronomical frequencies (including solar day, lunar day, sidereal month and tropical year) and $\sigma_0 = 0$. The properties of the k^{th} ellipse defined in Fig. 5 in real form can be readily calculated from A_k and B_k: the semi-major axis (Eq. 9), semi-minor axis (Eq. 10) and inclination (Eq. 11).

$$\left|\mathbf{U}_k\right|_{\max} = \left|A_k\right| + \left|B_k\right| \qquad (9)$$

$$\left|\mathbf{U}_k\right|_{\min} = \left|\left(\left|A_k\right| - \left|B_k\right|\right)\right| \qquad (10)$$

$$\theta_k = \frac{1}{2}\left[\arg\left(A_k\right) + \arg\left(B_k\right)\right] \qquad (11)$$

The T_TIDE package for MATLAB [13] was used to determine the constituent ellipse properties by harmonic analysis, in which nodal corrections were applied based on the

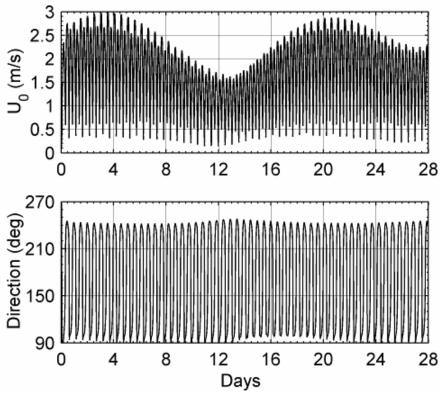

Fig. 4 Simulated tidal velocity data over a lunar month near Portland Bill [13].

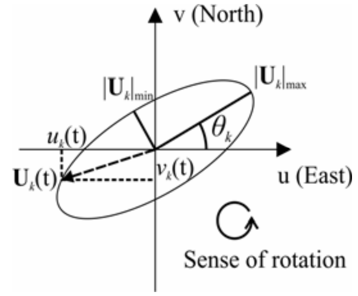

Fig. 5 Diagram illustrating the k^{th} ellipse.

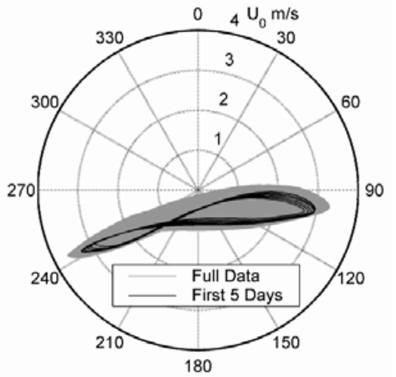

Fig. 6 Hodograph of predicted tidal stream over 2006 – 2024.

Table 3 Ellipse parameter constituents

Constituent	$\lvert \mathbf{U}_k \rvert_{\max}$ **(m/s)**	$\lvert \mathbf{U}_k \rvert_{\min}$ **(m/s)**	$\boldsymbol{\theta_k}$ **(deg)**
M_m	0.108	0.007	87.1
M_{sf}	0.137	0.014	90.9
μ_2	0.149	0.026	8.6
N_2	0.327	0.048	5.3
M_2	2.232	0.151	10.2
S_2	0.726	0.020	14.5
K_2	0.198	0.006	14.5
M_4	0.170	0.007	81.6

central time of the input time series. In this case, T_TIDE was used to produce estimates of signal-to-noise ratio (SNR) for the constituent ellipses by adding Gaussian noise with variance derived from the residual spectrum, to the signal reconstructed from the constituents.

The most significant eight constituents with ellipse semi-major axes over 0.1 m/s and SNR greater than 10 are presented Table 3. Standard nomenclature for the constituents has been used [14]. The two principal constituents are the lunar semi-diurnal (M_2) and solar semi-diurnal (S_2) There is also a significant constant southerly flow of 0.65 m/s.

Based on the constituents, predictions can be made from any start date with any time step. For the predictions in this paper, the tidal stream speeds and directions from the start of 2006 for 18 years have been generated at one minute intervals. A hodograph showing a forecast for 18 years is presented in Fig 6 and first 5 days are shown to demonstrate a typical cycle. The ellipse is offset south due to the constant flow component. This and the constituents with inclination close to 0° or 90° cause the tidal stream to swing away from rectilinearity.

In order to be able to examine this large data set, so that designs could be compared, the tidal data has been 'binned' in a histogram for each year and grouped in west and east data sets. The bins are defined by 1° intervals and in cubed speed steps of 1 m^3/s^3 from 0 to 35 m^3/s^3. Cubed speed steps were used to improve the accuracy of power integrations, as they are directly proportional to the power. (Eq. 2).

The averaged, leap-year corrected data over the 18 years, for both the east and west directions is presented in Fig 7. This averaged data set provides a basis for comparing designs of turbines as demonstrated in the next section.

Energy Yields for Yawed and Fixed Orientation Turbines

For comparisons between fixed and yawing design energy yields have been calculated assuming a 16m diameter turbine with the 'binned' tidal data set. This turbine is the same size as used in the comparisons in [15] and is applicable in this case, as at that location the minimum water depth is 32 m. The following turbine characteristics were assumed:

- the power and thrust to match the curve fitted data for the 20° pitch case, Fig 3(a, b);
- the gearbox and seals have a constant 97% efficiency;
- the generator operates at a constant RPM and efficiency of 95%;

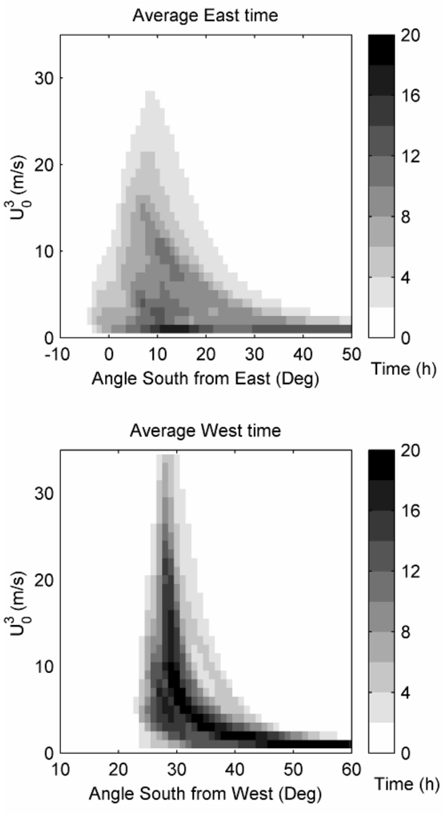

Fig 7 Binned data set showing a histogram of the times in the east and west.

- the blades are assumed to pitch to maintain a constant power above the rated speed;
- the cut-in speed is calculated assuming that power required to start was the sum of the loss of power at the rated speed;
- the velocity profile is constant across the turbine.

Table 4 shows various design combinations, assuming a design TSR of 4, close to the optimum found in [15], for both a yawing and a fixed orientation turbine. The orientation is defined as degrees north of east or degrees south of west when the flow direction is reversed. (θ_k in Fig. 5)

The results indicate that if designing at speed of 2.5m/s the best orientation for a fixed device is around 10° (Fig. 7, -10° East and 10° West). This is the same as the strongest ellipse constituent M_2. However, with a design speed of 3m/s, the favourable orientation is 12.5° (Fig. 7, -12.5° East and 12.5° West). This is due to the west side has having a stronger influence as there are many more hours around and above $27m^3/s^3$ (3^3) as shown in Fig 7. This orientation is now close to the average between lunar and solar constituents (M_2 and S_2).

The annual outputs for both design cases are shown in Fig 8. The results indicate that for this site then a yawing turbine could produce an extra 10% of energy over every year. The results also show change of 10% in annual energies over the 18 years with a peak in 2015. This is expected as the M_2 constituent has predicted maximum in Oct 2015 [14].

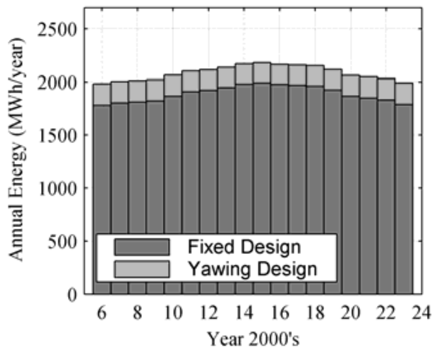

(a) 2.5m/s design speed, 553kW rated power with 10° orientation for the fixed design.

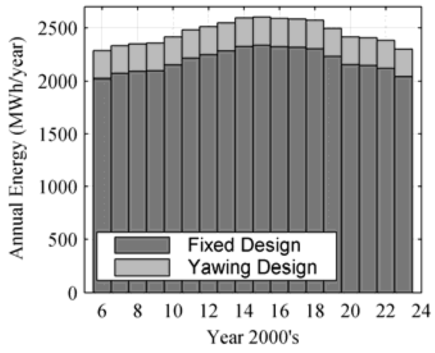

(b) 3.0m/s design speed, 956kW rated power with 12.5° orientation for the fixed design.

Fig. 8 Annual variation of power from start of 2006 to end 2023 for both design speeds.

The choice of design speed and orientation is not just dependent upon maximising energy output but installation and maintenance costs must be taken into account. From Table 4, the rated speed designs of 2.5m/s may be more profitable in the short term, due to the lower costs of a designing for lower powers and thrusts but only generating around 10% less energy. Nevertheless, to be able to justify one design over another, a full economic costing would be required.

Clearly, from these studies tidal energy is readily forecastable for long periods of time. Table 4 shows the choice of design also affects the load factor. The 2.5m/s design speed, yawing turbine, has the highest at 43%, and would supply the best quality of electricity to the grid. In the future with possible increasing energies from renewable sources, the quality and predictability of energy supplies may become critical.

Table 4 Possible configurations calculated using 18 years averaged data assuming a design TSR of 4.

				Yawing Turbine		**Fixed Turbine**		
Orientation (Deg)	**Design Speed (m/s)**	**Rated Power (kW)**	**Rated Thrust (kN)**	**Energy (MWh /year)**	**Load Factor (%)**	**Energy (MWh /year)**	**Load Factor (%)**	**Difference (MWh /year)**
7.5	2.5	553	317	2084	43	1887	39	197
7.5	3.0	956	457	2455	29	2179	26	277
10.0	2.5	553	317	2084	43	1888	39	196
10.0	3.0	956	457	2455	29	2187	26	268
12.5	2.5	553	317	2084	43	1887	39	198
12.5	3.0	956	457	2455	29	2190	26	265
15.0	2.5	553	317	2084	43	1879	39	205
15.0	3.0	956	457	2455	29	2186	26	269

Conclusions

1. An experimental rig has been design, built and successfully used to measure the power and thrust on a model tidal turbine under yawed flow conditions in a towing tank.
2. The results of the experimental investigation provide an insight into the loss of power due to yawed flow. The curve fitted results suggests that the power is proportional to the square of the cosine of yaw angle and the thrust as a cosine of the yaw angle.
3. The tidal simulation velocity data around Portland Bill has been extrapolated for 18 years and binned in order to demonstrate the true departure from rectilinearity of the tidal stream at this site. This general methodology could be applied to other sites.
4. For the example 16m turbine at Portland Bill, an extra 10% of energy could be harnessed if a yawing turbine was used.
5. The optimal orientation at Portland Bill is dependent upon the design speed chosen for the turbine.
6. At Portland Bill, there is a strong annual variation in power, with a change of around 10% over the 18 years and a peak, as predicted, in 2015.
7. The design of marine current turbine is a balance between the costs and energy yield.

References

[1] Fraenkel PL. Power from Marine Turbines. Proc Instn Mech Engrs A: J Power Energy 2002; 216(A1):1-14.

[2] Bahaj AS, Myers LE. Fundamentals applicable to the utilisation of marine current turbines for energy production. Renew Energy 2003; 28(14):2205-2211.

[3] Bryden I, Melville GT. Choosing and evaluating sites for tidal current development. Proc Instn Mech Engrs A: J Power Energy 2004; 218(A8):556-577.

[4] Burton T, Sharpe D, Jenkins N, Bossanyi E. Wind Energy Handbook. John Wiley & Sons Ltd; 2000.

[5] Batten WMJ, Bahaj AS, Molland AF, Chaplin JR. Hydrodynamics of marine current turbines. Renew Energy 2006; 31(2): 249-256.

[6] Molland AF, Bahaj AS, Chaplin JR, Batten WMJ. Measurements and predictions of forces, pressures and cavitation on 2-D sections suitable for marine current turbines. Proc Instn Mech Engrs M: J Eng Maritime Environ 2004; 218(2):127-138.

[7] Bahaj AS, Molland AF, Chaplin JR, Batten WMJ. Power and thrust measurements of marine current turbine under various hydrodynamic flow conditions in a cavitation tunnel and a towing tank. Renew Energy 2006; In Press.

[8] Marine Current Turbines^{TM} Ltd. Accessed Feb 2006: www.marineturbines.com.

[9] Tidal Generation^{TM} Ltd. Accessed Feb 2006: www.tidalgeneration.co.uk.

[10] Myers LE, Bahaj AS. Simulated electrical power potential harnessed by marine current turbine arrays in the Alderney Race. Renew Energy 2005; 30(11):713-1731.

[11] Blunden LS, Bahaj AS. Initial evaluation of tidal stream energy resource at Portland Bill, UK. Renew Energy 2006; 31(2):121-132.

[12] Bahaj AS, Batten WMJ, Molland AF, Chaplin JR. Experimental investigation into the hydrodynamic performance of marine current turbines. Sustainable Energy Series, Report 3, University of Southampton, 2005.

[13] Pawlowicz R, Beardsley B, Lentz S. Classical tidal harmonic analysis including error estimates in MATLAB using T_TIDE. Computers Geosciences 2002; 28(8):929-937.

[14] Pugh DT. Tides, surges and mean sea level, John Wiley & Sons Ltd; 1987.

[15] Batten WMJ, Bahaj AS, Molland AF, Chaplin JR. Experimentally validated numerical method for the hydrodynamic design of horizontal axis tidal turbines. Proceedings of sixth European Wave and Tidal Energy Conference; Glasgow, 29th Sept-2nd Oct 2005.

Appendix G

EWTEC-2007 conference paper

Conference paper presented at the the Seventh European Wave and Tidal Energy Conference, Porto, Portugal, 2007, with reference Blunden and Bahaj (2007a). The findings are referenced in Chapter 6, §6.3, as a 'first attempt' at modelling energy extraction, not yet underpinned at that stage by the theoretical model developed in this thesis.

Effects of tidal energy extraction at Portland Bill, southern UK predicted from a numerical model

L. S. Blunden[1]* and A. S. Bahaj[1]†

[1] Sustainable Energy Research Group,
School of Civil Engineering and the Environment,
University of Southampton, UK, SO17 1BJ
* E-mail: `lsb1@soton.ac.uk`
† E-mail: `A.S.Bahaj@soton.ac.uk`

Abstract

An array of tidal stream generators situated off Portland Bill headland (English Channel coast, Southern UK) was simulated using a two-dimensional finite element model developed with the TÉLÉMAC hydrodynamic modelling system. The effect of energy extraction was parameterized as a stress proportional to the square of flow speed, linearly interpolated in space across affected elements within the mesh. Different resolution finite element meshes were used to indicate the degree of mesh-independence of the simulation. For each run, one month of simulation results were analyzed in terms of harmonic constituents using T_TIDE. The distributions of cubed speeds over 18.6 years were then compared for cases with and without energy extraction, in order to quantify the difference in predicted input power to the generator array. It was found that in the bin that was closest to the rated speed chosen for the array, 15–16 (m/s)^3, there was a reduction in available energy of approximately one third. This implies that there could be a large impact upon individual generator design criteria in this case, subject to future validation of this method of simulating energy extraction, through experimental results.

Keywords: Tidal power, numerical model, finite elements

Nomenclature

A	Area	m^2
C_T	Thrust coefficient	
$\dot{E}$	Energy flux per unit width	J/m/s
F	Force per unit area	N/m^2
g	Acceleration due to gravity	9.81 m/s^2
h	Depth of water	m
N	Number of turbines in array	
t	Time GMT	hour
$\mathbf{u}$	Vector velocity	m/s
U	Complex velocity of tidal stream ellipse	m/s
u, v	Velocity components	m/s
V	Equilibrium phase of harmonic constituent	deg
Z	Free surface elevation	m
α, β	Complex amplitudes of tidal stream ellipse	m/s
ν	Kinematic viscosity	m^2/s
ϕ	Phase of harmonic constituent	deg
ρ	Density of sea-water	1025 kg/m^3
ω	Angular speed of tidal stream constituent	deg/hour
θ	Orientation of tidal stream ellipse major axis	deg
Ω	Angular speed of rotation of the earth	7.29×10^{-5} rad/s

Subscripts

a	array
d	rotor disk
e	effective
i	node number in finite element mesh
k	harmonic constituent
$\max$	maximum
r	rated (thrust or power of turbine)
x	in x direction

© Proceedings of the 7th European Wave and Tidal Energy Conference, Porto, Portugal, 2007

Introduction

Assessment of the energy resource available from the tidal stream remains an ongoing topic of research while energy conversion devices remain at the pre-commercial stage. Recent assessments, for example the UK Tidal Stream Energy Resource Assessment [1] have highlighted the need for modelling of potential sites to ascertain what are the local effects of energy extraction upon the tidal flow.

Analytical models have provided insights into tidal stream power generation in tidal channels—for example in the case of an enclosed basin connected to the sea—showing that tidal stream generation can extract a significant proportion of the power that a tidal barrage scheme would generate, with far less environmental impact [2]. A general expression for the maximum power that can be generated by turbines in a tidal channel has been derived in [3], which can be evaluated given knowledge of the discharge and surface elevations at the ends of the channel. This maximum has been evaluated for one location in British Columbia [4], where the value agreed well with the results of numerical modelling.

Little is known about the possible effects that a large number of tidal turbines would have on the local tidal regime, particularly in locations where the flow is not well bounded by a channel, for example the case of a headland such as Portland Bill. Having some idea is important, not only for the purpose of predicting power output (it could be reduced due to reduced 'up-current' flow speeds), but also for assessing environmental impact, for example on local sediment transport. Field data on these effects are lacking, as arrays of turbines are yet to be constructed; the effects are also difficult to reproduce in physical models due to scale effects. Other options are empirical, analytical or numerical models.

The performance of individual horizontal axis wind turbines in free-stream flow is well-understood and analytical models exist for relating energy extraction to far-upstream flow velocity [5]; these have been applied to tidal stream turbines in [6]. The situation becomes more complicated in arrays of turbines where wakes interact. A recent study compared measured data from a single turbine wake in an offshore wind farm with a number of models including semi-empirical and analytical wake models and a CFD simulation [7]. It was found that none of the models were clearly better than the others at predicting the momentum deficit behind the single turbine and that the variance of the results was large. It was therefore concluded that there is a considerable way to go in improving the models before they can be applied to multiple wakes. Hence there is not an obvious choice of modelling method to apply to the case of arrays of tidal stream generators.

It was decided here to go down the route of CFD simulation for this work as it was necessary to simulate tidal streams around the headland in the first instance to 'fill in the gaps' in the sparse tidal stream data available in the form of tidal stream diamonds on navigational charts (There were no relevant current meter records available in the region as listed on the BODC catalogue [8]). The results of the simulation without artificial energy extraction were then used to find the spatial and temporal distribution of cubed flow speeds, which informed the selection of a site for energy extraction. However, individual turbines are too small to be simulated directly in a coastal numerical model on the scale of tens of kilometers, as to resolve both the smallest and largest scales in the flow would entail excessive computational expense. There are a number of solutions to the problem of representing this sub-grid scale process, including:

1. Use a coarse scale model or other means to provide input boundary conditions as time series to a highly localized model of the generator array. This assumes that there is negligible effect of the generators upon the flow at the boundary between the models, and this is not known a priori. At some level, this approach will be necessary to restrict the size of the domain to manageable proportions; however, the boundary will generally be chosen to ensure that the flow perturbations within the domain are small when propagated to the boundary.

2. Couple a coarse scale model to an inset fine scale model of the array where the generators are better or fully discretized, and run the two models concurrently. This would require a significant amount of programming and computational effort and may not be possible to implement with a commercial software package.

3. Apply forces distributed to nodes within the modelling domain to represent the generators as 'sinks' of momentum. The effect of this is to add roughness to portions of the mesh; this method can not reproduce the wake structure behind the turbines, but may be able to adequately reproduce the large scale flow patterns. This solution was chosen and implemented in the TÉLÉMAC model.

Added roughness has been used to investigate the effects of tidal fences in specific idealized channels in [9] and with a more general treatment in [3]. In [4], added roughness was used to simulate turbine fences across the whole width of a tidal channel in a numerical model. The roughness coefficient was increased during the simulation to find the maximum energy extraction at a number of locations. The use of added roughness with a quadratic drag law to simulate a tidal stream generator array in an open sea location has been implemented previously in a coastal finite element model [10], but few details of the model were given in this case.

Having decided to take an added roughness approach to extract momentum, it was necessary to consider what effect this would have on energy extraction in the model, as compared to reality. The effect of a tidal stream generator is to produce a normal force acting against the flow, caused by the step-like pressure change across the generator working surface; for example, the vertical area swept out by the blades of an horizontal axis turbine. The rate of energy extraction of the tidal stream generator is the force on the flow multiplied by the mean velocity of the flow through its working surface.

In the 2-D finite element model, the vertically-averaged velocity field in the model is approximated by the basis functions of the finite elements, linear in this case. These functions do not resolve the velocity gradients around the turbines, so the expected force due to a number of generators must be approximated from the velocity field and then transformed into a stress acting over a larger horizontal area consisting of 2-D elements. The stress is also linearly interpolated between the nodes of each element and is then integrated across the area of the affected elements to provide a term in the momentum equation. The rate of energy extraction in the model is then the double integral of the scalar product of the friction field and the velocity field. This is physically different from the real-life situation, so experimental validation of the energy extraction method is necessary.

1 Methodology

This work continues that described by the authors in [11], in which the results of a numerical model of tidal flows around the headland at Portland Bill (on the south coast of the UK) were used to predict the output of a single generator at a location off the headland. In this new work, energy extraction by tidal generators has now been parameterized and included in the model in order to investigate possible effects of a large number of tidal generators on local tidal dynamics. it should be noted that the purpose in this case is not to determine the limits of energy extraction at this location, but the effects of a plausible tidal stream generator array.

The raw bathymetry used to produce the finite element mesh was digitized from sounding sheets. The nominal resolution of the bathymetry in the immediate vicinity of Portland Bill was 50 m, rising to approximately 1 km toward the edges of the domain. Tidal elevation data were obtained from the National Tidal Sea-Level Facility (NTSLF) in the form of validated annual data files. All three files were complete and without any bad or missing data; the years covered were 2004 (Devonport), 2004 (Weymouth) and 1999 (Bournemouth). The sample interval was 15 minutes in all cases.

To investigate the sensitivity of the results to varying finite element size, meshes of increasing density were used, with target mesh node separation distance for the triangulation process varying from 1 km in the coarsest mesh down to 250 m in the finest mesh. Information on the meshes are summarized in Table 1 and Figure 1 shows a close-up view of the portion of the meshes close to the tip of the headland.

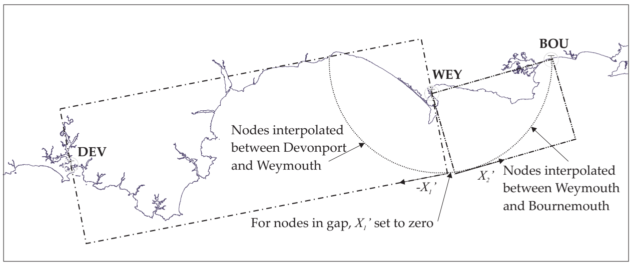

Figure 2: Bilinear interpolation of tidal elevation constituent amplitudes and phases between Devonport (DEV), Weymouth (WEY) and Bournemouth (BOU) tide gauges (marked with 'T' symbol).

The TÉLÉMAC-2D code was used to solve the well-documented vertically integrated equations of continuity (1) and momentum balance (2, 3) within the domain:

$$\frac{\partial h}{\partial t} + \mathbf{u} \cdot \nabla h + h \nabla \cdot \mathbf{u} = 0 \tag{1}$$

$$\frac{\partial u}{\partial t} + \mathbf{u} \cdot \nabla u - 2v\Omega \sin\lambda = -g\frac{\partial Z}{\partial x} + \frac{F_x}{\rho} + \frac{1}{h}\nabla \cdot (h\nu_e \nabla u) \tag{2}$$

$$\frac{\partial v}{\partial t} + \mathbf{u} \cdot \nabla v + 2u\Omega \sin\lambda = -g\frac{\partial Z}{\partial y} + \frac{F_y}{\rho} + \frac{1}{h}\nabla \cdot (h\nu_e \nabla v) \tag{3}$$

Where u, v are depth-averaged velocity components in the x, y directions respectively (aligned with grid East and North in the domain) and $\mathbf{u} \equiv u\,\mathbf{i} + v\,\mathbf{j}$; h and Z are water depth and sea-surface elevation; F_x, F_y are body force components (per unit volume) representing the sum of sea-bed friction and sinks of momentum; ν_e is an effective viscosity representing dispersion and turbulent diffusion of momentum. Bed friction was given by the Strickler formula with a spatially-uniform coefficient of 40 $\mathrm{m}^{1/3}\mathrm{s}^{-1}$, and the k-ε closure method [12] was adopted for turbulence modeling. The Coriolis acceleration term was included in the hydrodynamic equations due to the scale of the domain (order 100 km) where Ω is the rate of rotation of the earth and λ the latitude, which was taken at the centre of the domain.

The model was forced by imposing elevations at the open boundary nodes, synthesized from the fourteen most significant harmonic constituents. The horizontal components of velocity were not specified at the boundary, meaning that the solution was under-constrained at these points. To overcome this problem, the TÉLÉMAC-2D code uses Thompson boundary conditions, a method involving using the rate of change of incoming characteristics and the imposed elevation to calculate the new horizontal velocity [13]. The co-ordinates of the mesh boundary nodes are translated and rotated onto axes parallel to lines joining Devonport—Weymouth and Weymouth—Bournemouth tide gauge positions, X_1' and X_2' (see Figure 2). The imposed elevations are recalculated at each time step using bilinear interpolation along the transformed axes of amplitudes and phases of tidal constituents, analyzed from tidal records at the gauges.

Table 1: Finite element meshes used in model

Mesh	**1**	**2**	**3**	**4**	**5**
Nominal node separation (m)	1000	500	400	300	250
Number of nodes ($\times 10^3$)	2.2	8.2	12.6	22.2	31.9
Number of elements ($\times 10^3$)	4.1	16	24.7	43.7	62.9
Wall time for 1 month simulation $\approx$ (hr)	1	6	10	26	34

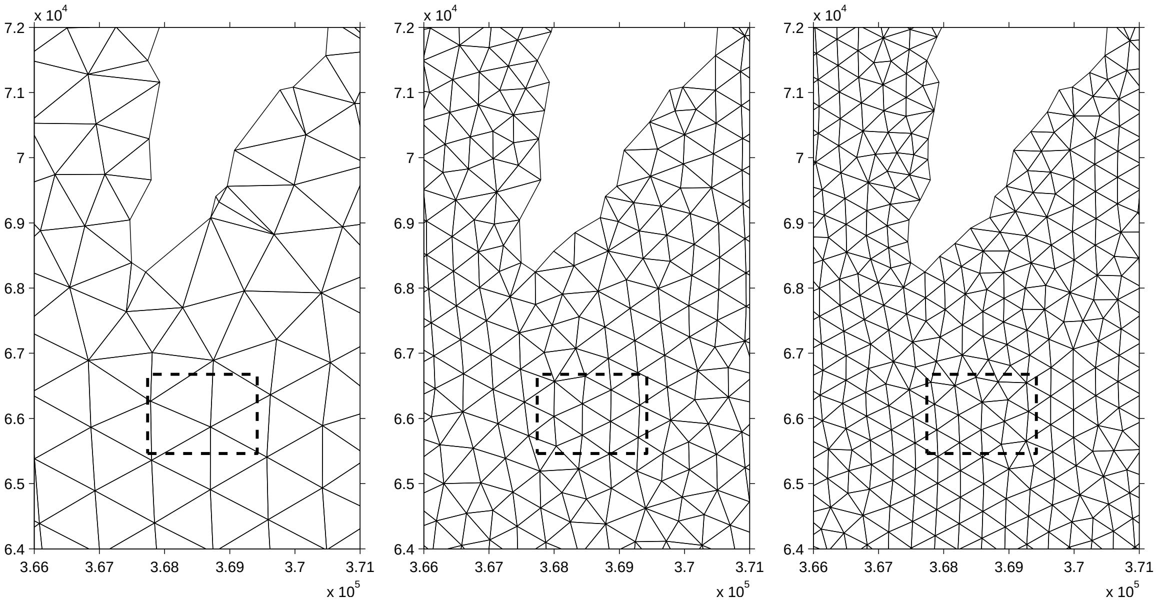

(a) Mesh 1 (b) Mesh 2 (c) Mesh 3

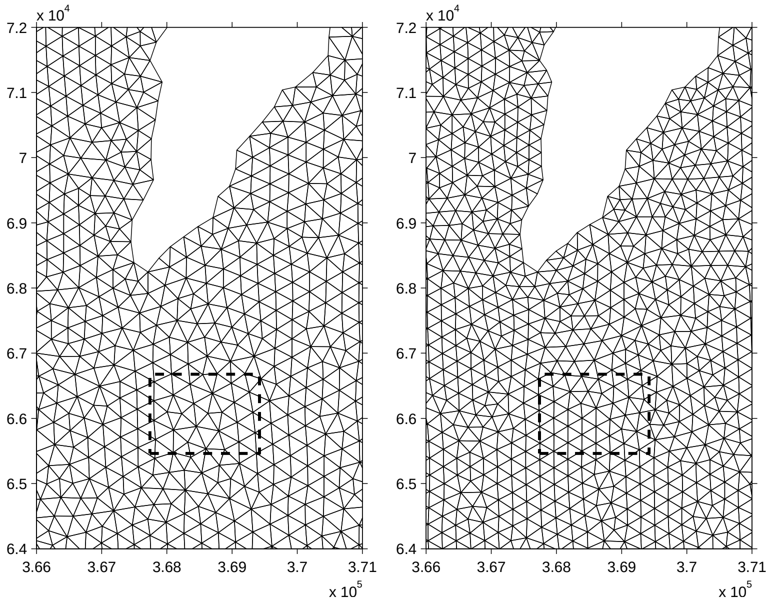

(d) Mesh 4 (e) Mesh 5

Figure 1: Detail of part of mesh showing area of energy extraction (dashed line). National Grid co-ordinates.

1.1 Parameterization of drag due to turbines

The location of the area in the model where energy extraction was to take place, was selected on the basis of:

1. Mean cube speed $\overline{U^3}$ greater than 5.5 (m/s)^3
2. Depth greater than 25 m with respect to Chart Datum.

The mean power density at a point is proportional to the mean cubed speed $\overline{U^3}$ [14] and while the full distribution of U^3 is needed for assessing the output of a given device, $\overline{U^3}$ gives a good metric for the performance of an isolated turbine located at that point. The first criterion would ensure that a 15 m diameter rotor horizontal axis turbine is presented with a flow of time-average kinetic power of at least 500 kW, assuming that it can yaw to face the flow. The second criterion is to ensure adequate submergence of the rotor. This might be relaxed with some designs of energy converter, although in the case of Portland Bill, the use of shallower areas would encroach upon the tidal race with associated highly turbulent flows and breaking waves (clearly not resolved in the finite element model).

The thrust on the turbine due to the flow was assumed to be proportional to the square of the flow speed (forces due to flow acceleration were considered negligible given the long periods of tidal oscillations). For the purposes of the simulation, a generator unit was assumed to be an horizontal axis turbine with rotor disk area $A_d = 201$ m^2 (diameter 16 m), rated speed $U_r = 2.5$ m/s and thrust coefficient $C_T = 0.8$. These values were informed by a case study in [15]. The thrust was limited to rated thrust (515 kN) for $U > U_r$ (see Figure 3). A more realistic model of turbine performance would have limited the power rather than thrust, with the thrust peaking at the rated speed and then falling away; a lower cut-in speed could also be implemented as could variation of C_T with U. In reality the response of the array to incident flow would also be anisotropic, as the relative generator spacing would change. This feature was not reproduced in the model, but in theory a direction-dependent drag function could be introduced.

For a mesh node with index i lying within array area A_a, which has a total of N tidal turbines, the force on the flow due to the thrust of the turbines in the x and y directions per unit volume was given by:

$$F_{ix} = -\frac{1}{2}\rho C_T^* |\mathbf{u}_i| u_i \frac{A_d}{h_i} \frac{1}{\cancel{A_i}} \frac{\cancel{A_i}}{A_a} N \tag{4}$$

$$F_{iy} = -\frac{1}{2}\rho C_T^* |\mathbf{u}_i| v_i \frac{A_d}{h_i} \frac{1}{\cancel{A_i}} \frac{\cancel{A_i}}{A_a} N \tag{5}$$

C_T^* is here distinguished from C_T as it is not based on the far-upstream speed for an isolated turbine, rather it is an empirical value used to extract momentum from the model. As has been mentioned above, the model cannot resolve the velocity gradients around the individual turbines. However, the value of 0.8 was used for C_T^* in this case as experimental data were not available for validation. It can be seen from Equations 4–5 that A_d/h_i is an equivalent diameter that varies with h, the factor $1/A_i$ transforms the point forces on the generators into a distributed stress, A_i/A_a is the fraction of the array area corresponding to node i and the area A_i cancels from the expression. The nodal forces were then multiplied by the basis functions of the triangular finite elements and integrated element-wise. The array to be simulated had the following properties:

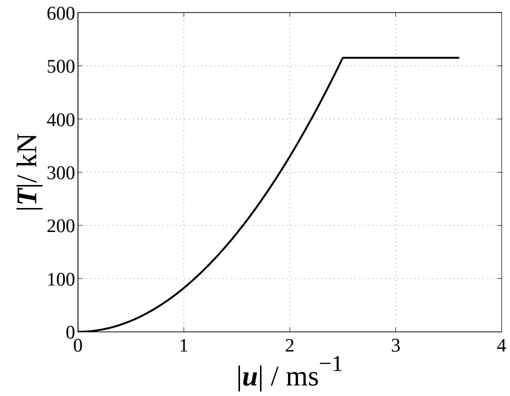

Figure 3: Variation of thrust on the flow due to one rotor with flow speed

Table 2: Array configurations

	A	B
Number of generators	0	160
Rows × number per row		7 × 21
Longitudinal spacing (diameters, [m])		15 [240]
Lateral spacing (diameters, [m])		4 [64]
Total thrust at rated speed (MN)		10.3

- Array density: 160 units $15D$ by $4D$ spacing
- Array area 1.680 km by 1.216 km = 2.04 km^2
- Envisaged array rated power based on this number of turbines: ≈ 90 MW

These parameters resulted in an added roughness coefficient averaged over the energy extraction area of 0.013, which lies in the range investigated in [4].

1.2 Tidal analysis

The velocity of the tidal stream at a point can be represented in complex form U as the sum of N constituent ellipses,

$$U = \sum_{k=0}^{N} \alpha_k \exp^{i\omega_k t} + \beta_k \exp^{-i\omega_k t} \tag{6}$$

where α_k and β_k are complex. The constituent frequencies are integer combinations of the fundamental astronomical frequencies and $\omega_0 = 0$. The properties of the kth ellipse defined in Figure 4 in real form can be readily calculated from α_k and β_k: the semi-major axis (Eq. 7), semi-minor axis (Eq 8), the inclination (Eq. 9) and the

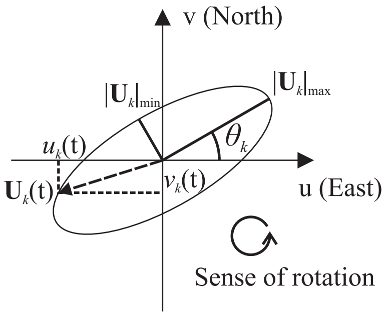

Figure 4: Definition of tidal stream ellipse parameters for constituent k.

phase of the major axis relative to the equilibrium phase V (Eq. 10).

$$
\begin{aligned}
|U_k|_{\max} &= |\alpha_k| + |\beta_k| && (7)\\
|U_k|_{\min} &= |(|\alpha_k| - |\beta_k|)| && (8)\\
\theta_k &= \frac{1}{2}\left[\arg(\alpha_k) + \arg(\beta_k)\right] && (9)\\
\phi_k &= V_k - \frac{1}{2}\left[\arg(\alpha_k) - \arg(\beta_k)\right] && (10)
\end{aligned}
$$

The T_TIDE package for MATLAB [16] was used to determine the constituent ellipse properties at each finite element node by harmonic analysis. T_TIDE applies nodal corrections to constituent amplitudes and phases based on the central time of the input time series. In addition, T_TIDE was used to produce estimates of signal-to-noise ratio (SNR) for the constituent ellipses by using a nonlinear bootstrap method adding Gaussian noise with variance derived from the spectrum of the residual values, to the signal reconstructed from the constituents. Using these constituents, time series of tidal stream velocity can be predicted with any time step and start date.

2 Results and discussion

Table 3 is a comparison of observed and simulated tidal elevation constituents at the only coastal tide gauge within the domain, at Weymouth. It can be seen that there was little difference between the meshes in terms of sea level elevations; the error in the model was 1–2 cm (1.7–3.4%) in amplitude and 9 deg in phase in all cases. These error estimates do not translate directly into tidal streams however, as currents are highly dependent on bathymetry and Weymouth Bay is only a small area within the domain; errors may be larger further away from the coast.

Figure 5 compares the mean power dissipated by the energy extraction within the five meshes over the one month period. The values can be seen to converge as the mesh density was increases; the difference in mean power dissipation between meshes 4 and 5 was +1.2% and the difference in maximum power dissipation was -2.9%. The values converge as both the array area and the velocity field are better resolved. The results used for analysis in the following sections were all taken from the second most refined mesh (Mesh 4) as a compromise between convergence and computational expense. It can be seen that the power dissipated is higher than envisaged by a factor of around two, which highlights the need for validation of the added roughness method of energy extraction and in particular the value of C_T^*. Nevertheless, the energy extraction is of the right order of magnitude to represent a real generator array.

Table 3: Amplitude and phase with 95% confidence intervals (C.I.) for M_2 elevation constituent at Weymouth. Letter and number refer to case and mesh respectively; TG refers to analysis of annual tide gauge records.

Results	H_{M_2} (m)	CI_{95} (m)	g_{H,M_2} (deg)	CI_{95} (deg)
TG	0.59	0.01	190.1	0.6
A1	0.58	0.05	199.1	4.3
A2	0.58	0.05	199.0	4.3
A3	0.58	0.05	199.1	5.3
A4	0.58	0.05	199.1	4.7
A5	0.57	0.05	199.2	4.3
B1	0.59	0.05	199.1	4.7
B2	0.58	0.04	198.9	4.4
B3	0.58	0.05	199.1	4.8
B4	0.58	0.05	198.9	5.2
B5	0.58	0.05	199.1	4.7

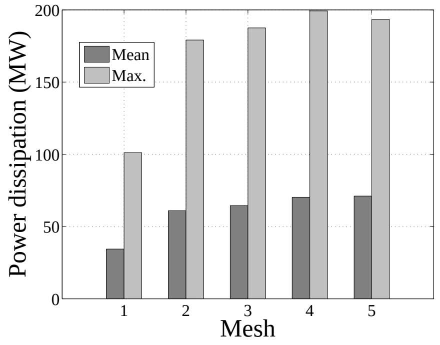

Figure 5: Mean and maximum power dissipated by added friction within the meshes over period of simulation (MW)

Figures 6(a) and 6(b) give co-tidal and co-amplitude lines for the largest harmonic constituent, M_2. The co-tidal lines are not at equal intervals of phase, for clarity; the rate of propagation of the eastward going wave decreases sharply on passing the headland, so the co-tidal lines bunch up. In the model, this is the result of the interpolated phase distribution on the boundary; in reality it is a result of the wider tidal dynamics of the English Channel. The distortion of the contours at the bottom right hand corner of Figure 7(c) is likely to be an artifact introduced by the bi-linear approximation of the phase distribution, resulting in a step in phase gradient with respect to distance along the boundary.

The tides in the English Channel are well explained by a combination of an eastward going Kelvin wave travelling up the Channel with highest amplitudes on the French coast and a much weaker reflected westward travelling wave with highest amplitudes on the English coast. The combination of these waves results in the co-tidal lines in

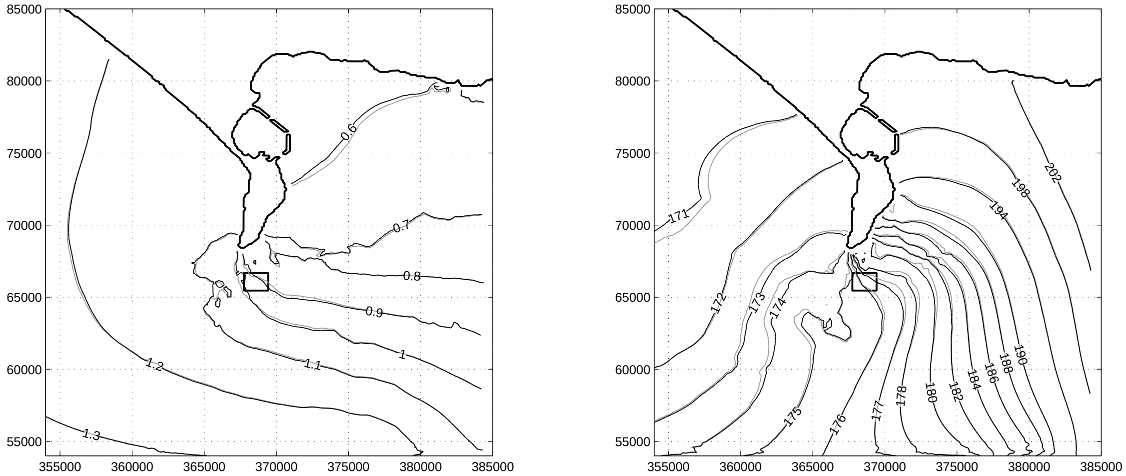

(a) Co-amplitude lines for the M_2 elevation constituent (m)

(b) Co-tidal lines for the M_2 elevation constituent (deg)

Figure 6: Contours of parameters for tidal elevation for the M_2 constituent. Grey: natural state; black: with energy extraction applied

the Channel radiating outwards from a point inland of the English coast, known as a degenerate amphidrome, which is situated to the east of Portland Bill [17, 5:4:2]. The position of the co-tidal lines in the model results agrees to about 10 degrees of phase with those produced from observations and models of the English Channel, which have the 180 degree contour slightly to the west of the headland [18–20]. This error in the model is explained by the phase distribution used along the boundary, which is derived from the coastal gauges and applied to $\approx$20 km offshore. The effect of adding extra roughness is to locally decrease the wavelength and consequently the speed of the progressive wave [21, 5.6.2]. This effect can be seen in Figure 6(b) as the co-tidal lines are ‘pulled in’ towards the headland. Figures 7(a) and 8(a) show a reduction in major axis for the M_2 tidal stream ellipses in and around the area of energy extraction of around 0.25 m/s. This represents a reduction in maximum speed cubed of 30%, indicating a significant reduction in available power at the location. The change predicted in ellipse orientation is generally small (see Figure 8(c)), less than 1 degree, apart from close to area of energy extraction where variations of up to 10 degrees are found.

For a long wave, the total energy flux per unit width normal to U is given by:

$$\dot{E} = \frac{1}{2}\rho g h |Z|_{\max} |U|_{\max} \cos(\phi_H - \phi_U) \tag{11}$$

It can be seen by comparison of Figures 6(b) and 7(c) that the phase difference between elevation and currents in the area concerned is less than 15 degrees, so the cosine term in Eq. 11 is close to unity and is relatively insensitive to small changes in phase difference. One way of estimating the energy dissipation—equivalent to the divergence of energy flux—within a bounded area is to apply Green’s theorem in the plane and find the closed line integral of the energy flux normal to the boundary [22]. Over a long enough period the total energy flux due to a number of constituents is simply the sum of the individual energy fluxes [17, A4:1]. This would in principle enable the average energy dissipation in a region to be calculated analytically from the tidal harmonic constituents around the boundary. Unfortunately, this was found to result in a poorly conditioned problem due to the subtraction of large numbers to find a relatively small difference, therefore the dissipation was calculated directly. It is possible to use the binomial expansion to generate an analytical approximation to the energy dissipation from the harmonic constituents [17, 7:9:1]. However, given that there were number of constituents with significant amplitude, it was considered more straightforward to calculate the average dissipation numerically from a time series of cubed speeds.

For each node, a time series of quarter-hourly velocity components was generated for 18.61 years, the period of the lunar nodal cycle. This allowed the full variation of tidal streams to be captured, rather than simply that over the simulation period of one month, as in the author’s previous work [11], or over one year, as in published reports [23, 24]. The time series was then used to create a histogram of cubed speeds, with hourly data sorted in bins of 1 $(m/s)^3$ in the range 0–35 $(m/s)^3$. For Mesh 3, the distribution of cubed speeds was spatially averaged over the area of energy extraction and compared for the cases with and without energy extraction. The histogram is shown in Figure 9. In the bin that was closest to the rated speed chosen for the array in this case, 15–16 $(m/s)^3$, there was a reduction in available energy of approximately one third. This implies that there could be a large impact upon individual generator design criteria in this case.

3 Conclusions

For all four meshes, when extra roughness simulating a generator array was applied, the simulation results predicted measurable changes in tidal stream ellipse major

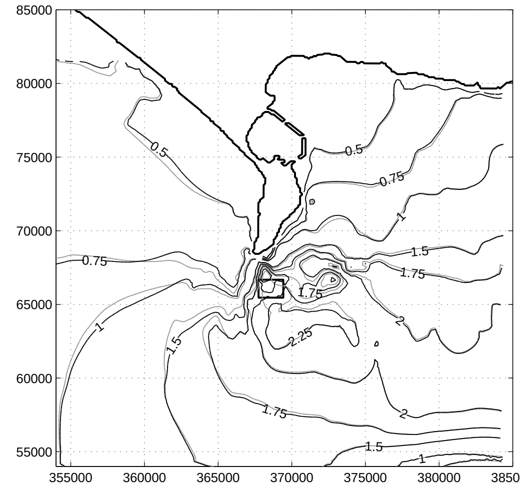

(a) M$_2$ tidal ellipse major axis (m/s)

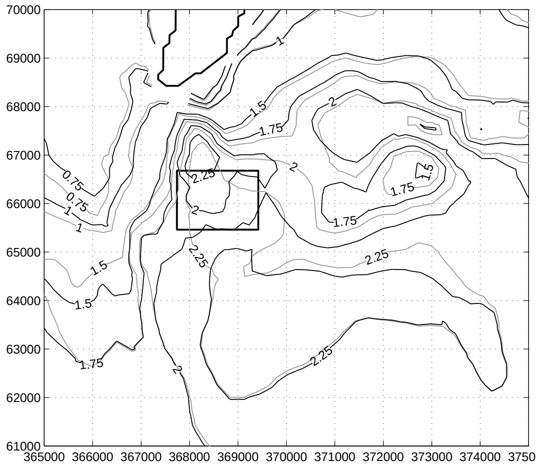

(b) M$_2$ tidal ellipse major axis (m/s); detail of the area of energy extraction

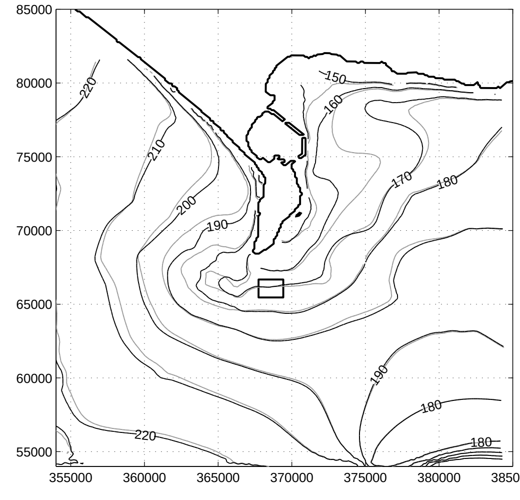

(c) M$_2$ tidal ellipse phase of major axis (deg)

Figure 7: Contours of parameters for tidal stream ellipse for the M$_2$ constituent. Grey: natural state; black: with energy extraction applied

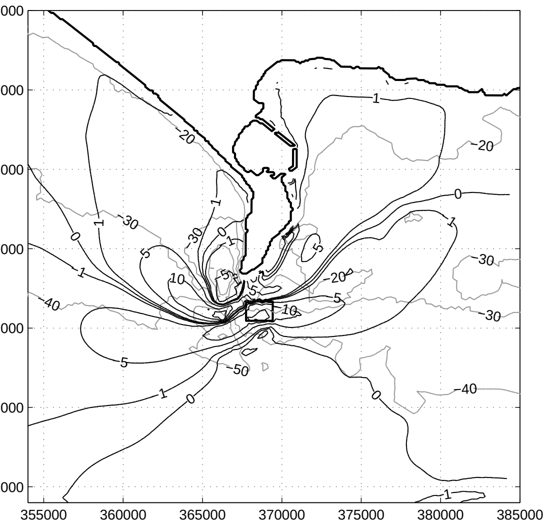

(a) Percentage change in major axis

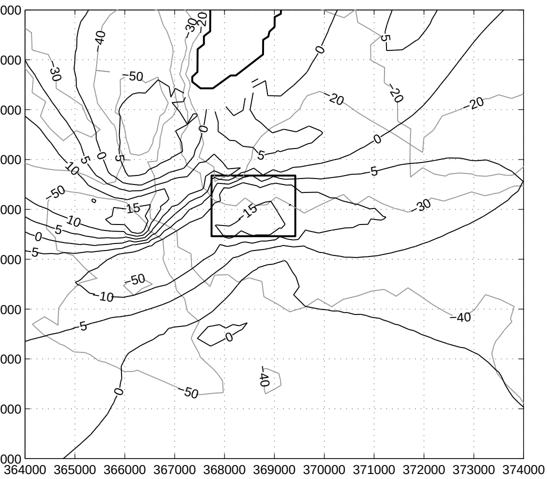

(b) Percentage change in major axis; detail

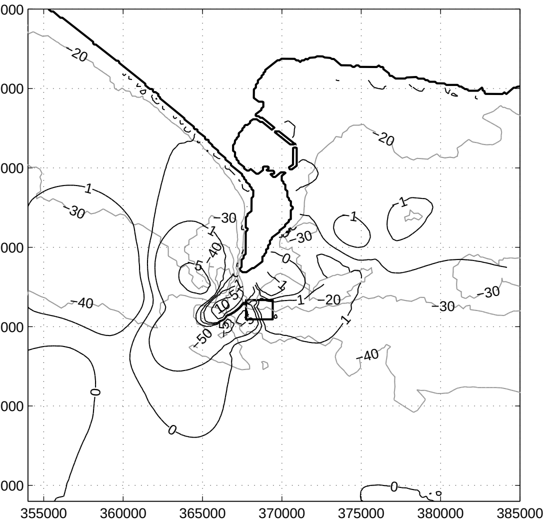

(c) Change in inclination of major axis (deg ACW from horizontal)

Figure 8: Change from natural state in tidal stream ellipse parameters for the M$_2$ constituent when energy extra. Grey lines indicate bathymetric contours (m ACD)

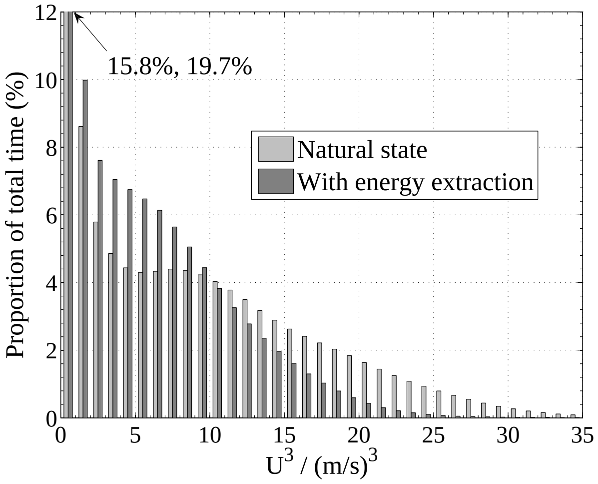

Figure 9: Histograms of cubed speeds averaged over area of energy extraction and derived from 18.6 year predicted currents for cases with and without energy extraction.

axes in the domain. These were mainly in the form of decreases but increases in speed also occurred where the flow was constrained between the array and the headland. These increases imply that there is case for optimizing the layout of an array or arrays deployed at the headland to exploit the blocking effect. There may also be implications for the accumulations of sand on either side of the headland, (described in [25]) as small changes in tidal stream speed and direction may have a significant impact on sediment transport [26, 4.3]. The model results predicted no significant change in elevation amplitude and phase for largest harmonic constituent at Weymouth. The results should be treated with caution until they are validated against experimental or field data on the flow around tidal stream arrays; specifically to ensure that the model of energy extraction used can adequately reproduce the momentum deficit due to the real array.

The tidal forcing at the boundary will be improved by using results from a model of the English Channel, rather than interpolating between coastal tide gauges. In particular, this will constrain the solution in the north-south direction; this will help to confirm or disconfirm the model prediction of significant north-south constant flow off the tip of the headland. The finite element meshes will be refined in the area of energy extraction and along the coastline to improve the resolution in the areas where the flow is complex, due to the wake of the generator array and to drying effects respectively. This work has only considered one possible location and size of generator array, for simplicity; further work will consider different configurations. Consideration of turbulence quantities is also important for prediction of velocity deficits in multiple merged wakes caused by generator arrays.

Acknowledgements

The TÉLÉMAC hydrodynamic modelling software was used courtesy of HR Wallingford. Bathymetry data for Portland was provided by Dr. Alex Bastos, formerly of the National Oceanography Centre. Thanks to the two reviewers for their helpful comments.

References

[1] Black and Veatch Ltd. Phase II UK tidal stream energy resource assessment. Technical Report 107799/D/2200/03, Carbon Trust, July 2005.

[2] C. Garrett and P. Cummins. Generating power from tidal currents. *ASCE Journal of Waterway Port Coastal and Ocean Engineering*, 130(3):114–118, 2004.

[3] C. Garrett and P. Cummins. The power potential of tidal currents in channels. *Proc. R. Soc. Lond. A*, 461(2060):2563–2572, 2005.

[4] G. Sutherland, M. Foreman, and C. Garrett. Tidal current energy assessment for Johnstone Strait, Vancouver Island. *Proceedings of the Institution of Mechanical Engineers, Part A: Journal of Power and Energy*, 221(2):147–157, 2007.

[5] A. Burton, D. Sharpe, N. Jenkins, and E. Bossanyi. *Wind Energy Handbook.* John Wiley & Sons, 2001.

[6] W. M. J. Batten, A. S. Bahaj, A. F. Molland, and J. R. Chaplin. Hydrodynamics of marine current turbines. In A. A. M. Sayigh, editor, *World Renewable Energy Conference VIII*, Denver, Colorado, USA, 2004. Elsevier Ltd.

[7] R. J. Barthelmie, L. Folkerts, G. C. Larsen, K. Rados, S. C. Pryor, S. T. Frandsen, B. Lange, and G. Schepers. Comparison of wake model simulations with offshore wind turbine wake profiles measured by sodar. *Journal of Atmospheric and Oceanic Technology*, 23(7):888–901, 2006.

[8] BODC. British Oceanographic Data Centre internet site, Accessed March 2007. `http://www.bodc.ac.uk`.

[9] Ian G. Bryden and Scott J. Couch. ME1–marine energy extraction: tidal resource analysis. *Renewable Energy*, 31(2):133–139, 2006.

[10] C. Abonnel, J-L. Achard, A. Archer, C. Buvat, L. Guittet, A. Lénès, T. Maître, M. Maniati, C. Peyrard, T. Renaud, and D. Violeau. Some aspects of EDF modelling and testing activities, within its marine current energy research and development project. In C. Johnstone and A. D. Grant, editors, *6th European Wave and Tidal Energy Conference*, Glasgow, UK, 2005.

[11] L. S. Blunden and A. S. Bahaj. Initial evaluation of tidal stream energy resources at Portland Bill, UK. *Renewable Energy*, 31(2):121–132, 2006.

[12] A. K. Rastogi and W. Rodi. Predictions of heat and mass transfer in open channels. *American Society of Civil Engineers, Journal of the Hydraulics Division*, 104(3):397–420, 1978.

[13] EDF-DRD. 2D hydrodynamics. TÉLÉMAC-2D software. Version 5.2 user manual. Technical report, Electricité de France — Direction des Études et Recherches, Département Laboratoire National d'Hydraulique, June 2002.

[14] P. L. Fraenkel. Power from marine currents. *Proceedings of the Institution of Mechanical Engineers, Part A (Journal of Power and Energy)*, 216(A1):1–14, 2002.

[15] W. M. J. Batten, A. S. Bahaj, A. F. Molland, and L. S. Blunden. Yawed performance of horizontal axis marine current turbines. In *Second International Conference on Renewable Energy in Maritime Island Climates*, Dublin, Ireland, 2006. The Solar Energy Society.

[16] R. Pawlowicz, R. Beardsley, and S. Lentz. Classical tidal harmonic analysis including error estimates in MATLAB using T_TIDE. *Computers and Geosciences*, 28(8):929–937, 2002.

[17] D. T. Pugh. *Tides, surges and mean sea-level. A handbook for Engineers and Scientists*. John Wiley & Sons, 1987.

[18] R. D. Pingree and L. Maddock. The M_4 tide in the English Channel derived from a non-linear numerical model of the M_2 tide. *Deep-Sea Research*, 25:53–63, 1978.

[19] C. Le Provost and M. Fornerino. Tidal spectroscopy of the English Channel with a numerical model. *Journal of Physical Oceanography*, 15:1009–1031, 1985.

[20] M. J. Howarth. Atlas of tidal elevations and currents around the British Isles. Technical Report OTH–89-293, Department of Energy, 1990.

[21] R. G. Dean and R. A. Dalrymple. *Water wave mechanics for engineers and scientists*. World Scientific Publishing, Singapore, 1991.

[22] G. I. Taylor. Tidal friction in the Irish Sea. *Philosophical Transactions of the Royal Society of London. Series A*, 220:1–33, 1920.

[23] ETSU. Tidal stream energy review. Technical Report ETSU-T–05/00155/REP, Harwell Laboratory, Energy Technology Support Unit, DTI, 1993.

[24] European Commission. The exploitation of tidal and marine currents. Wave energy. Project results. Technical Report EUR 16683 EN, Commission of the European Communities. Directorate-General for Science, Research and Development, 1996.

[25] A. Bastos, M. Collins, and N. Collins. Water and sediment movement around a coastal headland: Portland Bill, southern UK. *Ocean Dynamics*, 53:309–321, 2003.

[26] J. Brown, A. Colling, D. Park, J. Phillips, D. Rothery, and J. Wright. *Waves, tides and shallow-water processes*. Open University, Milton Keynes, 1997.

Appendix H

OMAE 2008 conference paper

Conference paper presented at the 27th International Conference on Offshore Mechanics and Arctic Engineering, Estoril, Portugal, 15–20 June 2008 with reference Blunden et al. (2008). It is included here as an appendix because part of the paper contains significant input from a co-author. The findings are commented on in Chapter 7, §7.4.

Proceedings of the 27th International Conference on Offshore Mechanics and Arctic Engineering
OMAE 2008
June 15-20, 2008, Estoril, Portugal

OMAE2008-57763

DRAFT: COMPARING ENERGY YIELDS FROM FIXED AND YAWING HORIZONTAL AXIS MARINE CURRENT TURBINES IN THE ENGLISH CHANNEL

Luke S. Blunden **William M.J. Batten**+ **'Bakr S. Bahaj**
Sustainable Energy Research Group, School of Civil Engineering and the Environment,
The University of Southampton, Southampton SO17 1BJ, UK,
+ Corresponding Author, Email: W.M.Batten@soton.ac.uk, Phone: 02380593940, Fax: 02380677519

ABSTRACT

At some sites with high tidal stream velocities there is an appreciable change in flow direction ('swing') away from 180 degrees between the two maxima of flow speed. In order to assess the performance of horizontal axis marine current turbines in non-rectilinear currents, measurements of a model rotor subject to yawed flows, have been applied in a case study to investigate the impact of rotor design on average annual energy output at three locations in the English Channel. All three sites are of the type where flow is accelerated around a headland or cape, but their tidal streams vary in deviation from rectilinearity. For two of the sites - Portland Bill (Dorset, UK), Race of Alderney (Alderney, Channel Islands/Normandy, France) and St. Catherine's Point (Isle of Wight, UK) - available data consisted of tidal stream diamonds printed on Admiralty navigational charts. At the other site – St. Catherine's Point, Isle of Wight, Hampshire – current meter measurements were available at the location of a tidal diamond, allowing a direct tidal analysis. The annual power output for each design of turbine was then calculated using the known performance at each value of cubed speed. This process was repeated for each year over an 18.6-year lunar nodal cycle in order to ascertain the inter-annual variation in power output.

INTRODUCTION

The oceans around the world offer a large energy source that is yet to be tapped. Although the power from waves and ocean thermal currents are far larger, tidal or marine currents with peak flows over 2.0 m/s (~ five knots), amplified by topography, offer an exciting proposition for the extraction of predictable energy. Several devices are being studied for marine current energy conversion and many are designed using wind turbine principles. Examples include standard horizontal axis turbines mounted on piles [1,2], ducted turbines [3,4] and neutrally buoyant turbines [5].

To an extent, much can be transferred from the design and operation of wind turbines [6] as discussed in Batten et al. [7]. This is particularly true for horizontal axis turbines mounted on a fixed pile, which is the focus of this paper. There are however, a number of fundamental differences, which require further investigation, research and development, such as cavitation [8,9].

One other unique feature of tidal streams, different from winds, is that at many locations with high tidal stream velocities – and potential for tidal stream energy generation – the flow is approximately rectilinear, i.e. the flow direction is always 0 degrees or 180 degrees with respect to a particular orientation. Consequently, some proposed marine current turbines are designed to have a fixed orientation to the flow and invert the blades in order to operate the turbine in the reverse direction [1,2]. The closer the flow is to rectilinear the more efficient these turbine designs will be. However, some sites with flow separation can have a swing upon flow reversal of 20° or more away from 180°, such as flows around islands and headlands.

In previous assessments of tidal energy, reviewed in [10], generally the assumption was made that any deviation from rectilinearity of the flow would have no effect on the energy extractable by tidal generators at the site, as would be the case for vertical axis turbines or yawing horizontal axis turbines. One report [11] did include a simple correction, but it was not based on theoretical or experimental results and therefore was of limited validity. An initial study, focussing on only the Portland Bill location and derived from numerical model results, highlighted the issues surrounding the choice of yawing or bi-directional turbines and the effect on energy yields [12]. The work described in this paper has extended the analysis to two other locations: the Race of Alderney (Alderney, Channel Islands/Normandy, France) and St. Catherine's Point (Isle of Wight, UK) and has been based on publicly available tidal stream data, rather than model results.

Copyright © 2008 by ASME

In order to investigate this flow variation, a 1/20th scale model rotor of a possible 16m diameter horizontal axis tidal turbine has been tested in a towing tank to determine its hydrodynamic characteristics under yawed flow conditions. The energy yield calculations presented here strictly apply to individual turbines, widely spaced and in small enough numbers not to interact significantly with other units or the tidal flow regime. Experimental work has begun to characterize wakes of tidal turbines [13] in order to predict wake interaction within arrays of turbines. Theoretical advances have been made in predicting maximum power extraction from tidal channels [14], but difficulties remain in the case of flows in unbounded open sea locations, such as the three considered here.

EXPERIMENTAL PROCEDURE

Measurements of the torque and thrust characteristics of an 800mm rotor in yaw were carried out in a towing tank at Southampton Solent University. The tank has a length of 60m, breadth, 3.7m, a depth of, 1.8 m and a maximum carriage speed of 4.5 m/s. However, due to design loads, tests were carried out at 1.5 m/s [15]. The tank has a manned carriage with various computer and instrumentation facilities, which was used to log the carriage speed to an accuracy of 1 per cent. The test rig was mounted from a pair of aluminium channel beams mounted aft of the carriage as shown in Fig 1.

The blades were developed from the profile shape of a NACA 63-8xx and were milled on a 5-axis CNC machine from aluminium alloy. The rotor is attached to a main shaft, which drives a DC generator from a pulley though a belt carried up through the vertical support tube. The electrical power is absorbed with rheostats, which also allowed regulation of the rotor speed.

An in-line strain gauge dynamometer mounted next to the turbine was used to measure the thrust and torque. This dynamometer was designed to run wet so measurements could be made before any bearing or seal losses. The strain gauge bridge circuit is connected via a slip-ring assembly to conditioners and output signals were acquired on a computer. Full details of the experimental test rig, models and results are presented in Bahaj et al [16,9].

EXPERIMENTAL RESULTS AND CURVE FITTING

The influence of inflow yaw angle on rotor performance, as tested in the towing tank, is shown in Fig. 2 for hub pitch angles of 20º and 25º. Both cases show a consistent decrease in power and thrust with increasing yaw angle. For example, for both the 20º and 25º hub pitch angles, a 30º yaw angle reduced the power coefficient by about 30%, whilst the thrust coefficient was reduced by about 15% for the 20º pitch angle and 25% for the 25º pitch angle.

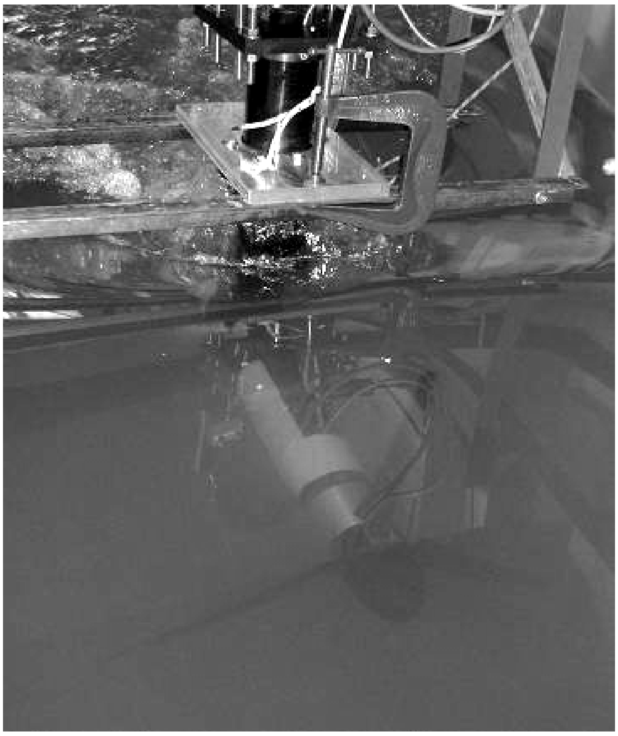

Figure 1: Photograph of the assembled test rig in the towing tank (Bahaj et al, 2005, 2007)

Momentum theory suggests that the power is proportional to the square of the cosine of yaw angle γ and the thrust as a cosine of the yaw angle [6]:

$$C_P = 4a(\cos\gamma - a)^2, \quad (1)$$

$$C_T = 4a(\cos\gamma - a), \quad (2)$$

where a is an axial flow factor.

In order to curve fit the data $a = f(TSR)$ is assumed, therefore the power coefficient was assumed to be of the form:

$$C_P = 4A(\cos\gamma - B)^2, \quad (3)$$

where: $A = c_1 + c_2\ TSR$ and $B = c_3 + c_4\ TSR$.

The thrust coefficient was assumed to be of the form:

$$C_T = 4A(\cos\gamma - B)c_5 + TSR\ c_6. \quad (4)$$

The coefficients c_1 to c_6 have been found from curve fitting the experimental data points. These are presented in Table 1. All the data was used except the 22.5º pitch angle, which was kept as a check. The fits are presented in Fig. 2 against the experimental data and show good agreement with the data, along with the 22.5º test. This demonstrates that the data fits to the momentum equations and the cosine square rule. These curve fits can therefore be used confidently to compare the effect of fixed and yawing turbines at different locations.

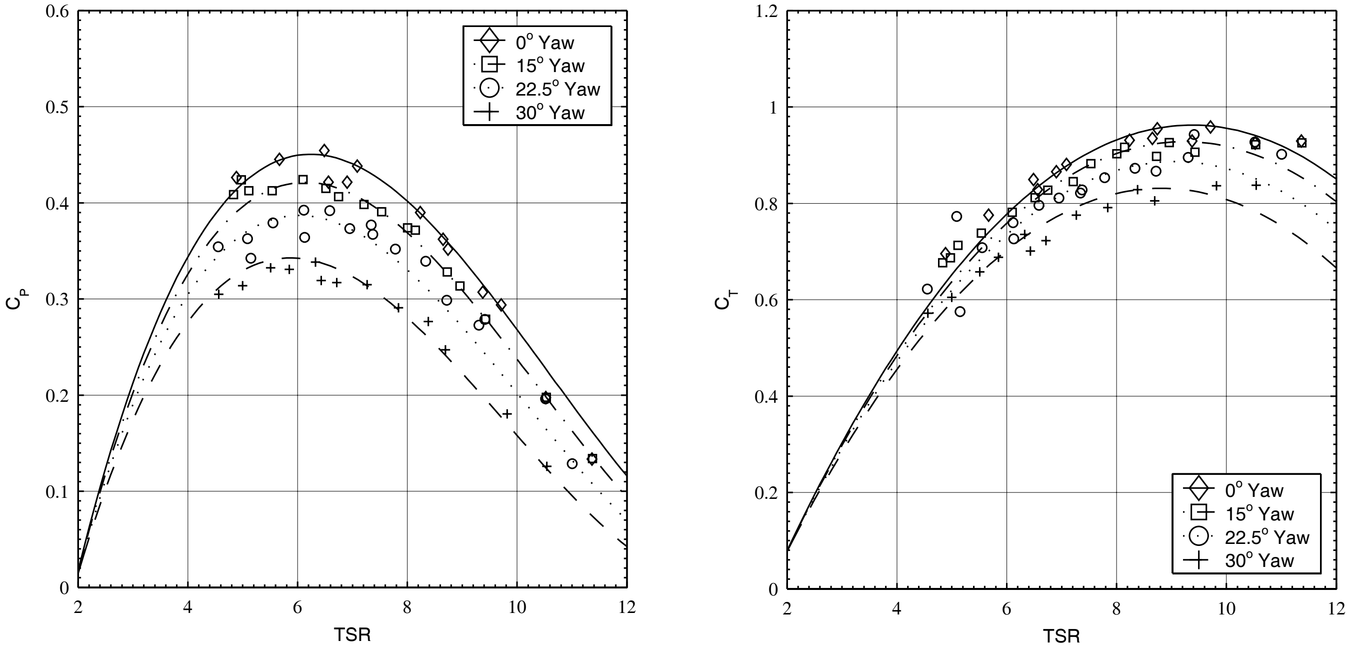

(a) Power Coefficient (b) Thrust Coefficient

FIGURE 2: Comparison of the effect of yaw with 20º hub pitch at towed speed of 1.4 m/s. The symbols are the experimental points [9, 16] and the lines from the curve fits using Eqs. (3) & (4).

Table 1: Solved constants from curve fitting the yaw experimental data

Constant	20º hub pitch	25º hub pitch
c1	-0.0479	-0.113
c2	0.0249	0.0634
c3	-0.765	-0.159
c4	0.119	0.100
c5	1.370	1.100
c6	0.0318	-0.0177

TIDAL DATA ANALYSIS - METHODOLOGY

Tidal stream time series of duration one year were generated using data included on Admiralty navigational charts at three locations in the English Channel: Portland Bill, the Race of Alderney and St. Catherine's Point (Isle of Wight). The locations were chosen to give a range of tidal stream velocities and swing upon flow reversal.

The chart data, known as 'tidal diamonds' (due to the purple diamond symbol marked on the chart) give tidal stream speeds and directions for ±6 hours with respect to high water (HW) times at a reference port. Information about the tidal diamonds used is included in Table 2. For many locations, including Portland Bill and the Race of Alderney considered here, raw current meter records from hydrographical surveys are not publicly available [17], so navigational charts (and associated tidal stream atlases) are the only source of field data on tidal streams.

The main drawback of using tidal diamonds is that they were likely to be produced using short time series of 13-50 hours [18,19], and consequently rely on two pieces of information known at the reference port in order to reproduce longer period variations: time of high water (HW) and tidal range [20, chap. 4:4:1]. Tidal ranges and tidal streams are physical connected through horizontal pressure gradients set up by phase differences in tidal elevation over an area of sea. The tidal stream speeds are given at the times of mean spring and neap tidal range at the reference port. At a general time *t*, the rate is linearly interpolated between, or extrapolated from these rates using the tidal range at the HW closest to time *t*. Depending on whether the HW occurs before or after *t*, the tidal range is calculated by subtracting the following or preceding low water (LW) elevation from the HW elevation (for example, see [21]).

Tidal stream rates derived from tidal diamonds strictly apply to the top 10 m of the water column; however, well-mixed tidal flows have been observed to vary little in the vertical above the near-bed layer [20 chap. 5:4:3].

At St. Catherine's Point, raw current meter records were available at a point close (65 m nominal separation) to a tidal diamond (see Fig 3), which enabled independent comparison of tidal harmonic constituents analyzed at that location. The

Table 2. Admiralty chart data used for analysis

	Portland Bill	**Race of Alderney**	**St. Catherine's Point**	
Admiralty Chart diamond	2615 F	2669 E	2045 D	2045 F
Water depth (m)	30	34	30	34
Reference port	Devonport	St. Helier (Jersey)	Portsmouth	
Annual data file	2004	2003	1997	
Mean spring range (m)	4.75	9.75	4.10	
Mean neap range (m)	1.96	3.64	2.01	
Bad/missing data	None	None	None	

records were sourced from the BODC inventory (see Table 3 for details, also [22]) and the measurements originally made by the then Directorate of Fisheries Research of the Ministry of Agriculture, Fisheries and Food (MAFF), Lowestoft, using a string of two moored impeller-type current meters [23].

For navigational purposes, HW times and tidal ranges at the reference port would be taken from printed tide tables or commercial software. For this work, it was considered desirable to start from raw sea level elevation data at the reference port, in order to keep track of the variance of the residual signal after tidal analysis. Tidal elevations from tide gauges at the reference ports of Devonport (for Portland Bill), St. Helier (Race of Alderney) and Portsmouth (Isle of Wight) were obtained from the National Tidal Sea-Level Facility (NTSLF) in the form of validated annual data files. The elevation data was analyzed using the TIRA program in the TASK 2000 package [24] into harmonic constituents and then the tidal signal for the same year was reconstructed from the constituents, with a smaller time step (one minute). This gave the original signal, with the surge (meteorological) component removed, making the usual assumption that tidal constituent amplitudes and phases are stationary over the period of observation [20, chap. 4:6]. Another program in the TASK package was then used to pick out HW and LW times and elevations from the reconstructed signal. A smoothing window of 15-35 minutes was applied to ensure each HW/LW was followed by a LW/HW. With this data, it was then straightforward to calculate tidal ranges throughout the year and hence the mean spring and mean neap tidal ranges at the reference port.

The tidal stream speed and direction at the diamond location were then calculated for each HW ±6 hours. These values were converted into Cartesian components u and v to avoid 360° jumps in direction and then interpolated onto an evenly spaced time vector. The velocity of the tidal stream at that point was then finally represented in complex form, $U = u + v\mathrm{i}$.

Table 3. Current meter time series used in analysis

BODC ref.	6369	6382
Year	1974	
Duration (days)	28.7	
Sampling interval (min)	10	
Meter depth MLWS (m)	9.5	12
Bottom depth MLWS (m)	32	
Bad/missing records	3	28

The T_TIDE package for MATLAB [25] was used to determine the constituent ellipse properties by harmonic analysis of the complex time series. T_TIDE decomposes $U(t)$ into the form of a sum of N constituent ellipses (Eq. 5), where A_k and B_k are complex and u_0 and v_0 are the constant current components.

$$U(t) = u_0 + v_0\mathrm{i} + \sum_{k=1,\ldots,N} A_k \mathrm{e}^{\mathrm{i}\sigma_k t} + B_k \mathrm{e}^{-\mathrm{i}\sigma_k t} \qquad (5)$$

The constituent frequencies σ are integer combinations of the fundamental astronomical frequencies (including solar day, lunar day, sidereal month and tropical year). The properties of the *k*th ellipse defined in Fig. 4 in real form can be readily calculated from A_k and B_k: the semi-major axis (Eq. 6), semi-minor axis (Eq. 7; negative value indicates opposite sense of rotation), inclination θ (Eq. 8) and Greenwich phase φ (Eq. 9), where G is the phase of the equilibrium tide at Greenwich.

$$|U_k|_{\max} = |A_k| + |B_k| \qquad (6)$$

$$|U_k|_{\min} = |A_k| - |B_k| \qquad (7)$$

$$\theta_k = \frac{1}{2}\left[\arg(A_k) + \arg(B_k)\right] \qquad (8)$$

$$\phi_k = \frac{1}{2}\left[\arg(B_k) - \arg(A_k)\right] + G_k \qquad (9)$$

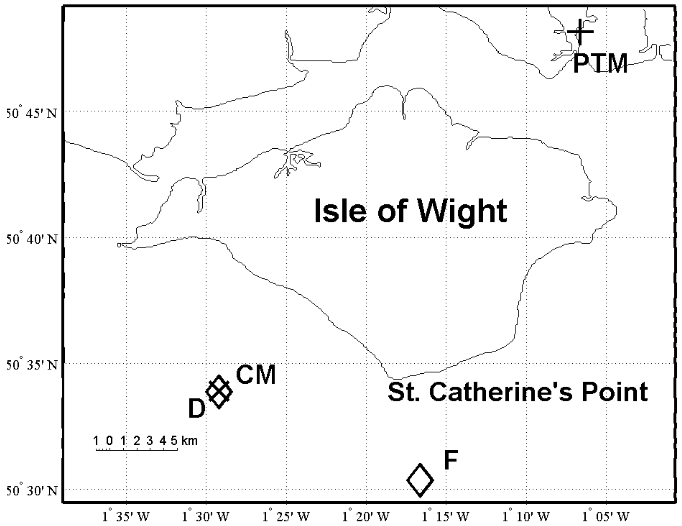

FIGURE 3: Location of Tidal Diamonds **D** and **F** ('◊') and current meter deployment **CM** ('**X**') near St. Catherine's Point, Isle of Wight. Also is included Portsmouth Tide Gauge **PTM** ('+')

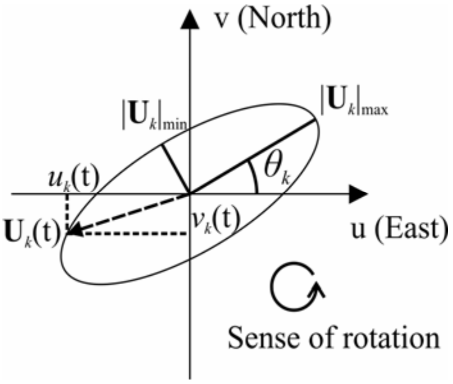

FIGURE 4: Diagram illustrating the parameters of the k^{th} tidal constituent ellipse

TIDAL ANALYSIS - RESULTS

Three constituents derived from the analysis are presented in Table 4, in addition to the constant current component. The constituents are all semi-diurnal: the principal lunar (M_2), principal solar (S_2) and the larger elliptical lunar (N_2). The inclination is given in polar form, in degrees anticlockwise from East. There are a number of similarities between the analyses evident in Table 4. Firstly, reconstructing the signal from the three constituents mentioned above, plus the constant components, captured over 90% of the variance in the original signal when applied to both the current meter records and the reconstructed tidal diamond time series. Variance capture is defined as:

$$\left(1 - \mathrm{Var}(X - X_m) / \mathrm{Var}(X)\right) \times 100\,\%,$$

where X is the original time series of a variable and X_m is the modelled time series of that variable, in this case the sum of the three harmonic constituents and the constant current components. In all cases, the semi-minor axes of the constituent ellipses were always of similar magnitude to the residual signal, around 5% of the semi-major axis.

To increase the variance capture to a uniform 97.5% across all the locations, extra constituents were included in the modelled time series, in order of major axis length, until this level was reached. These extra constituents are indicated in Table 5, from which it is clear that the most complicated tidal stream signal is at Portland Bill.

The swing observed at Portland Bill was partly explained in the harmonic analysis by the constant current, a significant southerly flow of 0.8 m/s, caused by the headland topography. In addition, the presence of a large number of constituents with significant amplitude indicates the non-linear nature of the flows in the vicinity of the headland. At the other two sites, the constant component was very small and in all cases, the inclination of the semi-diurnal ellipses fell within 5 degrees of that of the principal lunar constituent (M_2).

The ratios of amplitudes of tidal constituents are observed to remain constant over wide areas [20, 5:4:3]. Consequently, the major axes of the constituents derived from the analysis of the current meter records were plotted against those derived from tidal diamond D (St. Catherine's Point). There was a good linear fit (with zero y-intercept), with a slope of 0.86 and 95% confidence interval of +/-3% of major axis length. The agreement in phase and inclination was close in both cases (see final three columns of Table 4). The causes of the discrepancy in major axes are unknown: possible explanations are local changes in depth due to difference in horizontal position; instrument error; the effect of the meteorological component on the original tidal diamond measurements or the error introduced by the tidal diamond method of predicting tidal streams itself. A conservative estimate of the uncertainty in the constituent major axes derived from tidal diamonds at this location would therefore be +/-14%. If it were assumed that the linear factor of the discrepancy was deterministic, then a more optimistic estimate would be +/-3%.

Copyright © 2008 by ASME

Table 4. Tidal stream parameters derived from harmonic analysis. (AC indicates Admiralty chart, CM current meter measurements)

		Portland Bill	Race of Alderney	St. Catherine's Point			
		AC 2615 F	AC 2669 E	AC 2045F	AC 2045D	CM 6369	CM 6382
	u_0 (m/s)	-0.17	-0.03	0.03	0.11	0.05	0.05
	v_0 (m/s)	-0.82	-0.01	0.00	0.01	0.00	-0.01
M_2	U_{max} (m/s)	2.22	2.06	1.67	0.95	1.13	1.05
	U_{min} (m/s)	-0.06	0.10	-0.03	-0.03	-0.07	-0.06
	θ (deg)	10.0	55.1	171.9	167.8	165.6	167.4
	φ (deg)	194.3	199.3	39.7	35.0	37.5	44.3
S_2	U_{max} (m/s)	0.77	0.77	0.51	0.29	0.37	0.37
	U_{min} (m/s)	-0.03	0.04	-0.01	-0.01	-0.02	-0.01
	θ (deg)	10.2	55.2	171.9	167.8	164.9	167.0
	φ (deg)	250.6	248.4	80.9	76.7	83.1	90.6
N_2	U_{max} (m/s)	0.43	0.38	0.34	0.19	0.23	0.26
	U_{min} (m/s)	-0.01	0.02	-0.01	-0.01	-0.02	-0.02
	θ (deg)	9.9	54.9	171.9	167.8	168.0	167.8
	φ (deg)	183.2	180.6	18.1	13.4	7.2	7.9
Variance capture (%)		91.0	96.8	97.3	97.3	96.6	95.7

Table 5. Extra constituents included to increase variance capture to 97.5%. Values refer to major axis length (m/s). (Isle of Wight (IoW) constituents were selected for inclusion by rank in current meter analysis.)

	μ_2	K_2	M_{SF}	M_4	$2MS_6$	M_6	$2N_2$	MS_4	υ_2	L_2	λ_2	M_M	$2MN_6$
PB	0.24	0.23	0.22	0.21	0.19	0.16	0.14	0.14	0.14	0.13	0.10	0.09	0.08
RA		0.22											
IoW	0.05	0.15								0.09			

APPLICATION OF TIDAL ANALYSIS RESULTS TO ESTIMATION OF ENERGY YIELD

Based on the constituents derived from the analysis, predictions can be made from any start date and with any time step. For the predictions in this paper, the tidal stream speeds and directions from the start of 2006 for 18.6 years have been generated at one-minute intervals. The significance of 18.6 years is that it is the period of the lunar ascending node, over which M_2 and N_2 constituents vary by +/-3.7% in amplitude and +/-2.1 degrees in phase [20 chap. 4:2:2]. A time series of this length would be expected to include all the significant variation in the tidal signal, excluding changes in ocean response due to sea-level rise [26]. Hodographs for all three tidal cases for the 18.6 years forecast are presented in Fig 6, where direction of the tidal stream velocity vector is a bearing measured clockwise from North. The black lines demonstrate a diurnal cycle between spring and neap conditions and the Admiralty chart data for the spring and neap tides are shown as symbols. The forecast for Portland Bill (Fig. 5(a)) shows the hodograph is offset south due to the constant flow component. By contrast, the Race of Alderney and St. Catherine's Point appear to be almost rectilinear and central on the axis. Tidal streams approaching rectilinearity are known to occur close to steep cliffs, where little lateral tidal motion is possible [20 chap. 5:4:3], which provides an explanation for the currents observed off St. Catherine's Point.

In order to be able to examine this large data set, so that designs could be compared, the tidal data has been 'binned' into a 3-D histogram for each year and grouped in west and east data sets. The bins are defined by 1° intervals and in cubed speed steps of 1 m^3/s^3 from 0 to 35 m^3/s^3. Cubed speed steps were used to improve the accuracy of power integrations, as they give equal increments of power (Eq. 2).

The averaged, leap year corrected data over the 18.6 years, for both the east and west directions are presented in Fig. 5. Fig. 5(a) again shows the strong swing from rectilinearity at Portland Bill as the west and east peaks are offset by around 40°, but for the Race of Alderney (Fig. 5(b)) and St. Catherine's Point (Fig 5(c)), the west and east sides are closely aligned. This averaged data set provides a basis for comparing designs of turbines as demonstrated in the next section.

ENERGY YIELDS FOR YAWED AND FIXED ORIENTATION TURBINES

A range of comparisons between fixed and yawing design energy yields have been calculated assuming a 16m diameter turbine with the 'binned' tidal data set. This turbine is the same size as used in the comparisons in [27] and is applicable in this case, as at that location the minimum water depth is 32 m. The following turbine characteristics were assumed:

Copyright © 2008 by ASME

1. Power and thrust to match the curve fitted data for the 20° pitch case, Fig 2(a, b);
2. Gearbox and seals have a constant 97% efficiency;
3. Generator operates at a constant RPM and efficiency of 95%;
4. Blades are assumed to pitch to maintain a constant power above the rated speed;
5. Cut-in speed is calculated assuming that power required to start was the sum of the loss of power at the rated speed;
6. Velocity profile is constant across the turbine.

Tables 6, 7 and 8 show various design combinations, assuming a design TSR of 4, close to the optimum found in [27], for both a yawing and a fixed orientation turbine. The orientation α is defined as a bearing in degrees clockwise from north.

For the Portland Bill location (Table 6), the results indicate that if designing at speed of 2.5 m/s the best orientation for a fixed device is around 10° (Fig. 5(a), -10° East and 10° West). This is the same as the strongest ellipse constituent M_2. However, with a design speed of 3 m/s, the favorable orientation is 12.5° (Fig. 5(a), -12.5° East and 12.5° West). This is due to the west side has having a stronger influence as there are many more hours around and above $27\ m^3/s^3$ (33) as shown in Fig 5(a). This orientation is now close to the average between M_2 and S_2.

The choice of design speed and orientation at Portland Bill is not simply dependent upon maximizing energy output; installation and maintenance costs must also be taken into account. From Table 6, the rated speed designs of 2.5 m/s may be more profitable in the short term, due to the lower costs of a designing for lower powers and thrusts at the cost of generating around 10% less energy. Nevertheless, to be able to justify one design over another, a full economic costing would be required. Table 6 shows that the choice of design also affects the load factor. The yawing turbine with the 2.5 m/s design speed has the highest load factor at 43%, and would supply the best quality of electricity to the grid. In the future, with increasing energy generation from renewable sources, the quality and predictability of energy supplies may become critical.

The final column of Table 7 shows the increase in energy yield that would be obtained at the Race of Alderney if a yawing turbine was installed in place of a simpler bi-directional design. In all the design cases considered, the difference was minimal, due to the small departure of the currents from rectilinearity. The optimal orientation was the same for both design speeds and coincided with that of the principal constituent M_2.

The results in Table 8 for St. Catherine's Point were qualitatively similar to those of the Race of Alderney, although the tidal stream speeds and associated energy yields were lower. The three estimates of energy yield shown in Table 8 correspond to the pessimistic uncertainty estimates discussed above and indicate the risk in extrapolating energy yields into the future based on limited observational data.

CONCLUSIONS

1. An experimental rig has been designed, built and successfully used to measure the power and thrust on a model tidal turbine under yawed flow conditions in a towing tank.
2. The results of the experimental investigation provide an insight into the loss of power due to yawed flow. The curve-fitted results suggest that the power is proportional to the square of the cosine of yaw angle and the thrust as a cosine of the yaw angle.
3. The navigational tidal stream velocity data at three locations in the English Channel - Portland Bill, the Race of Alderney and St. Catherine's Point (Isle of Wight) - has been extrapolated for 18.6 years and binned in order to demonstrate the true departure from rectilinearity of the tidal stream at these sites and its effect on energy yields. This general methodology could be applied to other sites.
4. At St Catherine's Point, reasonable agreement was found between a harmonic analysis of current meter records and analysis based on navigational data (tidal diamond) at the same location. A pessimistic estimate of the error in constituent ellipse major axis length was found to be 14%. This estimate was used to determine upper and lower bounds of energy yield at this location.
5. For the example 16m turbine at Portland Bill, an extra 10% of energy could be harnessed if a yawing turbine was used. The optimal orientation at this location is also dependent upon the design speed chosen for the turbine.
6. The tidal streams at the Race of Alderney show a very small departure from rectilinearity. Consequently, the extra energy yield from the yawing turbine is insignificant and the location is therefore suitable for a bi-directional turbine.
7. St Catherine's Point experiences less extreme currents than the other two sites and is therefore probably more suitable for first generation tidal energy converters.
8. The design of a horizontal-axis tidal turbine is a balance between the costs of production, installation and maintenance, and energy yield.

NOMENCLATURE

a	axial flow factor
A	complex constant
B	complex constant
c	chord (m)
$c_{1\text{-}6}$	constant
$C_T = \dfrac{T}{0.5\rho\pi R^2 U_T^2}$	thrust coefficient
$C_P = \dfrac{Q\Omega R}{0.5\rho\pi R^2 U_T^3}$	power coefficient
G	equilibrium phase (deg)
M_2	lunar semi-diurnal constituent
N_2	larger elliptical lunar semi-diurnal constituent

Q	rotor torque (Nm)
r	local radius (m)
R	radius (m)
S_2	solar semi-diurnal constituent
t	thickness (m)
T	rotor thrust (N).
$TSR = \frac{\Omega R}{U_T}$	Tip Speed Ratio
u, v	east, north velocity components (m/s)
u_0, v_0	east, north constant components (m/s)
U	complex tidal stream velocity (m/s)
U_T	tidal speed in natural state (m/s)
$\alpha = 90 - \theta$	Orientation of bi-directional turbine clockwise from North (degrees)
ρ	density of water (kg/m^3)
σ	tidal constituent frequencies (rad/s)
θ	orientation of tidal ellipse (deg)
φ	phase of tidal constituent (deg)
Ω	rotation speed (rad/s)

REFERENCES

[1] Marine Current Turbines. http://www.marineturbines.com. Accessed January 2008.

[2] Tidal Generation Limited. http://www.tidalgeneration.co.uk. Accessed January 2008.

[3] Lunar Energy. http://www.lunarenergy.co.uk. Accessed January 2008.

[4] OpenHydro Group Limited. http://www.openhydro.com/home.html. Accessed January 2008.

[5] DTI, 2005, “Novel Moored Tidal Stream Generating Equipment.” Project Profile No. PP228 http://www.dti.gov.uk/files/file15998.pdf. Accessed January 2008.

[6] Burton T, Sharpe D, Jenkins N, Bossanyi E., 2000, Wind Energy Handbook. John Wiley & Sons Ltd.

[7] Batten, W.M.J., Bahaj, A.S., Molland, A.F., Chaplin, J.R., 2006, “Hydrodynamics of marine current turbines.” Renewable Energy 31(2), 249-256

[8] Molland, A. F., Bahaj, A. S., Chaplin, J. R. & Batten, W. M. J., 2004, “Measurements and predictions of forces, pressures and cavitation on 2-D sections suitable for marine current turbines.” Proc. Instn Mech. Engrs M: J Engineering for the Maritime Environment, 218, 127-138.

[9] Bahaj, A. S., Molland, A. F., Chaplin, J. R. & Batten, W. M. J., 2007, “Power and thrust measurements of marine current turbines under various hydrodynamic flow conditions in a cavitation tunnel and a towing tank.” Renewable Energy, 32, 407-426.

[10] Blunden, L.S., Bahaj, A.S., 2007. “Tidal energy resource assessment for tidal stream generators.” Proc. Instn Mech. Engrs A: J Power Energy 221(2): 137-146.

[11] ETSU, 1993, Tidal stream energy review. Harwell Laboratory, Energy Technology Support Unit, DTI.

[12] Batten, W. M. J., Bahaj, A. S., Molland, A. F. & Blunden, L. S., 2006, Yawed Performance of Horizontal Axis Marine Current Turbines. Second International Conference on Renewable Energy in Maritime Island Climates. Dublin, Ireland, The Solar Energy Society.

[13] Bahaj, A. S., Myers, L. E., Thomson, M. D. & Jorge, N., 2007, “Characterising the wake of horizontal axis marine current turbines.” IN FALCÃO, A. (Ed.) Seventh European Wave and Tidal Energy Conference. Porto, Portugal.

[14] Garrett, C. & Cummins, P., 2005, “The power potential of tidal currents in channels.” Proc. R. Soc. Lond. A, 461, 2563-2572.

[15] Solent University towing tank, www.solent.ac.uk/ceo/Towing%20Tank.aspx (accessed Feb 2006).

[16] Bahaj, A. S., Chaplin, J. R., Molland, A. F. & Batten, W. M. J., 2005, Experimental investigation into the hydrodynamic performance of marine current turbines. Sustainable Energy Series. Southampton, University of Southampton.

[17] British Oceanographic Data Centre: http://www.bodc.ac.uk. Accessed January 2008.

[18] Hydrographic Department, 1965, Admiralty manual of hydrographic surveying, Vol.1. 1965 edition, London.

[19] Bell, C., Carlin L., 1998, “Generation of UK Tidal Stream Atlases from Regularly Gridded Hydrodynamic Modelled Data.” Journal of Navigation 51(1), 73.

[20] Pugh DT., 1987, Tides, surges and mean sea level, John Wiley & Sons Ltd.

[21] Hydrographic Department., 1973, Admiralty Tidal Stream Atlas NP 257. Approaches to Portland.

[22] British Oceanographic Data Centre: http://www.bodc.ac.uk/data/documents/series/6369/. Accessed January 2008.

[23] Bedwell, J. A., K. J. Medler, et al., 1975. MAFF current meter data inventory. Lowestoft, MAFF Directorate of Fisheries Research. Technical report number 15.

[24] Bell, C., Vassie, J.M., Woodworth, P.L., 1999, POL/PSMSL Tidal Analysis Software Kit 2000. Bidston Observatory, Birkenhead, UK.

[25] Pawlowicz R, Beardsley B, Lentz S., 2002, “Classical tidal harmonic analysis including error estimates in MATLAB using T_TIDE.” Computers and Geosciences 28(8), 929-937.

[26] Flather, R. A. & Williams, J., 2000, “Climate Change Effects on Storm Surges: Methodologies and Results.” In Beersma, J., Agnew, M., Viner, D. & Hulme, M. (Eds.) Climate scenarios for water-related and coastal impacts. KNMI, the Netherlands, published by Climatic Research Unit, UEA, Norwich UK.

[27] Batten, W.M.J., Bahaj, A.S., Molland, A.F., Chaplin, J.R., 2007, “Experimentally validated numerical method for the hydrodynamic design of horizontal axis tidal turbines.” Ocean Engineering 34(7), 1013-1026.

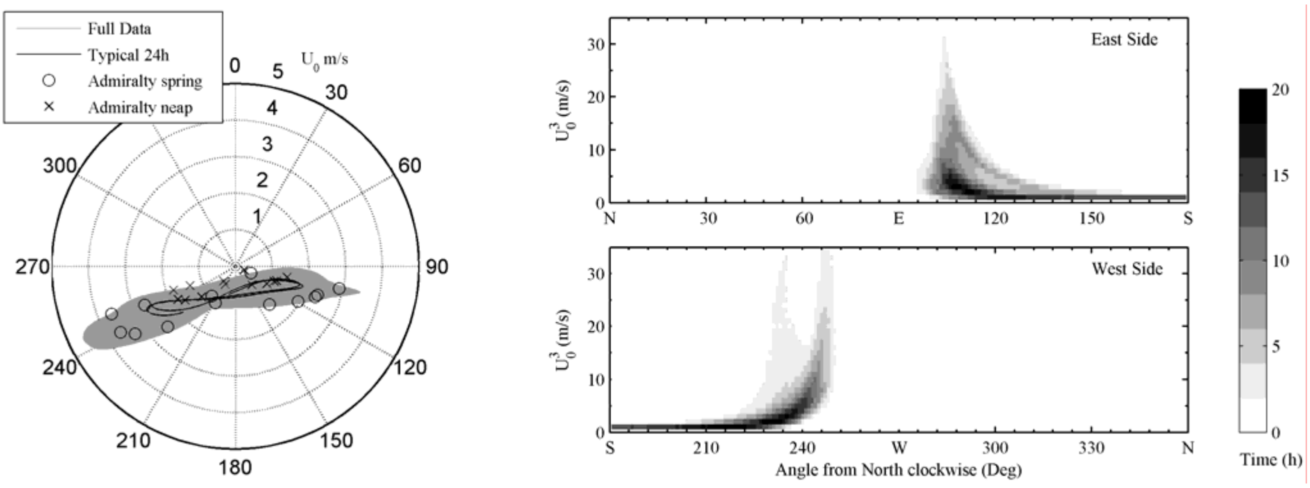

(a) Hodograph and annual average binned dataset for Portland Bill (AC 2615 F)

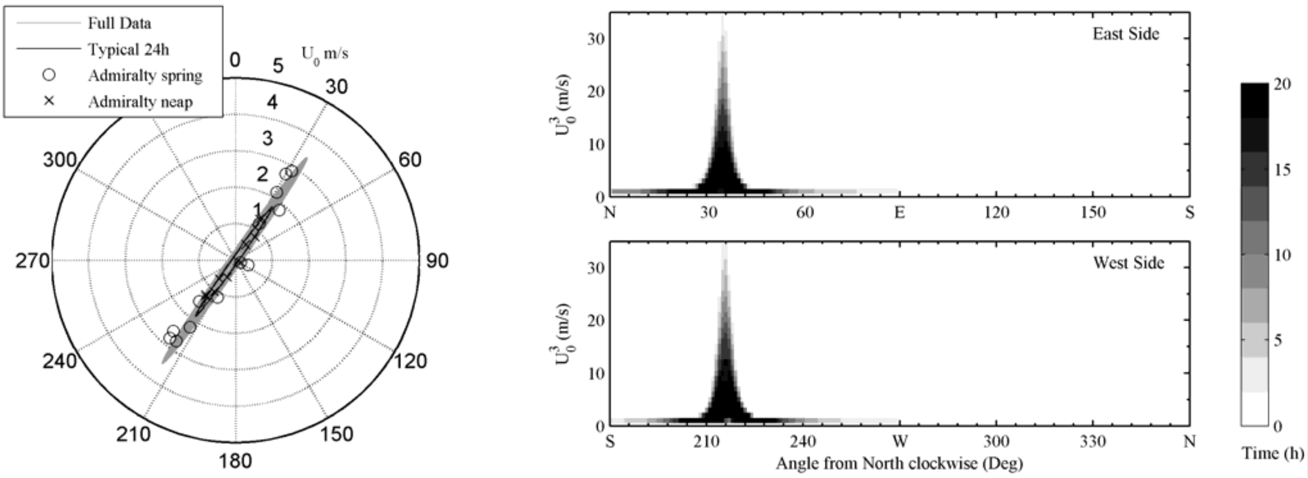

(b) Hodograph and annual average binned dataset for Race of Alderney (AC 2669 E)

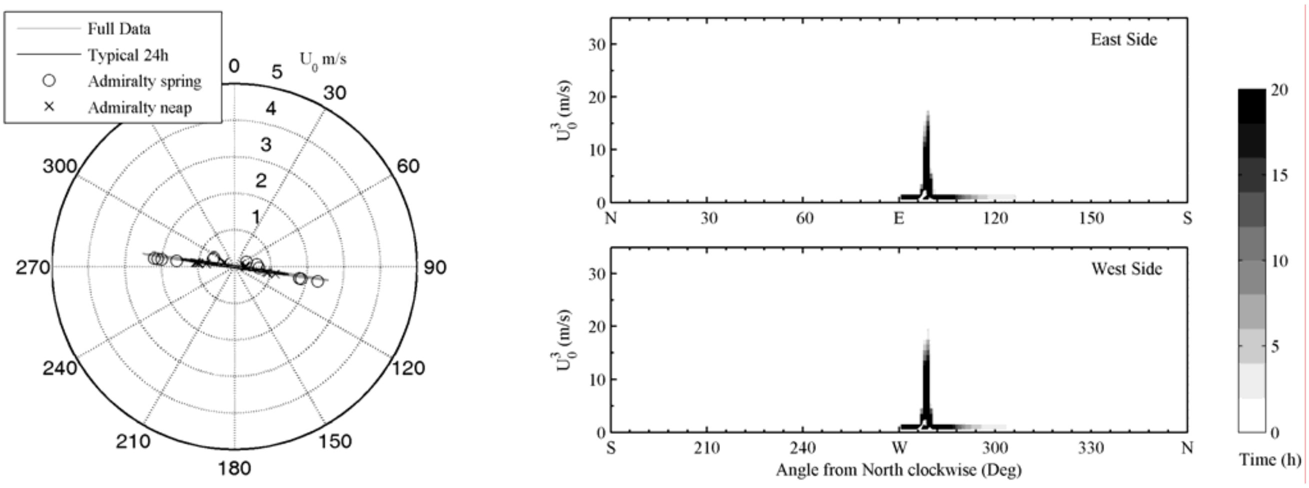

(c) Hodograph and annual average binned dataset for St. Catherine's Point (AC 2045 F)

Figure 5: Analysis of tidal data showing hodographs for 3 test cases and binned data sets showing a histogram of the times in the east and west. (Direction as a bearing in Deg., clockwise from North)

Copyright © 2008 by ASME

Table 6: Energy yield estimates at Portland Bill for both yawing and bi-directional turbines

α	Design speed (m/s)	Design Power (kW)	Design Thrust (kN)	Yawing		Bi-directional		Energy Difference (MWh)
				Energy (MWh)	Load factor (%)	Energy (MWh)	Load factor (%)	
70	2.5	553	317	1947	40	1633	33	314
70	3	956	457	2304	27	1932	23	372
75	2.5	553	317	1947	40	1659	34	288
75	3	956	457	2304	27	1949	23	355
80	2.5	553	317	1947	40	1672	34	275
80	3	956	457	2304	27	1946	23	358
85	2.5	553	317	1947	40	1676	34	271
85	3	956	457	2304	27	1929	23	375
90	2.5	553	317	1947	40	1663	34	284
90	3	956	457	2304	27	1893	22	411

Table 7: Energy yield estimates for the Race of Alderney for both yawing and bi-directional turbines

α	Design speed (m/s)	Design Power (kW)	Design Thrust (kN)	Yawing		Bi-directional		Energy Difference (MWh)
				Energy (MWh)	Load factor (%)	Energy (MWh)	Load factor (%)	
30	2.5	553	317	1586	32	1578	30	8.1
30	3	956	457	1803	21	1790	30	12.3
32.5	2.5	553	317	1586	32	1584	32.5	2.1
32.5	3	956	457	1803	21	1799	32.5	3.3
35	2.5	553	317	1586	32	1585	35	0.4
35	3	956	457	1803	21	1803	35	0.2
37.5	2.5	553	317	1586	32	1584	37.5	1.8
37.5	3	956	457	1803	21	1800	37.5	2.7
40	2.5	553	317	1586	32	1578	40	7.5
40	3	956	457	1803	21	1792	40	11.1

Table 8: Energy yield estimates at St. Catherine's Point for a bi-directional turbine

α	Design speed (m/s)	Central estimate		Lower bound estimate			Upper bound estimate		
		Energy (MWh)	Load factor (%)	Energy (MWh)	Load factor (%)	Energy Difference (%)	Energy (MWh)	Load factor (%)	Energy Difference (%)
98	1.5	582	56	496	47	-15	651	62	12
98	2	809	33	565	23	-30	1021	41	26
98	2.5	949	20	595	12	-37	1332	27	40
98	3	897	11	497	6	-45	1386	17	55

Copyright © 2008 by ASME

Appendix I

WREC-2008 conference paper

Conference paper presented at the Tenth World Renewable Energy Congress, Glasgow, 2008, with reference Blunden and Bahaj (2008). The paper is mentioned in Chapter 11 and lays out the ideas that were developed further in Chapter 6.

Flow through large arrays of tidal energy converters: is there an analogy with depth limited flow through vegetation?

L. S. Blunden[1,2] and A. S. Bahaj[2]

Abstract

Estimates of the performance of large wind turbine arrays have been made using a similar theory to that of vegetated canopy flows, where the flow reaches a spatially averaged equilibrium with the drag caused by a large number of individual obstacles. By contrast, tidal turbines are likely to interact with a large fraction of the water column and consequently bear similarities to the flow through and over aquatic vegetation with shallow immersion. There are however obvious differences in terms of obstacle density and turbulence production. Nevertheless, the application of ideas from boundary layer flows to large tidal arrays may be worth pursuing as it provides a conceptual model linking the properties of individual tidal turbines to a global roughness value for a tidal turbine array, suitable for kilometer-scale tidal modeling.

Keywords: Tidal power, turbulent flow, flow velocity, canopy

Nomenclature

A	Area of isolated turbine	m^2
C_{Dh}	Sea-bed drag coefficient $= \tau/\frac{1}{2}\rho u_h^2$	
C_T	Isolated turbine drag coefficient $= T/\frac{1}{2}\rho u_h^2 A$	
g	Acceleration due to gravity	9.81 m/s^2
h	Geometric roughness height, turbine hub height	m
H	Depth of water	m
k	Von Kármán constant $= 0.41$	
T	Thrust on isolated turbine	N
u	Spatially-averaged mean velocity	m/s
u_*	Friction velocity	m/s
x	Longitudinal coordinate	m
z	Vertical coordinate	m
z_0	Roughness length of sea-bed	m
δ	Boundary layer thickness	m
λ	Ratio of frontal area of obstacles or turbines to array area parallel to flow	
τ	Frictional stress on sea bed	N/m^2
ψ_h	Roughness sub-layer influence function	

Subscripts

$+$	Far downstream of the leading edge of obstacle or turbine array
$-$	Upstream of the leading edge of obstacle or turbine array

1 Introduction

There are two competing objectives in determining the longitudinal spacing of units in an array of turbine generators, whether wind or tidal:

1. To make the array as compact as possible in order to both maximize the flow capture area of the array and to minimize the extent of cable-laying and other works required.
2. To make the inter-unit spacing large enough to minimize the downstream velocity deficit at each successive row, caused by upstream turbines.

The result is a compromise, where the wake does not fully recover to free-stream conditions before encountering the next turbine in the row of an array. The per-unit power loss of an array of wind turbines when compared to the first row facing

---

[1] Corresponding author, E-mail:`lsb1@soton.ac.uk`

[2] Sustainable Energy Research Group, School of Civil Engineering and the Environment, University of Southampton, UK, SO17 1BJ

the wind is thought to be of the order 10-20%, so there is scope for optimization of the longitudinal spacing of turbines within the available area (Barthelmie et al. 2007). Before this can be carried out, it is necessary to be able to predict the power output of the array as a function of relative spacing between generating units.

For the first commercial arrays of tidal turbines, the uncertainty involved in wake interactions may be avoided by configuration in a single row normal to the predominant flow direction. Tidal turbines have an advantage in this case with respect to wind turbines as tidal flows are mainly rectilinear, so the units in a single-row tidal turbine array may have much closer lateral spacing than a wind turbine array. Despite this advantage, individual units are limited in size by the depth of water and if tidal stream arrays are to make a significant contribution to sustainable power generation on a national scale, then multiple row arrays will need to be built. Therefore, the interaction of wakes and the overall performance of large tidal arrays needs to be considered.

2 Wakes of individual turbines

Experimental characterization of the wakes of tidal turbines has only recently begun, for example by using porous disk simulators as described in Bahaj et al. (2007). Attempts have been made to simulate the interactions of wakes in tidal turbine arrays using Computational Fluid Dynamics (CFD) models representing the turbines as porous disks (MacLeod et al. 2002; Batten and Bahaj 2006), but these have not been validated by experimental data. By contrast, the interaction of the wakes of wind turbines has been the subject of theoretical and experimental study for over thirty years (for a comprehensive review, see Vermeer et al. (2003)) and continues to be so today (Barthelmie et al. 2006). Much can be learned from wind turbine research in predicting the performance of tidal generator arrays, but there are specific differences in terms of boundary conditions, namely the constrained nature of the flow and the presence of a free surface.

In general, wakes of turbines are characterized by a near-wake region, extending up to five rotor diameters (5D) downstream; followed by a transition region, and a far-wake region beyond this. In the near-wake region, the wake is dominated by the properties of the rotor. The vortices shed by the rotor merge and form a annular shear layer, which thickens downstream—mainly due to mechanical turbulence production but also influenced by ambient turbulence levels—until the layer reaches the axis of rotation. Downstream of this location, the swirl introduced in the flow has dissipated and the velocity in the wake can be considered as a jet, with a core velocity lower than free-stream (Lissaman 1979). The far-wake region is the region of interest when considering wake interactions.

The downstream velocity deficit in the wake of wind turbines is known to be strongly affected by the ambient turbulence of the flow (Baker et al. 1985). Part of the challenge involved in predicting tidal turbine wake interactions is the paucity of available data on the turbulence structure of continental shelf tidal flows. Velocity profiles from tidal locations have only recently become available due to the availability of acoustic-Doppler current profilers (ADCPs). Turbulence profiles are rarer still, as they are difficult to measure remotely. The use of commercial-off-the shelf ADCPs for estimating turbulence quantities has been investigated by Wiles et al. (2006). This method may in the future provide a cost-effective means for producing turbulence profiles in the sea.

3 Multiple wake interactions

Frandsen et al. (2006) identified three main regimes characterizing wake interactions within a large array of wind turbines, ignoring complicated edge effects and starting from the upwind rows and moving downstream:

1. Wakes not merged laterally; turbines are only affected by the wakes of turbines directly upstream.
2. Wakes merged in the lateral direction; combined wake can only expand vertically.
3. Wakes merged in a very large wind farm; the combined wakes are in balance with the boundary layer and the flow is uniform in a spatially-averaged sense.

In this paper only the third regime is considered, as the object here is the performance of large tidal arrays which have reached a saturation level of energy extraction. There are three main families of wake interaction models used to estimate velocity deficit in wind turbine arrays: (Crespo et al. 1999):

Wake superposition models are based on the principle of the conservation of momentum-deficit within the wake. The expansion of the far wake is governed by the thrust coefficient of the generator unit and the ambient turbulence intensity (Lissaman 1979). There may also be a small contribution from rotor-generated turbulence. The momentum deficits from each wake are superposed and then the performance of each turbine is calculated and summed to give the output of the whole array. Wake interaction with the ground is handled by a reflection plane with an 'image' turbine.

Field models calculate flow variables at every point in the farm using a numerical model (with spatial discretization). They range from simplified models with assumptions similar to the wake superposition models (Ainslie 1987), to computationally-intensive three-dimensional CFD models (Ammara et al. 2002). The simplified models have been widely used as tools to predict wind turbine array performance, whereas CFD models remain computationally expensive (Crespo et al. 1999).

Boundary Layer models only apply to 'large' wind farms, where it is assumed that there is a spatially-averaged balance between momentum input and drag forces. Observations have shown that velocity deficit at hub height downstream of the first row of turbines in an array rapidly attains a steady value as each successive row is encountered (Frandsen et al. 2006). Consequently, a wind turbine array with more than four rows can be considered a 'large' farm. The turbine drag can then in principle be modelled as an additional uniform roughness over the surface area of the array. These models have not been widely used due to the success of the wake superposition and simplified field models above, and the difficulty in making measurements of flow profiles in and above wind turbine arrays.

4 Rationale for modelling approach

In this present paper, the boundary layer approach to estimating speed deficit in large turbine arrays has been revisited in the context of tidal stream power generation. There are two reasons for considering this type of model. First, it has relevance to the question of maximum power extraction from tidal flow at a particular location, which has been analyzed for the general case of a tidal 'fence' across a well-bounded channel (Garrett and Cummins 2005), but remains an open problem for less well bounded situations. Second, a simplified approach using distributed roughness is attractive from the point of view of modelling the impact of large tidal turbine arrays on tidal flows, using existing coastal modelling software. Individual turbines are too small to be simulated directly in a coastal numerical model with horizontal extent of tens of kilometers, as to resolve both the turbines and the largest scales in the flow would entail excessive computational expense.

A distributed roughness approach has been applied to specific geographic locations by Sutherland et al. (2007) in the case of tidal flows in channels, and by Blunden and Bahaj (2007) to headland-accelerated tidal flow. In the former, the drag coefficient was increased until the maximum power was dissipated through the increased friction. In the latter, values of drag coefficient and spacing of turbines within the array were assumed prior to modelling, and averaged over the affected elements in the model mesh. In neither case were taken into account the changes in spatially-averaged vertical velocity shear profile due to the change in momentum balance within the array.

5 Boundary layer modelling

The modelling of wind turbine arrays using distributed roughness has been informed by boundary layer meteorology, which has developed in the context of measuring and predicting flows over crops, forests and urban landscapes. These are classed as rough-wall turbulent boundary layer flows; 'rough-wall' as the Reynolds number of the roughness obstacle is high and viscosity is irrelevant. A comprehensive review is found in (Raupach et al. 1991). According to a classic analysis, the flow profile (whether in the atmosphere or a open channel) is considered to consist of a roughness sublayer, influenced by the friction velocity and the properties of the roughness, and an outer layer, influenced by the friction velocity and the boundary layer thickness, but not the roughness properties. Between the two layers is an overlap layer which must follow the well-known logarithmic profile due to dimensional arguments:

$$\frac{u}{u_*} = \frac{1}{k} \ln\left(\frac{z-d}{z_0}\right) \tag{1}$$

where the zero-plane displacement d is a parameter for adjusting the profile for a better logarithmic fit; physically it is linked to the mean level of momentum absorption. The roughness sub-layer extends from the surface up to a few multiples of geometric roughness height. For arrays of bluff-bodies such as cubes, or within forest canopies, measurements of the mean flow profile within the roughness sub-layer have been fitted to an empirical exponential profile, derived assuming a constant mixing length throughout the layer. However, flow profiles through comparatively sparse arrays of turbines, where there is no large-scale flow separation, can not necessarily be expected to fit the same function. Values of frontal area to array area ratio, λ, for tidal arrays might be expected to be in the range 0.005–0.05, compared to 0.05–10 for flows over vegetation (Raupach et al. 1991). It has been observed that in atmospheric flows over arrays of obstacles of various shapes and arrangements, that at low obstacle densities, the ratio of roughness length to roughness height is approximately linearly related to the obstacle density. (Raupach et al. 1991; Stephan and Gutknecht 2002).

Where boundary layer theory has been applied to wind turbines, in some cases, the velocity profile has been considered logarithmic over the entire planetary boundary layer, ignoring the roughness of the ground between rows of turbines (Newman 1977). Frandsen (1992) proposed dual logarithmic profiles matching at hub height, noting that flow below hub height had been observed to be logarithmic within a wind turbine array. The geostrophic drag law was used to eliminate the roughness length in the upper layer. In the inner layer, deep within the outer planetary boundary layer, the bed roughness height was assumed to be known and the lower flow profile matched to the upper by velocity at hub height, resulting in a quadratic expression for hub height velocity.

Definition sketches for different types of flow over obstacle roughness are included in Figure 1. The differences are apparent in terms of frontal area ratio and fraction of boundary layer occupied by roughness height. Flows through submerged vegetation bear the most resemblance to those in large tidal turbine arrays, in terms of fraction of depth of flow occupied. However, the high frontal area ratio in submerged vegetation results in a large zero-plane displacement in comparison to plant height, with a logarithmic profile above the canopy, observed in the laboratory with synthetic plants (Nepf and Vivoni 2000) and saltmarsh vegetation (Neumeier 2007).

6 Simplified model for large tidal array

The assumptions made in deriving this present model are as follows:

Assumption 1. The flow is a quasi-steady balance between longitudinal pressure gradient, shear stresses and drag caused by the tidal turbines and bed friction. A possible shear stress at the surface caused by wind is ignored; the effects of waves and acceleration of the tidal stream are also not considered here.

Assumption 2. The thrust due to the turbine and the friction of the bed are assumed to be concentrated at hub height h and at the bed respectively. In reality, these forces would be distributed in the vertical and there would also be a contribution due to drag caused by the structure providing reaction against the thrust of the turbine rotor.

Assumption 3. The spatially averaged mean velocity profile is assumed to be logarithmic over the whole depth H, both far upstream and far downstream of the change of roughness due to the tidal turbine array. In reality, the vertical velocity profile in a tidal stream varies over the tidal cycle, with phase differences in velocity over the water column. Observations made in a moderately fast tidal stream of amplitude 1.2 m/s in depth of around 50 m (Elliott 2002) indicated a good fit to a logarithmic profile over most or all of the depth sampled (30–40 m above the bed) during the ebb and flood periods. In a fast, unstratified tidal stream, the turbulent boundary layer would be expected to extend all the way to the free surface, consistent with the logarithmic profile (Dyer 1986). There is no experimental data for flow within large arrays of obstacles of a similar nature to tidal turbines (low frontal area ratio, large fraction of depth occupied, no flow separation) for comparison, but the similar approach used for wind turbines provides the basis for the assumption. An alternative approach would be to use the empirical exponential function mentioned earlier.

Under these assumptions, the hub height velocity can be expressed as:

$$\frac{u_{h+}}{u_{*+}} = \frac{1}{k} \ln\left(\frac{h}{z_{0+}}\right) \tag{2}$$

There are now two unknown independent variables: the friction velocity u_{*+}, and the roughness length for the large array, z_{0+}. The friction velocity can be related to the streamwise free surface

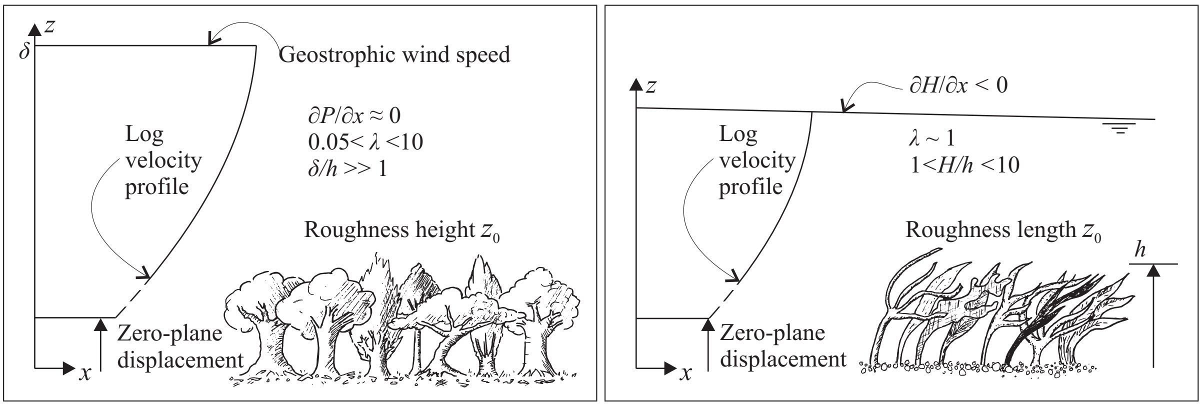

(a) Terrestrial canopy (b) Aquatic canopy

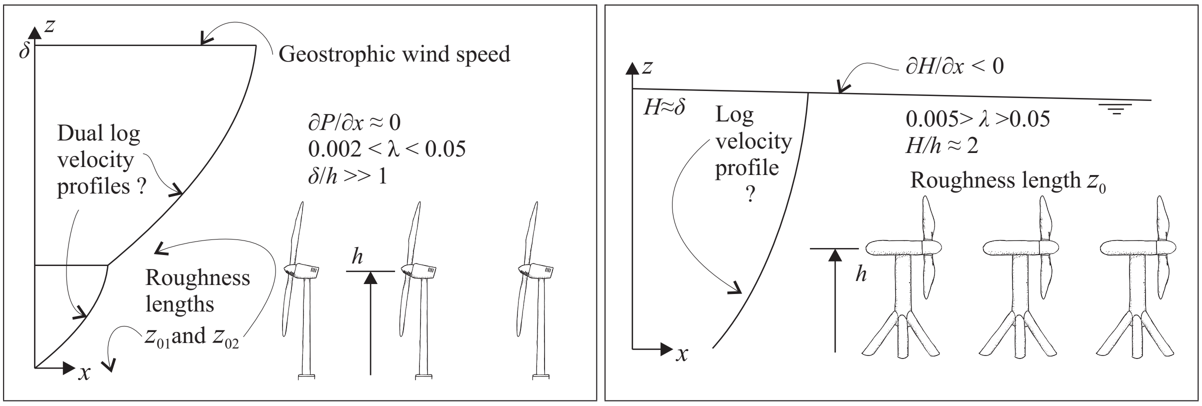

(c) Large wind turbine array (density exaggerated) (d) Large tidal turbine array (density exaggerated)

Figure 1: Conceptual models for flows over canopies and flow through turbine arrays

slope by:

$$u_{*+} = \sqrt{gH\frac{\partial H}{\partial x}} \tag{3}$$

An expression for roughness length has been given by Raupach (1994) (cited in Grimmond and Oke (1999)) based on the frontal area ratio, roughness height—taken here as hub-height of the turbines—and drag coefficients an isolated obstacle (turbine) C_T and underlying surface C_{Dh}:

$$\frac{z_{0+}}{h} = \exp\left(-\frac{k}{\sqrt{C_{Dh} + C_T\lambda}} + \psi_h\right) \tag{4}$$

Where ψ_h is a 'roughness sub-layer influence function,' which parameterizes the interaction of the underlying surface roughness with the distributed obstacle drag. The function is unknown in this case, but has been given as $\psi_h = 0.193$ for vegetated surfaces in Raupach (1994). The expression has been simplified by assuming no zero-plane displacement, due to the sparsity of the obstacles in the array. The bed friction drag coefficient at hub-height in the absence of the obstacles can be expressed in terms of the upstream roughness z_{0-}:

$$C_{Dh} = 2k^2 \Bigg/ \left(\ln\left(\frac{h}{z_{0-}}\right)\right)^2 \tag{5}$$

Equation 5 may then be substituted into (4) in order to give an expression for z_{0+} suitable for numerical modelling purposes.

7 Conclusion

The model briefly proposed here is based on analogies with relationships derived for rough-wall boundary layer flow, where the obstacle densities are in general much higher and flow separation around obstacles occurs. Consequently, the model should be regarded as a tentative first step towards characterizing flow in large tidal arrays, highlighting the need for suitable experimental data for comparison.

References

J. F. Ainslie. Calculating the flowfield in the wake of wind turbines. *Journal of Wind Engineering and Industrial Aerodynamics*, 27(1-3):213–224, 1987.

I. Ammara, C. Leclerc, and C. Masson. A viscous three-dimensional differential/actuator-disk method for the aerodynamic analysis of wind farms. *Journal of Solar Energy Engineering, Transactions of the ASME*, 124(4):345–356, 2002.

A. S. Bahaj, L.E. Myers, M.D. Thomson, and N. Jorge. Characterising the wake of horizontal axis marine current turbines. In A. Falcão, editor, *Seventh European Wave and Tidal Energy Conference*, Porto, Portugal, 2007.

R. W. Baker, S. N. Walker, and P. C. Katen. Wake measurements around operating wind turbines. *Transactions of the ASME. Journal of Solar Energy Engineering*, 107(2):183–5, 1985.

R. J. Barthelmie, L. Folkerts, G. C. Larsen, K. Rados, S. C. Pryor, S. T. Frandsen, B. Lange, and G. Schepers. Comparison of wake model simulations with offshore wind turbine wake profiles measured by sodar. *Journal of Atmospheric and Oceanic Technology*, 23(7):888–901, 2006.

R. J. Barthelmie, S. T. Frandsen, M. N. Nielsen, S. C. Pryor, P. E. Rethore, and H. E. Jorgensen. Modelling and measurements of power losses and turbulence intensity in wind turbine wakes at Middelgrunden offshore wind farm. *Wind Energy*, 10(6): 517–528, 2007.

W. M. J. Batten and A. S. Bahaj. CFD simulation of a small farm of horizontal axis marine current turbines. In A. A. M. Sayigh, editor, *World Renewable Energy Congress IX*, Florence, Italy, 2006. Elsevier.

L. S. Blunden and A. S. Bahaj. Effects of tidal energy extraction at Portland Bill, southern UK predicted from a numerical model. In A. Falcão, editor, *Seventh European Wave and Tidal Energy Conference*, Porto, Portugal, 2007.

A. Crespo, J. Hernández, and S. Frandsen. Survey of modelling methods for wind turbine wakes and wind farms. *Wind Energy*, 2(1):1–24, 1999.

K. Dyer. *Coastal and Estuarine Sediment Dynamics*. John Wiley & Sons, Chichester, 1986.

A. J. Elliott. The boundary layer character of tidal currents in the eastern Irish sea. *Estuarine, Coastal and Shelf Science*, 55(3):465–480, 2002.

S. Frandsen. On the wind speed reduction in the center of large clusters of wind turbines. *Journal of Wind Engineering and Industrial Aerodynamics*, 39(1-3): 251–265, 1992.

S. Frandsen, R. Barthelmie, S. Pryor, O. Rathmann, S. Larsen, J. Hojstrup, and M. Thogersen. Analytical modelling of wind speed deficit in large offshore wind farms. *Wind Energy*, 9(1-2):39–53, 2006.

C. Garrett and P. Cummins. The power potential of tidal currents in channels. *Proc. R. Soc. Lond. A*, 461(2060):2563–2572, 2005.

C. S. B. Grimmond and T. R. Oke. Aerodynamic properties of urban areas derived from analysis of surface form. *Journal of Applied Meteorology*, 38(9): 1262–92, 1999.

P. B. S. Lissaman. Energy effectiveness of arbitrary arrays of wind turbines. *Journal of Energy*, 3(6): 323–328, 1979.

A. J. MacLeod, S. Barnes, K. G. Rados, and I. G. Bryden. Wake effects in tidal current turbine farms. In *MAREC 2002*, Newcastle, UK, 2002. Institute of Marine Engineering, Science and Technology.

H. M. Nepf and E. R. Vivoni. Flow structure in depth-limited, vegetated flow. *Journal of Geophysical Research*, 105(C12):28547–57, 2000.

U. Neumeier. Velocity and turbulence variations at the edge of saltmarshes. *Continental Shelf Research*, 27(8):1046–1059, 2007.

B. G. Newman. Spacing of wind turbines in large arrays. *Energy Conversion*, 16(4):169–171, 1977.

M. R. Raupach. Simplified expressions for vegetation roughness length and zero-plane displacement as functions of canopy height and area index. *Boundary-Layer Meteorology*, 71(1):211–216, 1994.

M. R. Raupach, R. A. Antonia, and S. Rajagopalan. Rough-wall turbulent boundary layers. *Applied Mechanics Reviews*, 44(1):1, 1991.

U. Stephan and D. Gutknecht. Hydraulic resistance of submerged flexible vegetation. *Journal of Hydrology*, 269(1-2):27–43, 2002.

G. Sutherland, M. Foreman, and C. Garrett. Tidal current energy assessment for Johnstone Strait, Vancouver Island. *Proceedings of the Institution of Mechanical Engineers, Part A: Journal of Power and Energy*, 221(2):147–157, 2007.

L. J. Vermeer, J. N. Sorensen, and A. Crespo. Wind turbine wake aerodynamics. *Progress in Aerospace Sciences*, 39(6-7):467–510, 2003.

P. J. Wiles, T. P. Rippeth, J. H. Simpson, and P. J. Hendricks. A novel technique for measuring the rate of turbulent dissipation in the marine environment. *Geophysical Research Letters*, 33(21):1–5, 2006.

Appendix J

EWTEC-2009 conference paper

Pre-print of paper submitted to the Eighth Wave and Tidal Energy Conference, Uppsala, Sweden, 2009, with reference Blunden et al. (2009). This paper was referred to in §6.8 and is currently subject to review.

Comparison of boundary-layer and field models for simulation of flow through multiple-row tidal fences

Luke S Blunden, William M J Batten, Matthew E Harrison and AbuBakr S Bahaj[1]

[1]University of Southampton, School of Civil Engineering and the Environment, University Road, SO17 1BJ, Southampton, UK

Abstract

A simple conceptual model of an array of tidal stream generators is a series of porous fences subject to flow in one direction, neglecting lateral velocity variations, but allowing for vertical velocity shear. In the far-wake of a fence deep inside the array, the flow might be expected to have reached an equilibrium, where the longitudinal pressure gradient is balanced by the drag of the fences and the friction on the sea-bed. This paper compares two approaches to estimating the downstream decrease in velocity in multiple-row tidal fences; firstly a simplified model using ideas from boundary layer theory previously applied to wind turbine arrays; second, a CFD simulation of the flow field around a ten-row array using a general purpose off-the-shelf RANS Finite Volume solver. The CFD simulations have been themselves compared with measurements gained in a laboratory flume.

Keywords: Tidal power, Tidal streams, CFD, Boundary layers

Nomenclature

A_r	Area of generator rotor disk	m^2
c_f	Sea-bed drag coefficient	$= \tau / \frac{1}{2} \rho U_h^2$
c_d	Isolated fence/turbine drag coefficient	$= T / \frac{1}{2} \rho U_h^2 A$
g	Acceleration due to gravity	$= 9.81\ \mathrm{m/s}^2$
h	Depth of water	m
z_H	fence/turbine centroid height	m
κ	Von Kármán constant $= 0.4$	
L_x, L_y	Spacing of fence/turbine	m
l_r	Characteristic dimension of roughness element	m
l_y, l_z	Extent of fence/turbine	m
S_0	Negative of free-surface slope	$= -\partial Z / \partial x$
T	Drag on isolated turbine	N
U	Depth-averaged flow speed	m/s
u_*	Friction velocity	m/s
u, v, w	Velocity components	m/s
x, y, z	Longitudinal, vertical and lateral coordinates	m
Z	Free surface elevation	m
z_0	Roughness length of sea-bed	m
λ	Area ratio	$= A_r / (L_x L_y)$
ν	Molecular kinematic viscosity	$= 1 \times 10^{-6}\ \mathrm{m}^2/\mathrm{s}$
ρ	Density of fluid	$= 1 \times 10^3\ \mathrm{kg/m}^3$
σ_y	Width ratio	$= L_y / l_z$
τ	Frictional stress on sea bed	$\mathrm{N/m}^2$

Subscripts

$+$	Far downstream of the leading edge of fence/turbine array
$-$	Upstream of the leading edge of fence/turbine array

1 Introduction

In this paper, a distributed roughness approach, taken previously in estimating speed deficit in large wind turbine arrays has been revisited in the context of tidal stream power generation. This work extends that described previously in [1] by deriving an expression for displacement height and velocity profile in the part of the water column above the turbines or fences.

In the first part of the paper the simplified distributed roughness model is described. The predictions made by the model are then compared with CFD simulations of a series of tidal fences, simulated by porous surfaces within the computational domain. A tidal fence is a special case of an array of tidal stream turbines where the lateral spacing is as small as possible. Consequently, flow variations in the lateral direction may be ignored and the problem reduced to two dimensions, vertical and longitudinal.

© Proceedings of the 8th European Wave and Tidal Energy Conference, Uppsala, Sweden, 2009

There are two reasons for considering a distributed roughness model. First, it has relevance to the question of maximum power extraction from tidal flow at a particular location, which has been analyzed for the general case of a tidal 'fence' across a well-bounded channel [2], but remains an open problem for less well bounded situations. Second, a simplified approach using distributed roughness is attractive from the point of view of modelling the impact of large tidal turbine arrays on tidal flows, using existing coastal modelling software. Individual turbines are too small to be simulated directly in a coastal numerical model with horizontal extent of tens of kilometers, as to resolve the turbines and include the largest scales in the flow would entail excessive computational expense.

A distributed roughness approach has been applied previously to specific geographic locations by Sutherland et al. [3] in the case of tidal flows in channels, and by Blunden and Bahaj [4] to headland-accelerated tidal flow. In the former, the drag coefficient was increased until the maximum power was dissipated through the increased friction. In the latter, values of drag coefficient and spacing of turbines within the array were assumed prior to modelling, and averaged over the affected elements in the model mesh. In neither case were taken into account the changes in spatially-averaged vertical velocity shear profile due to the change in momentum balance within the array. Bryden et al. [5] have considered energy extraction in a layered 3-D model for some idealized cases, using 80 × 80 m grid cells. However, their work was focused on single-row tidal fences in channels rather than representing multi-row arrays.

1.1 Rough-wall flow through obstacle arrays

The modelling of wind turbine arrays using distributed roughness has been informed by boundary layer micro-meteorology, which has developed in the context of measuring and predicting flows over crops, forests and urban landscapes. These are classed as rough-wall turbulent boundary layer flows; 'rough-wall' as the Reynolds number $u_* l_r/\nu$ based on the characteristic height of the roughness obstacles l_r is high enough to attain similarity and viscosity is irrelevant. For a comprehensive review of rough-wall boundary layer flow, see Raupach et al. [6]. According to a classic analysis, the flow profile (whether in the atmosphere or an open channel) is considered to consist of a roughness sublayer, influenced by the friction velocity and the properties of the roughness, and an outer layer, influenced by the friction velocity and the boundary layer thickness, but not the roughness properties. Between the two layers is an overlapping region that follows the well-known logarithmic profile:

$$\frac{u}{u_*} = \frac{1}{\kappa} \ln\left(\frac{z-d}{z_0}\right) \tag{1}$$

where the zero-plane displacement d is used as a parameter for adjusting the profile for a better logarithmic fit; physically it is equivalent to the mean level of momentum absorption. The roughness sub-layer extends from the surface up to some multiple of the characteristic roughness obstacle size. However, all of the layers are only vaguely defined within the limits of experimental accuracy. For arrays of bluff-bodies such as cubes, or within forest canopies, measurements of the mean flow profile within the roughness sub-layer have been fitted to an empirical exponential profile, derived assuming a constant mixing length throughout the layer. Flow profiles through comparatively sparse arrays of porous obstacles have not received the same degree of experimental investigation.

Table 1: Variation of frontal area to plan area ratio λ with tidal stream turbine size and configuration. n is the number of rotors per generator unit

l_z (m)	A (m^2)	n	σ_x (L_x/l_z)	σ_y (L_y/l_z)	λ $(nA_r/(L_xL_y))$
10	79	1	15	7.5	0.007
16	201	1	15	4	0.013
20	314	2	7.5	4	0.052
0.1	-	-	7.0	-	0.143

The key geometric parameter of an obstacle array has been found to be the ratio of projected frontal area of obstacles to the horizontal area, λ [6]. Values of λ for tidal stream turbine arrays might be expected to be in the range 0.005–0.05 and for tidal fences 0.05–0.15 (see Table 1), compared to 0.05–10 for flows over vegetation. It has been observed that in atmospheric flows over arrays of obstacles of various shapes and arrangements, that at low obstacle densities $\lambda < 0.2$, plots of z_0/l_r against λ collapse onto a linear relationship [6, 7].

1.2 Previous application of approach to large wind turbine arrays

Where boundary layer theory has been applied to wind turbines, in most cases, the velocity profile has been considered logarithmic over the entire planetary boundary layer down to the hub height of the rotor, with a single new roughness length describing the flow through the array compared to the flow in the undisturbed state. The 'gradient wind' at height was assumed constant, although the boundary layer thickness was allowed to vary in some cases. A difficulty arises with the momentum approach to this type of model in that the distribution of drag between friction (and possibly form drag if there are large-scale features) at the bed and the turbines is not known [8]. The energy approach is even more uncertain however as the rotor- and wake-generated turbulence production is also not known. Newman [9] assumed that the shear stress on the ground was constant i.e. no change from upstream to within the array. The new roughness length could then be calculated from the sum of the shear stress on the ground and the spatially-averaged drag on the turbines.

Frandsen [10] proposed dual logarithmic velocity profiles matching at hub height, noting that flow below hub height had been observed to be logarithmic within a wind turbine array. The 'gradient wind' was used to eliminate the roughness length in the upper layer. In the inner layer, deep within the outer planetary boundary layer, the bed roughness height was assumed to be known and the lower flow profile matched to the upper by velocity at hub height, resulting in a quadratic expression for hub height velocity.

The model of Frandsen bears similarities to the growth of a new internal boundary layer from the bed due to a change of bed roughness, where the upper layer retains the memory of the upstream roughness, whereas the slowly-growing internal layer is adapted to the new conditions. However, it is not clear why the internal layer would only extend to hub height and not grow to fill the whole external boundary layer. The velocity measurements cited by Frandsen as evidence of a logarithmic profile below hub height were taken within the onshore wind turbine array Nørrakær Enge II, Jutland, Denmark [11, page 27] where there were two to three points in the vertical below hub height and the measurements were taken at effectively two rows into the array. The measurements do not therefore represent conclusive evidence for the model being correct.

1.3 Similarities and differences with natural rough-wall flows through obstacle arrays

Definition sketches for different types of flow over obstacle roughness are included in Figure 1 and for flow through turbine arrays in Figure 2. The differences are apparent in terms of frontal area ratio and fraction of boundary layer or depth occupied by roughness height. Flows through submerged vegetation bear the most resemblance to those in large tidal turbine arrays, in terms of fraction of depth of flow occupied. However, the high frontal area ratio in submerged vegetation results in a large zero-plane displacement in comparison to plant height, with a logarithmic profile above the canopy, observed in the laboratory with synthetic plants [12] and saltmarsh vegetation [13].

There is little experimental data for flow above and especially below the geometric roughness height of large arrays of obstacles of a similar nature to tidal turbines (low frontal area ratio, large fraction of depth occupied, high porosity, no flow separation) for comparison, although work has begun in this area [14]. MacDonald [15] investigated flow among and above arrays of cuboid obstacles and derived a semi-empirical exponential expression for the velocity profile below the obstacle height. In doing so, it was assumed that at each height above the surface, the drag coefficient experienced by the flow was constant and that the length scale for the turbulent viscosity was also constant. Moreover the lowest value of area ratio investigated was at the upper end of the range that might be expected for a tidal turbine array. Bentham and Britter [16] proposed an even simpler model, with the velocity constant below obstacle height. This gives results similar to [15] for low values of area ratio, and was proposed by in the context of modelling flow through and over urban canopies.

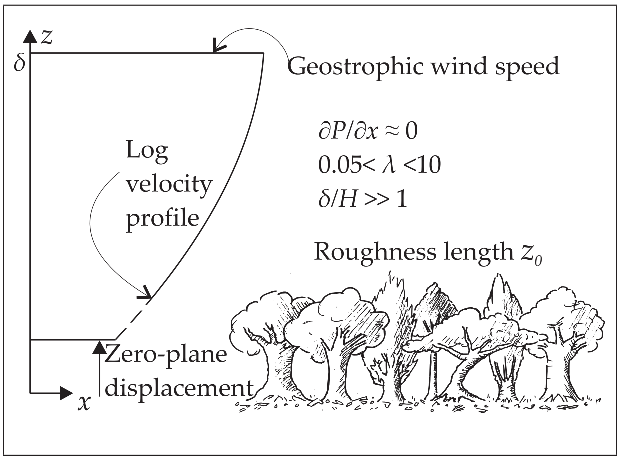

(a) Terrestrial canopy

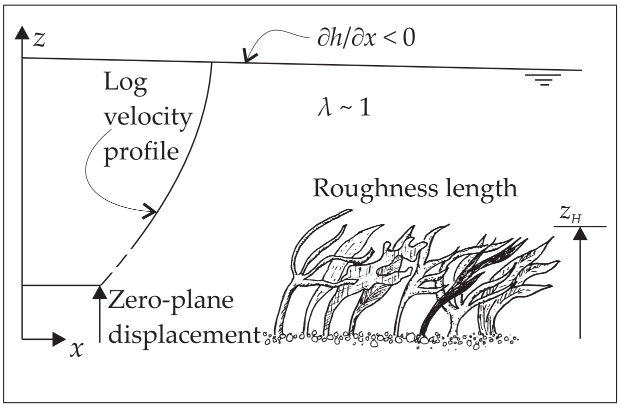

(b) Aquatic canopy

Figure 1: Conceptual models for flows over atmospheric and aquatic canopies

1.4 Vertical velocity profiles in fast tidal streams

The shape of the vertical velocity profile in a tidal stream varies over the tidal cycle, with phase differences in velocity over the water column as the upper portion is more affected by inertia and the lower by friction at the bed. These effects are most important when the velocities are low and are therefore likely to have little effect on the energy capture of a tidal turbine, which would be generating at low efficiency or not at all (if below cut-in speed). The external balance of forces in the flow during most of a tidal cycle is between longitudinal pressure gradient due to sea-surface slope and frictional stresses on the sea bed [17], which is in contrast to the atmospheric boundary-layer case where the flow is driven by the geostrophic wind from above.

Observations made in a moderately fast tidal stream of amplitude 1.2 m/s in depth of around 50 m [18] indicated a good fit to a logarithmic profile over most or all of the depth sampled (30–40 m above the bed) during the ebb and flood periods. In a fast, unstratified tidal stream, the logarithmic profile may extend all the way to the free surface [19].

The portion of the water column close to the surface is avoided by most designs of full-scale tidal stream turbine rotor assembly, for many reasons including cavitation or

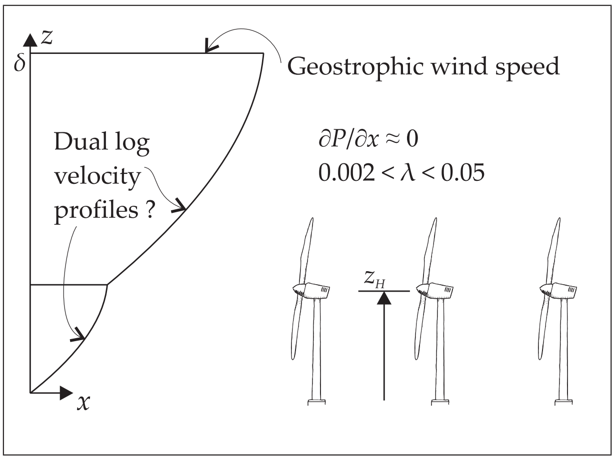

(a) Large wind turbine array after Frandsen [10] (density exaggerated)

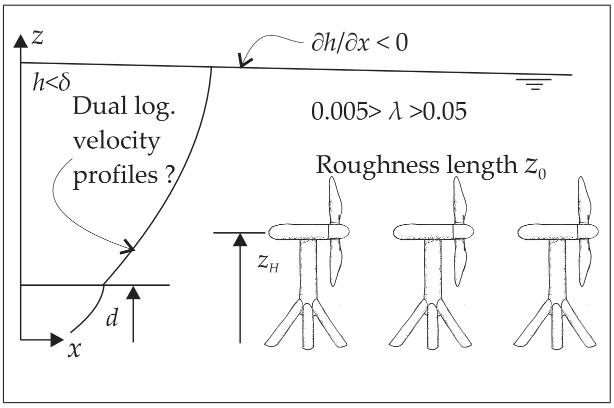

(b) Large tidal turbine array (density exaggerated)

Figure 2: Conceptual models for flow through wind and tidal turbine arrays

ventilation on the blade tips; hazards to surface vessels and wave action. Consequently the deviation from a logarithmic profile in this region is unlikely to have a large effect on the energy capture of such turbines.

The evidence above leads to the following assumption that will be used in developing the new model:

Assumption 1 *The flow in the natural state is fully rough-turbulent and the mean vertical profile can be described by a logarithmic profile over most of the depth.*

2 Distributed roughness model for a large tidal stream turbine array

The following part of this paper details a new model which extends the methodology previously used for wind turbine arrays, to tidal stream arrays. The velocity profile above the fences is derived based on a logarithmic profile. In order to develop the new model, two further assumptions need to be made.

Assumption 2 *The resultant force upon each fence/turbine acts at the height of the centroid of the swept area of the fence/turbine.*

It would be possible to use multiple-streamtubes with varying velocities to integrate the profile across the swept area of the turbine, but given the generic and approximate nature of the model, this is probably not justified. In reality, there would also be a contribution to the total drag experienced by the flow, caused by the structure providing reaction against the thrust of the turbine. This could be added into the model at a later stage based on the estimated drag on a particular structural configuration.

Assumption 3 *The flow within the array as a function of space may be considered the sum of a constant and fluctuating terms, stationary in space and time.*

This assumption relies on equilibrium conditions being reached at some number of rows into the array. The mean flow is considered uniform in the horizontal; the slope in the free-surface is not considered to have a significant effect on either the depth or on the depth-averaged velocity.

A true finite-array added roughness model would need to take into account the non-equilibrium growth of an internal boundary layer from the leading edge of the tidal stream turbine array. Similarly, downstream of the array, the flow will require a certain distance to re-attain equilibrium. Parameters derived for an infinite array may be applied to a finite array in a similar manner to a standard assumption in open channel hydraulics, that a coefficient of friction derived for uniform flow can be applied to spatially-varied flow [20, page 217]. As the number of rows in the array increase, the edge-effects should diminish in importance and the solution converge on the case of an infinite array.

2.1 Hub height velocity within the large array

Under these assumptions, the velocity above the fences, several rows into the turbine array can be expressed as:

$$\frac{u_+}{u_{*+}} = \frac{1}{\kappa} \ln\left(\frac{z-d_+}{z_{0+}}\right) \tag{2}$$

There are three unknown variables: the friction velocity u_{*+}, the zero-plane displacement d_+ and the roughness length for the large array, z_{0+}. By analogy with flow over submerged vegetation, where it is assumed that $z = d$ is effectively a lower boundary to the flow and $h-d$ is the effective depth [12], the friction velocity can be related to the streamwise free surface slope by:

$$u_{*+} = \sqrt{gS_{0+}(h-d_+)} \tag{3}$$

Where $S_{0+} = -\partial Z/\partial x$. The free-surface slope (pressure gradient) S_{0+} is not known; for a finite array, it will be a function of upstream and downstream conditions. In addition it may be affected by the geometry of the array and the proximity of lateral boundaries. Assuming a fixed free-surface slope gives the most pessimistic estimate and the fixed flow-rate the most optimistic. Reality will lie somewhere between the extremes of constant slope and constant flow rate, i.e. the flow is likely to back-up in front of the array resulting in a local steepening of the free-surface slope across the array in the streamwise direction, but there will also be a local decrease in the depth averaged velocity.

u_{*+} is also known independently through the sum of the resistive forces, assuming equilibrium:

$$u_{*+} = \frac{1}{\sqrt{2}}\sqrt{c_d \lambda U_+^2 + \alpha c_{f-} U_-^2} \tag{4}$$

where

$$\alpha = \frac{c_{f+} U_+^2}{c_{f-} U_-^2} \tag{5}$$

If $\alpha = 1$, then there is no change in drag on the sea-bed with respect to the undisturbed case. When the free-surface slope is assumed constant and as $\lambda \rightarrow \{0, \infty\}$, $\alpha \rightarrow \{1, 0\}$, but for intermediate values of λ, α would depend on the distribution of shear stresses in the flow between the sea-bed and hub-height. For the previous wind turbine array models, authors have taken $\alpha \propto (u_{H+}/u_{H-})^2$ [8]. This is attractive as it links the upper and lower velocity profiles together, but is only valid where the velocity profile decreases monotonically to the bed. An alternative approach is adopted here, typical in marine applications; the friction coefficient is related to the flow velocity at 1 m above the bottom, u_{100} (10 mm in the 1/100 scale model). In the absence of any better information, the constant of proportionality is taken as unity:

$$\alpha = (u_{100+}/u_{100-})^2 \tag{6}$$

If there is acceleration of the flow underneath the fence then there is the possibility of an *increase* in bed friction inside the array. This will be discussed later in the light of the CFD model results (§5). The zero-plane displacement d, as mentioned previously, is the mean level of momentum absorption. It is often ignored for flow over surfaces as it is of the same order as the height of the roughness elements, i.e. $d_- \approx 0$ and consequently small compared to the depth. However, in the case of an obstacle array it may be raised significantly. The wind turbine models considered previously have assumed a zero-plane displacement of zero, presumably either for the sake of simplicity—it introduces awkward algebra into the expressions—or because the turbine hub height was much less than the thickness of the planetary boundary layer. Deep within the array, then mean level of momentum absorption may be estimated as:

$$\frac{d_+}{z_H} = \frac{\lambda c_d U_+^2}{\lambda c_d U_+^2 + \alpha c_{f-} U_-^2} \tag{7}$$

with the requirement that $(z_H - d_+)/z_{0+} > 1$. The drag coefficient of the fences/turbines c_d is here referred to the local depth-averaged velocity.

In order to estimate the roughness length z_{0+}, reference must be made to the literature for rough-wall flow through obstacles. an empirical fit to data cited in [21] gives:

$$z_0/l_r = 0.5\lambda \tag{8}$$

Where l_r is the height of the roughness elements. In the case of the porous fences it is not clear what height corresponds to l_r as there is flow underneath a fence; the possible choices are the fence height l_z the centroid height z_H or the total height $z_H + l_z/2$.

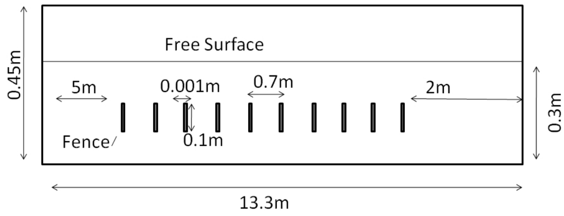

Figure 3: CFD problem geometry

At this point u_{*+}, d_+ and z_{0+} are all specified providing α can be estimated; here the CFD results will be used to determine c_d and c_{f+}.

3 CFD model of a ten-row tidal fence array

In this section the methodology is described for the computational model of a finite array of tidal fences. A tidal fence may be regarded as a close-packed row of tidal turbines (i.e. $\sigma_y \rightarrow \infty$). The array was represented by a series of porous surfaces in a channel. The results using the CFD methodology are then compared with experimental results (§4) in order to show the degree of agreement.

3.1 Computational method

The porous fences were spaced at $7l_z$ ($l_z = 0.1$ m) apart and were modelled as sub domains, with the porous loss modelled as a directional momentum loss. The resistance loss coefficient was calculated using Equation 9. The value was then iterated until the measured pressure drop across one fence in the solution was similar to that measured in the flume.

$$c_d = C_R \Delta x \tag{9}$$

Where Δx is the thickness of the fence, and C_R is the resistance coefficient.

The domain was modelled at the same scale as the experiments (see §4), but with configurations of up to ten fences. The problem dimensions are shown in Figure 3. The inlet velocity profile in the experiments fell into either the smooth or transitional categories of hydraulic roughness, depending on the value of geometric roughness height assumed. Therefore, the velocity at the inlet boundary was defined by fitting a smooth-turbulent logarithmic profile (10) [19] to the measured data from the experiments.

$$u_{\text{in}}(y) = \frac{1}{\kappa} u_* \ln\left(\frac{u_* y}{\nu}\right) + A \tag{10}$$

Where u_{in} is the modelled inlet velocity, u_* the friction velocity and A an arbitrary constant. Curve-fitting gave $u_* = 0.0070$ m/s and $A = 0.14$ m/s; the velocity profile was entered in CFX Expression Language (CEL) for the inlet boundary. The model inlet profile is shown

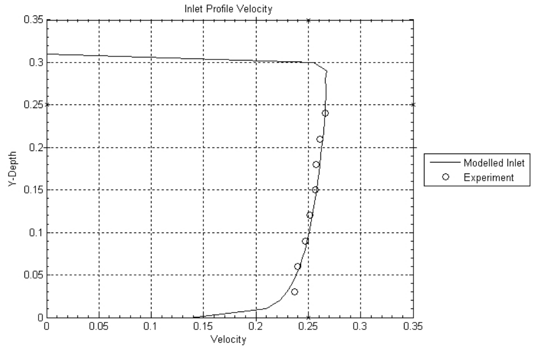

Figure 4: Inlet velocity profile

Table 2: CFD model parameters

Parameter	Setting
Water	Incompressible fluid
Air	Ideal Gas
Multi-phase Control	Homogeneous coupled free surface
Turbulence Model	SST
Inlet	Boundary layer model. See Figure 4. Free surface height 0.3 m
Bottom Boundary	No Slip Condition Smooth Wall
Sides Boundaries	Symmetry
Outlet	Static pressure 0 Pa, Free surface height $(0.3-0.0054)$ m
Top	Opening, Air, 0 Pa
Convergence criteria	RMS residual 1×10^{-6}

with the measured points in Figure 4. The pressure at the outlet boundary was estimated by subtracting the pressure drop (in terms of static head loss) across the fences derived using open channel hydraulics. A head loss of 0.0054 m was estimated across ten fences with $c_d \approx 0.63$, and a hydrostatic pressure profile was set at the outlet based on this value (as an initial condition). This pressure value was used for all fence configurations. Assuming that most of the head loss occurred over the part of the channel containing the fences, the imposed head loss gave a friction velocity of approximately $u_* = 0.048$ m/s. Boundary conditions and other model parameters are summarized in Table 2.

The model calculations were made using ANSYS® CFX 11 Academic Research [22], which solves the Reynolds-Averaged Navier-Stokes (RANS) mass and momentum equations. CFX uses a hybrid finite-element/finite-volume discretization approach, which supports arbitrary mesh topology. Advection fluxes were evaluated using the second-order high resolution scheme.

For engineering applications, two-equation models have been most widely to model turbulence. They have sufficient flexibility for modelling a variety of flows, at modest computational expense. The k-ε model is known to be insensitive to inlet turbulence intensity, but behaves poorly close to boundaries. The k-ω model by contrast, performs well close to boundaries but is sensitive to the specification of inlet turbulence intensity. A blended combination of the two models was proposed by Menter [23] to capture the best of both. The model, known as a shear-stress transport (SST) model, redefined the turbulent viscosity within boundary layers to effectively make the turbulent shear stresses equal to a constant multiple of the transported turbulence kinetic energy. The Menter SST model has been shown to have superior performance in adverse pressure gradients and separated flow [23]. These conditions exist in the present simulation as there is a positive (adverse) pressure gradient in the region upstream of a fence, and there is effective flow separation above and below each fence. As a consequence, the Menter SST model was chosen for turbulence closure in the simulation.

A coupled volume-fraction algorithm was used to solve the free surface. The problem was defined in 2-D, in order to solve the XY plane behind the fences. In CFX, 2-D problems are modelled using a 3-D mesh of single element thickness.

3.2 Mesh refinement study

The basic mesh was a structured hexahedral arrangement, consisting of 2.66×10^5 nodes, and 1.32×10^5 elements. The CFX mesh adaptation system was used to refine the mesh in areas where the velocity gradients were high. Three mesh adaptation steps were undertaken for each model, with a node factor of 3.0 (i.e. the final mesh had around three times more nodes than the original). A sample of the basic and adapted mesh is shown in Figure 5, which shows that nodes were added in the wake region, and at the bottom boundary. Basic mesh values were chosen to ensure wall $20 \le y_+ \le 100$ giving good boundary layer resolution.

A mesh refinement study across the four meshes (basic mesh plus three successive adaptation steps) showed that the c_d modelled across the fences demonstrated convergence with increasing refinement. Table 3 shows the c_d values for each fence, at each adaptation step.

4 Physical model of four-row fence array

The experimental method and results are included here to compare with the CFD results. A set of four mesh fences was installed in a flume to simulate rows of tidal stream turbines with close lateral spacing. The results have been presented previously in [24]. The measurements were carried out at the University of Southampton Chilworth Research Laboratory. The flume is 1.37 m wide and 21 m in length. For these measurements the flume was run at 0.3 m depth ($3l_z$), with a mean inlet velocity of 0.23 m/s. The geometric scaling of the experiments was 1/100 compared to a 10 m high fence in 30 m channel. Scaling the flow speed with channel Froude number gives a full-scale tidal speed of approximately 2.5 m/s. The Reynolds number based on the fence height, calculated at 3×10^5 is lower than full scale, but still within the fully turbulent range.

Table 3: Thrust coefficient of each porous fence derived from model results. Thrust coefficient has been normalized by flow speed upstream of the first fence

Mesh	Number of: Nodes	Number of: Elements	Thrust coefficient c_d at fence number: 1	2	3	4	5	6	7	8	9	10
Basic mesh	2.7×10^5	1.3×10^5	0.76	0.49	0.45	0.48	0.50	0.53	0.55	0.56	0.56	0.57
Refinement 1	5.1×10^5	3.7×10^5	0.76	0.50	0.46	0.48	0.51	0.53	0.55	0.56	0.56	0.57
Refinement 2	6.5×10^5	5.8×10^5	0.76	0.50	0.47	0.49	0.52	0.54	0.56	0.57	0.58	0.58
Refinement 3	8.2×10^5	8.0×10^5	0.75	0.50	0.47	0.48	0.51	0.54	0.55	0.56	0.57	0.57

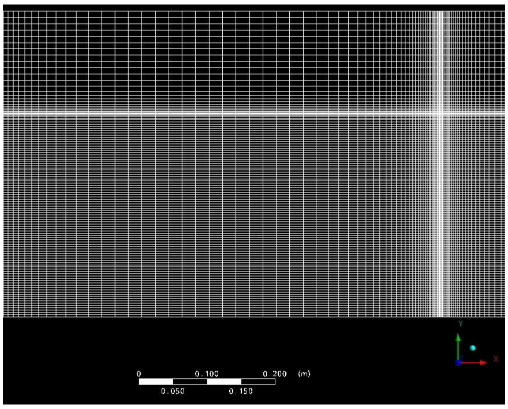

(a) Initial structured mesh.

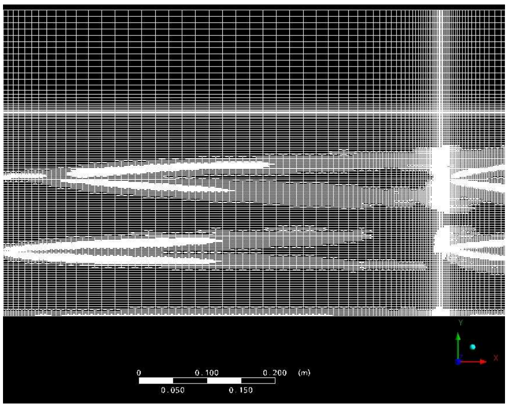

(b) Mesh resolution increased in areas of high velocity shear

Figure 5: Adaptive meshing

(a) Fixing arrangements.

(b) Front view showing end discs to minimize vortices shed from ends.

Figure 6: Porous fence arrangement

Four identical fences were constructed from a wire mesh, with width of 0.95 m and a height l_z of 0.1 m, simulating an arbitrary row of turbines with diameter 0.1 m across the same width. At either end of the fence end discs were fitted (with diameter twice the height of the fence) to reduce vortex shedding from the fence ends. Fences were installed at the centre of the flume depth, with the midpoint at 0.15 m (1.5 l_z). A 10 N load cell was used to measure the reaction of the supporting arm, and allow the thrust coefficient of the fence assembly to be calculated. Measurements were made over a period of approximately five minutes. The fence arrangement is shown in Figure 6.

The data from the load cells were used to calculate c_d:

$$c_d = T/(1/2)\rho U_0^2 A \tag{11}$$

Where U_0 is the undisturbed velocity at the first fence row. The measured voltages were translated to thrust values based on a calibration curve for the load cell, and moments around the pivot point for the supporting arm.

An Acoustic Doppler Velocimeter (ADV) was used to profile the flow velocity around the fences. It has been shown that mean velocity errors of less than 1% are achievable with this equipment [25]. A three-minute sample was made at each measurement location, at a sample rate of 50 Hz. Measurements were made at 3, 5, 7, 9, 11, 15, 20 and 25 l_z behind each fence, with eight measurements made vertically through the water column at each location. In the depth-wise direction, the measurement spacing was 10% of the depth i.e. 0.03 m. It was not possible to measure at 0%, 90% or 100% depth due to the limitations of the ADV methodology. At each fence location (with the fence removed) measurements were made at the centroid of the fence and $\pm 4.5 l_z$ laterally for an average velocity across the fence. The velocity behind each fence was profiled individually, such that data exists for the flow behind 1-, 2-, 3- and 4-fence configurations. A total of 328 measurements were made, each of duration three minutes.

5 Results and Discussion

5.1 Experimental results

Figure 7 shows reasonable agreement between measured and modelled velocities on the fence centre-line. This gives a degree of confidence that the CFD model can reproduce the velocity deficit on the centre-line behind a ten fence array. It should be emphasized that each set of measurements was separate, e.g. one set made behind one fence only, another behind two fences only and so on. Figure 8 shows that the agreement between modelled and measured velocity profiles measured above the centre-line was also reasonable but below the fences was poor. The region below the fences is of particular interest from the point of view of distributed roughness modelling, in order to determine the partition of resistance to the flow between the bottom and the fences. Consequently, further experiments are required to determine how the velocity profile varies with different gap heights $z_H - l_z/2$ and bottom roughness.

Tidal fences are a special case of tidal stream generator array; whereas the wakes of individual generators in a sparser array are able to expand and mix in the lateral direction, the wake of a tidal fence cannot. Continuity requires that there must be acceleration in a vertical plane above and/or below the porous fence. In contrast with the porous fence experiments, similar experiments with single isolated porous disks in a channel indicated that acceleration beneath the disks was insignificant [14, 26].

As mentioned in §3.1, the flow profile in the flume (upstream of the fences) either fell into the category of hydraulically-smooth or transitional. However, at full-scale the flow would fall into the hydraulically-rough category, with the simpler logarithmic velocity profile independent of wall Reynolds number. This highlights the problem of scale in experimental investigation of large arrays of tidal turbines. Introduction of artificial roughness on the bottom of the flume would be desirable for future experiments in order to bring the flow into the fully rough-turbulent regime. It would also be desirable to measure the pressure gradient directly; this is likely to be very small and in a laboratory may require special head amplification techniques for accurate measurement.

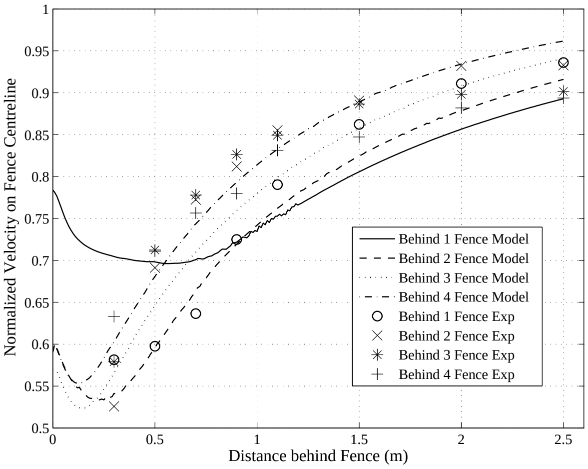

Figure 7: Comparison of experimental and modelled longitudinal velocity variation behind one to four fence arrays

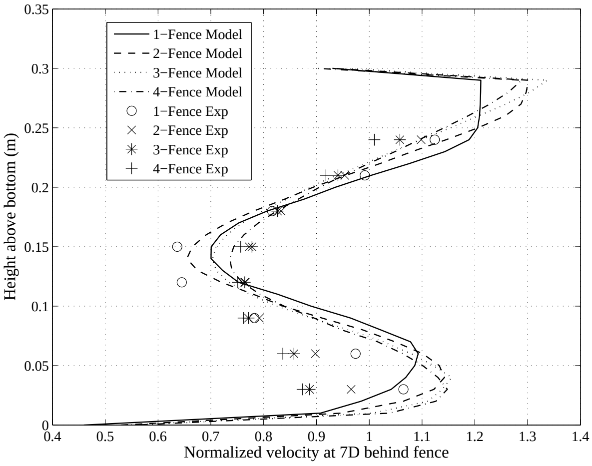

Figure 8: Comparison of experimental and modelled vertical velocity profiles behind one to four fence arrays, at $7l_z$ downstream.

5.2 CFD results

Figure 9 shows that the CFD model predicts an increase in friction coefficient downstream of the leading edge of the array, which has not fully converged after ten rows. The raw bed shear stress is noisy (related to the velocity gradient) and is clearly sensitive to the discretization of the mesh. An empirical build-up exponential curve was fitted to the smoothed results in order to estimate the equilibrium value which gave $c_f = 0.00873$ with a 95% confidence interval of 5×10^{-5}. The curve fit predicted convergence to within 1% of the final value by a distance equivalent to fifteen fences deep into the array. Figure 10 shows the modelled drag coefficient of the porous fences multiplied by the area ratio λ, indicating convergence. The values may then be compared directly with those in Figure 9 and it is immediately clear that in case the area-averaged fence drag is larger than bottom friction by a factor of ten.

5.3 Simplified model

Using the equilibrium values for friction and drag coefficient, values for the zero-plane displacement and friction velocity may be calculated using Equations (7) and (4), giving $d_+ = 0.137$ m and $u_{*+} = 0.0575$ m/s. Using (3), the imposed head drop in the model of 0.0054 m implies an average friction velocity over all the fences of $u_* = 0.0476$ m/s. Using the total height of the fence above the bottom as the appropriate length for Equation (8) gives $z_{0+} = 0.0142$ m. Based on these parameters, the velocity profile for $z \geq z_H + l_z/2$ may be plotted. Figure 11 shows the predicted profile along with those taken from three sections along the channel in the CFD results. It can be seen that the predicted profile lies in the

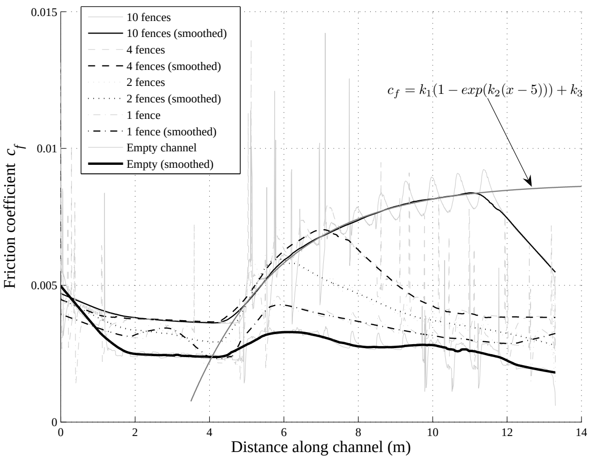

Figure 9: Variation of bed friction coefficient with distance along channel. Friction coefficient c_f is referred to the local depth-averaged flow speed.

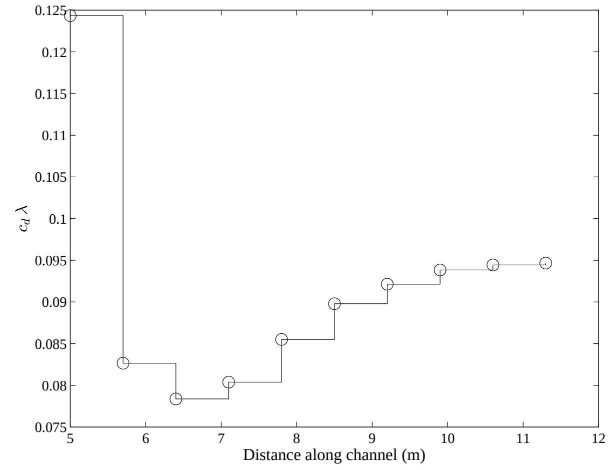

Figure 10: Variation of area-averaged fence drag $c_d\lambda$ with distance along channel. Drag coefficient is referred to the local depth-averaged flow speed.

same range of values as the CFD results but shows some differences in form. This new model has been based on both previous theories applied to wind turbine arrays and analogies with rough-wall boundary layer obstacle flows, in particular that over submerged vegetation. In the latter, obstacle densities are in general much higher and flow separation around obstacles occurs. In the former, arbitrary assumptions are made concerning the distribution of drag in the vertical. Consequently, the new model should be regarded as a tentative first step towards characterizing flow in large tidal arrays, highlighting the need for suitable experimental data for comparison.

Apart from λ, other geometric ratios such as lateral and longitudinal spacing and areal blockage may be important in determining the equilibrium drag and velocity profiles for an infinite array, but their inclusion in a distributed roughness model would be at the expense of simplicity and currently without sufficient experimental data to compare.

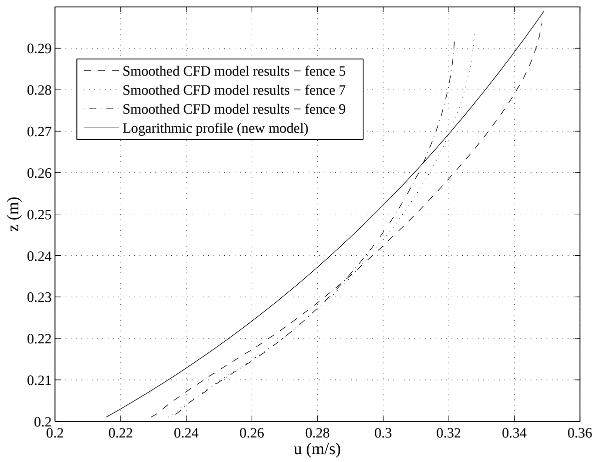

Figure 11: Comparison of velocity profiles above fences from smoothed CFD results with prediction from new model

The results of the previous equilibrium models applied to wind turbine arrays have indicated that they tend to give pessimistic estimates of the array efficiency when compared to experimental data [27] and empirical finite array models [8, 28].

6 Conclusions

1. A new model has been proposed for the velocity profile above a large array of tidal stream turbines. An important difference between this model and previous models is the inclusion of the upward displacement of the spatially-averaged mean level of the momentum absorption, the zero-plane displacement d, significant for plausible array densities.

2. A set of experiments were carried out on an array of four porous mesh fences in a channel. Measurements were made of flow velocities and drag on the fences. The results were compared with those of a CFD model with similar geometry and with the fences represented as imposed pressure gradients. Reasonable agreement in velocity profile was found above and on the centre-line of the fences, but was poorer below.

3. The CFD model was extended to an array of ten fences to examine the degree of convergence on equilibrium values for an array with an infinite number of fences. The area-averaged drag coefficient of the fences $c_d\lambda$ converged to 0.0947 ± 0.0002. The variation of bottom friction coefficient with distance from the first fence was fitted to a build-up exponential curve which predicted an equilibrium value $c_f = 0.00873$ with a 95% confidence interval of 5×10^{-5}.

4. The new model was compared with the predicted equilibrium values from the CFD model, giving an RMS difference of 0.0127 m/s over the interval $0.2 \leq y \leq 0.3$ when compared to the profile 10.6 m downstream from the CFD results.

5. There is more work to do, both theoretical, computational and experimental in linking the bottom friction and the lower velocity profile to the velocity on the centreline and the upper velocity profile, in order to make the model useful for predicting the output of tidal stream turbine arrays.

References

[1] L. S. Blunden and A. S. Bahaj. Flow through large arrays of tidal energy converters: is there an analogy with depth limited flow through vegetation? In A. A. M. Sayigh, editor, *Tenth World Renewable Energy Congress*, Glasgow, 2008. Elsevier.

[2] C. Garrett and P. Cummins. The power potential of tidal currents in channels. *Proc. R. Soc. Lond. A*, 461(2060): 2563–2572, 2005.

[3] G. Sutherland, M. Foreman, and C. Garrett. Tidal current energy assessment for Johnstone Strait, Vancouver Island. *Proceedings of the Institution of Mechanical Engineers, Part A: Journal of Power and Energy*, 221(2): 147–157, 2007.

[4] L. S. Blunden and A. S. Bahaj. Effects of tidal energy extraction at Portland Bill, southern UK predicted from a numerical model. In A. Falcão, editor, *Seventh European Wave and Tidal Energy Conference*, Porto, Portugal, 2007.

[5] I. G. Bryden, S. J. Couch, A. Owen, and G. Melville. Tidal current resource assessment. *Proceedings of the Institution of Mechanical Engineers, Part A: Journal of Power and Energy*, 221(2):125–135, 2007.

[6] M. R. Raupach, R. A. Antonia, and S. Rajagopalan. Rough-wall turbulent boundary layers. *Applied Mechanics Reviews*, 44(1):1, 1991.

[7] U. Stephan and D. Gutknecht. Hydraulic resistance of submerged flexible vegetation. *Journal of Hydrology*, 269(1-2):27–43, 2002.

[8] E Bossanyi, C. Maclean, G. E. Whittle, P. D. Dunn, N. H. Lipman, and P. J. Musgrove. The efficiency of wind turbine clusters. In *Third international symposium on wind energy systems*, pages 401–416, Technical University of Denmark, Lyngby, 1980. BHRA, Cranfield, UK.

[9] B. G. Newman. Spacing of wind turbines in large arrays. *Energy Conversion*, 16(4):169–171, 1977.

[10] S. Frandsen. On the wind speed reduction in the center of large clusters of wind turbines. *Journal of Wind Engineering and Industrial Aerodynamics*, 39(1-3):251–265, 1992.

[11] J. Højstrup, M. S. Courtney, C. J. Christensen, and P. Sanderhoff. Full scale measurements in wind turbine arrays. Nørrakær Enge II. CEC/JOULE. Technical Report Risø-I-684(EN), Risø National Laboratory, March 1993.

[12] H. M. Nepf and E. R. Vivoni. Flow structure in depth-limited, vegetated flow. *Journal of Geophysical Research*, 105(C12):28547–57, 2000.

[13] U. Neumeier. Velocity and turbulence variations at the edge of saltmarshes. *Continental Shelf Research*, 27(8): 1046–1059, 2007.

[14] A. S. Bahaj, L.E. Myers, M.D. Thomson, and N. Jorge. Characterising the wake of horizontal axis marine current turbines. In A. Falcão, editor, *Seventh European Wave and Tidal Energy Conference*, Porto, Portugal, 2007.

[15] R. W. MacDonald. Modelling the mean velocity profile in the urban canopy layer. *Boundary-Layer Meteorology*, 97(1):25–45, 2000.

[16] T. Bentham and R. Britter. Spatially averaged flow within obstacle arrays. *Atmospheric Environment*, 37(15):2037–2043, 2003.

[17] A. R. Campbell, J. H. Simpson, and G. L. Allen. The dynamical balance of flow in the Menai Strait. *Estuarine, Coastal and Shelf Science*, 46(3):449–455, 1998.

[18] A. J. Elliott. The boundary layer character of tidal currents in the eastern Irish sea. *Estuarine, Coastal and Shelf Science*, 55(3):465–480, 2002.

[19] K. Dyer. *Coastal and Estuarine Sediment Dynamics*. John Wiley & Sons, Chichester, 1986.

[20] V. T. Chow. *Open-channel hydraulics*. McGraw-Hill, 1959.

[21] R. Wooding, E. Bradley, and J. Marshall. Drag due to regular arrays of roughness elements of varying geometry. *Boundary-Layer Meteorology*, 5(3):285–308, 1973.

[22] ANSYS®. ANSYS academic solutions. `http://www.ansys.com/academic/`, 2009.

[23] F. R. Menter. A comparison of some recent eddy-viscosity turbulence models. *Journal of Fluids Engineering*, 118(3):514–519, 1996.

[24] M. E. Harrison, W. M. J. Batten, L. S. Blunden, L. E. Myers, and A. S. Bahaj. Comparisons of a large tidal turbine array using the boundary layer and field wake interaction models. In *Second International Conference on Ocean Energy (ICOE 2008)*, Brest, 2008.

[25] G. Voulgaris and J. H. Trowbridge. Evaluation of the Acoustic Doppler Velocimeter (ADV) for turbulence measurements. *Journal of Atmospheric and Oceanic Technology*, 15(1):272–289, 1998.

[26] L. E. Myers, A. S. Bahaj, G. Germain, and J. Giles. Flow boundary interaction effects for marine current energy conversion devices. In A. A. M. Sayigh, editor, *Tenth World Renewable Energy Congress*, Glasgow, 2008. Elsevier.

[27] D. J. Milborrow. The performance of arrays of wind turbines. *Journal of Industrial Aerodynamics*, 5(3-4):403–30, 1980.

[28] P. J. H. Builtjes and D. J. Milborrow. Modelling of wind turbine arrays. *Precision Engineering*, pages 417–430, 1980.

Glossary

ACD *Above chart datum* See also CD.

Amphidrome Point at which a particular tidal constituent has zero amplitude. If the point of zero amplitude appears to occur inland the amphidrome is said to be degenerate.

AODN *Above Ordnance Datum Newlyn* The datum was fixed as MSL Newlyn 1915-1921 and is the vertical datum for mainland UK.

CD *Chart datum* Chart datum is defined as LAT for a particular port in the chart area

Co-range Contours of tidal amplitude on a map for a particular tidal constituent. See also Co-tidal.

Co-tidal Lines of equal phase on a tidal elevation map. These lines meet at an Amphidrome.

Darrieus turbine Turbine with blades rotating about an axis normal to the plane in which flow occurs (horizontal plane in the case of tidal stream), therefore not affected by changes in flow direction in this plane.

DTI *Department of Trade and Industry* Former department of UK government; now known as BERR.

Equilibrium tide The variation in gravitational potential at the earth's surface due to the relative motions of the earth, moon and sun. Hence Equilibrium phase.

Equilibrium phase The phase of a particular constituent in the equilibrium tide; a linear combination of the displacements of the sun and moon relative to earth. Also known as astronomical argument.

GIS *Geographical Information Systems* Software for creating and manipulating spatial databases.

LAT *Lowest Astronomical Tide* Lowest tidal elevation possible at a location, ignoring meteorological effects.

(M)(H/L)W(S/N) *(Mean) (High/Low) Water (Springs/Neaps)* Calculated from the parameters of the most significant tidal elevation constituents. See also Spring/neap tides and Tidal constituent.

MSL *Mean Sea Level* Calculated using the longest period of records available, ideally greater than 18.6 years.

RMS *Root Mean Square* Square root of the arithmetic mean of a number of squared values

Savonius turbine Simple but inefficient design of rotor often used in measurement devices consisting of two opposing semicylindrical components rotating about an axis. See also Darrieus turbine.

Spring/neap tides Refer to fortnightly variation in tidal elevation amplitude caused principally by the beating of the main lunar and solar semidiurnal tidal constituents, but also by a small non-linear tidal constituent with a period of a fortnight. Springs refers to the period of maximum elevation which occurs one or two days after new or full moon; neaps, the period of minimum elevation which occurs similarly after the first and third quarter of the moon.

Tidal range Difference in elevation between lowest and highest tide in a particular day. Varies over a fourteen day spring-neap-spring cycle.

Tidal stream diamonds Positions marked on Admiralty Charts where tidal stream measurements have been made, usually from a surface vessel and for at least 12hours. Tidal stream speed and direction for spring and neap tides over a 12-hour tidal cycle are included in the chart. The values are averaged for diurnal variation and over the upper 10m of flow. The spring and neap values are obtained by interpolation using the tidal range at the nearest reference port. See also Spring/neap tides.

Tidal constituent A frequency existing in the tidal spectrum. It may correspond to a frequency in the gravitational forcing spectrum, or one of its harmonics in the case of non-linear tidal constituents. A tidal elevation constituent at a point will have an associated amplitude and phase. A tidal stream constituent may be resolved into two horizontal velocity components each with an associated amplitude and phase, or two counter-rotating vectors of the same frequency but different amplitude. See also Tidal ellipse.

Tidal ellipse Locus of tidal stream velocity vectors over a period. For individual constituents, the locus will describe an ellipse over its period; for the signal as a whole, the locus may vary in shape, particularly where non-linear constituents have significant amplitude.

References

ABPmer, The Met Office, Garrad Hassan, and Proudman Oceanographic Laboratory. Atlas of UK marine renewable energy resources. Technical Report R.1106, September 2004.

S. M. Abu Sharkh, D. Morris, S. R. Turnock, L. Myers, and A. S. Bahaj. Performance of an integrated water turbine pm generator. In *International Conference on: Power Electronics, Machines and Drives*, IEE Conference Publication, pages 486–491, Bath, United Kingdom, 2002. Institution of Electrical Engineers.

J. F. Ainslie. Calculating the flowfield in the wake of wind turbines. *Journal of Wind Engineering and Industrial Aerodynamics*, 27(1-3):213–224, 1987.

I. Ammara, C. Leclerc, and C. Masson. A viscous three-dimensional differential/actuator-disk method for the aerodynamic analysis of wind farms. *Journal of Solar Energy Engineering, Transactions of the ASME*, 124(4): 345–356, 2002.

A. S. Bahaj and L. Myers. Analytical estimates of the energy yield potential from the Alderney Race (Channel Islands) using marine current energy converters. *Renewable Energy*, 29(12):1931–1945, 2004.

A. S. Bahaj, J. R. Chaplin, A. F. Molland, and W. M. J. Batten. Experimental investigation into the hydrodynamic performance of marine current turbines. Technical Report 3, University of Southampton, 2005. Sustainable Energy Series.

A. S. Bahaj, A. F. Molland, J. R. Chaplin, and W. M. J. Batten. Power and thrust measurements of marine current turbines under various hydrodynamic flow conditions in a cavitation tunnel and a towing tank. *Renewable Energy*, 32(3): 407–426, 2007a.

A. S. Bahaj, L.E. Myers, M.D. Thomson, and N. Jorge. Characterising the wake of horizontal axis marine current turbines. In A. Falcão, editor, *Seventh European Wave and Tidal Energy Conference*, Porto, Portugal, 2007b.

A. C. Baker. *Tidal power*. IEE energy series 5. Peter Peregrinus/IEE, London, 1991.

R. W. Baker, S. N. Walker, and P. C. Katen. Wake measurements around operating wind turbines. *Transactions of the ASME. Journal of Solar Energy Engineering*, 107(2):183–5, 1985.

N. Barltrop, K. S. Varyani, A. Grant, D. Clelland, and X. P. Pham. Investigation into wave-current interactions in marine current turbines. *Proceedings of the Institution of Mechanical Engineers, Part A: Journal of Power and Energy*, 221(2): 233–242, 2007.

R. J. Barthelmie, L. Folkerts, G. C. Larsen, K. Rados, S. C. Pryor, S. T. Frandsen, B. Lange, and G. Schepers. Comparison of wake model simulations with offshore wind turbine wake profiles measured by sodar. *Journal of Atmospheric and Oceanic Technology*, 23(7):888–901, 2006.

R. J. Barthelmie, S. T. Frandsen, M. N. Nielsen, S. C. Pryor, P. E. Rethore, and H. E. Jorgensen. Modelling and measurements of power losses and turbulence intensity in wind turbine wakes at Middelgrunden offshore wind farm. *Wind Energy*, 10(6):517–528, 2007.

A. Bastos, M. Collins, and N. Collins. Water and sediment movement around a coastal headland: Portland Bill, southern UK. *Ocean Dynamics*, 53:309–321, 2003a.

A. C. Bastos, M. Collins, and N. H. Kenyon. Morphology and internal structure of sand shoals and sandbanks off the dorset coast, english channel. *Sedimentology*, 50(6):1105–1122, 2003b.

P. D. Bates, M. G. Anderson, J. M. Hervouet, and J. C. Hawkes. Investigating the behaviour of two-dimensional finite element models of compound channel flow. *Earth Surface Processes and Landforms*, 22(1):3–17, 1997.

G. N. Bathurst, J. Weatherill, and G. Strbac. Trading wind generation in short term energy markets. *IEEE Transactions on Power Systems*, 17(3):782–789, 2002.

W. M. J. Batten and A. S. Bahaj. CFD simulation of a small farm of horizontal axis marine current turbines. In A. A. M. Sayigh, editor, *World Renewable Energy Congress IX*, Florence, Italy, 2006. Elsevier.

W. M. J. Batten, A. S. Bahaj, A. F. Molland, and J. R. Chaplin. Experimentally validated numerical method for the hydrodynamic design of horizontal axis tidal turbines. In C. Johnstone and A. D. Grant, editors, *Sixth European wave and tidal energy conference*, pages 39–45, Glasgow, UK, 2005.

W. M. J. Batten, A. S. Bahaj, A. F. Molland, and L. S. Blunden. Yawed performance of horizontal axis marine current turbines. In *Second International Conference on Renewable Energy in Maritime Island Climates*, Dublin, Ireland, 2006. The Solar Energy Society.

J. A. Bedwell, K. J. Medler, and J. W. Read. Maff current meter data inventory. Technical Report 15, MAFF Directorate of Fisheries Research, October 1975.

C. Bell, J. M. Vassie, and P. L. Woodworth. POL/PSMSL Tidal Analysis Software Kit 2000. Proudman Oceanographic Laboratory, December 1999.

T. Bentham and R. Britter. Spatially averaged flow within obstacle arrays. *Atmospheric Environment*, 37(15):2037–2043, 2003.

A. Betz. *Introduction to the theory of flow machines*. Pergamon Press, Oxford, 1966.

Black and Veatch Consulting Ltd. UK, Europe and global tidal stream energy resource assessment. Peer review issue 107799/D/2100/05/1, Carbon Trust, September 2004.

Black and Veatch Ltd. Phase II UK tidal stream energy resource assessment. Technical Report 107799/D/2200/03, Carbon Trust, July 2005.

L. Blunden and A. Bahaj. Tidal energy resource assessment for tidal stream generators. *Proceedings of the Institution of Mechanical Engineers, Part A: Journal of Power and Energy*, 221(2):137–146, 2007a.

L. S. Blunden and A. S. Bahaj. Initial evaluation of tidal stream energy resources at Portland Bill, UK. *Renewable Energy*, 31(2):121–132, 2006.

L. S. Blunden and A. S. Bahaj. Effects of tidal energy extraction at Portland Bill, southern UK predicted from a numerical model. In A. Falcão, editor, *Seventh European Wave and Tidal Energy Conference*, Porto, Portugal, 2007b.

L. S. Blunden and A. S. Bahaj. Flow through large arrays of tidal energy converters: is there an analogy with depth limited flow through vegetation? In A. A. M. Sayigh, editor, *Tenth World Renewable Energy Congress*, Glasgow, 2008. Elsevier.

L. S. Blunden, W. M. J. Batten, and A. S. Bahaj. Comparing energy yields from fixed and yawing horizontal axis marine current turbines in the English Channel. In B. Leira, editor, *27th International Conference on Offshore Mechanics and Arctic Engineering*, Estoril, Portugal, 2008. American Society of Mechanical Engineers.

L. S. Blunden, W. M. J. Batten, M. E. Harrison, and A. S. Bahaj. Comparison of boundary-layer and field models for simulation of flow through multiple-row tidal fences. In A. Falcão, editor, *Eighth European Wave and Tidal Energy Conference*, Uppsala, Sweden, 2009. In review.

BODC. British Oceanographic Data Centre internet site, Accessed March 2007. `http://www.bodc.ac.uk`.

J. Bosc and L. Megnint. Evolution des groupes axiaux pour l'equipement des installations maremotrices (development of axial flow units for use in tidal power plants). *Houille Blanche*, 39(8):591–595, 1984.

E Bossanyi, C. Maclean, G. E. Whittle, P. D. Dunn, N. H. Lipman, and P. J. Musgrove. The efficiency of wind turbine clusters. In *Third international symposium on wind energy systems*, pages 401–416, Technical University of Denmark, Lyngby, 1980. BHRA, Cranfield, UK.

J. Brown, A. Colling, D. Park, J. Phillips, D. Rothery, and J. Wright. *Waves, tides and shallow-water processes*. Open University, Milton Keynes, 1997.

I. Bryden and G.T. Melville. Choosing and evaluating sites for tidal current development. *Proceedings of the Institution of Mechanical Engineers, Part A (Journal of Power and Energy)*, 218(A8):567–77, 2004.

I. G. Bryden, S. J. Couch, and G. Harrison. Overview of the issues associated with energy extraction from tidal currents. In A. A. M. Sayigh, editor, *World Renewable Energy Congress IX*, Florence, Italy, 2006. Elsevier.

I. G. Bryden, S. J. Couch, A. Owen, and G. Melville. Tidal current resource assessment. *Proceedings of the Institution of Mechanical Engineers, Part A: Journal of Power and Energy*, 221(2):125–135, 2007.

P. J. H. Builtjes and D. J. Milborrow. Modelling of wind turbine arrays. *Precision Engineering*, pages 417–430, 1980.

A. Burton, D. Sharpe, N. Jenkins, and E. Bossanyi. *Wind Energy Handbook*. John Wiley & Sons, 2001.

A. R. Campbell, J. H. Simpson, and G. L. Allen. The dynamical balance of flow in the Menai Strait. *Estuarine, Coastal and Shelf Science*, 46(3):449–455, 1998.

D. E. Cartwright. Oceanic tides. *Reports on Progress in Physics*, 40(6):665–708, 1977.

D. E. Cartwright, A. C. Edden, R. Spencer, and J. M. Vassie. The tides of the northeast Atlantic Ocean. *Philosophical Transactions of the Royal Society of London. Series A*, 298(1436):87–139, 1980.

P. R. Cave and E. M. Evans. Tidal streams and energy supply in the Channel Islands. In *Energy for rural and island communities IV: Proceedings of the fourth international conference*, volume 4, pages 159–164, Inverness, UK, 1985.

P. R. Cave and E. M. Evans. Tidal stream energy: Economics, technology and costs. In *Water for Energy: Third international symposium on wave, tidal, OTEC and small scale hydro*, pages 133–146, Brighton, UK, 1986. BHRA, Cranfield, UK.

P. R. Cave, E. M. Evans, and K. J. George. Assessment of tidal streams as an energy resource. In *Fifth international conference on energy options — the role of alternatives in the world energy scene*, pages 153–156, University of Reading, UK, 1987. IEE.

R. H. Charlier. Re-invention or aggorniamento? tidal power at 30 years. *Renewable and Sustainable Energy Reviews*, 1(4):271–89, 1997.

V. T. Chow. *Open-channel hydraulics*. McGraw-Hill, 1959.

D. C. Christodoulidis and D. E. Smith. Observed tidal braking in the earth/ moon/ sun system. *Journal of Geophysical Research*, 93(B6):6216–6236, 1988.

J. Clarke, G. Connor, A. Grant, and C. Johnstone. Design and testing of a contra-rotating tidal current turbine. *Proceedings of the Institution of Mechanical Engineers, Part A: Journal of Power and Energy*, 221(2):171–179, 2007a. 10.1243/09576509JPE296.

J.A. Clarke, G. Connor, A.D. Grant, C.M. Johnstone, and D. Mackenzie. Development of a contra-rotating tidal current turbine and analysis of performance. In A. Falcão, editor, *Seventh European Wave and Tidal Energy Conference*, Porto, Portugal, 2007b.

D. Coiro, A. De Marco, F. Nicolosi, S. Melone, and F. Montella. Dynamic behaviour of the patented Kobold tidal current turbine: Numerical and experimental aspects. *Acta Polytechnica*, 45(3):77–84, 2005.

D. Coiro, U. Maisto, F. Scherillo, S. Melone, and F. Grasso. Horizontal axis tidal current turbine: Numerical and experimental investigations. In *OWEMES 2006*, Civitavecchia, Italy., 2006.

A. Crespo, J. Hernndez, and S. Frandsen. Survey of modelling methods for wind turbine wakes and wind farms. *Wind Energy*, 2(1):1–24, 1999.

M. E. C. Damen, F. E. Gardner, and W. te Velde. Results and prospects of full scale two blade fixed pitch free flow Tocardo 2800 tidal turbine in exhaust flume in the netherlands. In A. A. M. Sayigh, editor, *World Renewable Energy Congress IX*, Florence, Italy, 2006. Elsevier.

R. G. Dean and R. A. Dalrymple. *Water wave mechanics for engineers and scientists*. World Scientific Publishing, Singapore, 1991.

C. A. Douglas, G. P. Harrison, and J. P. Chick. Life cycle assessment of the Seagen marine current turbine. *Proceedings of the Institution of Mechanical Engineers, Part M (Journal of Engineering for the Maritime Environment)*, 222 (M1):1–12, 2008.

K. Dyer. *Coastal and Estuarine Sediment Dynamics*. John Wiley & Sons, Chichester, 1986.

e-ROC. `http://www.eroc.co.uk/trackrecord.htm`, October 2008.

EDF-DRD. TELEMAC–2D Version 5.0 validation document. Technical report, Electricité de France Direction des Études et Recherches, Département Laboratoire National d'Hydraulique, July 2000.

EDF-DRD. 2D hydrodynamics. TÉLÉMAC-2D software. Version 5.2 user manual. Technical report, Electricité de France — Direction des Études et Recherches, Département Laboratoire National d'Hydraulique, June 2002.

G. D. Egbert and R. D. Ray. Estimates of M_2 tidal energy dissipation from TOPEX/Poseidon altimeter data. *Journal of Geophysical Research—Oceans*, 106 (C10):22475–22502, 2001.

G. D. Egbert and R. D. Ray. Semi-diurnal and diurnal tidal dissipation from TOPEX/Poseidon altimetry. *Geophysical Research Letters*, 30(17):OCE 9–1–9–4, 2003. 1907.

Gary D. Egbert and Svetlana Y. Erofeeva. Efficient inverse modeling of barotropic ocean tides. *Journal of Atmospheric and Oceanic Technology*, 19(2): 183–204, 2002.

A. J. Elliott. The boundary layer character of tidal currents in the eastern Irish sea. *Estuarine, Coastal and Shelf Science*, 55(3):465–480, 2002.

Engineering Village. `http://www.engineeringvillage2.org`, November 2008.

Darren Engwirda. `http://www.mathworks.com/matlabcentral/fileexchange/10408`, March 2006.

ETSU. Tidal stream energy review. Technical Report ETSU-T–05/00155/REP, Harwell Laboratory, Energy Technology Support Unit, DTI, 1993.

European Commission. The exploitation of tidal and marine currents. Wave energy. Project results. Technical Report EUR 16683 EN, Commission of the

European Communities. Directorate-General for Science, Research and Development, 1996.

E. M. Evans. *Tidal stream energy*. PhD thesis, Plymouth Polytechnic, 1987.

R. A. Flather. A tidal model of the north-west European continental shelf. *Mémoires Société Royale des Sciences de Liège*, 10(6):141–64, 1976.

R. A. Flather and J. Williams. Climate change effects on storm surges: Methodologies and results. In J. Beersma, M. Agnew, D. Viner, and M. Hulme, editors, *Climate Scenarios for Water-Related and Coastal Impacts*, KNMI, the Netherlands, 2000. Climatic Research Unit, UEA, Norwich UK.

Roger A. Flather. Existing operational oceanography. *Coastal Engineering*, 41 (1):13–40, 2000.

P. Fraenkel. Marine current turbines: pioneering the development of marine kinetic energy converters. *Proceedings of the Institution of Mechanical Engineers, Part A: Journal of Power and Energy*, 221(2):159–169, 2007. 10.1243/09576509JPE307.

P. L. Fraenkel and P. J. Musgrove. Tidal and river current energy systems. *IEE Conference Publication*, (171):114–117, 1979.

S. Frandsen. On the wind speed reduction in the center of large clusters of wind turbines. *Journal of Wind Engineering and Industrial Aerodynamics*, 39 (1-3):251–265, 1992.

S. Frandsen, R. Barthelmie, S. Pryor, O. Rathmann, S. Larsen, J. Hojstrup, and M. Thogersen. Analytical modelling of wind speed deficit in large offshore wind farms. *Wind Energy*, 9(1-2):39–53, 2006.

Jean-Charles Galland, Nicole Goutal, and Jean-Michel Hervouet. Telemac. a new numerical model for solving shallow water equations. *Advances in Water Resources*, 14(3):138–148, 1991.

C. Garrett and P. Cummins. Generating power from tidal currents. *ASCE Journal of Waterway Port Coastal and Ocean Engineering*, 130(3):114–118, 2004.

C. Garrett and P. Cummins. The power potential of tidal currents in channels. *Proc. R. Soc. Lond. A*, 461(2060):2563–2572, 2005.

C. Garrett and D. Greenberg. Predicting changes in tidal regime: The open boundary problem. *Journal of Physical Oceanography*, 7(2):171–181, 1977.

A. N. Gorban, A. M. Gorlov, and V. M. Silantyev. Limits of the turbine efficiency for free fluid flow. *Transactions of the ASME. Journal of Energy Resources Technology*, 123(4):311–17, 2001.

Thomas James Hammons. Tidal power. *Proceedings of the IEEE*, 81(3):419–433, 1993.

W. E. Heronomus, P. A. Margarella, R. A. McPherson, and D. L. Ewing. On the extraction of kinetic energy from oceanic and tidal river currents. In H. B. Stewart, editor, *MacArthur workshop on the feasibility of extracting useable energy from the Florida current*, Palm Beach Shores, Florida, 1974.

J. M. Hervouet. Comparison of experimental data and laser measurements with the computational results of TELEMAC code (shallow water equations). In *Computational modelling and experimental methods in hydraulics (Hydrocomp '89)*, pages 107–116, 1989.

J-M. Hervouet and L. Van Haren. TELEMAC–2D Version 3.0 principle note. Technical Report HE–43/94/051/B, Electricité de France Direction des Études et Recherches, Département Laboratoire National d'Hydraulique, 5 January 1994.

J. Højstrup, M. S. Courtney, C. J. Christensen, and P. Sanderhoff. Full scale measurements in wind turbine arrays. Nørrakær Enge II. CEC/JOULE. Technical Report Risø-I-684(EN), Risø National Laboratory, March 1993.

House of Commons Science and Technology Committee. Seventh Report. Wave and tidal energy, April 2001.

House Of Lords Science And Technology Committee. Inquiry into the practicalities of renewable energy, 28 January 2004. Oral Evidence submitted by the Office of Gas and Electricity Markets (OFGEM).

M. J. Howarth. Atlas of tidal elevations and currents around the British Isles. Technical Report OTH–89-293, Department of Energy, 1990.

Hydrographic Department. *Admiralty manual of hydrographic surveying*, volume 1. London, 1965.

IOC, IHO, and BODC. Centenary edition of the GEBCO digital atlas. Published on CD-ROM, 2003.

S. R. Jayne and L. C. St. Laurent. Parameterizing tidal dissipation over rough topography. *Geophysical Research Letters*, 28(5):811–814, 2001.

Jet Propulsion Laboratory. `http://ssd.jpl.nasa.gov/horizons.cgi`, 2008.

J. E. Jones. Coastal and shelf-sea modelling in the european context. *Oceanography and Marine Biology : An Annual Review*, 40:37–141, 2002.

J. E. Jones and A. M. Davies. Processes influencing storm-induced currents in the Irish Sea. *Journal of Physical Oceanography*, 33(1):88–104, 2003.

J. E. Jones and A. M. Davies. An intercomparison between finite difference and finite element (TELEMAC) approaches to modelling west coast of britain tides. *Ocean Dynamics*, 55(3-4):178–198, 2005.

S. Kiho, M. Shiono, and K. Suzuki. Power generation from tidal currents by Darrieus turbine. *Renewable Energy*, 9(1-4):1242–1245, 1996.

E. Kreyszig. *Advanced Engineering Mathematics*. John Wiley & Sons, New York, 8th edition, 1999.

K. Lambeck. *The Earth's Variable Rotation*. Cambridge University Press, Cambridge, UK, 1980.

Landsvirkjun. `http://lv.is/EN/article.asp?catID=130\&artId=336`, September 2008.

B. E. Launder and D. B. Spalding. *Lectures in Mathematical Models of Turbulence*. Academic Press, London, 1972.

C. Le Provost and M. Fornerino. Tidal spectroscopy of the English Channel with a numerical model. *Journal of Physical Oceanography*, 15:1009–1031, 1985.

J. C. Lee and A. M. Davies. Influence of data assimilation upon M_2 tidal elevations and current profiles in the Irish Sea. *Journal of Geophysical Research*, 106(C12):30961–86, 2001.

LEGI. `http://www.coriolis-legi.org/coriolis_turntable.htm`, 2008.

P. B. S. Lissaman. Energy effectiveness of arbitrary arrays of wind turbines. *Journal of Energy*, 3(6):323–328, 1979.

P. B. S. Lissaman and R. L. Radkey. Coriolis Program: a review of the status of the ocean turbine energy system. In *Oceans '79*, pages 559–65, San Diego, CA, USA, 1979. IEEE.

Lunar Energy. `http://www.lunarenergy.co.uk/`, 2007.

R. W. MacDonald. Modelling the mean velocity profile in the urban canopy layer. *Boundary-Layer Meteorology*, 97(1):25–45, 2000.

A. J. MacLeod, S. Barnes, K. G. Rados, and I. G. Bryden. Wake effects in tidal current turbine farms. In *MAREC 2002*, Newcastle, UK, 2002. Institute of Marine Engineering, Science and Technology.

Marine Current Turbines Ltd. `http://www.marineturbines.com/home.htm`, 2007.

A. Mason-Jones, T. O'Doherty, D. M. O'Doherty, P. S. Evans, and C. F. Wooldridge. Characterisation of a HATT using CFD and ADCP site data. In A. A. M. Sayigh, editor, *Tenth World Renewable Energy Congress*, Glasgow, 2008. Elsevier.

B. Metz, O.R. Davidson, P.R. Bosch, R. Dave, and L.A. Meyer, editors. *Climate Change 2007: Mitigation. Contribution of Working Group III to the Fourth Assessment Report of the Intergovernmental Panel on Climate Change.* Cambridge University Press, Cambridge, UK, 2007.

D. J. Milborrow. The performance of arrays of wind turbines. *Journal of Industrial Aerodynamics*, 5(3-4):403–30, 1980.

J. W. Miles. Resonant response of harbours: an equivalent-circuit analysis. *Journal of Fluid Mechanics*, 46:241–65, 1971.

Ministry of Fuel and Power. Severn barrage scheme. Non-parliamentary papers, 1945.

L. Myers and A. S. Bahaj. Simulated electrical power potential harnessed by marine current turbine arrays in the Alderney Race. *Renewable Energy*, 30 (11):1713–31, 2005.

National Audit Office. Department of trade and industry. renewable energy. Technical report, London, February 2005.

National Grid. `http://www.nationalgrid.com/uk/interconnectors/`, September 2008.

National Grid Company plc. Great Britain seven year statement. Technical report, 2005.

H. M. Nepf and E. R. Vivoni. Flow structure in depth-limited, vegetated flow. *Journal of Geophysical Research*, 105(C12):28547–57, 2000.

U. Neumeier. Velocity and turbulence variations at the edge of saltmarshes. *Continental Shelf Research*, 27(8):1046–1059, 2007.

B. G. Newman. Spacing of wind turbines in large arrays. *Energy Conversion*, 16 (4):169–171, 1977.

NTSLF. National Tidal Sea-Level Facility. `http://www.pol.ac.uk/ntslf/tidalp.html`, 2006.

Office of Gas and Electricity Markets (OFGEM). The review of the first year of NETA. A review document. Volume 1. Available from `http://www.ofgem.gov.uk`, July 2002.

J. A. C. Orme and I. Masters. Design and testing of a direct drive tidal stream generator. *Proceedings of the Institute of Marine Engineering, Science and Technology Part B: Journal of Marine Design and Operations*, (9):31–36, 2005.

Oxera. What is the potential for commercially viable renewable generation technologies? Technical report, Oxford, January 2005.

M.L. Parry, O.F. Canziani, J.P. Palutikof, P.J. van der Linden, and C.E. Hanson, editors. *Climate Change 2007: Impacts, Adaptation and Vulnerability. Contribution of Working Group II to the Fourth Assessment Report of the*

Intergovernmental Panel on Climate Change. Cambridge University Press, Cambridge, UK, 2007.

R. Pawlowicz, R. Beardsley, and S. Lentz. Classical tidal harmonic analysis including error estimates in MATLAB using T_TIDE. *Computers and Geosciences*, 28(8):929–937, 2002.

Martin Pehnt. Dynamic life cycle assessment (LCA) of renewable energy technologies. *Renewable Energy*, 31(1):55–71, 2006.

A. Petitjean, J. M. Hervouet, and N. Goutal. Validation test-cases for dam-break models. volume B pt 2 of *Proceedings, Congress of the International Association of Hydraulic Research, IAHR*, pages 821–826, San Francisco, CA, USA, 1997. ASCE, New York, NY, USA.

R. D. Pingree and L. Maddock. The M_4 tide in the English Channel derived from a non-linear numerical model of the M_2 tide. *Deep-Sea Research*, 25: 53–63, 1978.

R. D. Pingree and L. Maddock. Tidally induced residual flows around an island due to both frictional and rotational effects. *Geophysical Journal International*, 63(2):533–546, 1980.

G. W. Platzman. Planetary energy balance for tidal dissipation. *Reviews of Geophysics and Space Physics*, 22(1):73–84, 1984.

G. W. Platzman. An observational study of energy balance in the atmospheric lunar tide. *Pure and Applied Geophysics*, 137(1-2):1–33, 1991.

Pontes et al. Wavenet. Results from the work of the European Thematic Network on Wave Energy. Technical Report ERK5-CT-1999-20001, European Community, March 2003.

D. T. Pugh. *Tides, surges and mean sea-level. A handbook for Engineers and Scientists*. John Wiley & Sons, 1987.

M. R. Raupach, R. A. Antonia, and S. Rajagopalan. Rough-wall turbulent boundary layers. *Applied Mechanics Reviews*, 44(1):1, 1991.

M. M. Rienecker and M. D. Teubner. Note on frictional effects in Taylor's problem. *Journal of Marine Research*, 38(2):183–191, 1980.

W. Rodi. *Turbulence models and their application in hydraulics*. IAHR, Delft, 1980.

M. S. Roulston, J. Ellepola, J. von Hardenberg, and L. A. Smith. Forecasting wave height probabilities with numerical weather prediction models. *Ocean Engineering*, 32(14-15):1841–1863, 2005.

K.-P. Schröder and R. Connon Smith. Distant future of the sun and earth revisited. *Monthly Notices of the Royal Astronomical Society*, 386(1):155–163, 2008.

Toshiaki Setoguchi, Norimasa Shiomi, and Kenji Kaneko. Development of two-way diffuser for fluid energy conversion system. *Renewable Energy*, 29 (10):1757–1771, 2004.

Mitsuhiro Shiono, Katsuyuki Suzuki, and Seiji Kiho. Experimental study of the characteristics of a Darrieus turbine for tidal power generation. *Electrical Engineering in Japan (English translation of Denki Gakkai Ronbunshi)*, 132(3): 38–47, 2000.

G. Sinden. Variability of UK marine resources. Technical report, The Environmental Change Institute (for The Carbon Trust), July 2005.

R. M. Snyder. Tidal hydraulics in estuarine channels. *ASCE J Hydraul Div*, 106 (2):237–245, 1980.

S. Solomon, D. Qin, M. Manning, Z. Chen, M. Marquis, K. B. Averyt, M. Tignor, and H. L. Miller, editors. *Climate Change 2007: The Physical Science Basis. Contribution of Working Group I to the Fourth Assessment Report of the Intergovernmental Panel on Climate Change*. Cambridge University Press, Cambridge, United Kingdom, 2007.

B. K. Sovacool. Valuing the greenhouse gas emissions from nuclear power: A critical survey. *Energy Policy*, 36(8):2940–2953, 2008.

L. C. St. Laurent, H. L. Simmons, and S. R. Jayne. Estimating tidally driven mixing in the deep ocean. *Geophysical Research Letters*, 29(23):21–1 – 21–4, 2002.

U. Stephan and D. Gutknecht. Hydraulic resistance of submerged flexible vegetation. *Journal of Hydrology*, 269(1-2):27–43, 2002.

G. Sutherland, M. Foreman, and C. Garrett. Tidal current energy assessment for Johnstone Strait, Vancouver Island. *Proceedings of the Institution of Mechanical Engineers, Part A: Journal of Power and Energy*, 221(2):147–157, 2007.

G. I. Taylor. Tidal friction in the Irish Sea. *Philosophical Transactions of the Royal Society of London. Series A*, 220:1–33, 1920.

G. I. Taylor. Tidal oscillations in gulfs and rectangular basins. *Proc. London Math. Soc.*, s2–20:148–181, 1922.

J. Thake. Development, installation and testing of a large-scale tidal current turbine. Technical Report T/06/00210/00/REP, UK Department of Trade and Industry, October 2005.

The Engineering Business Ltd. Research and development of a 150kW tidal stream generator. Technical Report URN 02/1400, DTI, 2002.

The Engineering Business Ltd. Stingray tidal stream energy device - Phase 3. Technical Report URN 05/864, DTI, 2005.

K. W. Thompson. Time dependent boundary conditions for hyperbolic systems. *Journal of Computational Physics*, 68(1):1–24, 1987.

K. W. Thompson. Time-dependent boundary conditions for hyperbolic systems, II. *Journal of Computational Physics*, 89(2):439–461, 1990.

S. V. Tsynkov. Numerical solution of problems on unbounded domains. a review. *Applied Numerical Mathematics*, 27(4):465–532, 1998.

A. M. Tuckey, D. J. Patterson, and J. Swenson. A kinetic energy tidal generator in the Northern Territory—results. In *23rd International Conference on Industrial Electronics, Control, and Instrumentation*, volume 2 of *Proceedings of the IECON'97 23rd International Conference on Industrial Electronics, Control, and Instrumentation (Cat. No.97CH36066)*, pages 937–42, New Orleans, LA, USA, 1997. IEEE.

UK Department for Business, Enterprise and Regulatory Reform. Electricity. In *Digest of United Kingdom Energy Statistics*, number 06/87, chapter 5. National Statistics and The Stationary Office, London, 2007.

UK Department of Trade and Industry. Reform of the Renewables Obligation and Statutory Consultation on the Renewables Obligation Order 2007. `http://www.dti.gov.uk/files/file34470.pdf`, October 2006.

UK Department of Trade and Industry. The future of nuclear power. the role of nuclear power in a low carbon uk economy. Technical report, May 2007a.

UK Department of Trade and Industry. Energy trends. Technical report, March 2007b.

UK Department of Trade and Industry. Electricity. In *Digest of United Kingdom Energy Statistics*, number 06/87, chapter 5. 2006.

UK Department of Trade and Industry. Renewables obligation consultation. government response. Technical report, January 2008.

UK Government. Draft climate change bill. The Stationary Office, 2007.

UK Health & Safety Executive. Offshore technology report: Environmental considerations. Technical Report 2001/010, 2001.

UK Hydrographic Department. Admiralty tidal stream atlas NP 257. Approaches to Portland, 1973.

UK Hydrographic Department. Admiralty Chart 2615, 1979.

G. J. W. van Bussel. The science of making more torque from wind: diffuser experiments and theory revisited. *Journal of Physics: Conference Series*, 75(1): 012010–1, 2007.

L. J. Vermeer, J. N. Sorensen, and A. Crespo. Wind turbine wake aerodynamics. *Progress in Aerospace Sciences*, 39(6-7):467–510, 2003.

D. Wang, M. Atlar, and R. Sampson. An experimental investigation on cavitation, noise, and slipstream characteristics of ocean stream turbines. *Proceedings of the Institution of Mechanical Engineers, Part A: Journal of Power and Energy*, 221(2):219–231, 2007.

M. J. Watson and T. L. Shaw. Energy generation from a Severn barrage prior to full commissioning. *Proceedings of the Institute of Civil Engineers: Engineering Sustainability*, 160(1):35–39, 2007.

D. J. Webb. Green's function and tidal prediction. *Reviews of Geophysics*, 12(1): 103–116, 1974.

D. J. Webb. Model of continental-shelf resonances. *Deep-Sea Research and Oceanographic Abstracts*, 23(1):1–15, 1976.

D. J. Webb. Tides and tidal energy. *Contemporary Physics*, 23:419–442, 1982.

D. Weisser. A guide to life-cycle greenhouse gas (GHG) emissions from electric supply technologies. *Energy*, 32(9):1543–1559, 2007.

E. W. Weisstein. Fundamental lemma of calculus of variations. `http://mathworld.wolfram.com/FundamentalLemmaofCalculusofVariations.html`, 2008a.

E. W. Weisstein. Leibniz integral rule. `http://mathworld.wolfram.com/LeibnizIntegralRule.html`, 2008b.

E. W. Weisstein. Rotation operator. `http://mathworld.wolfram.com/RotationOperator.html`, 2008c.

B. W. Wilcox. Tidal movement in the Cape Cod Canal, Massachusetts. *Journal of the Hydraulics Division, Proceedings of the ASCE*, 84:1–9, April 1958. Paper 1586.

P. J. Wiles, T. P. Rippeth, J. H. Simpson, and P. J. Hendricks. A novel technique for measuring the rate of turbulent dissipation in the marine environment. *Geophysical Research Letters*, 33(21):1–5, 2006.

B. Wu, H. Schuh, and P. Bibo. New treatment of tidal braking of earth rotation. *Journal of Geodynamics*, 36(4):515–521, 2003.

C. Wunsch. Moon, tides and climate. *Nature*, 405, 2000.

P. R. Wyman and C. J. Peachey. Tidal current energy conversion. *IEE Conference Publication*, (171):164–166, 1979.

Index